



UNIVERSITÀ  
DEGLI STUDI  
DI PADOVA

Sede Amministrativa: Università degli Studi di Padova  
Dipartimento di Fisica Tecnica

SCUOLA DI DOTTORATO DI RICERCA IN INGEGNERIA INDUSTRIALE  
INDIRIZZO FISICA TECNICA  
CICLO XXIV

**INNOVATIVE TECHNOLOGIES IN HVAC&R SYSTEMS  
FOR ENERGY SAVING AND ENVIRONMENT  
PRESERVATION**

**Direttore della scuola:** *Ch.mo Prof. Paolo Bariani*

**Coordinatore d'indirizzo:** *Ch.mo Prof. Luisa Rossetto*

**Supervisore :** *Ch.mo Prof. Ezio Fornasieri*

**Correlatore:** *Prof. Claudio Zilio*

**Dottorando :** *Riccardo Brignoli*



*Alla mia famiglia*



## Index

<b>ABSTRACT .....</b>	<b>IX</b>
<b>SOMMARIO .....</b>	<b>XI</b>
<b>CHAPTER 1 INTRODUCTORY GENERAL CONSIDERATIONS.....</b>	<b>1</b>
1.1 EFFICIENCY OF THE REFRIGERATION/HEAT PUMP SYSTEM .....	1
1.2 CONDENSER SUBCOOLING .....	8
1.3 HEAT EXCHANGER TWO-PHASE EXERGY LOSSES .....	10
1.4 REFERENCE.....	13
<b>CHAPTER 2 MINICHANNEL HEAT EXCHANGERS .....</b>	<b>15</b>
2.1 MINICHANNEL HEAT EXCHANGERS, STATE OF THE ART .....	15
2.1.1 <i>Introduction</i> .....	15
2.1.2 <i>Flat tube heat exchanger</i> .....	16
2.1.3 <i>Air side predictive models for heat exchanger and pressure drops</i> .....	20
2.1.4 <i>Refrigerant side predictive models for heat transfer coefficient and pressure drops</i> .....	24
2.1.5 <i>Technological constrain: the refrigerant maldistribution</i> .....	25
2.1.6 <i>Technological constrain: the moisture drainage</i> .....	34
2.1.7 <i>Technological constrain: the frosting formation</i> .....	38
2.1.8 <i>Reference</i> .....	41
2.2 DESIGN AND EXPERIMENTAL ANALYSIS OF AN AIR-WATER REVERSIBLE HEAT PUMP WITH A MINICHANNEL HEAT EXCHANGER .....	46
2.2.1 <i>Introduction</i> .....	46
2.2.2 <i>Nomenclature</i> .....	47
2.2.3 <i>The tested heat pump</i> .....	48
2.2.4 <i>Test facilities and testing procedure</i> .....	52
2.2.5 <i>Experimental results</i> .....	58
2.2.6 <i>Conclusions</i> .....	76
2.2.7 <i>Reference</i> .....	78
2.3 DEVELOPMENT OF A SIMULATION TOOL FOR MINICHANNEL CONDENSER AND EVAPORATOR HEAT EXCHANGERS.....	79
2.3.1 <i>Introduction</i> .....	79
2.3.2 <i>Program input/output windows</i> .....	82
2.3.3 <i>Refrigerant property</i> .....	109
2.3.4 <i>Numerical model</i> .....	112
2.3.5 <i>Conclusion</i> .....	121

2.3.6	<i>Reference</i> .....	122
2.4	<b>AUTOMOTIVE MINICHANNEL CONDENSER: COMPARISON OF R1234YF AND R134A REFRIGERANTS PERFORMANCE AND SIMULATION TOOL VALIDATION</b> .....	124
2.4.1	<i>Introduction</i> .....	124
2.4.2	<i>Test facility and test conditions</i> .....	126
2.4.3	<i>Numerical analysis</i> .....	130
2.4.4	<i>Results</i> .....	133
2.4.5	<i>Conclusion</i> .....	138
2.4.6	<i>Reference</i> .....	138
CHAPTER 3	<b>DESIGN AND EXPERIMENTAL ANALYSIS OF A WATER CHILLER USING AMMONIA AS REFRIGERANT</b> .....	<b>143</b>
3.1	INTRODUCTION .....	143
3.2	REFRIGERANT CHARGE NORMATIVE CONSTRAINS .....	146
3.3	SYSTEM CONCEPT AND DESIGN .....	148
3.4	TEST FACILITY AND TESTING PROCEDURE .....	159
3.5	SIMULATION MODEL .....	161
3.6	EXPERIMENTAL RESULTS .....	170
3.7	CONCLUSION .....	177
3.8	REFERENCE .....	179
CHAPTER 4	<b>HEAT PUMPS WITH CARBON DIOXIDE WORKING FLUID</b> .....	<b>183</b>
4.1	ENERGY ASSESSMENT OF A CARBON DIOXIDE HEAT PUMP FOR RESIDENTIAL APPLICATION .....	183
4.1.1	<i>Introduction</i> .....	184
4.1.2	<i>System layout</i> .....	185
4.1.3	<i>Test facility</i> .....	190
4.1.4	<i>Experimental results</i> .....	191
4.1.5	<i>Chiller/heat pump model</i> .....	191
4.1.6	<i>Building model</i> .....	195
4.1.7	<i>Simulation results</i> .....	197
4.1.8	<i>Conclusions</i> .....	200
4.1.9	<i>Reference</i> .....	201
4.2	EXPARIMENTAL ANALYSIS OF A R744 HEAT PUMP WITH AN EJECTOR .....	203
4.2.1	<i>Introduction</i> .....	203
4.2.2	<i>Heat pump and ejector design</i> .....	204
4.2.3	<i>Test rig</i> .....	209
4.2.4	<i>Experimental results and discussion</i> .....	210

4.2.5	<i>Conclusions</i> .....	216
4.2.6	<i>Reference</i> .....	217
<b>CHAPTER 5 FLOW BOILING PERFORMANCE OF REFRIGERANTS CONSIDERING EXERGY LOSSES FOR HEAT TRANSFER AND PRESSURE DROPS .....</b>		<b>219</b>
5.1	INTRODUCTION.....	219
5.2	NOMENCLATURE .....	221
5.3	EVAPORATOR MODEL .....	222
5.4	EVAPORATOR OPTIMIZATION .....	225
5.5	VALIDATION OF MODEL.....	231
5.6	CONCLUSION .....	243
5.7	REFERENCE.....	244
<b>CHAPTER 6 CONCLUSIONS .....</b>		<b>247</b>





# Abstract

Energy savings and the environmental impacts of energy systems are distinctive issues which have driven scientific research in heating, ventilation and air conditioning systems over the last couple of decades.

The main reasons are increasing energy costs and concerns related to negative environmental impacts, in particular anthropic greenhouse effect. There are two contributors to the greenhouse effect for refrigerating systems. The first is due to the primary input energy, in large part from fossil energy, that is, organic substances which produce carbon dioxide upon burning. Therefore, if the energy efficiency increases, this contribution will decrease.

The second contribution is directly due to the operating fluid or refrigerant; the principal halogenated refrigerant fluids utilized are strong greenhouse gases when they leak to the atmosphere.

In order to change these fluids there are two primary options being pursued. The first is the use of natural fluids: carbon dioxide, hydrocarbon, ammonia; the second is the use of new synthetic fluids such as HFOs (hydrofluoroolefins). Both of these solutions have lower (or zero) greenhouse impact relative to halogenated refrigerants. Unfortunately both approaches involve several efficiency and technological problems.

Another way to reduce the working fluid's contribution is to decrease the system refrigerant charge, accounting for standard charge restrictions.

After an introductory chapter, this work presents an air-water commercial reversible heat pump with an aluminium louver-fin flat-tube minichannel heat exchanger, with a small internal volume, allowing for high charge reduction.

Further a user friendly code to simulate the minichannel heat exchanger working as an evaporator or condenser is described. The model allows the user to calculate the heat exchanger performance and to optimize the circuitry.

The model has been used to validate and simulate an automotive air

conditioning condenser working with the new HFO-1234yf fluid, including the effects of the presence of oil.

Later, three applications with natural fluids are investigated: the first is a low charge ammonia chiller for an air conditioning system; the second is a simple reversible water/water carbon dioxide heat pump working for a residential building winter heating, summer cooling and tap water production; the third is a carbon dioxide reversible heat pump working with an ejector as the throttling device for increasing the system efficiency.

Finally, a method to optimize circuit length in a finned coil evaporator and a comparison of fluid evaporating performance, in particular for the new fluids HFO-1234yf and HFO-1234ze(E), is described. The new HFO refrigerants benefit more from circuit optimization than do the halogenated refrigerants they are designed to replace.

In summary the goal is to show some solutions for chiller and heat pump systems in reference to the energy efficiency, charge reduction, and halogenated fluid substitution problems, taking into account that there is no univocal solution to these problems, but each application needs to be studied and optimized considering its own features.

# Sommario

I temi dell'efficienza energetica e dell'impatto ambientale sono requisiti che sempre più negli ultimi decenni hanno guidato la ricerca scientifica riguardante i sistemi di refrigerazione, condizionamento dell'aria e riscaldamento.

Le principali ragioni sono: l'aumento del prezzo dell'energia con una conseguente maggiore attenzione ai costi di esercizio e la necessità di ridurre i contributi indiretto e diretto all'effetto serra antropico. Il contributo indiretto è legato all'energia primaria utilizzata, nella maggior parte dei casi energia fossile quindi combustione di sostanze organiche con produzione di anidride carbonica, attualmente il principale gas serra; per ridurre questo contributo è necessario incrementare l'efficienza energetica del sistema.

Il contributo diretto è dovuto ai refrigeranti, i fluidi alogenati attualmente utilizzati sono fortemente gas serra se immessi in atmosfera.

Si è indirizzati da un lato a sviluppare sistemi utilizzando fluidi naturali: l'anidride carbonica (il cui contributo all'effetto serra, nettamente inferiore agli HFC, è 0 se si utilizza quella esistente), gli idrocarburi, l'ammoniaca; dall'altro lato si sono introdotti nuovi fluidi sintetici HFO a ridotto effetto serra. Si cerca inoltre di ridurre la carica di refrigerante del sistema, tenendo conto che in alcuni casi vi sono vincoli normativi proprio sulla carica.

Nella prima parte di questo lavoro si presenta l'utilizzo di uno scambiatore di calore a minicanali in una PDC aria-acqua commerciale; questo tipo di scambiatori a basso volume interno consente di ridurre considerevolmente la carica di refrigerante del sistema.

In seguito si presenta un modello di simulazione per il calcolo delle prestazioni e l'ottimizzazione di evaporatori e condensatori a minicanali ed una sua validazione/applicazione per calcolare un condensatore funzionante con fluido R1234yf tenendo conto anche della presenza dell'olio.

Si presentano poi soluzioni utilizzanti i fluidi naturali: un chiller ad ammoniaca a bassa carica, una PDC ad anidride carbonica per un edificio residenziale, ed uno studio sperimentale sull'uso dell'eiettore come organo di laminazione per incrementarne l'efficienza di queste PDC.

Si presenta infine un metodo per l'ottimizzazione della lunghezza dei circuiti negli evaporatori a batteria alettata ed un confronto delle prestazioni di diversi refrigeranti in evaporazione con particolare riferimento ai nuovi HFO R1234yf e R1234ze(E).

In sintesi l'obbiettivo di questo lavoro è quello di offrire diverse soluzioni che vadano nella direzione dell'incremento dell'efficienza, della riduzione della carica e dell'impatto ambientale, tenendo conto che non esiste una soluzione univoca a tali problemi, ma che ciascuna applicazione va studiata ed ottimizzata nelle proprie peculiarità.

# Chapter 1 **Introductory general considerations**

In this chapter general considerations about the refrigeration and heat pump systems are presented.

These considerations must be taken as preparatory to the later chapters, where there will be developed aspects about the charge reduction, the use of natural refrigerants and the efficiency increasing.

Everything with the goals of reducing the environmental impact, the energy consumption, and the system costs.

## **1.1 Efficiency of the refrigeration/heat pump system**

The factors which affects the energy efficiency of the refrigeration/heat pump systems are related to:

1. the refrigerant;
2. the components of the unit;
3. the cycle designed configuration;
4. the management of the system;
5. the inertia of the hydraulic circuit.

The refrigerant choice is one of the most important aspects related to the unit efficiency, to the components design and, in the last decades, to the environmental impact.

In reference to the last aspect the laws and the standards are becoming more and more strict. The Kyoto Protocol (1997) and previously the Montreal

Protocol (1987) have banned the refrigerants responsible for the depletion of the ozone layer and are causing limits to the use of global warming responsible refrigerants.

The refrigerants research is looking both to find new synthetic refrigerants having low GWP (global warming potential) and to solve the technological constraints related to the natural refrigerants use.

In this thesis work the new low GWP refrigerants HFO (hydrofluoroolefin) R1234yf ( $\text{CF}_3\text{CF}=\text{CH}_2$ ) and R1234ze(E) ( $\text{CF}_3\text{CH}=\text{CHF}$ ) have been compared with R134a in an automotive minichannel condenser application, and evaluated their boiling heat transfer potential in plain evaporator tubes.

Regarding the natural refrigerant use, a low ammonia charge chiller, and two heat pumps working with carbon dioxide have been investigated.

The main refrigerant property, which need be considered are:

- thermal conductivity;
- the thermal mass capacity;
- the critical pressure;
- the molecular mass;
- the volumetric refrigerant effect.

The refrigerant whose properties realize the best compromise for each application need to be found.

Vio [1] and Fornasieri [2] presented some methods to compare the energy efficiency of different fluids by considering:

- the basic ideal cycle;
- the energy losses in a real system;
- aspect related to the compressor.

In Table 1.1 the basic refrigerant properties for a basic ideal cycle between an evaporator temperature of  $-3^\circ\text{C}$  and a condenser temperature of  $40^\circ\text{C}$  are reported.

Fluid	Molecular Mass	T critical [°C]	P.e.n. (glide) [°C]	Condenser pressure [10 <sup>5</sup> Pa]	Evaporator pressure [10 <sup>5</sup> Pa]	EER
R22	88.47	96.2	-40.8	15.34	1.64	6.12
R717	17.03	133.0	-33.3	15.55	1.19	6.40
R407C						
R32/125/134a (23/25/52)	86.20	86.7	-40.2 (6.9)	16.49	1.54	5.93
R410A						
R32/25 (50/50)	72.58	72.50	-51.4 (<0.1)	24.28	2.73	5.79
R290	44.10	96.8	-42.1	13.69	1.68	5.97
R134a	102.03	101.1	-26.1	10.16	3.26	6.09
R744	44.01	31.06	-87.9	-	37.66	-

*Table 1.1. Properties of different refrigerants for a basic ideal cycle –between temperatures evaporator/condenser of -3/40°C respectively. For carbon dioxide the cycle is between -30/30 °C.*

As detailed in Fornasieri [2] refrigerants with high critical pressure have greater EER. For carbon dioxide above a temperature of 31.06 °C a transcritical cycle has to be considered with a gas cooler instead of the condenser, so it is lower efficiency. For same application such as the tap water production, where the water could be heated from about 10 °C to 70 °C, the gas cooler heat transfer process could be very efficient, moreover the high operative pressure allows the system to get a high volumetric refrigerant effect.

The exergy losses in a real system are represented by:

- pressure drops in the pipes;
- compression losses;
- heat transfer losses.

The exergy losses related to the pressure drops in the pipes can be evaluated using the penalty factor introduced by Casson et al. [3].

$$Fp = \frac{1}{\Delta h_{evap} \cdot \rho_{evap,out}^2} \quad (1.1)$$

Where  $\Delta h_{evap}$  is the enthalpy difference at the evaporator (the mass flow rate is inversely proportional to it) and the  $\rho_{evap,out}$  is the refrigerant density at the evaporator outlet.

The exergy losses related to the compressor factor depends on several factors as detailed in Fornasieri [2].

In [2] the parameters related to exergy losses in a real system are reported for a temperature of 3 °C, a summary is reported in Table 1.2, where  $\lambda_l$  is the liquid thermal conductivity,  $\rho_v$  is the vapor density.

Fluid	Fp [(kg·m <sup>6</sup> )/J <sup>3</sup> ]	$\lambda_l$ [W/(mK)]	$\rho_v$ [kg/m <sup>3</sup> ]	Evaporator pressure [10 <sup>5</sup> Pa]
R22	$4.91 \cdot 10^{-19}$	0.0953	23.5	5.48
R717	$0.548 \cdot 10^{-19}$	0.517	3.84	4.80
R407C				
R32/125/134a (23/25/52)	$4.68 \cdot 10^{-19}$	0.104	23.33	5.52
R410A				
R32/25 (50/50)	$2.16 \cdot 10^{-19}$	0.114	33.19	8.84
R290	$3.98 \cdot 10^{-19}$	0.105	11.31	5.19
R134a	$13.97 \cdot 10^{-19}$	0.0924	16.00	3.26
R744	-	0.107	107.05	37.66

Table 1.2. Properties which affect the exergy losses in a a real cycle at 3°C.

It can be pointed out the fluids working with high operative pressure are less penalized.

In reference to the exergy losses related to the heat exchanger important properties are the liquid conductivity and the vapor density (the reason will be detailed in paragraph 1.3); the higher are the liquid conductivity and the vapor density, the lower are the heat exchanger exergy losses.

The effect of the liquid conductivity can be easily understood looking at the correlations used to calculate the heat transfer coefficient, it is almost proportional to  $\lambda_l$ .



The ammonia high liquid conductivity, which has to be added low exergy losses in the throttling processes, make this a very good refrigerant.

It can be pointed out the mixture R410A is a good refrigerant too, in general the low exergy losses refrigerants are the ones working with high pressure.

In reference to the compressor, the volumetric cooling effect is the heat flux at the evaporator divided by the compressor volumetric flow rate sucked.

$$\text{It became : } Q_{OV} = \frac{\Delta h_{ev}}{v_{out,ev}} \quad (1.2)$$

Where  $\Delta h_{ev}$  is the enthalpy difference at the evaporator, while  $v_{out,ev}$  is the refrigerant specific volume at the compressor suction.

Other important properties are the compressor discharge temperature and the attitude to cool the compressor engine. A high refrigerant discharge temperature could be a problem with the lubricant oil (oil carbonization).

The index is related to the attitude of cooling the compressor engine [2].

$$I_r = \frac{c_p}{\Delta h_{comp}} \quad (1.3)$$

Where  $c_p$  is the vapor specific heat at the compressor suction pressure, while  $\Delta h_{comp}$  is the enthalpy difference between the discharge and the suction of the compressor.

These parameters [2] are reported in Table 1.3 for a basic ideal cycle -3/40°C of evaporator/condenser temperatures as reported in [2].

Fluid	Q <sub>ov</sub> [kJ/m <sup>3</sup> ]	T <sub>discharge</sub> [°C]	I <sub>r</sub> [°C <sup>-1</sup> ]	Condenser pressure [10 <sup>5</sup> Pa]
R22	3632	56.0	0.0307	15.34
R717	4124	87.5	0.0162	15.55
R407C				
R32/125/134a (23/25/52)	3680	53.2	0.0354	16.49
R410A				
R32/25 (50/50)	5353	56.2	0.0371	24.28
R290	3052	43.8	0.0399	13.69
R134a	2304	44.0	0.0379	10.16

*Table 1.3. Properties which affect the exergy losses in the compression process for a basic ideal cycle -3/40 °C.*

It can be pointed out the ammonia has a very high discharge temperature, it depends on its limit curves shape, this refrigerant is usually used in application with opened compressor because it is aggressive with the copper used in electrical windings; the oil could be cooled by an apposite oil cooler.

In Figure 1.1 an example of the limit curves shape is reported:

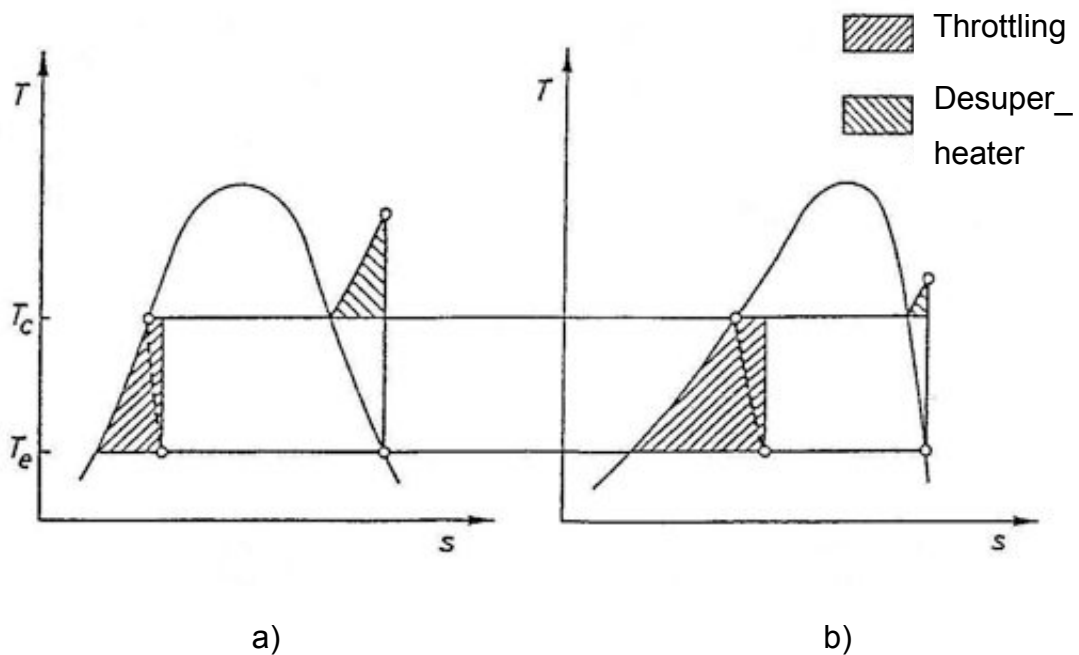


Figure 1.1. Limit curves for different fluids, the throttling and the desuperheater exergy losses are highlighting at the same evaporating and condenser temperatures.

In general (Trouton rule) the higher is the molecular mass, the higher is the ratio between the liquid phase specific heat and the evaporating latent heat, and the curves tends to a) type. It is the ammonia case, so ammonia has low throttling and high desuperheater exergy losses and high discharge temperature.

Opposite the carbon dioxide has a high throttling exergy loss, this kind of loss can be easier contained than desuperheater one by using for example two-stage throttling.

In reference to the component in the next paragraph a brief treatment about the heat exchangers will be made, for more info see [1] and [2].

Regard the management of the system, it depends on the application, the basic principle is the reduction between the condenser and the evaporator difference of pressure, the influence of the management is higher at part load ratio [1].

Regard the inertia of the hydraulic circuit it can affect the energy efficiency at part load ratio [1].

## 1.2 Condenser subcooling

The subcooling obtained in the last part of the condenser refrigerant path can increase or decrease the system efficiency, it depends on the refrigerant characteristics and the ratio between the subcooling and the condensation areas.

The higher is the subcooling the higher is the condensation temperature and the lower is the throttling exergy loss, so an optimal value of the ratio between the subcooling and the condensation areas must exist for each refrigerant.

Fornasieri and Cavallini [5] investigated this aspect by simulating a cycle with isobars evaporation and condensation, uniform heat transfer coefficient, the same cooling capacity and secondary fluid (air) mass flow rate; the ratio between the subcooling and the condensation areas is the independent variable, the simulation conditions are:

- $T_{\text{air,in,cond}} = 35^{\circ}\text{C}$ ;
- $T_{\text{air,out,cond}} = 45^{\circ}\text{C}$ ;
- $T_{\text{cond}} = 50^{\circ}\text{C}$ ;
- $T_{\text{evap}} = 0^{\circ}\text{C}$ ;
- Superheating =  $6^{\circ}\text{C}$ ;
- $\eta_{\text{is}} = 0.8$  (isentropic compression efficiency).

The results are reported in the Figure 1.2.

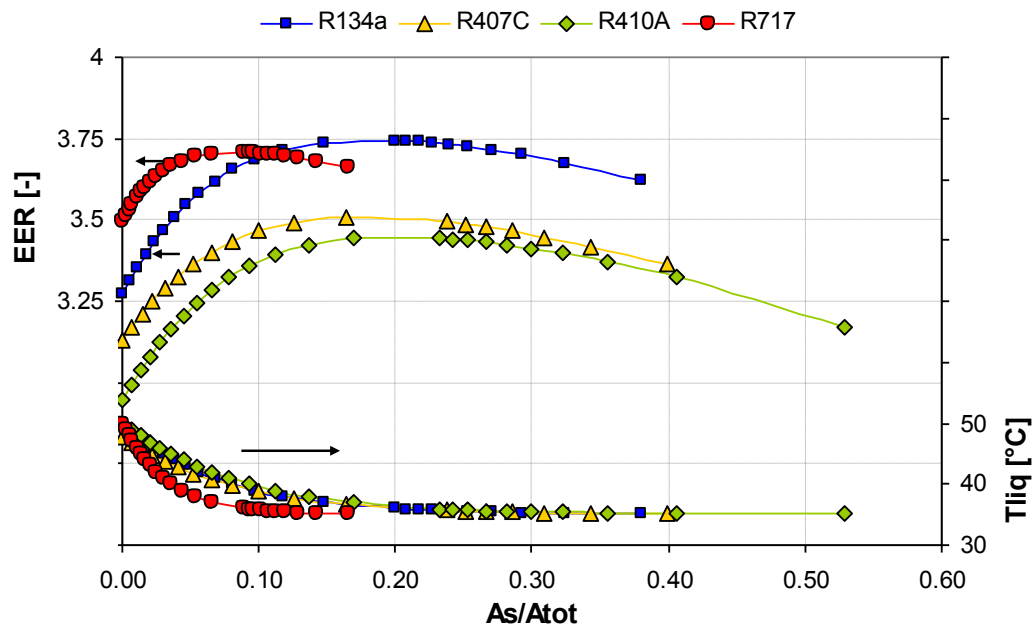


Figure 1.2. EER vs. condenser subcooling and total areas ratio, on the secondary axis the condenser liquid outlet temperature is pointed.

As expected the low throttling exergy losses refrigerants take more advantage by the subcooling, the subcooling optimal area is almost the 15-20% of the total. Ammonia has lower areas ratio and less advantage in EER because of its low throttling exergy losses.

An appropriate condenser circuitry design with confluences where the refrigerant is subcooling state allows the heat transfer coefficient increase because it increases the refrigerant specific mass flow rate in one phase state without getting penalizations in the heat transfer by the pressure drops increasing. A liquid receiver into which condenser circuits flow, and from which the subcooling circuitry is fed could be very helpful to obtain better performance.

### 1.3 Heat exchanger two-phase exergy losses

The exergy losses in the heat exchangers strongly affect the system efficiency.

During a heat exchange with two-phase refrigerant state, the exergy losses are related both the heat transfer coefficient and the pressure drops.

In two-phase state the pressure is directly related to the temperature according to the Clapeyron-Clausius equation (written for liquid-vapor phases equilibrium).

$$\frac{dT}{dp} = \frac{T}{r} \cdot \left( \frac{1}{\rho_v} - \frac{1}{\rho_l} \right) \quad (1.4)$$

Where  $p$  is the pressure,  $T$  is the absolute temperature,  $r$  is the latent heat,  $\rho_v$  and  $\rho_l$  are the vapor and the liquid density respectively.

The temperature drops related to the pressure drops decrease the total temperature difference between the refrigerant and the secondary fluid i.e. the heat exchanger driving potential.

The optimization of the circuitry means finding the optimal circuitry specific mass flow rate value. This optimal value must exist because the higher is the specific mass flow rate, the higher is the heat transfer coefficient and the higher are the pressure/temperature drops.

In a heat exchanger having a certain numbers of parallel circuits with the same hydraulic diameter and the same tubes length (for example a finned coil), finding the optimal specific mass flow rate means trying the optimal circuit length that realize the maximum heat flux, with assigned boundary conditions.

Cavallini [6] introduced a penalty factor which takes into account both the mentioned components in the exergy losses.

By applying the heat balance over an elementary tube length  $dz$ , and the equation (1.4), the local temperature drops can be written as:

$$\frac{dT_s}{dx} = \frac{G \cdot d \cdot T_s}{4 \cdot \alpha \cdot \Delta T_{dr}} \cdot \left( \frac{1}{\rho_l} - \frac{1}{\rho_v} \right) \cdot \frac{dp_f}{dz} \quad (1.5)$$

Where  $T_s$ : is the saturation temperature,  $x$ : is the refrigerant quality,  $G$  is the specific mass flow rate,  $d$  is the tube hydraulic diameter,  $\alpha$  is the heat transfer coefficient,  $\Delta T_{dr}$  is the driving temperature difference (difference between the saturation and the tube wall),  $\rho_v$  and  $\rho_l$  are the vapor and the liquid density respectively,  $p_f$  is the saturation pressure.

It can be pointed out both the two-phases heat exchanger exergy losses are in the equation 1.5.

The penalty factor can be defined as:

$$PF = \frac{dT_s}{dx} \cdot \Delta T_{dr} = \frac{G \cdot d \cdot T_s}{4 \cdot \alpha} \cdot \left( \frac{1}{\rho_l} - \frac{1}{\rho_v} \right) \cdot \frac{dp_f}{dz} \quad (1.6)$$

It can be used as a criterion to rank different working fluids, when it is calculated at the same heat transfer coefficient, the smaller is the PF the better is the potential performance of a refrigerant, in fact the heat transfer exergy losses term is the same for all refrigerants, so the exergy losses associated to the refrigerants temperature drops can be compared.

The penalty factor can also be used for the same fluid working in different geometries at the same heat transfer coefficient, the smaller the better.

Another parameter that can be used for the same purpose is the TTP: Two temperature penalization which is defined as:

$$TTP = DT_{dr} + 0.5 \cdot DT_{sr} \quad (1.7)$$

Where  $DT_{dr}$  is the driven temperature difference (saturation minus tube wall), while  $DT_{sr}$  is the saturation temperature difference (the temperature drops due to the pressure drops), the coefficient 0.5 is due to the consideration that only almost a half of the refrigerant saturation temperature drops is lost as heat transfer driving potential.

In Figure 1.3 the idealized temperature profiles within the  $DT_{dr}$  and the  $DT_{sr}$  quoted, for a counter-current condenser are shown.

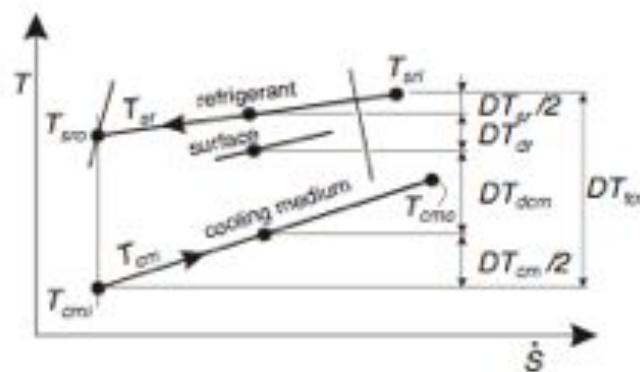


Figure 1.3. Idealized temperatures profiles for a counter-current condenser.

These parameters can also be used either to compare the attitude of heat exchanger of different refrigerants or to find the best geometry configuration for the same refrigerant.

It will be used in Chapter 5 to compare different refrigerants flow boiling penalization including the new HFO R234yf and R1234ze(E).

Cavallini et al. [7] showed a relation between the  $PF$  and the  $TTP$ .

The refrigerant vapour density importance can now be pointed out, if the vapor density decreases both the pressure drops and the heat transfer coefficient decrease; moreover, looking at the equation 1.4 the lower is the vapor density, the higher is the derivative of the temperature and the pressure drops.



## 1.4 Reference

1. Vio M., (2006), Air-water chillers energetic performances at full and partial load, Proc. of AICARR Conf., First session, 113-159.
2. Fornasieri E. (2002), Refrigeratori d'acqua con compressore volumetrico: come promuovere l'efficienza energetica, 43° Convegno annuale AICARR, 3: 17-46.
3. Casson V., Cecchinato L., Fornasieri E. (2001), Quale fluido per quale impianto: un esame ragionato dei requisiti e delle caratterizzazioni dei fluidi frigorigeni, Il Freddo, 5/01: 37-45.
4. A. Cavallini, J.S. Brown, D. Del Col, C. Zilio. In tube condensation performance of refrigerant considering penalization terms (exergy losses) for heat transfer and pressure drop. International J. Heat and Mass Transfer 53 (13-14) (2010) 2886-2896.
5. E. Fornasieri, A. Cavallini. Recenti sviluppi delle conoscenze sull'uso dei fluidi operatori nei cicli frigoriferi. Padova, 2004.
6. A. Cavallini. In-tube condensation performance of refrigerants. 11<sup>th</sup> International Refrigeration and Air Conditioning Conference at Purdue. July 17-20, 2006.
7. Cavallini A., J:S: Brown, D. Del Col, C. Zilio. In tube condensation performance of refrigerants considering penalization terms (exergy losses) for heat transfer and pressure drop. International J. Heat and Mass Transfer 53 (13-14) (2010) 2886-2896



## Chapter 2 **Minichannel heat exchangers**

This chapter includes four sub-chapters within:

- 2.1) a brief review of louver-fin flat-tube with internal minichannel heat exchangers state of the art;
- 2.2) the design and the experimental analysis of a reversible air-water heat pump working with a minichannel heat exchanger;
- 2.3) the development of minichannel evaporator/condenser heat exchangers simulation tool;
- 2.4) a first validation of this tool and an experimental analysis of an automotive minichannel condenser.

### **2.1 Minichannel heat exchangers, state of the art**

In this sub-chapter a brief review of a louver-fin flat-tube with internal minichannel heat exchanger is presented.

The application of this kind of heat exchanger is actually increasing. It is of interest to HVAC&R industry because it has some advantages over the round tube heat exchanger, but some of its technological limits have not been solved yet.

#### **2.1.1 Introduction**

With reference to global and local environment growing concern, refrigeration and heat pump equipment is shifting to small internal volume components in order to decrease the charge inventory. This tendency is advantageous both with HFCs or other high GWP-fluids and with natural refrigerants. Low charge

reduces the total possible leakage of synthetic refrigerants and reduces the risks of accidents in case ammonia, hydrocarbons or carbon dioxide leaks. To reduce heat exchangers internal volume on the refrigerant side without decreasing the energy efficiency of the whole component, the channel area cross-section, i.e. the hydraulic diameter, can be decreased and micro or mini-channel heat exchangers can be adopted.

Heat pump and refrigeration industry introduced multi-port extruded aluminium flat tube parallel flow heat exchangers in air-air or air-water vapour compression units.

### 2.1.2 Flat tube heat exchanger

A flat tube heat exchanger can be built by brazing aluminum fins to an extruded flat aluminum tubes, but other ways and other materials could also be used.

The flat extruded tube has an internal mini or micro-channel. The definition of mini-micro channel is not univocal in the literature; Thome and Ribatski (2005) [1] considered two definitions by Kandlikar - Grande (2003) and Kew - Cornwell (1997).

The first definition, considering  $D_h$  as the hydraulic diameter, is the following:

- $D_h > 3$  mm: conventional channel;
- $200 \text{ mm} < D_h < 3$  mm: minichannel;
- $D_h < 200$  mm: microchannel.

The second definition considers a threshold hydraulic diameter calculated as:

$$D_{th} = \left( \frac{4\sigma}{g(\rho_l - \rho_v)} \right)^{0.5} \quad (2.1.1)$$

Where:

- $\sigma$ : surface tension [N/m];
- $g$ : acceleration of gravity [9.801 m/s<sup>2</sup>];

- $\rho_l$ : liquid density [ $\text{kg}/\text{m}^3$ ];
- $\rho_v$ : vapor density [ $\text{kg}/\text{m}^3$ ].

Using this last definition the hydraulic diameter changes with the two-phase operative fluid saturation pressure.

In following of this treatise the difference between minichannel and microchannel will be neglected.

In his PhD thesis Chiarello [2] reported some figures relating to a minichannel heat exchanger:

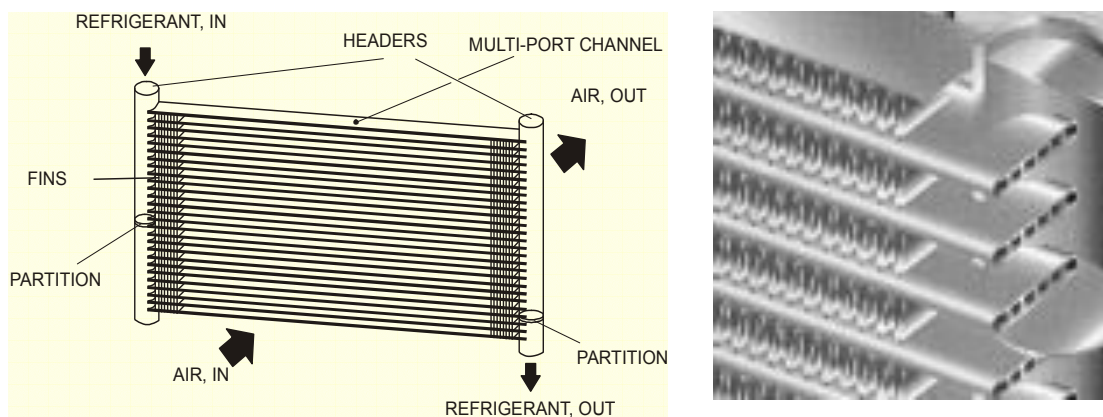


Figure 2.1.1. Examples of minichannel, Chiarello [2] (2009).

Use of a flat tube heat exchanger.

Numerous studies have been conducted to compare the performance of flat tube heat exchanger with that of a round tube one, they have demonstrated that the flat tube presents many advantages in many systems. This work focuses on its refrigeration and air conditioning applications for an air-refrigerant heat exchanger.

The general advantages are:

- low internal volume and consequently low refrigerant charge;
- low costs;
- high heat transfer area to core volume ratio;
- the shape of the flat tube improves the air heat exchanger coefficient;

- high pressure resistance;
- compactness and smaller size.

The flat tube geometry provides higher fin efficiency than the round tube one, because the wake region behind the tube does not decrease slightly the heat transfer in the fin area downstream the tube as it could occur in round tube shape.

Chiarello [2] in his PhD thesis well shown this effect.

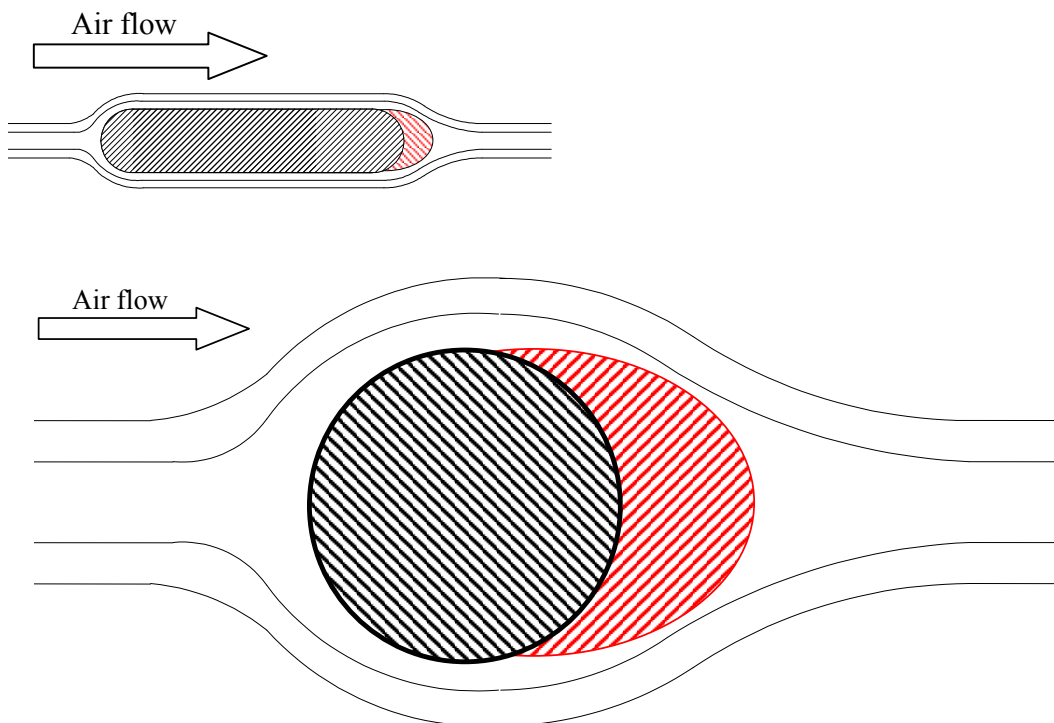


*Figure 2.1.2. Tube section, wake and streamlines respectively of a minichannel and a round tube; Chiarello [2].*

Park and Jacobi [3] compared the thermal hydraulic performance of a round tube to flat tube heat exchanger under optimal conditions with the second thermodynamic law and found the flat tube design can achieve the same thermodynamic performance of round tube one with very smaller surface area and core volume.

Jacobi et al. [4] observed that the full potential of flat tube heat exchanger was not been explored, their work goals were to investigate of dry-wet and frosted surface working conditions.

In fact some application still need to be investigated to solve technological problems, in particular looking at the evaporator use:

- the moisture drainage in dehumidification and in defrosting modes;
- the defrosting management on the air side;
- the refrigerant distribution in the headers;

Another heat exchanger constrains are the high pressure drops on both sides.

As regards the behavior of the louver fin, Beauvais [5] was the first to examine the flow structure in the louvered-fin heat exchanger, the flow visualization images suggested that a large part of the flow rate is louver directed, nearly parallel to the louver, therefore the louver does not act as a surface roughness as believed before this study.

In the next Figure a louver fin geometry with the two main flow direction is shown.

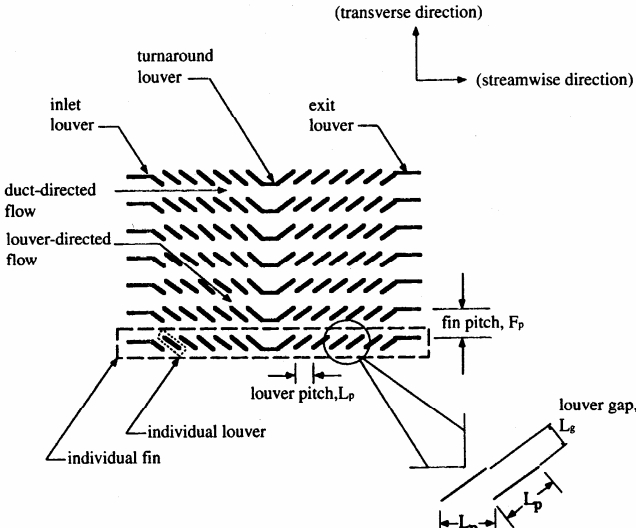


Figure 2.1.3. Louvered fin geometry, with the two main directions in Jacobi et al. [4].

Davenport [6] executed many experiments with different louvered heat exchanger geometries, the data was casted in terms of Reynolds number based on louver pitch, instead the hydraulic diameters finding a lower scatter. Achaichia and Cowell [7-8] made experiments to determine the heat transfer and pressure drops performance for louvered fin with  $120 < \text{Re} < 8000$ , the results were used to developed a heat transfer coefficient and friction factor correlations.

They found a low Reynolds number and large boundary layers cause a duct directed flow, which corresponds to a lower heat transfer coefficient than the louvered direct flow. Smaller louver angle, larger ratio between fin pitch and louver pitch, cause higher Reynolds number for which the flow type changes from duct direct to louver direct.

Zhang and Lang [9] made experiments with a certain number of louvered fins array and studied the effect of louver angle, they developed a method for evaluate the best tradeoff between heat exchanger and pressure drops; a louver angle of 25 degrees and a fin pitch of about 2 mm was suggested.

Suga and Aoki [10] performed a numerical analysis of heat transfer and pressure drops and suggested a relation for finding the optimum ratio between the fin pitch and the louver pitch for each louver angle, a louver angle in a range of 20-30 degrees was suggested.

### **2.1.3 Air side predictive models for heat exchanger and pressure drops**

The air side thermal resistance is the most important thermal resistance in minichannel heat exchanger.

Here the heat transfer coefficient and pressure drops correlations of Chang-Wang and the heat transfer coefficient correlation of Jacobi et al are reported. In their work Chang and Wang [11] reported a generalized heat transfer correlation for louver fin geometry, they presented the previous models of



Davenport, Achaichia and Cowell, Sunden and Svantesson, and finally they developed a new airside heat transfer coefficient correlation with a regression of their data bank.

The data bank consisted in 91 louvered heat transfer geometry with different louver angle, tube width, louver length, louver pitch, fin length and fin pitch; the 89.3% of data were correlated within  $\pm 15\%$ .

In figure below the airside geometry parameters are schematically show.

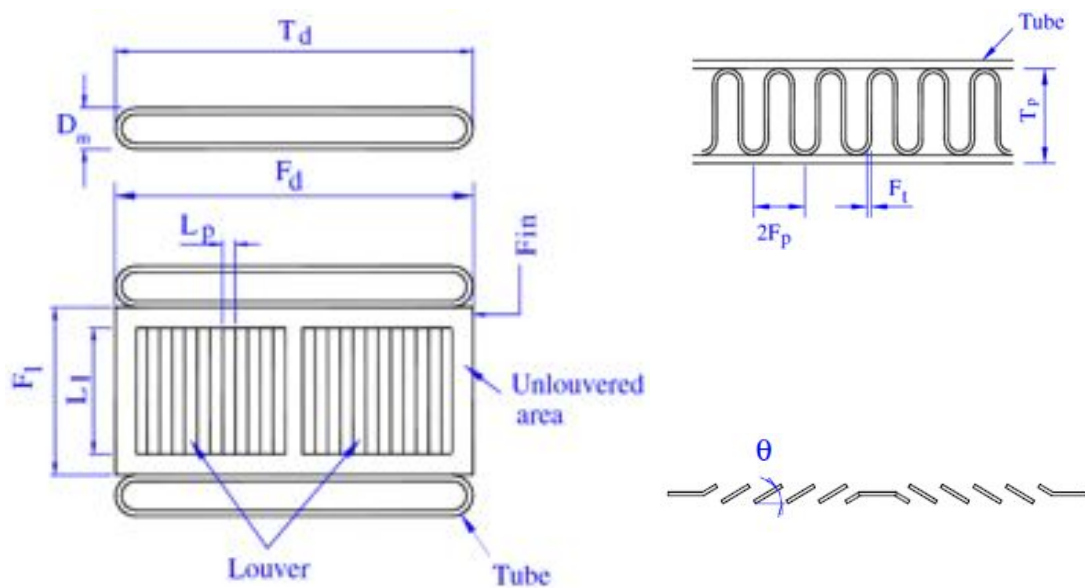


Figure 2.1.4. Minichannel airside geometrical parameters.

In particular:

- plate depth ( $T_d$ ), plate thickness ( $D_m$ ), plate pitch ( $T_p$ );
- fin thickness ( $F_t$ ), fin pitch ( $F_p$ ), fin length ( $F_l$ ), fin depth ( $F_d$ );
- louver length ( $L_l$ ), louver pitch ( $L_p$ ) and louver angle ( $\theta$ ).

The Chang-Wang equation is:

$$J = Re_{lp}^{-0.49} \left(\frac{\theta}{90}\right)^{0.27} \left(\frac{F_p}{L_p}\right)^{-0.14} \left(\frac{F_l}{L_p}\right)^{-0.29} \left(\frac{T_d}{L_p}\right)^{-0.23} \left(\frac{L_l}{L_p}\right)^{0.68} \left(\frac{T_p}{L_p}\right)^{-0.28} \left(\frac{F_t}{L_p}\right)^{-0.05} \quad (2.1.2)$$

Where  $J$  is the Colburn factor and  $Re_{Lp}$  is the Reynolds number based on louver pitch, the  $Re_{Lp}$  range is  $100 < Re_{Lp} < 3000$ ,  $\theta$  is in degrees.

Jacobi et al [4] observed the Chang and Wang equation shows the better agreement with their experimental data at high  $Re_{Lp}$  numbers, while it over predict the data at low  $Re_{Lp}$  numbers when  $Re_{Lp} < 100$ ; they investigated the reasons and developed a new equation using the Chang-Wang data, their new experimental data, and others data.

The new equation has a larger  $Re_{Lp}$  range than Chang-Wang one, provides a better fit with the experimental data and includes a power-law dependence as Chang-Wang one, but also it includes the observed fluttering at low  $Re_{Lp}$  ( $Re_{Lp} > 50$ ) and it recognizes an optimal fin pitch relation.

The Jacobi et al equation equation is:

$$J = 1.43 F_{Re} F_{lowRe} F_{louver} \theta^{0.247} \left(\frac{F_l}{L_p}\right)^{-0.201} \left(\frac{F_l}{F_d}\right)^{0.306} \left(\frac{L_l}{F_l}\right)^{0.801} \left(\frac{F_l}{T_p}\right)^{-0.0162} \left(1 - \frac{F_t}{L_p}\right)^{2.32} \left(\frac{L_p}{F_p}\right)^{0.226} \quad (2.1.3)$$

$$F_{Re} = Re_{Lp}^{(-0.435 - 0.0286 \cosh(\frac{F_p}{L_p} - 2.14))}$$

$$F_{lowRe} = 1 - \frac{\sin\left(\frac{L_p}{F_p} \theta\right)}{\cosh\left(0.0482 Re_{Lp} - 0.0763 \frac{F_d}{F_p}\right)}$$

$$F_{louver} = 1 + 0.00245 \left(\frac{F_d}{F_p}\right) \tan(\theta) \cos\left(2\pi \left(\frac{F_p}{L_p} \cot(\theta) - 1.77\right)\right)$$

The Colburn factor is related to the Nusselt number by:  $J = \frac{Nu}{Re Pr^{1/3}}$

In reference to the airside pressure drops, Chang and Wang [12] developed a correlation to calculate the friction factor for louver fin geometry, and later an amendment [13] to avoid the equation discontinuity at  $Re_{Lp}=150$ . The equation is reported below:

$$f_1 = \begin{cases} 14.39 Re_{Lp}^{\left(-0.805\frac{F_p}{F_l}\right)} \left(\log_e \left(1 + \frac{F_p}{L_p}\right)\right)^{3.04} & Re_{Lp} < 150 \\ 4.97 Re_{Lp}^{\left(0.6049 - \frac{1.064}{\theta^2}\right)} \left(\log_e \left(\left(\frac{F_t}{F_p}\right)^{0.5} + 0.9\right)\right)^{-0.527} & 150 < Re_{Lp} < 5000 \end{cases}$$

$$f_2 = \begin{cases} \left(\log_e \left(\left(\frac{F_t}{F_p}\right)^{0.48} + 0.9\right)\right)^{-1.435} \left(\frac{D_h}{L_p}\right)^{-3.01} \left(\log_e(0.5Re_{Lp})\right)^{-3.01} & Re_{Lp} < 150 \\ \left(\left(\frac{D_h}{L_p}\right) \log_e(0.3Re_{Lp})\right)^{-2.966} \left(\frac{F_p}{L_l}\right)^{-0.7931\left(\frac{T_p}{T_h}\right)} & 150 < Re_{Lp} < 5000 \end{cases}$$

$$f_3 = \begin{cases} \left(\frac{F_p}{L_l}\right)^{-0.308} \left(\frac{F_d}{L_l}\right)^{-0.308} \left(e^{-0.1167\frac{T_p}{D_m}}\right) \theta^{0.35} & Re_{Lp} < 150 \\ \left(\frac{T_p}{D_m}\right)^{-0.0466} \log_e \left(1.2 + \left(\frac{L_p}{F_p}\right)^{1.4}\right)^{-3.553} \theta^{-0.477} & 150 < Re_{Lp} < 5000 \end{cases}$$

$$f = f_1 \times f_2 \times f_3 \quad (2.1.4)$$

$$f = \frac{A_c \rho_m}{A \rho_1} \left[ \frac{2\rho_1 \Delta P}{G_c^2} - (K_c + 1 - \sigma^2) - 2 \left( \frac{\rho_1}{\rho_2} - 1 \right) + (1 - \sigma^2 - K_e) \right] \quad (2.1.5)$$

Where

- DP: Pressure drop [Pa];
- $f$ : Fanning frictional factor;
- all the lengths are in [mm];
- $T_h = T_p - D_m$ ;
- $D_h$ : hydraulic diameter, defined in [14];
- $q$ : louver angle in degrees;

- $r_1, r_2, r_m$ : are respectively the inlet, the outlet, the average density [ $\text{kg/m}^3$ ];
- $A_c, A$ : are the minimum flow area, the total area [ $\text{m}^2$ ];
- $G_c = r_m \cdot V_c$ ,  $V_c$  is the maximum velocity in the core heat exchanger [ $\text{m/s}$ ];
- $s$ : contraction ratio, dimensionless;
- $K_c$  and  $K_e$ : are the entrance and exit loss coefficients evaluate from Figure 5.4 of Kays and London [14] at  $\text{Re}_{dh} = \infty$ .

Jacobi et al [4] observed that the equation (2.1.4) tends to under predict their experimental data, only 49% of their experimental data are predicted with  $\pm 20\%$ , however they suggested (appendix H) to use this equation (2.1.4).

#### **2.1.4 Refrigerant side predictive models for heat transfer coefficient and pressure drops**

Cavallini et al. [15] (2005) presented a review relative to condensation in minichannel: after a review of the available experimental data they assessed different methods to evaluate the heat transfer coefficient and the pressure drops.

Authors compared the condensation heat transfer coefficient models with experimental data from several authors and finally they developed a new model based on an analogy between heat transfer and momentum transfer.

They also compared several literature pressure drops models and found the models are not able to predict the high pressure fluid R410A pressure drops while some models are able to predict the R134a and with a few the low pressure fluid R236ea, then they developed a new pressure drops correlation which is able to estimate the halogenated fluid pressure drops in the reduced pressure range between 0.1 to 0.5.

Recently Zhang et al [16] proposed a new model for the pressure drops and void fraction inside minichannel, they modified the Mishima and Hibiki correlation [17] and compared the results with other existing literature models. The Mishima-Hibiki model was one of the model used by Cavallini et al. [15] to compare the literature models with the experimental data: it is in good agreement for R134a and satisfactory estimate the low pressure R236ea while it over predict the high pressure refrigerant R410A.

As regards evaporation Sun and Mishima [18] (2009) compared thirteen prediction models for flow boiling heat transfer coefficient evaluation in minichannel with 2505 data, which come from published literature. They observed that the nucleate boiling may be the dominant mechanism in minichannel heat exchanger as suggested by Lazarek and Blank because their correlation was the best to predict the database and it was supported from the work of Tran et al who introduced the Weber number in their correlation. Finally Sun-Mishima found a weakly dependence from the vapor quality.

They developed a new correlation for which 65.6% data falling within  $\pm 30\%$  error band.

### **2.1.5 Technological constrain: the refrigerant maldistribution**

It is one of the most important problems to solve.

The reduced refrigerant cross-section area of each tube requires many parallel tubes to keep the pressure drop across the heat exchanger within a reasonable range.

If the minichannel is used as condenser the maldistribution problem could be at the outlet header, where the fluid exits or saturated or in two-phase state; the following throttling valve should be fed with liquid, to avoid possible malfunction.

The refrigerant maldistribution is a strong problem if the minichannel heat exchanger works as an evaporator: after the throttling valve the refrigerant is in two-phase state, so it enters into the header where the phases separate, consequently the parallel tubes are not fed with the same liquid flow rate, and not all the heat exchanger internal surface is wetted by the refrigerant, the dry surface realizes a low heat transfer coefficient.

It also is a problem in the exit manifold, the refrigerant in some of the tubes outlet is superheated vapor, in others outlet is in two-phases state, so a mixing between all that fluid states occurs and a part of the liquid evaporate while mixing with the superheated vapor.

Furthermore the liquid phase at the outlet header increase the possibility of a liquid suction at the compressor.

Therefore it is very important to distribute the inlet two-phase refrigerant (especially the liquid) evenly into each tube otherwise the evaporator performance is significantly deteriorated.

The higher is the inlet quality, the greater the refrigerant maldistribution.

According to Hrnjak [27] and Kulkarni [28] the performance reduction by flow maldistribution could be as large as 20%.

To highlighting the maldistribution there are mainly three not intrusive methods.

The infrared camera gives information about the distribution of external surface temperature, highlighting the area with the two-phase and the area with the subcooling liquid for a condenser or superheated vapor for an evaporator.

The second method is the external surface frost distribution, this method can be used only for the evaporator: when the external surface temperature is below the air dew point temperature, water moisture occurs on the surface, if its temperature is below 0°C the moisture will freeze. The surface covered with frost corresponds the place where the liquid refrigerant is evaporating, obviously under 0°C, hence these tubes are fed by liquid flow rate; while the

remaining surface corresponds the place where the superheated refrigerant is flowing.

In the next Figure an example from the tests made by department of “Fisica Tecnica” is shown.

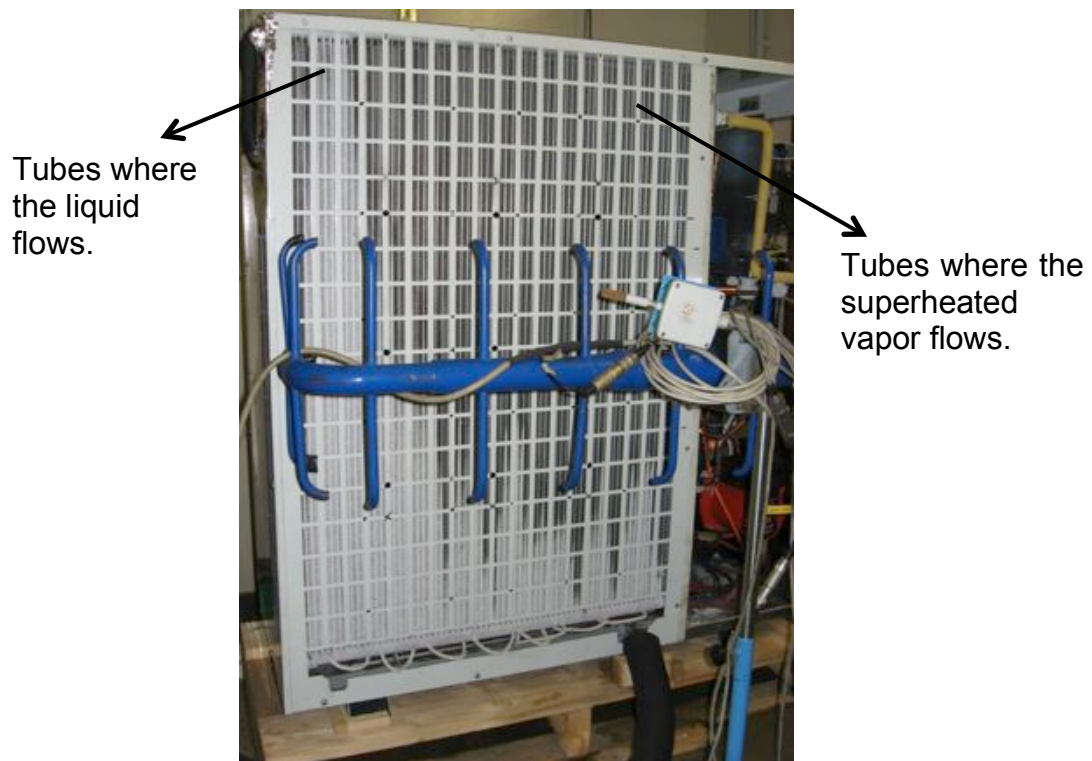


*Figure 2.1.5. Minichannel airside geometrical parameters. External surface frost distribution could be used for highlighting the liquid refrigerant distribution: the frost corresponds to place where the liquid refrigerant is evaporating.*

This method is cheaper and easier than the previous.

Another method is to measure the exit air temperature profile.

The main factors, which affect the refrigerant distribution, are:

- geometrical factors related to the headers;
- two phase flow regime;
- factors due to the heat transfer itself.

In his PhD thesis Chiarello [2] presented the Webb and Chung (2005) [19] review of the factors that affect the refrigerant distribution, the authors looked in particular at the effect of the header design.

The refrigerant distribution is strongly affected by the:

- header orientation;
- number of tubes;
- header shape;
- flow direction in the header (up flow/down flow);
- location and orientation of the inlet and the outlet ports.

Webb and Chung [19] classification of all these geometrical header design characteristics is reported in the following Figures.

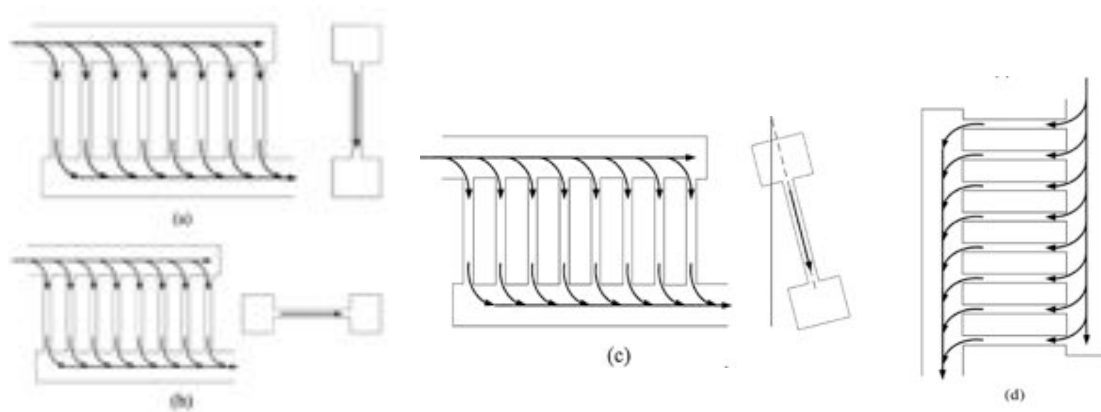


*Figure 2.1.6. Classification of the header-tube junctions: (a) Horizontal header-Vertical tube junction, (b) Horizontal Header- Horizontal tube junction, (c) Horizontal Header- Inclined tube junction, (d) Vertical Header-Horizontal tube junction. (Webb and Chung [19]).*



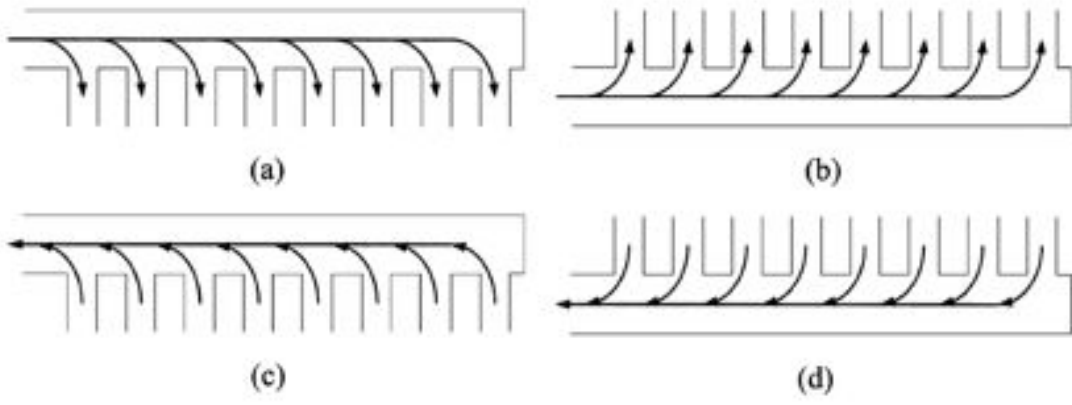


Figure 2.1.7. Classification of the header function and location: (a) top-dividing header (downflow), (b) bottom-dividing header (upflow), (c) top-combining header (upflow), (d) bottom-combining header (downflow). (Webb and Chung, [19]).

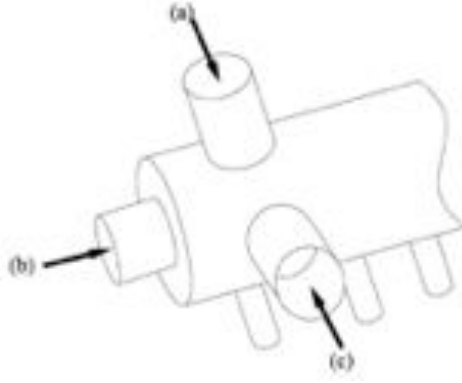


Figure 2.1.8. Classification of header connecting pipes: (a) normal inlet (parallel of the tubes), (b) normal inlet (perpendicular of the tubes), (c) side inlet (normal to the tubes). (Webb and Chung, [19]).

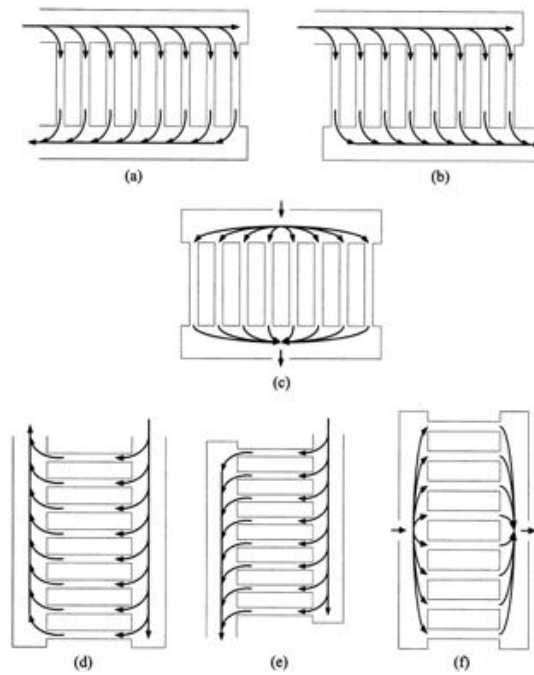


Figure 2.1.9. Classification of header flow direction: (a) horizontal reverse flow, (b) horizontal parallel flow, (c) horizontal normal flow, (d) vertical reverse flow, (e) vertical parallel flow, (f) vertical normal flow. (Webb and Chung, [19]).

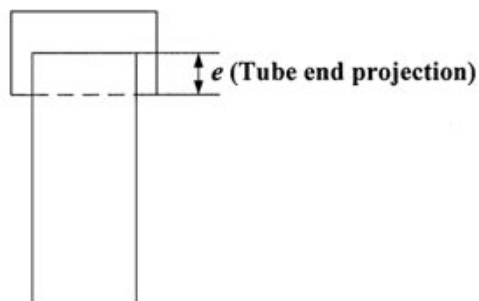


Figure 2.1.10. Tube end projection. (Webb and Chung, [19]).

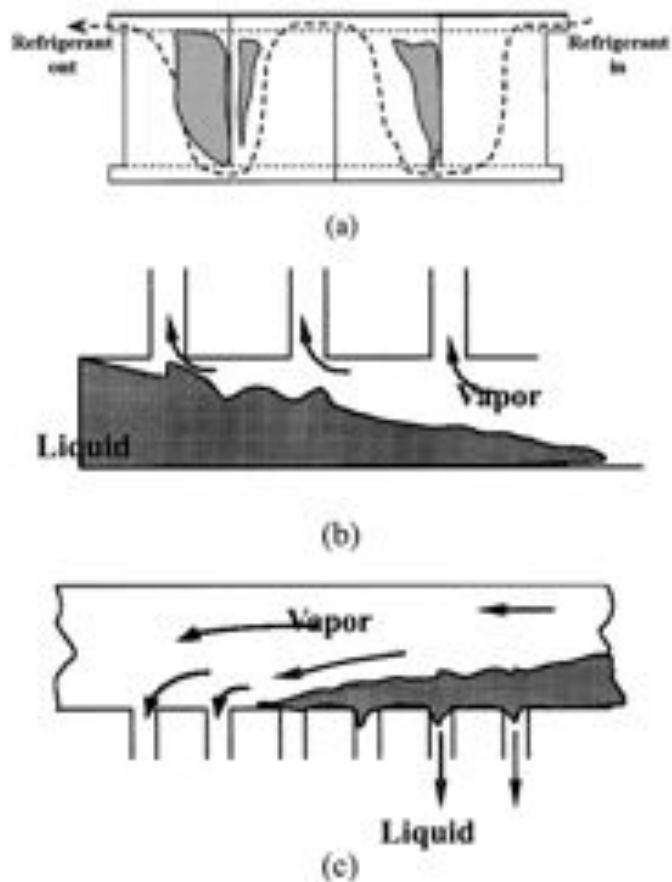


Figure 2.1.11. Horizontal header-Vertical tube junction, (a) illustration of multi-pass design, (b) bottom-dividing header, (c) top dividing header. (Webb and Chung, [19]).

For vertical tube configuration evaporators the refrigerant can be supplied parallel, normal or vertical to the header, Kim et al [29], it is shown in next Figure.

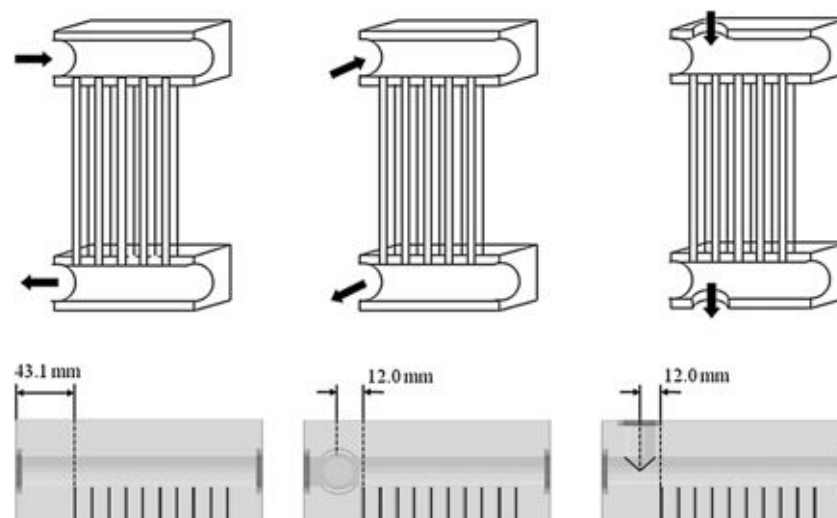


Figure 2.1.12. Flow inlet configuration in Kim et al. (2011) [29] parallel, normal and vertical to the header respectively.

The outlet may be located at the same or at the opposite side of the heat exchanger.

These configurations are defined as horizontal reverse flow and horizontal parallel flow respectively in Webb and Chung classification.

Kim et al. experiments demonstrated that for R134a the flow distribution is better for normal or vertical inlet configuration than for parallel inlet configuration. They found that for all configurations, flow distribution improves as the mass flux increases while for normal or vertical inlet configurations, the effect of quality is not prominent.

Similarly Ahmad et al. [30] found that the two phase distribution in a compact heat exchanger is strictly related to the flow configuration at the header inlet and the two-phase momentum together with the header geometry. The presence of high-momentum phases and especially that of liquid favours the occurrence of impacts, fragmentation of liquid phase, the presence of a homogenized multidirectional two phase structure and this renders the distribution more homogeneous.

Hwang et al [20] investigated the effects of geometry and operative conditions on distribution of refrigerant R410A in minichannel evaporator with horizontal header.

As regards the geometry, they found that the gravitational force and momentum force between the liquid and the vapor phase affect the phase separation in horizontal header; they also changed the header inlet side and found the branch tube inlet vapor quality decrease steadily from the inlet along the header. Finally they found the distribution is strongly dependent of the manifold inlet location and the inlet mass flow rate, but it is primarily independent of the tube pitch.

Lee [31] showed that for vertical headers to horizontal channel there should be an optimum intrusion depth for even flow distribution around 1/8 of the header hydraulic diameter.

Kim et al [32] examined tube end projection for a horizontal header, for the upward flow configuration, most of the fluid (water in this case) flowed through the rear part of the header. The protrusion depth, mass flux or quality was not significantly alter the flow distribution.

The main solution to improve the liquid distribution are:

- modify the header geometry;
- feed the evaporator with low quality refrigerant if possible with saturated liquid, this solution is only for evaporator;
- improving the local thermal transmittance.

In reference to the first solution Webb and Chung (2005) [19] reported that the header geometry can be modified mainly in two ways: first by installing obstacles at the headers inlet/outlet and modifying the tubes projection in the header; second by installing distributors to feed locally a branch of tubes. Webb and Chung concluded that many of these devices require an empirical design, but if the operative condition change the design will require to change, so the flexibility and the costs of these devices is a still open issue.

Feeding evaporator with low quality refrigerant, is simple and good solution, but it can require adding some components having extra costs, a simple way is add an internal heat exchanger; other proposed solutions use an internal heat exchanger and a liquid separator to feed a large part (or all) of the evaporator with saturated liquid, see for example Elber- Hrnjak (2004) [21].

This solution avoids or reduces the liquid maldistribution for one passage minichannel heat exchanger; it solves the problem only in the first passage, not in the intermediate ones for a multi-passage heat exchanger.

### **2.1.6 Technological constrain: the moisture drainage**

The problem of the moisture drainage and the defrosting management is a big still opened technological problem in the use of minichannel heat exchanges as evaporator. When the external surface temperature is below the air dew point temperature the air humidity condenses; the moisture formed in the surface give an additional thermal resistance, penalizing the efficiency.

The shape of the finned flat tube does not allow easily draining the moisture.

If the external surface temperature is below 0°C, the moisture will freeze blocking gradually the air flow and the heat exchanger until the evaporator need to be defrosted. The defrosting system melts the ice and the melted water needs to be drained, residual water after the defrosting period can strongly affect the frosting time by promoting frost accumulation associated phenomena after frosting/defrosting cycles.

Now the attention will be focused to the air conditioning applications where the air velocity is not sufficient to blow the moisture away as it happens in the automotive application.

Jacobi et alt [4] investigated the condensation retention and shedding, by a dynamic dip test in several selected heat exchanger geometries, in their results the water drains more rapidly from vertical round-tube than from vertical flat tube exchanger. They supposed for a vertical flat tube heat

exchanger that the moisture drainage is between the interlouver gaps so the gravitational force tries to drain while the viscous force is opposite; for a round tube the viscous force becomes important when the water velocity is well increased while for a flat tube there is a strong velocity gradient when the water crosses the interlouver gap so the viscous forces becomes great and can easily contrast the gravitational force.

They also observed the effect of fin pitch strongly affects the moisture water retention, the larger is fin pitch the greater is the water draining, and for a large fin pitch the water may pass through the inter fin spacing maybe by making liquid-bridge. Further they changed the fin geometry considering both triangular fin shape and rectangular fin shape, the results showed the triangular geometry retention is very higher than rectangular counterpart highlighting the effect of the surface force in water retention, water is accumulated close between the fin surface near to the fin base. If the heat exchanger is tilted the behavior will not change, but the water retention will decrease.

The condensate visualization shows water condensate collected on the bottom of heat exchanger where the condensate has to move horizontally to find a way to exit.

Memory et al (2006) [22] presented a new design of fin, the fin design allows the contact force to help the air to push the moisture on downstream side.

Below two pictures are reported to show the new fin design.

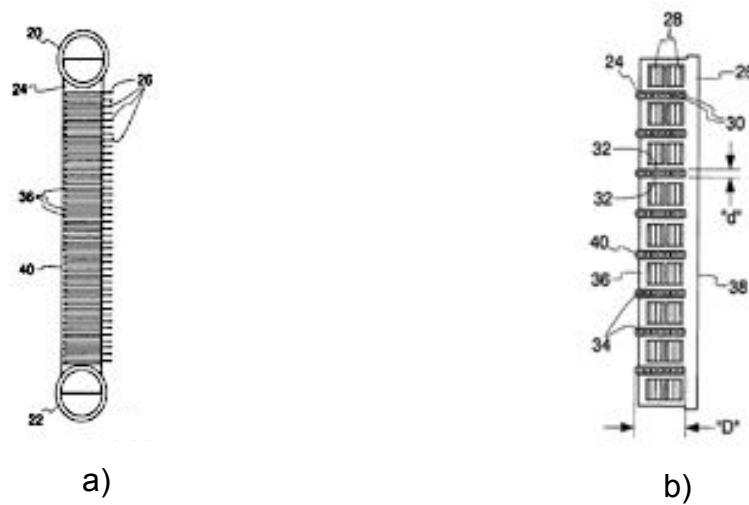


Figure 2.1.13. Schematic views of heat exchanger with new fin design: (a) top view, (b) side view.

Further Chiarello [2] described the experimental tests, conducted in the “Fisica Tecnica” Department of Padua University, with the purpose of comparing the moisture drainage attitude of several different geometries.

These tested geometries were placed vertically and designed with the same external area; first “A” is the usual design with the same fin depth and tube depth, the “B” design has the fin depth greater than the tube depth, the “B mod” one has the fin pitch greater than the “B”, finally the “C” design has the fin depth lower than the tube depth; this last one was interesting to investigate, it was expected that the part of tube without fin could help moisture drainage by combining the surface tension forces and the gravity force. All the geometries were made both with and without hydrophilic treatment.

In the next figure the test facility is schematically shown:



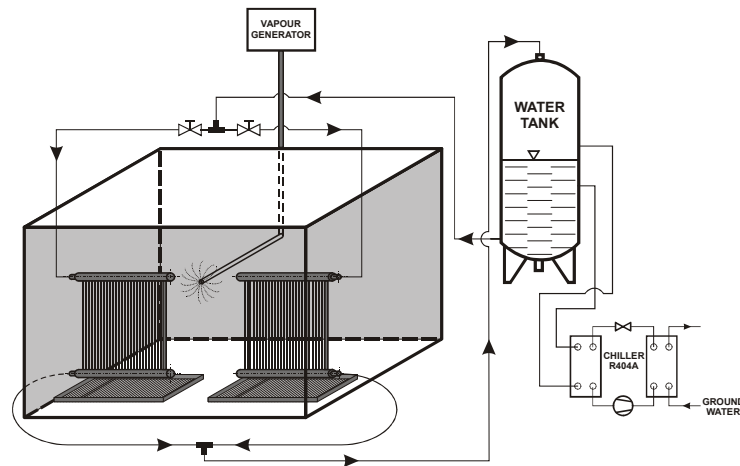


Figure 2.1.14. Test facility for different minichannel heat exchanger design comparative tests.

The two heat exchanger are placed in a box and fed with the same cold water mass flow rate, which come from a chiller at almost 7-8°C, by regulating the two control valves.

The heat exchangers are placed in the box and fed by cold water, then the box is closed and a saturated vapor flow rate is injected into it, when the vapor is in contact with the cold surface, it condensates, part of the condensate water drain until fall into the vessels, part remain into the heat exchanger.

After some time the vessels reach a certain water mass, their water weight is taken; the heaviest vessel corresponds to the heat exchanger which better drains the water.

The tests results showed that the best draining geometry is the “A” design, but the “C” design with the hydrophilic treatment has almost the same performance, it is an interesting result because the “A” design with larger fin pitch and tube pitch gives lower heat transfer coefficient than “C” one, consequently “A” design need a higher heat transfer area.

The “C” design with hydrophilic treatment seems to realize the best compromise between the water drainage and the heat transfer performance.

By starting for those results in the next chapter the “C” geometry design will be used to develop a reversible air-water commercial heat pump.

### **2.1.7 Technological constrain: the frosting formation**

The frost formation, occurring on evaporator surface when it is below 0°C, progressively decreases the air passage, creates louver ice-bridge, and steadily decreases the heat transfer, until the evaporator need to be defrosted; the defrosting decreases the system efficiency.

Wu et al [33] experimentally studied the frosting process of a folded–louvered-fin, parallel flow microchannel evaporator in a heat pump central air-conditioning system. They pointed out that the surface temperature distribution on the parallel flow evaporator was uneven and initial frost formation generally started on some partial surface areas of the louvered fins. They also demonstrated that the ice crystals distribution and frost thickness in frosting period could be obtained by the digital image processing method in which the initial pictures were converted into binary image.

Shao et al (2009) [24] compared the performance of minichannel evaporator with a finned tube one, they made both simulation and experimental results finding that the model, which take in count the refrigerant maldistribution effect, is the best predicts the experimental results. The minichannel heat exchanger has a shorter frost period than the finned tube one, then they made a parametric analysis of the factors which can affect the minichannel performance under frosting condition concluding the best one is the refrigerant maldistribution.

Zhang and Hrnjak (2010) [25] investigated the performance of the parallel-flow, parallel-fin geometry of [23] mentioned in the previous paragraph (Figure 13) placed horizontally in periodic frosting condition, that geometry can work 13 min. longer than the usual minichannel heat exchanger design with fin depth equal to tube depth.

Jacobi et al [4] analyzed the frost growing process, they observed the frost appears on the leading and trailing the edge of fin and louver, then it grows and it reaches the planar surface of louver and fin. The frost maldistribution is a strongly penalizations to avoid.

The fin pitch and the fin shape plays a role in water retention after defrost, so they strongly affect the frost formation, after the first defrosting.

For the considered geometry and operative condition ranges: low evaporating (coolant temperature in general) temperature, high air humidity, large air flow depth and low fin pitch lead a large frost accumulation and a fast increase of the pressure drops, while the air flow rate has a little impact. The evaporating temperature plays an important role in the frost density.

Jhee et al (2002) [26] investigated the effects of a hydrophilic and a hydrophobic surface treatment because as seen above the wettability has an important role in the water retention and in the defrost cycles which follow to the first.

With a hydrophilic surface treatment high density frost forms, so during the defrost the water draining is enhanced; while with a hydrophobic treatment a lower density frost forms and the drained water ratio in the frost melting increase because a large amounts of incompletely melted frost have drained by surface characteristics. Hence the hydrophilic treatment mainly influences the frost formation, while the hydrophobic one influence the defrosting behavior. The defrosting efficiencies of surface-treated heat exchangers are enhanced of about 3.5% for the hydrophilic treatment and about 10.8% for the hydrophobic one, by the influence of increments of the water drain rate. The residual water weight, which affects the performance of reoperation on the hydrophilic and hydrophobic heat exchangers, is reduced by about 20% compared to that of the bare one.

In the next figure an evaporator heat exchanger, used for tests executed by department of "Fisica tecnica" during and after a defrost cycle is shown.



*Figure 2.1.15. Minichannel heat exchanger with frost on the external surface and after the defrost cycle; the time between the two pictures is 120 s.*

### *Defrosting techniques*

When the frost covers the evaporator external surface the air flow rate is in part blocked, the frost gives an additional thermal resistance, the heat exchanger decreases, the evaporator pressure decreases, system efficiency decreases too, until the evaporator needs to be defrosted.

There are several common defrosting techniques:

- Defrosting with an electrical resistance, it uses the Joule effect for heating the evaporator surface, but it is a low efficiency system and the management is not easy, if the resistance is undersized the heating will not be sufficient and the water will not melt completely, so it will accumulate cycle by cycle, while if the resistance is oversized it can burn.
- Natural defrosting is simple by turning off the system, this system can work only if the evaporator temperature is close to 0°C and it can take a lot of time.

Reverse cycle defrosting: it is the most common technique, the system is turned off, a switch valve reverses the cycle and the evaporator becomes the condenser, therefore it is heated for a certain time, then the system is turned off again and the switch valve reverses the cycle restoring the normal working cycle.

During the cycle reversed mode the indoor heat exchanger works as an evaporator, therefore the indoor secondary fluid is cooled while normally it is heated by the condenser, so its surface became cold, when the normal

cycle is re-established it takes additional time due to indoor heat exchanger thermal inertia.

- Hot gas bypassing defrosting, the hot gas is injected through a by-pass valve, into the evaporator. This method is used for the multi-evaporator systems where each evaporator is defrosted while the others are normally working. A throttling valve placed after the point of deviation of the gas is placed to increase the gas pressure and ensure the refrigerant, which can be condensed in part, return from the evaporator

All these defrosting methods penalize the system efficiency because during the defrosting time the system does not supply the heating capacity, moreover they cause considerable energy consumption (with the exclusion of the natural).

An open issue is the defrosting management; it has to find the best combination between the frequency and the time of the defrosting cycle. Short time and frequent cycles allow low frost accumulation on the evaporator surface therefore they take lower energy for defrosting; opposite long time low frequency cycles allow high frost accumulation on the evaporator surface; therefore the defrosting management has to find the best compromise between higher frequency lower energy consumption, and lower frequency higher energy consumption.

The answer is not univocal depends from the evaporator type and its working conditions; probably it requires long expensive experimental tests.

### **2.1.8 Reference**

1. Thome, Ribatski, State of-the-art of two-phase flow boiling heat transfer and pressure drop of CO<sub>2</sub> in macro- and micro-channels. International journal of refrigeration 28 (2005) 1149-1168.
2. Chiarello M. (2010), Development of high efficiency air-conditioning and heating systems. Ph.D. thesis.

3. Park Y, Jacobi AM, (2003). A Second Law-Based Comparison of the Air-Side Thermal-Hydraulic Performance of Flat-Tube and Round-Tube Heat Exchangers, International Congress of Refrigeration, Washington, D.C.
4. Jacobi AM, Park Y, Zhong Y, Michna G, Xia Y. High performance heat exchangers for air-conditioning and refrigeration applications (non-circular tubes) – Final report. ARTI-21CR/605-20021-01, 2005.
5. Beauvais F.N. An aerodynamic look at automotive radiators. Sae Paper N° 650470. (1965).
6. Davenport C.J. Heat transfer and flow friction characteristics of louvered heat exchanger surfaces in Heat Exchanger: Theory and Practice. (1983). J. Taborek Editor Mc Graw-Hill, pp. 397-412.
7. Achaichia A., Cowell T.A. Heat transfer and pressure drop characteristics of flat tube and louvered plate fin surfaces. Experimental thermal and fluid science. (1988) Vol. 1(2). pp. 147-157.
8. Achaichia A., Cowell T.A. A finite difference analysis of fully developed periodic laminar flow in inclined louvre. Second UK national conference on heat transfer. Glasgow. (1988) pp. 883-892.
9. Zhang H. Lang X. The experimental investigation of oblique angles and interrupted plate lengths for louvered fins in compact heat exchanger. Experimental thermal and fluid science. (1989) Vol. 2(1), pp.100-106.
10. Suga K. Aoki H. Numerical study on heat transfer and pressure drop in multilouvered fins. (1991) ASME/JSME Thermal engineering joint conference, 4. pp. 361-368.
11. Yu Juei Chang, Chi Chuan Wang. A generalized heat transfer correlation for louver fin geometry. International Journal heat mass transfer. Vol. 40. (1997). pp. 533-544.
12. Yu Juei Chang, kwei Chang Hsu, Yur Tsai Lin, Chi Chuan Wang. A generalized friction correlation for louver fin geometry. International Journal heat mass transfer. Vol. 43. (2000). pp. 2237-2243.

- 
13. Yu Juei Chang, Wen Jeng Chang, Ming Chia Li, Chi Chuan Wang. An emendament of the generalized friction correlation for louver fin geometry. *International Journal heat mass transfer*. Vol. 49 2006. pp. 4250-4253.
  14. Kays W.M., London A.L. *Compact heat exchangers*, 3<sup>rd</sup> ed.. New York. Mc Graw-Hill.
  15. A. Cavallini, L. Doretti, M. Matkovic, L Rossetto. Update on condensate heat transfer and pressure drop inside minichannels. *Heat transfer engeneering* 27(4): 74-87, 2006.
  16. W. Zhang, T. Hibiki, K. Mischima. Correlations of two-phase frictional pressure drop and void fraction in mini-channel. *Internationa journal of heat and mass transfer*, Vol. 53 (2010) pp. 453-465.
  17. K. Mischima, T: Hibiki. Some characteristics of air-water two-phase flow in small diameters vertical tubes. *International journal multiphase flow*, N44, Vol 22 (1996) pp.703-712.
  18. L. Sun, K. Mischima. An evaluation of prediction methods for saturated flow boiling heat transfer in minichannels. *International journal of heat and mass transfer*, Vol. 52 (2009) pp. 5323-5329.
  19. Webb R.L., Chung K. Two phase flow distribution to tubes of parallel flow air-cooled heat exchanger. *Heat transfer engeneering* 2005. Vol 26, Number 4 pp. 3-18.
  20. Y. Hwang, D-H. Jin, R. Radermacher, Refrigerant distribution in minichannel evaporator manifolds. *HVAC&R Research*, July 2007. Vol. 13, Number 4.
  21. Elber S., P. Hrnjak. Flash gas bypass for improving the performance of transcritical R744 systems that use microchannel evaporators. *International journal of Refrigeration*. (2004) Vol. 27 pp. 724-735.
  22. Memory S., Huges G., Zhang W., Rogers C.J., Grohman C., Robinson E., Mielke R., Wattelet J.P., Gabbey L., Trapp R. L. Method of fabricating a heat exchanger. U.S. Patent No 7, 032,313 B2.

23. P.Zhang, P.S. Hrnjak. Air-side performance evaluation of there types of heat exchanger in dry, wet and periodic frosting conditions. International journal of refrigeration. Vol.32 (2009) pp. 911-921.
24. L. Shao, L. Yang, C. Zhang. Comparison of heat pump performance using fin-and-tube and microchannel heat exchanger under frost conditions. Applied energy (2009). Vol. 87. pp. 1187-1197.
25. P.Zhang, P.S. Hrnjak. Air-side performance of parallel-flow parallel-fin (PF<sup>2</sup>) heat exchanger in sequential frosting. International journal of refrigeration. Vol. 33 (2010) pp. 1118-1128.
26. S. Jhee, K-S. Lee, W-S. Kim. Effect of surface treatments on the frosting/defrosting behavior of a fin-tube heat exchanger. International journal of refrigeration. (2002) Vol. 25, pp. 1047-1053.2
27. Hrnjak PS. Developing adiabatic two-phase flow in headers- distribution issue in parallel flow microchannel heat exchangers. Heat transfer Eng. (2004); Vol.25, pp. 61-68.
28. Kulkarni T., Bullard CW, Cho k. Header design tradeoffs in microchannel evaporators. ApplThermal Eng (2004); Vol.24, pp. 759-776.
29. Kim NH, Kim DY, Byun HW. Effect of inlet configuration on the refrigerant distribution in a parallel flow minichannel heat exchanger. Int. J. Refrigeration (2011); Vol. 34, pp. 1209-1221.
30. Ahmad M., Berthoud G., Mercier P. General characteristics of two-phase flow distribution in a compact heat exchanger. Int. J. Heat and Mass Transfer (2009). Vol. 52. pp. 442-450.
31. Lee JK. Optimum channel intrusion depth for uniform flow distribution at header-channel junctions. J. of Mechanical Scand Tecnology. (2010). Vol. 24. pp. 1411-1416.
32. Kim NH. Shin TR., Two phase flow distribution of air water annular flow in a parallel flow heat exchanger. Int. J. Multiphase Flow. (2006). Vol. 32. pp. 1340-1353.



33. Wu J., Ouyang G., Hou O., Xiao H. Experimental investigation of frost formation on a parallel flow evaporator. *Applied Energy*. (2011). Vol. 88. pp. 1549-1556.

## **2.2 Design and experimental analysis of an air-water reversible heat pump with a minichannel heat exchanger**

In this sub-chapter a design and an experimental analysis of an air-water reversible heat pump with a minichannel heat exchanger is presented.

The experimental work was made in the Rhoss S.p.a. laboratory, the support of the engineers P. Faldelli and G. Betti at the experimental work is gratefully acknowledged.

### **2.2.1 Introduction**

A multi-port extruded (MPE) aluminium flat tube air heat exchanger was compared to a round tube finned coil one. The MPE heat exchanger has parallel flow vertical tube configuration with headers in horizontal position and conventional folded louvered fins. The two heat exchangers were mounted on a 10 kW cooling capacity R410A packaged air heat pump. They were sized to approximately obtain the same cooling and heating capacities in chiller and heat pump mode, respectively.

The heat pump unit with MPE was tested with the air heat exchangers placed in an environmental chamber at different temperature and relative humidity at full load steady state condition. The MPE heat exchanger was tested with different refrigerant inlet distributor/outlet tubes configurations to investigate the effect of liquid refrigerant distribution.

Cycling frosting/defrosting operations were tested with two equivalent machines placed in parallel on the outside and working at full load condition, one of the units was equipped with the MPE heat exchanger while the other mounted a standard finned coil. Penalization factors were analytically

---

introduced to evaluate frosting associated heating capacity and energy efficiency degradation.

### 2.2.2 Nomenclature

COP	heat pump energy efficiency [-]
$c_p$	specific heat at constant pressure [J kg <sup>-1</sup> K <sup>-1</sup> ]
E	energy [J]
EER	chiller energy efficiency [-]
$f$	penalty factor [-]
$\dot{m}$	mass flow rate [kg s <sup>-1</sup> ]
P	power [W]
T	temperature [°C]
X	air humidity ratio [-]

#### Greek letters

$\Delta$	difference [-]
$\phi$	air relative humidity [%]
$\tau$	time interval [s]

#### Subscripts

a	air
c	cooling
ch	chiller mode
drn	drainage operation
db	dry bulb
defr	de frosting operation
el	electric
ev	evaporation
fr	frosting operation
h	heating

hp heat pump mode  
sat saturated  
sf secondary fluid

### 2.2.3 The tested heat pump

The heat pump is a Rhoss THAEY 111 model with R410A as the refrigerant. In chiller mode, the unit has nominal cooling capacity of 10.80 kW and EER (energy efficiency defined as the ratio of nominal cooling capacity and total power absorption, fans included) of 2.62 in the following nominal operating conditions: air inlet temperature 35 °C, water inlet temperature 7 °C, evaporator water temperature glide 5 °C. In heat pump mode, the unit has nominal heating capacity of 11.52 kW and COP (coefficient of performance defined as the ratio of heating capacity and total power absorption, fans included) of 2.51 in the following nominal operating conditions: dry bulb air inlet temperature 7 °C, wet bulb air inlet temperature 5 °C; water inlet temperature 45 °C, condenser water temperature glide 6 °C. Nominal conditions are chosen according to EN 14511:2007 [1].

The vapour compression unit is equipped with a single hermetic scroll compressor and a brazed plate heat exchanger (BPHE) working as condenser or evaporator in heat pump or chiller operation, respectively. The unit capacity is controlled by varying the compressor operation time on the base of the water outlet temperature. A simple relay control law is used, where the compressor is switched on and off when the controlled temperature reaches threshold values. Under heat pump frosting conditions, the unit is defrosted after a set time period (delay time period) during which the evaporation pressure is below a threshold value. The four-way valve is activated and the unit operated in defrosting mode until the condensation pressure reaches a threshold value. The compressor is switched off and the water on the air heat exchanger drained for a set time period (drainage time period) after which the

unit is activated working in heat pump frosting mode. The machine main characteristics are reported in Table 2.2.1.

THAEY 111 data		
<i>Compressor</i>		
Number		1
Manufacturer		Copeland
Model		ZP50K3E-PFJ
Frequency range	[Hz]	50
Swept volume	[m <sup>3</sup> h <sup>-1</sup> ]	8.39
<i>Design info</i>		
Refrigerant		R410A
Refrigerant circuits		1
Superheat	[K]	5
Fan power absorption	[W]	280

Table 2.2.1. Heat pump machine main characteristics.

The unit standard air heat exchanger is a round tube finned coil, which main features are reported in Table 2.2.2.

Tube arrangement (material)		Staggered (Cu)
Longitudinal tube spacing	[mm]	21.65
Traverse tube spacing	[mm]	25
Inside tube diameter	[mm]	7.2
Fins geometry (material)	[mm]	Wave (Al)
Fin spacing	[mm]	1.8
Fin thickness	[mm]	0.1
Number of row		4
Number of tube per row		36
Number of circuits		8
Tube length	[mm]	660

Table 2.2.2. Standard unit finned coil air heat exchanger main features

The heat exchangers fins are treated with a hydrophilic coating.

THAEY 111 was also tested with a multi-port extruded (MPE) aluminium flat tube air heat exchanger, replacing the standard finned coil. The MPE heat exchanger was sized to approximately obtain the same chiller cooling and heat pump heating capacities with respect to the standard round tube

equipped unit; for installation constraints, the heat exchanger face area was kept fairly the same of the round tube finned coil. The same fan was used for both the heat exchanger types.

The heat exchanger has parallel flow vertical tube configuration with headers in horizontal position and conventional folded louvered fins. The heat exchanger is coated with a hydrophilic layer. The MPE heat exchanger air side geometric features are reported in Table 2.2.3.

Tube geometry (material)		Flat (Al)
Tube length	[mm]	900
Tube number		65
Tube depth	[mm]	21
Tube thickness	[mm]	2
Traverse tube spacing	[mm]	10
Fin geometry (material)		Louvered (Al)
Fin thickness	[mm]	1
Fin pitch	[mm]	1.3
Fin length	[mm]	8
Fin depth	[mm]	18

*Table 2.2.3. Minichannel heat exchanger air-side main features.*

In Figure 2.2.1 the heat exchanger refrigerant inlet and outlet connections are schematically shown.

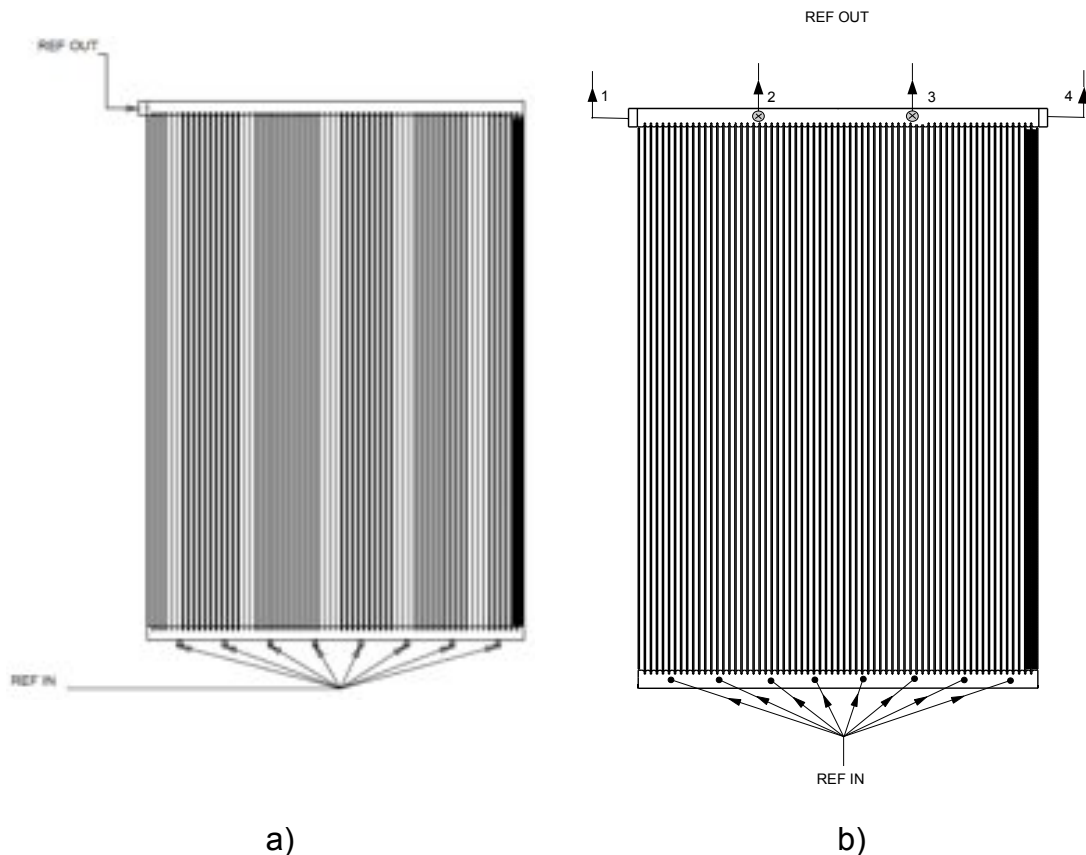


Figure 2.2.1. Multiport flat tube heat exchanger: a) with parallel inlet distributor and manifold lateral exit; b) with normal inlet distributor and five outlet tubes.

With reference to the evaporator operation mode, the inlet refrigerant distributor is a traditional finned coil distributor with eight 5 mm tubes equally spaced and brazed to the bottom manifold. Two distributors were tested, the DIST-1 distributor (Figure 2.2.1-a) has the tubes brazed parallel to the heat exchanger. Each tube distributes the refrigerant horizontally on the manifold internal lateral surface through two holes; the DIST-2 distributor has the tubes brazed normal to the heat exchanger (Figure 2.2.1-b).

Two outlet tubes arrangements were tested, the OUTAR-1 arrangement with a single horizontal 18 mm tube brazed on one manifold side parallel to the header (Figure 2.2.1-a), the second one with five 18 mm tube outlet tubes. Two tubes are brazed on the manifold sides parallel to the header and two tubes are equally spaced along the manifold and brazed normal to the header

(Figure 2.2.1-b). Each tube has a ball valve for testing different outlet configurations. With reference to Figure 2.2.1-b outlet tube enumeration, the OUTAR-2 arrangement has only tube 1 and 4 circuits open while the OUTAR-3 arrangement has only tube 2 and 3 circuits open.

### **2.2.4 Test facilities and testing procedure**

Two different series of tests were carried out. In the first one, the unit was tested in steady state and full load, with the air heat exchangers placed in an environmental chamber at different temperature and relative humidity conditions for heating and cooling mode. Instead, cycling frosting/defrosting operations were tested with two units placed on the outside and working at full load condition with constant evaporator secondary fluid inlet temperature and mass flow rate. In this latter test two equivalent machines, except for the heat air heat exchanger, were tested in parallel to compare MPE heat exchanger performance with the standard finned coil one. The two test rigs are detailed in the following.

#### **Climatic room test rig**

In Figure 2.2.2 the climatic room experimental test facility is schematically shown.



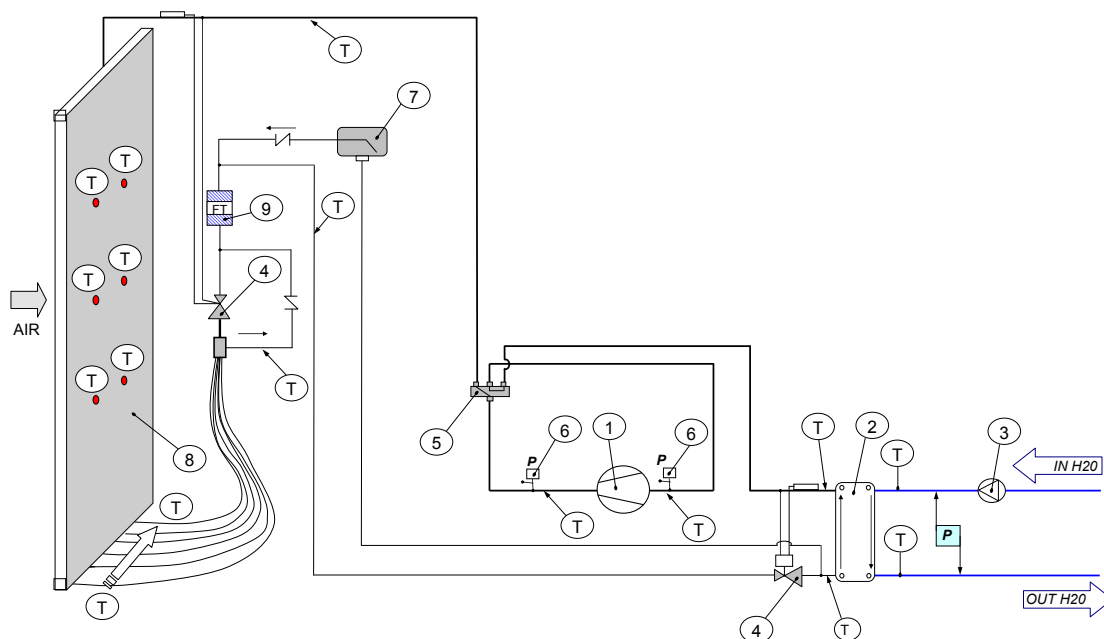


Figure 2.2.2. Climatic room test facility: 1) Compressor, 2) Plate heat exchanger, 3) Water pump, 4) Throttling valve, 5) Switch valve, 6) Pressure transducer, 7) Liquid receiver, 8) Minichannel heat exchanger, 9) Dehydrate filter.

The heat pump THAEY 111 with the round tube or the MPE heat exchanger is positioned in a climatic room connected with the laboratory hydraulic plants and data acquisition system. The room hydraulic section sets the BPHE (2) water inlet temperature. The system is equipped with a variable water flow rate pump (3) controlled to maintain the BPHE nominal water temperature difference. Water volumetric flow rate is measured by electromagnetic meters (accuracy  $\pm 0.2\%$  of reading). Water temperatures are measured with Pt100 thermometers placed inside mixing chambers at the inlet and outlet of the BPHE. Thermocouples and pressure transducers on the refrigerant circuit are placed as shown in Figure 2.2.2. The R410A temperatures are measured with Pt100 thermometers placed on the pipe wall and then covered with cellular polyethylene. Air temperatures are measured with a grid of thermocouples at the inlet and the outlet of the heat exchanger. A  $\pm 0.3$  °C accuracy is estimated for all the temperature measurements. The R410A pressures are recorded with strain-gauge transducers (6) at compressor suction and discharge. The

accuracy is  $\pm 10$  kPa according to the calibration report from the manufacturer. Compressor and fan electrical absorbed power is recorded with an electronic transducer (with an accuracy  $\pm 0.5\%$  of the reading value). All measurements signal are acquired with a 10 s sampling.

Tests have been carried out according to EN 14511:2007 standard [1] for chiller and heat pump operation with the air heat exchanger positioned in the climatic room. Chiller tests were made at full load condition with the room temperature set at 35 °C. BPHE water inlet and outlet temperatures were 12 °C and 7 °C, respectively. Heat pump tests were made at full load condition with 75÷80% relative humidity set point value. BPHE water inlet and outlet temperatures were 40 °C and 45 °C, respectively. Different room air temperature, namely 13, 10 and 7°C, were considered in order to compare different heat exchangers or heat exchanger distributors and outlet arrangements under wet conditions at the evaporator. With reference to the different MPE heat exchanger tested distributors and outlet arrangements, heat pump tests were carried with no frosting phenomena occurring and with the unit working in steady-state conditions.

The steady state systems efficiencies in terms of EER have been obtained by integrating the power absorption and the cooling capacity, computed on the water side from volumetric flow rate and temperature measurements.

### **Outdoor test rig**

Two Rhoss THAEY 111 reversible heat pumps, one using the multi-port extruded louvered finned tube heat exchanger (MPE-UNIT) while the other equipped with the standard round copper tube finned coil heat exchanger (FC-UNIT), were placed outdoor connected to the test rig in Figure 2.2.3.

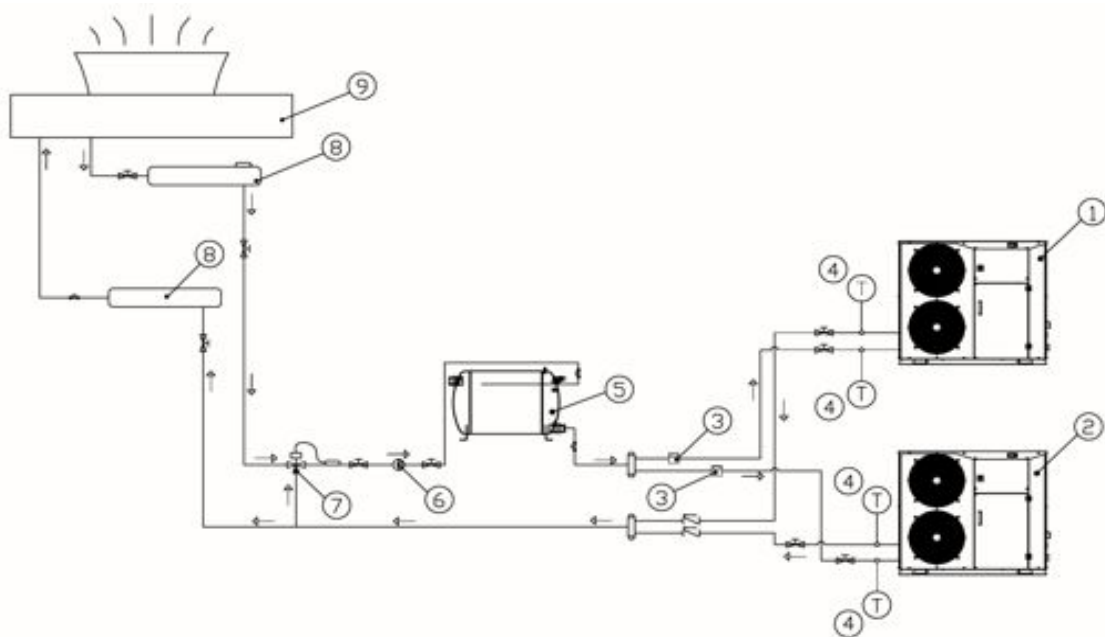


Figure 2.2.3. Outdoor test facility: 1) Reversible heat pump with multi-port extruded tube heat exchanger, 2) Reversible heat pump with round tube coil heat exchanger, 3) Coriolis mass flow rate meters, 4) In/out temperatures probes, 5) Water Tank, 6) Pump, 7) Mixing valve, 8) Collectors, 9) Dry cooler.

During the tests, the two heat pumps operate contemporarily under the same outdoor air temperature and humidity. The secondary fluid section of the test rig supplies the two heat pumps with constant secondary fluid inlet temperature. The secondary fluid is an antifreezing water/ethylene-glycol mixture, the volumetric ethylene-glycol concentration is 30%. In Figure 2.2.3 the hydraulic section is schematically shown, the two heat pumps (1-2) are connected in parallel, so that the water-glycol inlet temperature and mass flow rate are the same for both units, a three-way mixing valve (7) sets the units secondary fluid evaporator inlet temperature. The hydraulic section has a 270 litres tank (5) to minimize water temperature deviation from set point value; the pump (6) constant mass flow rate is 1.287 kg/s. Excess heat is dissipated by an air dry cooler (9) equipped with a variable speed fan. The water-glycol temperatures are measured with Pt100 thermometers (4) placed on the pipe wall; a  $\pm 0.3^{\circ}\text{C}$  accuracy is estimated for all the temperatures measurements. The water-glycol volumetric flow rates are measured with two electromagnetic

flow meters (3), the claimed accuracy is  $\pm 0.2\%$  of reading. The air temperature and relative humidity are measured with dew point meters having an accuracy  $\pm 0.2^\circ\text{C}$  of the reading value. The electrical absorbed power of compressor and fan is recorded with an electronic transducer (with an accuracy  $\pm 0.5\%$  of the reading value). All measurements signal are acquired with a 10 s sampling. Water-glycol BPHE inlet temperature is kept constant at  $40^\circ\text{C}$  for both units. Both the heat pumps work at full load conditions.

For dry and wet operating conditions, the average heat pumps efficiencies in terms of COP are obtained by integrating the power absorption and the heating capacity, computed from the instantaneous values of water-glycol mass flow rate and BPHE water-glycol temperature glide. For frosting/defrosting working conditions, water-glycol heating and cooling cycles must be considered for the determination of COP and heating capacity. The plate heat exchanger capacity and the electrical energy input are obtained from a time integration of the power for each frosting/defrosting duty cycle.

For each sampling, the water heating and cooling power are respectively:

$$P_h = (\dot{m}_{sf} \cdot c_{p,sf} \cdot \Delta T_{sf})_{hp}, \quad (2.2.1)$$

$$P_c = (\dot{m}_{sf} \cdot c_{p,sf} \cdot \Delta T_{sf})_{ch}. \quad (2.2.2)$$

A defrosting cycle involves the frosting, the defrosting and the drainage period. Considering a full frosting/defrosting/drainage working cycle with the compressor working at full load condition, the presence of frosting phenomena involves:

- the secondary fluid (water-glycol) is cooled down during the defrosting period when the air heat exchanger works as a condenser;
- during the defrosting period and the drainage period no heating is supplied to the plant by the heat pump.

Consequently the net supplied heat capacity,  $E_{h,net}$ , for each frosting/defrosting cycle can be obtained as:

$$E_{h,fr} = \int_{\Delta\tau_{fr}} P_h \cdot d\tau, \quad (2.2.3)$$

$$E_{c,defr} = \int_{\Delta\tau_{defr}} P_c \cdot d\tau, \quad (2.2.4)$$

$$E_{h,net} = E_{h,fr} - E_{c,defr}, \quad (2.2.5)$$

while the total absorbed electric energy is:

$$E_{el} = \int_{\Delta\tau_{fr}} P_{el} \cdot d\tau + \int_{\Delta\tau_{defr}} P_{el} \cdot d\tau. \quad (2.2.6)$$

Thus, the frosting/defrosting cycle COPF results:

$$COP_F = E_{h,net} / E_{el}. \quad (2.2.7)$$

If the machine works continuously without frosting phenomena occurring and the frost associated evaporation pressure penalization is neglected, its COP can be calculated as:

$$COP = \frac{\int_{\Delta\tau_{fr}} P_h \cdot d\tau}{\int_{\Delta\tau_{fr}} P_{el} \cdot d\tau}. \quad (2.2.8)$$

An energy efficiency penalty factor,  $f_{COP}$ , can now be defined as the complementary to the ratio between the frosting/defrosting  $COP_F$  and the COP calculated without frosting phenomena occurring:

$$f_{COP} = \frac{COP - COP_F}{COP} = 1 - \frac{COP_F}{COP} \quad (2.2.9)$$

A heating capacity penalty factor,  $f_{E_h}$ , can be also defined as the complementary to the ratio between the heating capacity obtained during a full frosting/defrosting/drainage working cycle and the heating capacity that would be obtained without frosting phenomena:

$$f_{E_h} = \frac{E_{h,fr} \cdot (\Delta\tau_{fr} + \Delta\tau_{defr} + \Delta\tau_{dm}) - E_{h,net}}{E_{h,fr} \cdot (\Delta\tau_{fr} + \Delta\tau_{defr} + \Delta\tau_{dm})} = 1 - \frac{E_{h,net}}{E_{h,fr} \cdot (\Delta\tau_{fr} + \Delta\tau_{defr} + \Delta\tau_{dm})} \quad (2.2.10)$$

The efficiency and capacity penalization factors are defined with reference to a single frosting/defrosting/drainage cycle.

All these parameters can be defined analogously considering longer time periods including several defrosting cycles. In that case, integrals in equations 2.2.-3-4-6-8 are extended to all the frosting, defrosting and drainage cycle times in the considered integration period.

### 2.2.5 Experimental results

As it has been detailed in the previous paragraph, two different series of tests has been carried out, one with the air heat exchanger placed in an environmental chamber, the other one testing two equivalent machines in parallel on the outdoor. The results of the two series of tests are detailed in the following.

## **Climatic room tests results**

### *Chiller mode*

The reversible heat pump with MPE heat exchanger was tested in chiller and heat pump operating conditions in accordance to the procedure detailed in the previous section. In particular, the unit was tested with different refrigerant inlet distributor/outlet tubes configurations as detailed in Section 2.2.3. Two refrigerant inlet distributors, DIST-1 and DIST-2, and three outlet tubes arrangements OUTAR-1, OUTAR-2, OUTAR-3, were analysed.

Chiller operation tests were carried out at 35°C dry bulb air inlet temperature, the results are summarized in Table 2.2.4 for the round tube finned coil heat exchanger and for DIST-1/OUTAR-1, DIST-1/OUTAR-2, DIST-2/OUTAR-1, DIST-2/OUTAR-3 MPE heat exchanger arrangements.

	unit	FC-unit	DIST-2 OUTAR- 1	DIST-1 OUTAR- 1	DIST-1 OUTAR- 2	DIST-2 OUTAR- 3
Air temperature	[°C]	35	34.9	34.9	35.1	35
Water inlet temperature	[°C]	12.1	12.0	11.9	11.9	12.0
Water outlet temperature	[°C]	7.1	7.0	7.0	7.0	7.1
Cooling capacity	[kW]	9.58	10.00	9.72	9.79	9.80
Power input	[kW]	4.38	4.51	4.28	4.30	4.36
Condensation pressure	[10 <sup>5</sup> Pa]	29.5	29.63	29.9	30.07	29.91
Condensation temperature (dew)	[°C]	48.5	48.7	49.1	49.3	49.1
Evaporation pressure	[10 <sup>5</sup> Pa]	8.65	9.04	8.92	8.87	8.87
Evaporation temperature (dew)	[°C]	2.7	4.1	3.7	3.5	3.5
Superheated	[K]	1.4	2.6	1.5	2.1	3.7
Subcooling	[K]	2.2	1.5	1.4	1.7	1.6
Water volumetric flow rate	[kg s <sup>-1</sup> ]	0.462	0.477	0.468	0.472	0.47
EER	[-]	2.19	2.22	2.27	2.27	2.25

*Table 2.2.4. Climatic room cooling tests at 35 °C room air dry bulb temperature.*

It can be pointed out that all the tested MPE flat tube heat exchanger configurations show slight performance improvements with respect to the round tube finned coil, a maximum improvement of 4.2% and 3.6% for cooling capacity and EER can be pointed out for the DIST-2/OUTAR-1 and DIST-1/OUTAR-1 configuration, respectively. Instead DIST-2/OUTAR-3 MPE corresponding differences are equal to -0.5% and 2.7% for cooling capacity and EER.



*Heat pump mode*

Heat pump mode tests were carried out at different room air dry bulb temperature values with no frosting phenomena occurring and the unit working in steady state conditions. Tests were made to compare DISTR-1 and DISTR-2 inlet distributor configurations; OUTAR-1 outlet tubes arrangement was adopted at 13 °C and 75% room air dry bulb temperature and relative humidity; tests results are reported in Table 2.2.5 first and second column, respectively.

	unit	DISTR-1 OUTAR-1	DISTR-2 OUTAR-1	DISTR-1 OUTAR-2
Air temperature	[°C]	12.9	12.9	13
Air relative humidity	[%]	72.3	74.6	75.3
Water inlet temperature	[°C]	39.9	40.0	40.0
Water outlet temperature	[°C]	45.4	45.7	45.1
Heating capacity	[kW]	10.63	11.48	12.63
Power input	[kW]	4.38	4.38	4.30
Condensation pressure	[10 <sup>5</sup> Pa]	29.46	29.78	29.78
Condensation temperature (dew)	[°C]	48.4	48.9	48.9
Evaporation pressure	[10 <sup>5</sup> Pa]	6.71	7.26	8.23
Evaporation temperature (dew)	[°C]	-5.3	-2.9	1.1
Superheated	[K]	0.8	1.2	5.5
Subcooling	[K]	0.4	0.3	0.3
Water volumetric flow rate	[kg s <sup>-1</sup> ]	0.469	0.4825	0.5942
COP	[-]	2.43	2.62	2.93

*Table 2.2.5. Climatic room heating tests at 13 °C and 75% room air dry bulb temperature and relative humidity.*

It can be pointed out that DISTR-2 works better than DISTR-1 configuration showing 8.0% and 7.8% increments for heating capacity and COP, respectively. These results are confirmed by frosting tests at lower room air temperature on the same MPE heat exchanger configurations, in 2.2.4a and 2.2.4b frost distribution is shown for DISTR-1/OUTAR-1 and DISTR-2/OUTAR-1, respectively.

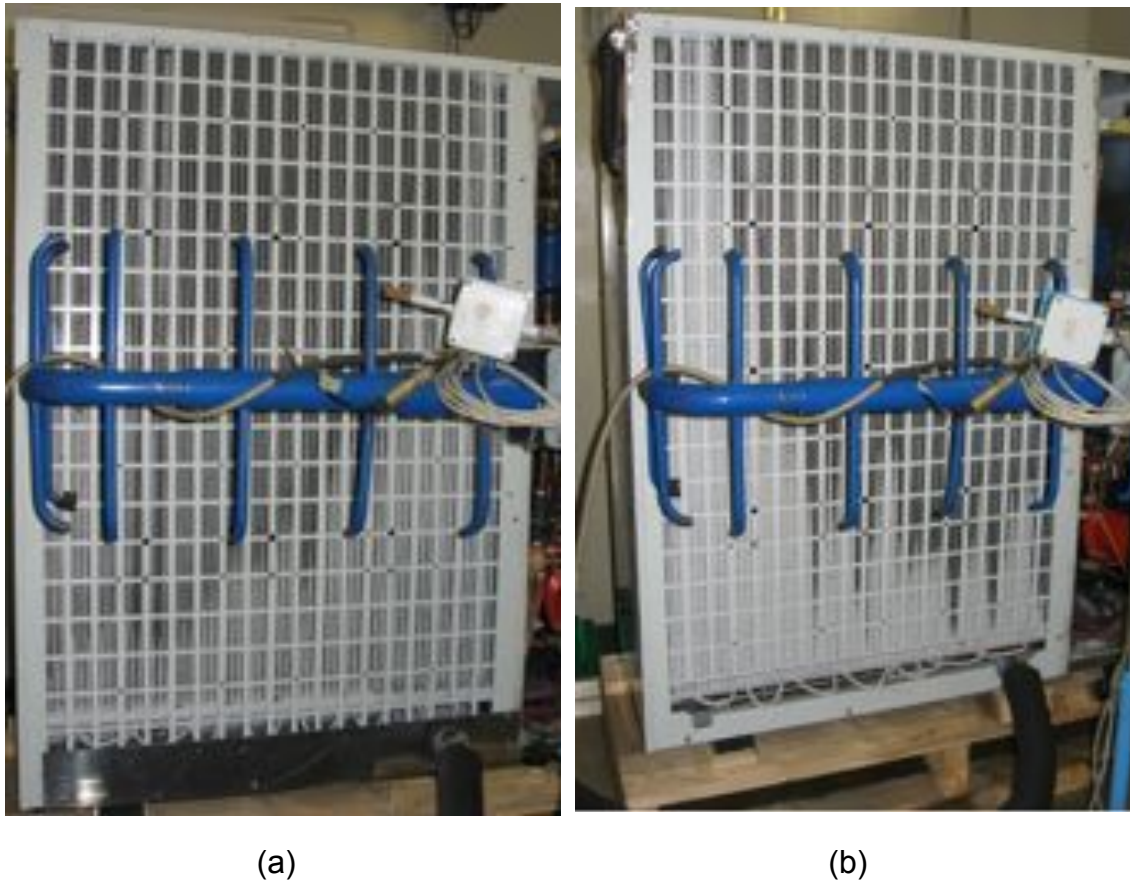


Figure 2.2.4. Frost distribution on MPE external surface for (a) DISTR-2 and OUTAR-1 configuration and (b) DISTR-1 and OUTAR-1 configuration.

DISTR-1 distributor performance with OUTAR-2 arrangement test results at 13 °C room air temperature are shown in the last column of Table 2.2.5. With respect to DISTR-1/OUTAR-2 configuration, OUTAR-2 arrangement associated improvements are equal to 10.0% and 11.8% for heating capacity and COP, respectively. In Figure 2.2.6 the DISTR-2/OUTAR-2 configuration operating under frosting condition is shown, the frost distribution appears more uniform than Figure 2.2.5 DISTR-1/OUTAR-1 and DISTR-2/OUTAR-1 configurations but a large central area of the heat exchanger without frost remains, thus indicating a not uniform liquid refrigerant distribution between the tubes.



*Figure 2.2.5. Frost distribution on MPE external surface for DISTR-2 and OUTAR-1 configuration.*

OUTAR-2 arrangement was tested also at 10 °C and 80% room air dry bulb temperature and relative humidity. DISTR-1/OUTAR-2 and DISTR-2/OUTAR-2 were tested in steady state working conditions without frosting phenomena occurring on the heat exchanger surface; tests results are reported in Table 2.2.6 first and second column.

	unit	DIST-1 OUTAR-2	DIST-2 OUTAR-2	DIST-2 OUTAR-3
Air temperature	[°C]	10.1	10	10
Air relative humidity	[%]	78.7	80.2	79.7
Water inlet temperature	[°C]	40.0	40.0	40.0
Water outlet temperature	[°C]	45.1	45.0	45.1
Heating capacity	[kW]	11.97	11.81	12.20
Power input	[kW]	4.30	4.28	4.31
Condensation pressure	[10 <sup>5</sup> Pa]	29.69	29.66	29.85
Condensation temperature (dew)	[°C]	48.8	48.7	49.0
Evaporation pressure	[10 <sup>5</sup> Pa]	7.69	7.71	8.11
Evaporation temperature (dew)	[°C]	-1.1	-1.0	0.6
Superheat	[K]	5.8	4.9	4.7
Subcooling	[K]	0.3	0.2	0.4
Water volumetric flow rate	[kg s <sup>-1</sup> ]	0.568	0.5631	0.5758
COP	[-]	2.78	2.76	2.83

*Table 2.2.6. Climatic room heating tests at 10 °C and 80% room air dry bulb temperature and relative humidity.*

With the OUTAR-2 outlet tubes arrangement, DISTR-1 and DISTR-2 configuration performances are comparable showing only 1.3% and 0.7% differences for heating capacity and COP, respectively.

OUTAR-3 arrangement performance with DISTR-2 distributor test results at 10 °C room air temperature are shown in the last column of Table 2.2.6. With respect to DISTR-2/OUTAR-2 configuration, OUTAR-3 arrangement associated improvements are equal to 3.3% and 2.5% for heating capacity and COP, respectively. In Figure 2.2.6 the DISTR-2/OUTAR-3 configuration operating under frosting condition is shown, the frost distribution appears more uniform than Figure 2.2.5 DISTR-1/OUTAR-2 configuration.



*Figure 2.2.6. Frost distribution on MPE external surface for DISTR-2 and OUTAR-3 configuration.*

In fact, with respect to this latter arrangement, DISTR-2/OUTAR-3 configuration has two outlet tubes equally spaced along the manifold instead of two tubes on the two manifold ends. This arrangement assures a rather uniform liquid refrigerant distribution between central and border heat exchanger tubes.

DISTR-2/OUTAR-3 arrangement was tested also at 7 °C and 80% room air dry bulb temperature and relative humidity, which is the standard testing condition according to EN 14511:2007 [1]. In this configuration, the MPE heat exchanger worked in steady state conditions without frosting phenomena occurring on the heat exchanger surface; tests results are shown in Table 2.2.7 together with the round tube finned coil ones. The MPE heat exchanger

heating capacity and COP improvement, with respect to the round tube finned coil, is 1.4% and 0%, respectively. It appears that the steady state performances of the heat pump equipped with the finned coil and with the DISTR-2/OUTAR-3 MPE heat exchanger are very close to each other both in heating and cooling operation, capacity and energy efficiency differences are below 5%.

	unit	FC-unit	DISTR-2 OUTAR-2
Air temperature	[°C]	7.1	7
Air relative humidity	[%]	80.5	80.7
Water inlet temperature	[°C]	40.04	40.0
Water outlet temperature	[°C]	45.9	45.0
Heating capacity	[kW]	11.3	11.46
Power input	[kW]	4.24	4.29
Condensation pressure	[10 <sup>5</sup> Pa]	30.0	29.64
Condensation temperature (dew)	[°C]	49.2	48.7
Evaporation pressure	[10 <sup>5</sup> Pa]	7.26	7.47
Evaporation temperature (dew)	[°C]	-2.88	-2.0
Superheated	[K]	3.2	3.9
Subcooling	[K]	0.8	0.5
Water volumetric flow rate	[kg s <sup>-1</sup> ]	0.461	0.545
COP	[-]	2.67	2.67

Table 2.2.7. Climatic room heating tests at 7 °C and 80% room air dry bulb temperature and relative humidity.

### Outdoor test results

Tests were carried out between January and March 2011 on two Rhoss THAEY 111 reversible heat pumps positioned on the outdoor and working continuously. As it was detailed in section 2.2.3, the MPE-unit mounted a DISTR-2/OUTAR-3 multi-port extruded louvered finned tube heat exchanger while the FC-unit was equipped with the standard round copper tube finned coil heat exchanger. Outdoor air dry bulb temperature and relative humidity trends for the testing period are plotted in Figure 2.2.7.

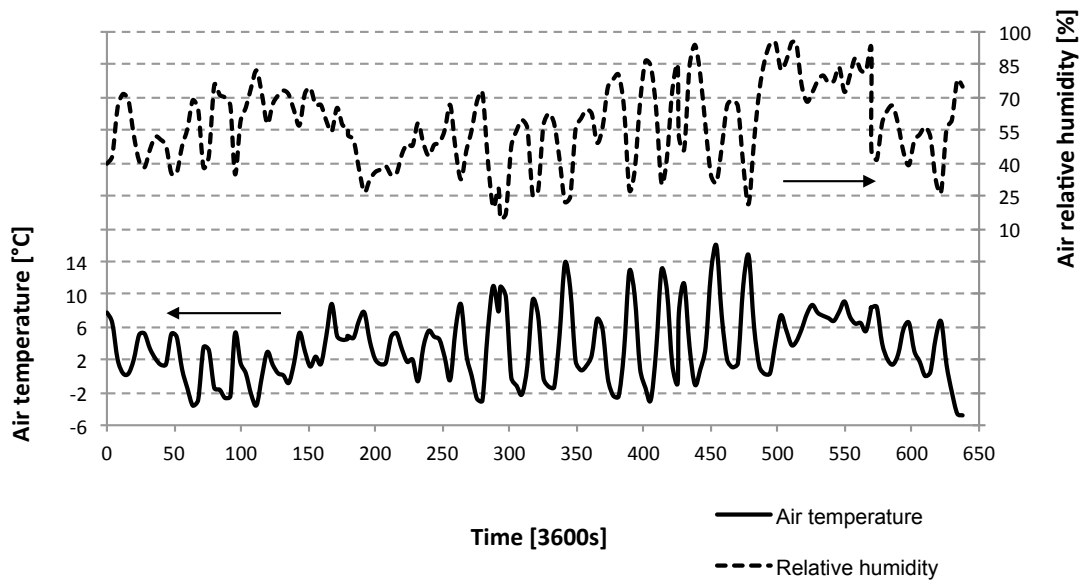


Figure 2.2.7. Air dry bulb temperature and relative humidity trends during all tests period time.

Considering the overall testing period, five representative days were chosen in order to compare the two machines performance under different outdoor temperature and relative humidity working conditions. Daily average air dry bulb and relative humidity values for the selected days are reported in Table 2.2.8, while the corresponding mean hourly profiles time sample acquisition are plotted in Figure 2.2.8. In Table 2.2.8, the two heat pumps daily cumulated heating energy, input energy and daily energy efficiency values are reported for day 1 to 5, respectively. Heating and input energy is calculated with equations (2.2.5) and (2.2.6) taking into account the daily frosting/defrosting cycles. Daily energy efficiency is calculated as the ratio between heating and input energy.

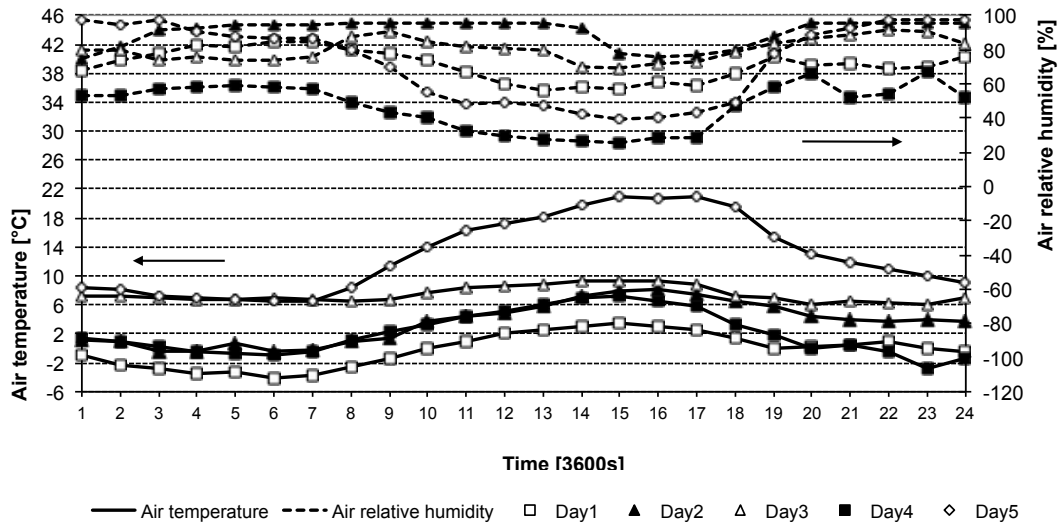


Figure 2.2.8 .Air dry bulb temperature and relative humidity trends for the selected days 1 to 5.

		Day -1	Day -2	Day -3	Day -4	Day -5
Air dry bulb temperature (average)	[°C]	-0.2	3.6	7.4	2	12
Air relative humidity (average)	[%]	70	90	80	47	73
<i>FC-unit</i>						
Heating energy	[MJ]	661.6	784.83	951.87	763.66	1025.86
Input energy	[MJ]	351.8	365.83	385.8	355.1	403.4
Daily energy efficiency	[-]	1.88	2.15	2.47	2.15	2.54
<i>MPE-unit</i>						
Heating energy	[MJ]	583.4	684.8	997.35	659.78	1004.6
Input energy	[MJ]	294.31	313.64	384	313.69	391.1
Daily energy efficiency	[-]	1.98	2.18	2.60	2.10	2.57

Table 2.2.8. Average air dry bulb temperature and relative humidity for days 1 to 5 together with MPE and FC heat pumps daily cumulated heating energy, input energy and daily energy efficiency.

In Figures 2.2. 9-10-11-12-13, the two heat pumps hourly COP values and the hourly cumulated number of defrosting cycles are plotted for days 1 to 5, respectively. COP is calculated every hour with equation (2.2.7) considering all the frosting/defrosting cycles starting during the considered hour.

Considering Table 2.2.8 cumulated daily input energy and efficiency results, the frosting associated penalization can't be clearly pointed out since for some days the MPE-unit has a strong heating capacity penalization but doesn't



show any energy efficiency reduction. For days 1, 2 and 4, the MPE-unit cumulated heating energy penalization is equal to 11.8, 12.8 and 13.6% being the daily average outdoor air dry bulb temperature equal to -0.2, 3.6 and 2.0 °C, respectively. Referring to Figures 2.2.-9-10-12, the MPE-unit inferior performance with respect to FC-unit one can be clearly associated to its higher number of defrosting cycles. When the external air temperature is higher and no frosting phenomena occurs (see Figures 2.2.11 and 2.2.13), such as in days 3 and 5 (with 7.4 and 12 °C average dry bulb air temperature values, respectively), the MPE-unit cumulated daily heating energy values are comparable or higher to FC-unit ones, with 4.8 and -1.2% difference, respectively.

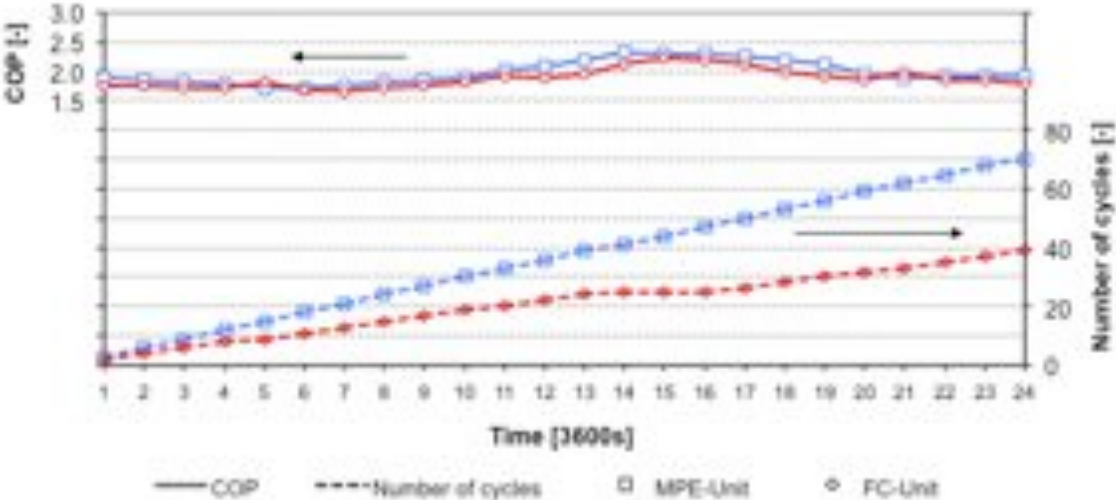


Figure 2.2.9. MPE-unit and FC-unit daily cumulated number of cycles and COP for day 1

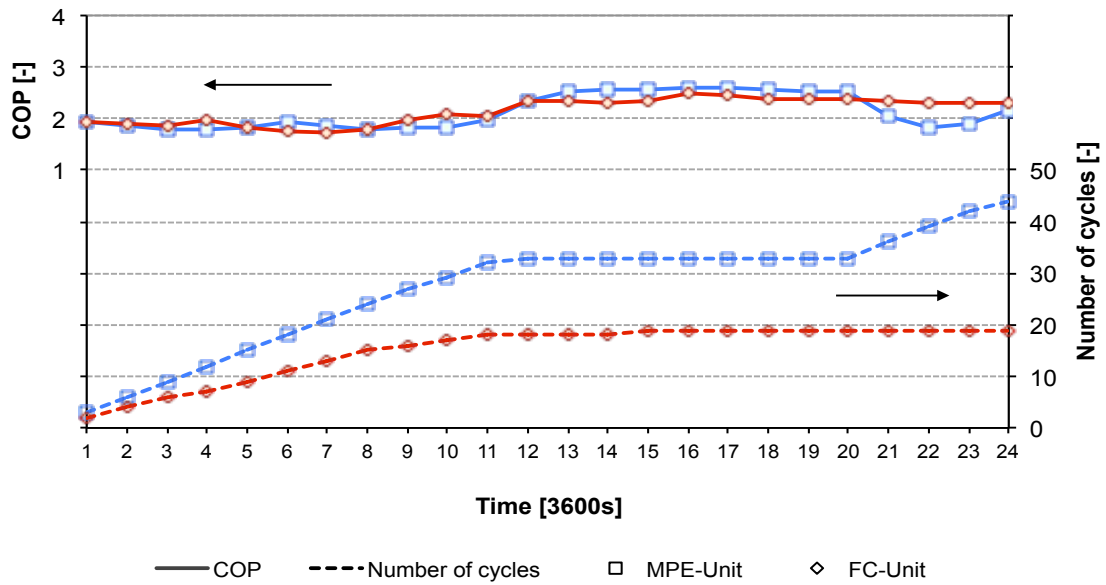


Figure 2.2.10. MPE-unit and FC-unit daily cumulated number of cycles and COP for day 2.

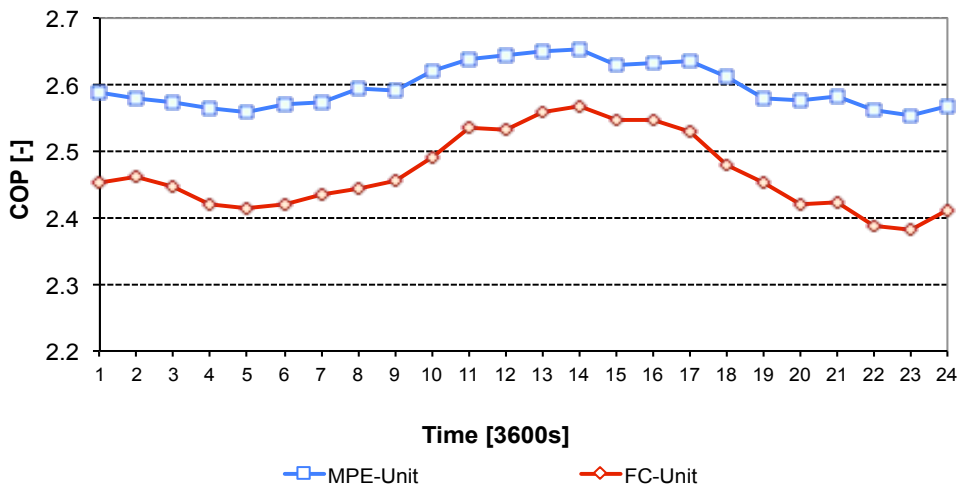


Figure 2.2.11. MPE-unit and FC-unit daily cumulated number of cycles and COP for day 3.

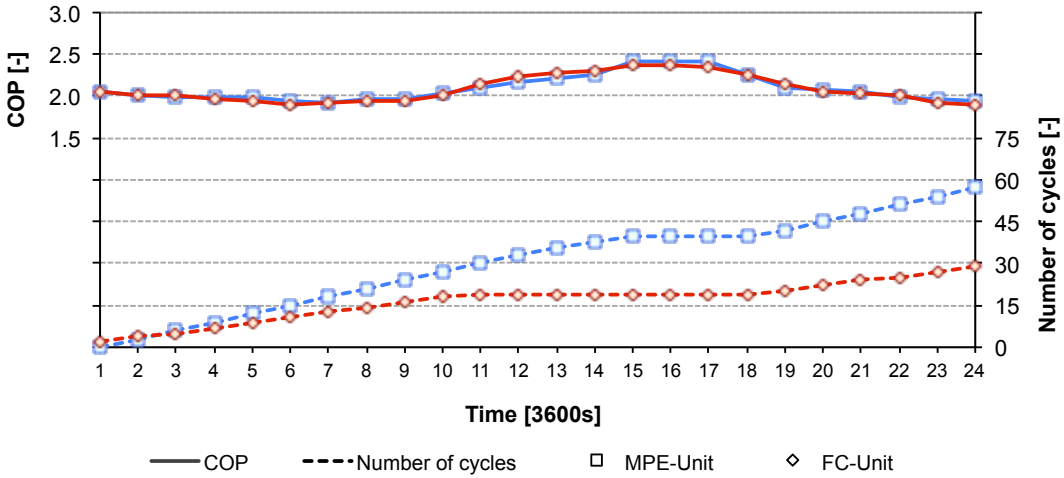


Figure 2.2.12. MPE-unit and FC-unit daily cumulated number of cycles and COP for day 4.

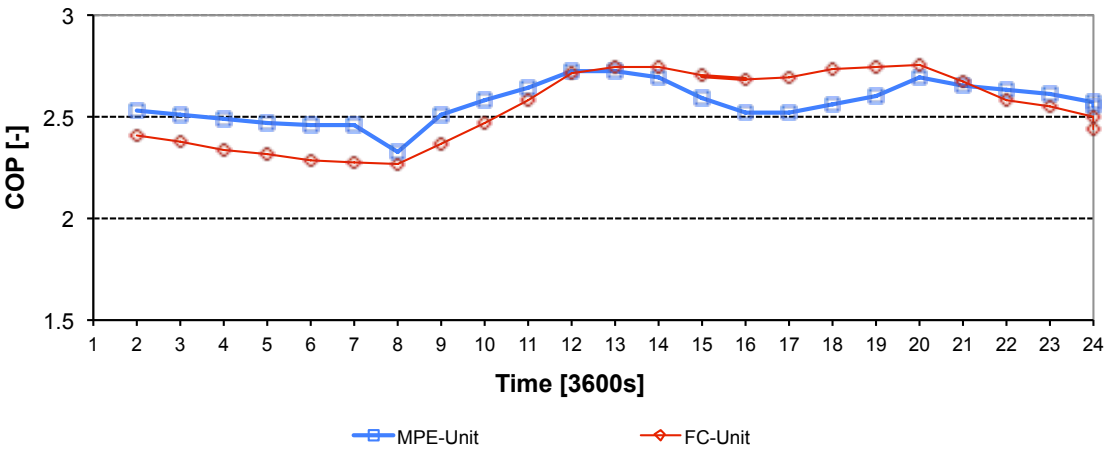
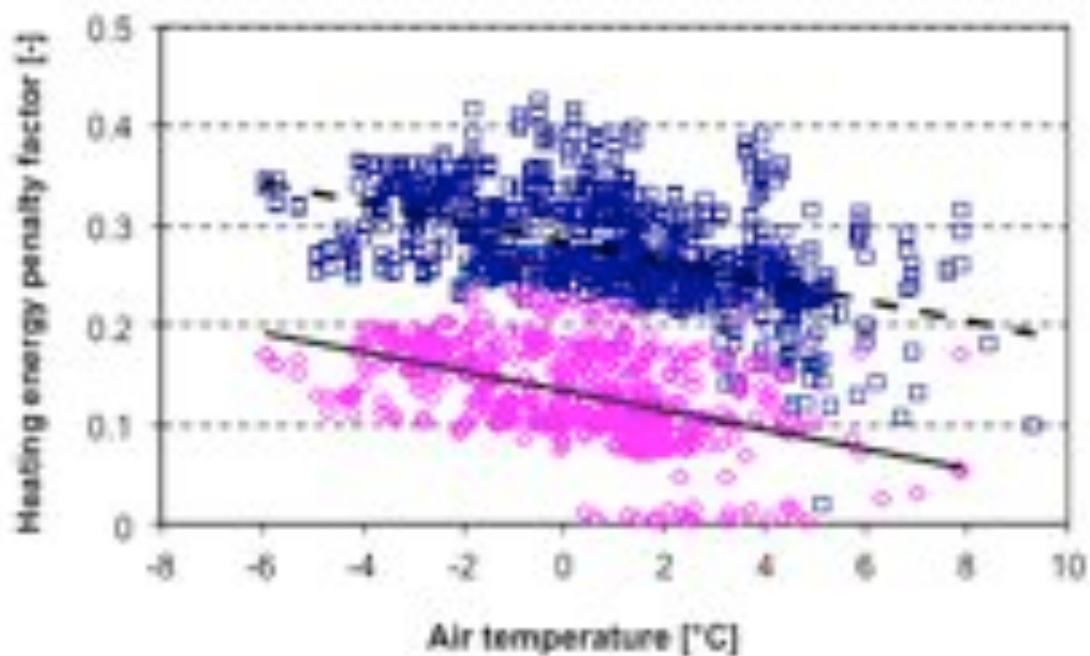


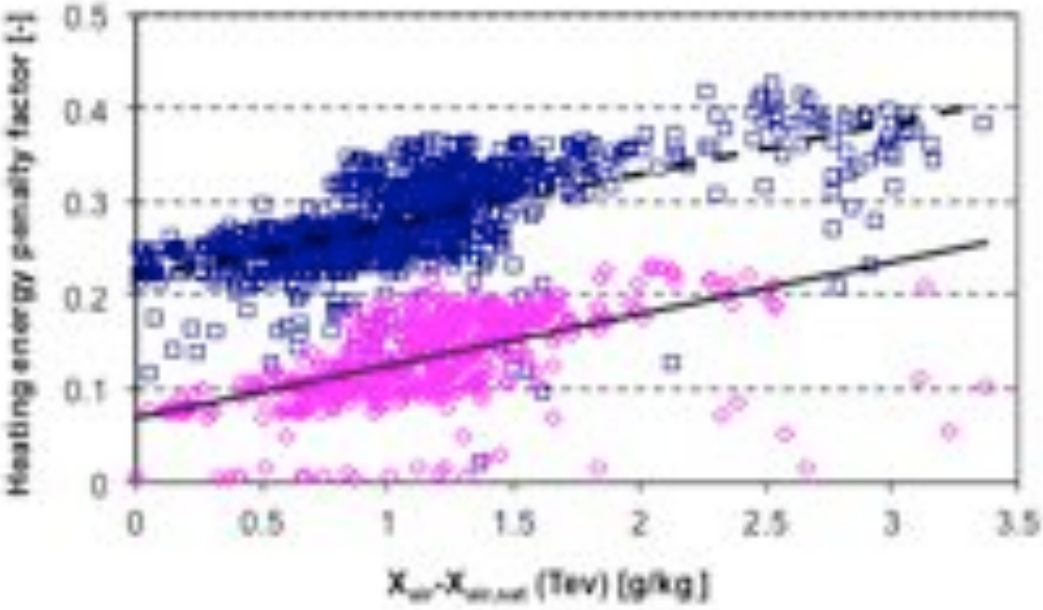
Figure 2.2.13. MPE-unit and FC-unit daily cumulated number of cycles and COP for day 5.

The effect of external air dry bulb temperature and humidity ratio on the heating capacity can be fully appreciated considering Figure 2.2.14 where the heating capacity penalization factor is plotted against the air temperature (Figure 2.2.14a) and the difference between air and saturated air at the evaporation temperature humidity ratio (Figure 2.2.14b). The penalization factor was calculated according to equation (2.2.10) considering each

frosting/defrosting/drainage cycle during the overall testing period. It appears that the heating capacity penalization factor for the MPE-unit is about 10÷18% higher than the FC-unit one in the  $-6\div4$  °C air dry bulb temperature range; this difference steeply reduces when the air temperature increases and disappears around 7 °C air dry bulb temperature when the penalization factor is close to unity. The heating capacity penalization factor variation is roughly linear with the humidity ratio difference; in fact it increases when the difference increases because of the higher water vapour condensation occurring on the external heat transfer surface.



a)



b)

□ Unit-1      ◇ Unit-2      - - Unit-1 trendline      — Unit-2 trendline

Figure 2.2.14. Heating capacity penalty factor for each defrosting cycle in the considered tests period time as function of a) the outdoor air dry bulb temperature and b) the difference between the outdoor air humidity ratio and the saturated air humidity ratio at the refrigerant evaporating temperature.

Considering Table 2.2.8 cumulated daily input energy and efficiency results, the frosting associated penalization can not be clearly pointed out. In fact, for days 1, 2 and 4, the MPE-unit cumulated input energy is sensibly lower than FC-unit one, -16.3, -14.3 and -11.7% respectively. The corresponding daily energy efficiency difference is equal 5.3, 1.4 and -2.3% for the three days, respectively. Both the input energy and efficiency results can be explained considering two opposite contributing phenomena occurring when the heat pump is working under frosting/defrosting condition: a) a defrosting cycle reduces the unit overall heating energy, thus reducing the daily energy efficiency-1 ratio, b) in defrosting operation the unit input power is lower than the

corresponding frosting operation one, thus reducing the daily energy input and energy efficiency ratio. The reduced input power can be appreciated considering Figure 2.215 where the suction and discharge pressures together with the input power are plotted for the MPE-unit from midnight to one o'clock of day 1.

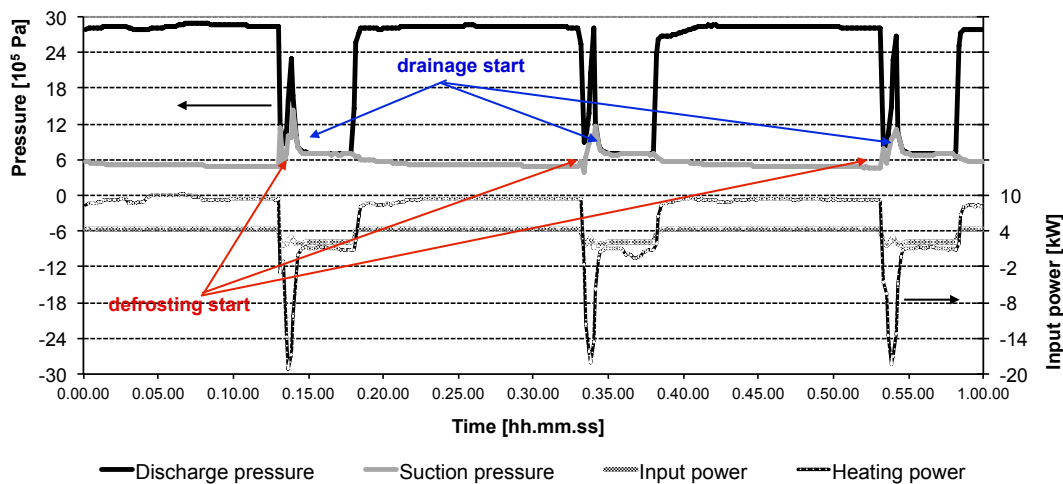
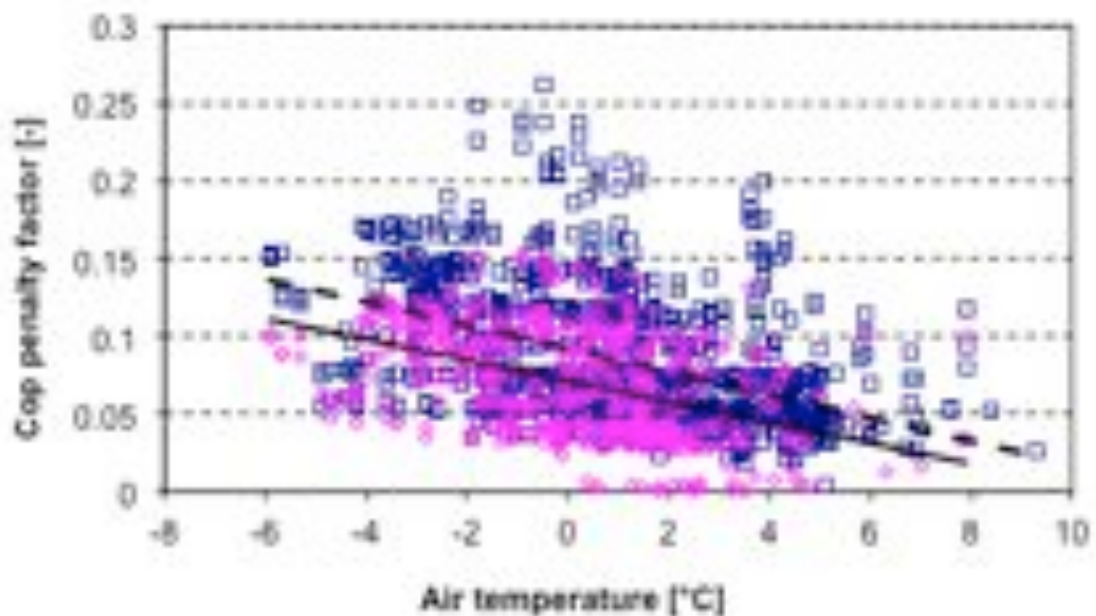


Figure 2.2.15. Input power, suction and discharge pressure trends of MPE-unit from midnight to one o'clock of day 1.

When the external air temperature is higher and no frosting phenomena occur (see Figures 2.2.11 and 2.2.13), such as in days 3 and 5, the MPE-unit cumulated daily input energy values are comparable or lower to FC-unit ones, with -0.5 and 5.3% difference, respectively. Also daily energy efficiency is similar with 5.3 and 1.2% improvement of the MPE-unit with respect to the standard finned coil unit.

The effect of external air dry bulb temperature and humidity ratio on the heat pump COP can be fully appreciated considering Figure 2.2.16 where the energy efficiency penalization factor is plotted against the air temperature (Figure 2.2.16a) and the difference between air and saturated air at the evaporation temperature humidity ratio (Figure 2.2.16b). The penalization factor was calculated according to equation (2.2.9) considering each

frosting/defrosting/drainage cycle during the overall testing period. It appears that energy efficiency penalization factor for the MPE-unit is about 3÷8% higher than the FC-unit one in the  $-6\div4$  °C air dry bulb temperature range; this difference reduces when the penalization factor is close to unity at around 7 °C air dry bulb temperature. As for the heating capacity penalization factor, also the energy efficiency penalization factor variation is roughly linear with the humidity ratio difference.



a)

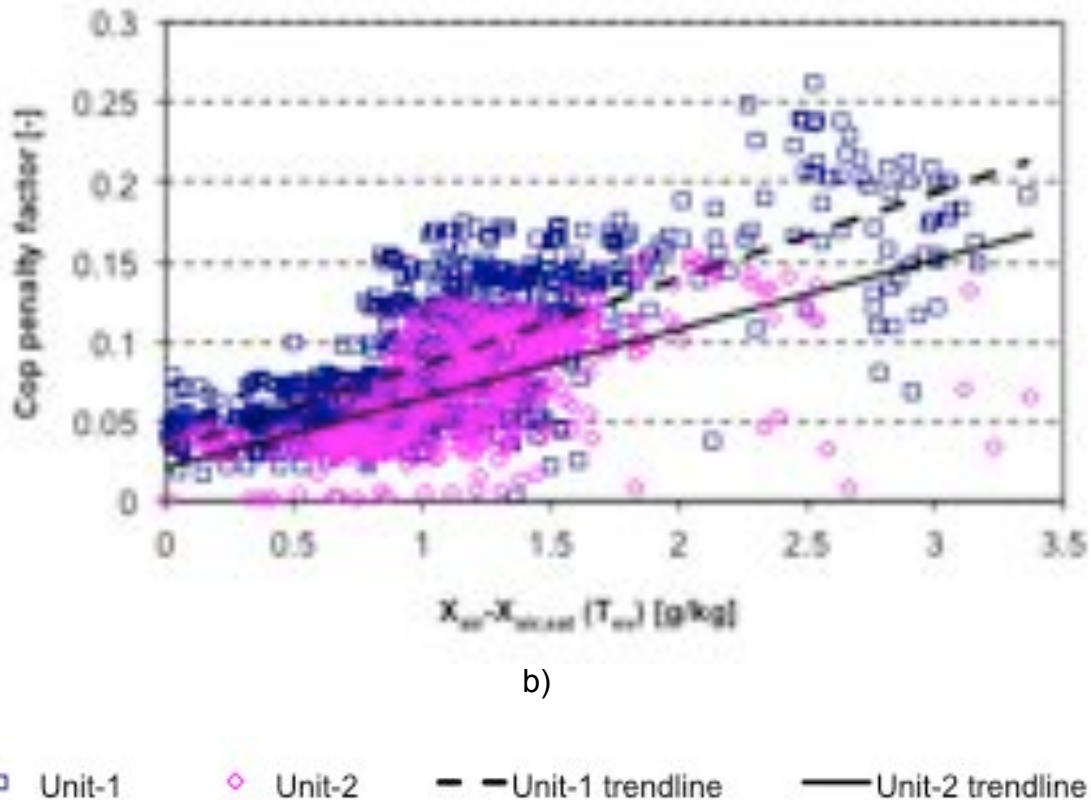


Figure 2.2.16. COP penalty factor for each defrosting cycle in the considered tests per time as function of a) the outdoor air dry bulb temperature and b) the difference between the outdoor air humidity ratio and the saturated air humidity ratio at the refrigerant evaporating temperature.

## 2.2.6 Conclusions

A 10 kW nominal cooling capacity R410A packaged air heat pump equipped with a round tube finned coil air heat exchanger was compared to the same unit using a multi-port extruded (MPE) aluminium flat tube air heat exchanger. The MPE heat exchanger was sized to approximately obtain the same cooling and heating capacities with respect to the standard round tube equipped unit in chiller and heat pump mode, respectively. The MPE heat exchanger has parallel flow vertical tube configuration with headers in horizontal position and conventional folded louvered fins. Tests were carried out according to



---

EN 14511:2007 [1] test conditions with different refrigerant inlet distributor/outlet tubes configurations without frosting phenomena occurring during heat pump operation. Both cooling and heating tests demonstrated that the round tube and the flat tube heat exchanger performance are comparable. In cooling tests at 35 °C air temperature, the MPE heat exchanger shows a 4.1% and 3.6% improvement of cooling capacity and EER with respect to the finned coil. In heating tests at 7 °C air temperature, the difference of heating capacity and COP is 1.4% and 0%, respectively, in favour of the MPE unit. Steady state tests demonstrated the importance of a rather uniform liquid refrigerant distribution between central and border tubes in the MPE heat exchanger; for the considered geometry this was obtained with two evenly distributed outlet tubes on the manifold.

Cycling frosting/defrosting operations were tested with two equivalent machines placed in parallel on the outside and working at full load condition, one of the units was equipped with the MPE heat exchanger while the other mounted a standard finned coil. The two heat pumps worked continuously between January and March 2011, penalization factors were analytically introduced to evaluate frosting associated heating capacity and energy efficiency degradation. Test results indicate that both the heat pumps are penalized by frost formation. The heating capacity penalization factor for the MPE-unit is about 10÷18% higher than the FC-unit one in the -6÷4 °C air dry bulb temperature range; the MPE energy penalization factor steeply closes the finned coil one when the air temperature rises to 7 °C air dry bulb temperature. Analogously, the energy efficiency penalization factor for the MPE-unit is about 3÷8% higher than the FC-unit one in the same temperature range while this difference disappears when the air temperature closes 7 °C air dry bulb temperature. For the two units, a roughly linear dependence of both the heating capacity penalization factor and the energy efficiency one from the difference between outdoor air and saturated air at the evaporation temperature humidity ratio can be pointed out.

### **2.2.7 Reference**

1. CEN. EN 14511:2007: Air conditioners, liquid chilling packages and heat pumps with electrically driven compressors for space heating and cooling. Terms and definitions, test conditions, test methods, requirements. Brussels, Belgium, 2007.
2. Lemmon E. W., Mc Linden M.O., Huber M.L. Refprop 7.0. NIST Standard Reference Database. (2002).

## **2.3 Development of a simulation tool for minichannel condenser and evaporator heat exchangers**

In this sub-chapter a simulation tool for extruded finned flat tube with internal minichannel heat exchanger operating as an evaporator or a condenser is presented.

The support and the suggestions of the engineer William Sausa of Skybyte Engineering at the coding work are gratefully acknowledged.

### **2.3.1 Introduction**

As detailed in 2.1, the minichannel heat exchanger are increasing the interest in the refrigeration industry and the research is focusing to solve some technological constrain as detailed in the previous chapters. A model that allows making analysis of the performance and the design of the prototype could help in the research activities.

The model was built with the target of offering a tool able to calculate performance and to help in a proper design of this type of heat exchangers operating as condenser or evaporator.

The model estimates the component performance and capacity for given geometrical fluid dynamic and thermodynamic boundary condition.

Because the heat transfer coefficient HTC varies significantly with the quality for a phase change refrigerant, a finite volume method is used in the heat exchanger schematization to discretize the domain.

Literature correlations for predicting the HTC and the pressure drops on the air side and on the refrigerant side are implemented, however new correlations could be easily added. On the air side the heat transfer coefficient and the pressure drops can be inserted directly by the user.

The user graphical interface allows the complete definition of the:

- 1) heat exchanger geometrical characteristics such as:
  - **Plates** number, length, depth ( $T_d$ ), thickness ( $D_m$ ), pitch ( $TP$ ), number of ports, port section and channels hydraulic diameter/lengths;
  - **Fins** thickness ( $F_t$ ), pitch ( $F_p$ ), length ( $F_l$ ), depth ( $F_d$ );
  - **Louver** length ( $L_l$ ), pitch ( $L_p$ ) and angle ( $\theta$ ).

All these geometrical features are shown in Figure 2.3.1.

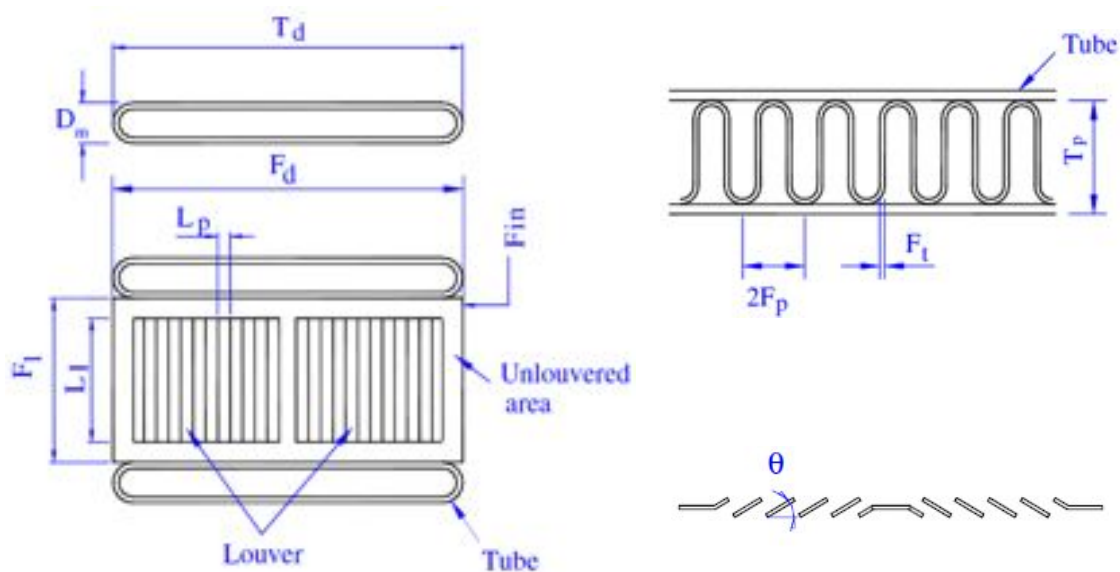


Figure 2.3.1. Some geometrical parameters, which can be inserted in the simulation tool.

- 2) Header internal subdivision pointing out the inlet and outlet plates from each header section.
- 3) Multi-row heat exchanger, in this case the air inlet direction needs to be set up.

In Figure 2.3.2 an example of two rows heat exchanger with the header internal subdivision and the inlet air direction is shown.

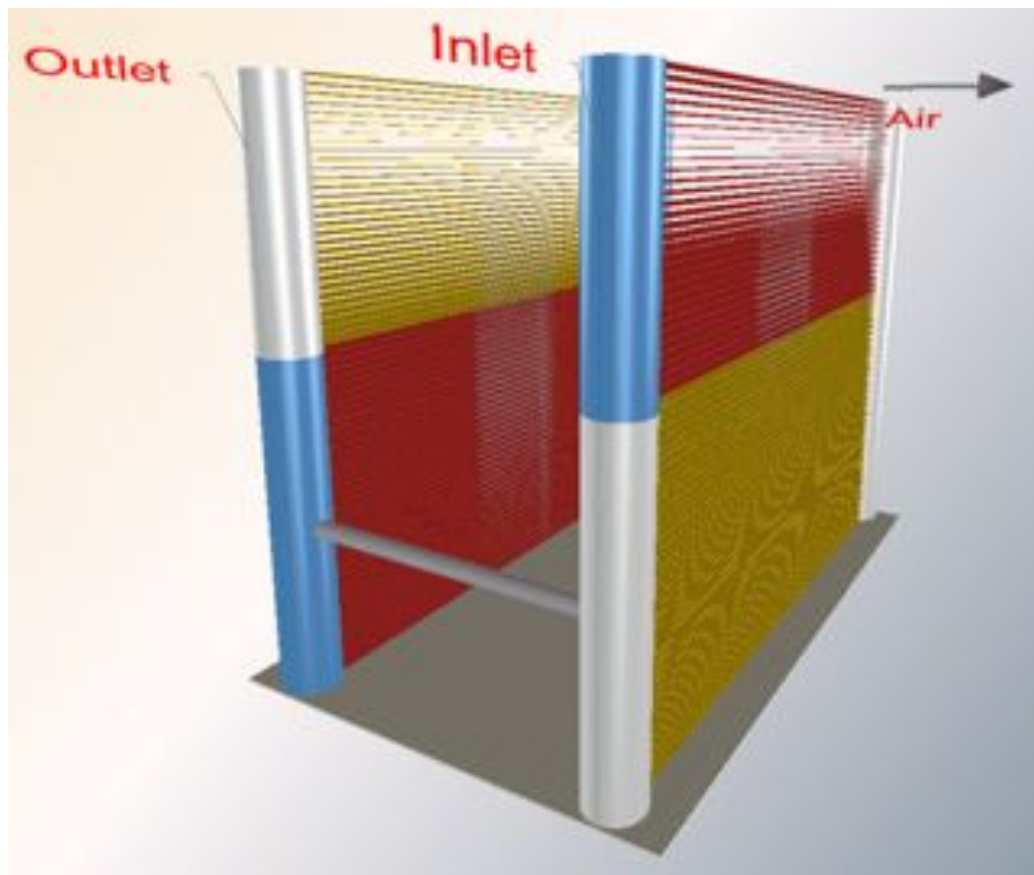


Figure 2.3.2. Example of two rows heat exchanger with the header internal subdivision and the inlet air direction.

- 4) Air inlet thermo-hygrometric conditions, and frontal velocity or the volumetric flow rate.
- 5) In condensation tests, the user can define refrigerant inlet pressure or condensation temperature, inlet temperature and outlet subcooling degree.

In evaporation tests, the user can define refrigerant outlet pressure or evaporation temperature, inlet enthalpy (or define the condenser outlet pressure and the subcooling) and outlet superheat degree.

**The model allows the user the choice between the following refrigerants:**

- pure synthetic fluids: R11, R12, R123, R1234yf, R1234ze(E), R125, R134a, R152a, R22, R32;
- synthetic mixtures: R404A, R407C, R404A, R507A;
- natural fluid: R290 (Propane), R600a (Isobutane), R717 (Ammonia), R744 (Carbon dioxide).

**The main simulation outputs are the following:**

- heat exchanger capacity;
- refrigerant mass flow rate and refrigerant pressure drops;
- outlet air thermo-hygrometric conditions;
- refrigerant and air average coefficient of heat transfer;
- refrigerant average void fraction and charge;
- nodal analysis which allows to get parameters trends along the heat exchangers.

### **2.3.2 Program input/output windows**

In this paragraph all user interfaces, how to enter data into them and the model results, are described. The user interfaces are designed with the goal to offer an easy, fast and intuitive way for inserting and saving the data input and the results.

#### **Main window**

In Figure 2.3.3 the Main window is shown.

It allows the user to choose the refrigerant, the type of the simulation, opening the window for inserting the refrigerant thermodynamic conditions, the geometric parameters, the air inlet thermo-hygrometric conditions, the ventilation; and below to manage the simulation.

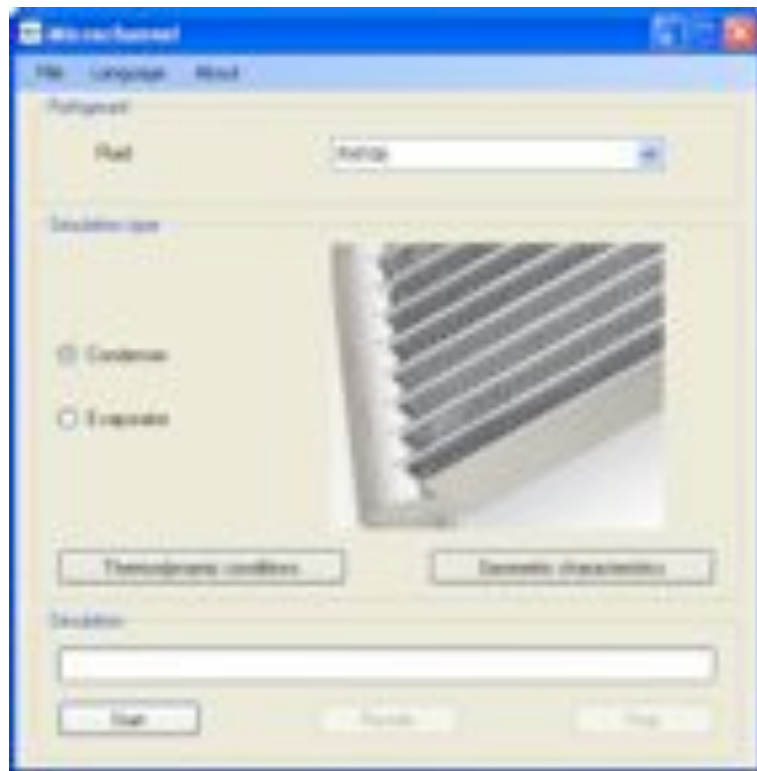


Figure 2.3.3. Main window.

## Menu

- File
  - Open project: loads a saved project including the refrigerant thermodynamic conditions, the heat exchanger geometric characteristics, the air thermo-hygrometric conditions and the ventilation;
  - Save project: saves the actual project considering the refrigerant thermodynamic conditions, the heat exchanger geometric characteristics, the air thermo-hygrometric conditions and the ventilation in the \Documents\MPE 2010\Master file\Input\Projects\"Simulation type" folder.
- Language: allows the user to choose the software language.
- About: allows the user to visualize information about the installed software version and the company data.

### Refrigerant

Fluid: allows the user to select the refrigerant from the list presented in the previous paragraph.

### Simulation type

- Condenser radio button: allows the user to simulate a condenser heat exchanger.
- Evaporator radio button: allows the user to simulate an evaporator heat exchanger.
- Thermodynamic conditions button: allows the user to set the refrigerant thermodynamic conditions for the chosen simulation type: condenser/evaporator.
- Geometric characteristics button: allows the user to set the geometric characteristics and the air thermo-hygrometric conditions and fan.

### Simulation

- Start button: allows the user to run the simulation, the progress bar below shows the simulation course.
- Results button: allows the user to visualize and to save the simulation results.
- Stop button: allows the user to stop the simulation.

### **Thermodynamic conditions window**

The window thermodynamic conditions changes by changing the simulation type.

In Figure 2.3.4 the “Thermodynamic conditions: condenser” conditions window is shown, and then a description of how to insert data is reported.



Section	Parameter	Value
Condensation	Condensing temperature (dew point) [°C]	45
	Condensing temperature (mean) [°C]	44.94
	Condensing temperature (bubble point) [°C]	44.98
	Condensing pressure [bar]	27.267
	Subcooling [K]	1.5
Evaporation	Evaporating temperature (dew point) [°C]	5.23
	Evaporating pressure [bar]	5.08
	Superheat [K]	2.6
Compression	Discharge temperature [°C]	75.87
	Isentropic efficiency [%]	0.6
	Compressor heat loss [%]	20

Figure 2.3.4. Window thermodynamic conditions for simulating a condenser.

### Condensation

- Condensing temperature (dew point) [°C]: is the condensing temperature in saturated vapor state, so for a zeotropic mixture it is the condensing dew point temperature.
- Condensing temperature (mean) [°C]: is the saturated condensing temperature corresponding to quality of 0.5.

- Condensing temperature (bubble point) [ $^{\circ}\text{C}$ ]: is the condensing temperature in saturated liquid state.
- Condensing pressure [bar]: is the condensing pressure in saturated state.
- Subcooling [K]: is the liquid subcooling at the condenser outlet.

The saturation state of condensing considered is at the inlet of the condenser. The program when a control text box is left will update the others. For example in the Figure 2.3.4 the values of Condensing temperature (mean), Condensing temperature (bubble point) and pressure are written after inserting and leaving the Condensing temperature (dew point) value of  $45^{\circ}\text{C}$ .

### Evaporation

- Evaporating temperature (dew point) [ $^{\circ}\text{C}$ ]: is the evaporator temperature in saturated vapor state.
- Evaporating pressure [bar]: is the evaporator pressure.
- Superheat [K]: is the vapor superheated at the inlet of the compressor.

The saturation state of evaporating considered is at the inlet of the compressor.

### Compression

- Discharge temperature [ $^{\circ}\text{C}$ ]: is the compressor discharge temperature.
- Isentropic efficiency [-]: is the isentropic efficiency in a compression process from the evaporating to condensing pressure, it cannot be lower than 0.1.
- Compressor heat loss (HL) [%]: is the fraction of compression work transferred to the ambient as heat from the compressor outer surface, it affects the compressor discharge temperature. Its maximum value corresponds to one evaluates to the condensing temperature in saturated vapor condition.

The discharge temperature is calculated from the condenser inlet condition, the evaporator pressure and superheat, the isentropic efficiency and the compressor heat loss. The discharge temperature will be updated when one

of the text boxes control, corresponding to the parameters mentioned above, is left.

The user can insert directly the discharge temperature; in this case the program updates the heat loss value without changing other parameters. In case the inserted discharge temperature is too high and the corresponding heat loss HL became negative, the program updates discharge temperature value at one corresponding at HL=0%.

The minimum acceptable discharge temperature is equal to the condensing one in saturated vapor conditions.

The *function of the buttons* is described in the following.

- Cancel button: allows coming back to the “Main” window without saving the data.
- Ok button: allows the user to go forward to the “Main” window with the inserted data saved.

In Figure 2.3.5 the “Thermodynamic conditions: evaporator” window is shown, and then a description of how to insert the data is reported.



Figure 2.3.5. Window thermodynamic conditions for the simulation of an evaporator.

### Evaporation

- Evaporating temperature (dew point) [°C]: is the evaporator temperature in saturated vapor state.
- Evaporating temperature (mean) [°C]: is the mean value between the saturation temperature corresponding to the evaporator outlet quality and the saturation temperature corresponding to evaporator inlet quality, calculated according to the evaporator outlet pressure.
- Evaporating pressure [bar]: is the evaporator pressure at the evaporator outlet.

The program when a control text box is left will update the others.

### Evaporation type

- Dry expansion: in this case the user has to set the Superheat [K], if the superheat value is set equal to zero then the Outlet quality text box is enabled and the outlet quality value automatically is set equal to 1. It is also possible set an exit quality below one.

- Flooded expansion: this type of expansion allows to set the evaporator outlet quality or its reciprocal called circulation number because it is the ratio between the mass flow rate and the evaporated mass flow rate. In this case the evaporator inlet quality is set to one.

#### Compression

- Isentropic efficiency: it is the compression isentropic efficiency; it cannot be lower than one.

#### Condensation

- Condensing temperature (dew point) [°C]: is the condensing temperature value in saturated vapor state.
- Condensing temperature (mean) [°C]: is the condensing temperature corresponding to a quality value of 0.5.
- Throttling device inlet pressure [bar]: is the saturation pressure at the inlet of the throttling device.
- Subcooling [K]: is the subcooling at the condenser outlet.
- Throttling device inlet temperature [°C]: is the temperature value at the inlet of throttling device, it is the saturated bubble temperature at the condenser outlet minus the subcooling value.
- Throttling device inlet enthalpy [kJ/kg]: is the enthalpy value at the inlet of throttling device.

The throttling device inlet enthalpy is calculated from the condenser outlet condition, the program will update it when one of the text boxes control corresponding to the condenser outlet conditions is left. The user can choose to insert directly this enthalpy value; in this case the other “Condensation” group box parameters will not be utilized in the subsequent calculations.

The *function of the buttons* is described in the following.

- Cancel button: allows coming back to the “Main” window without saving the data.

- Ok button: allows the user to go forward to the “Main” window with the inserted data saved.

### Geometric characteristics window

In this window the user can completely define the minichannel heat exchanger geometry, the air inlet condition and the ventilation.

In Figure 2.3.6 the “Geometric characteristics” window is shown, then a description of how to insert data is reported.

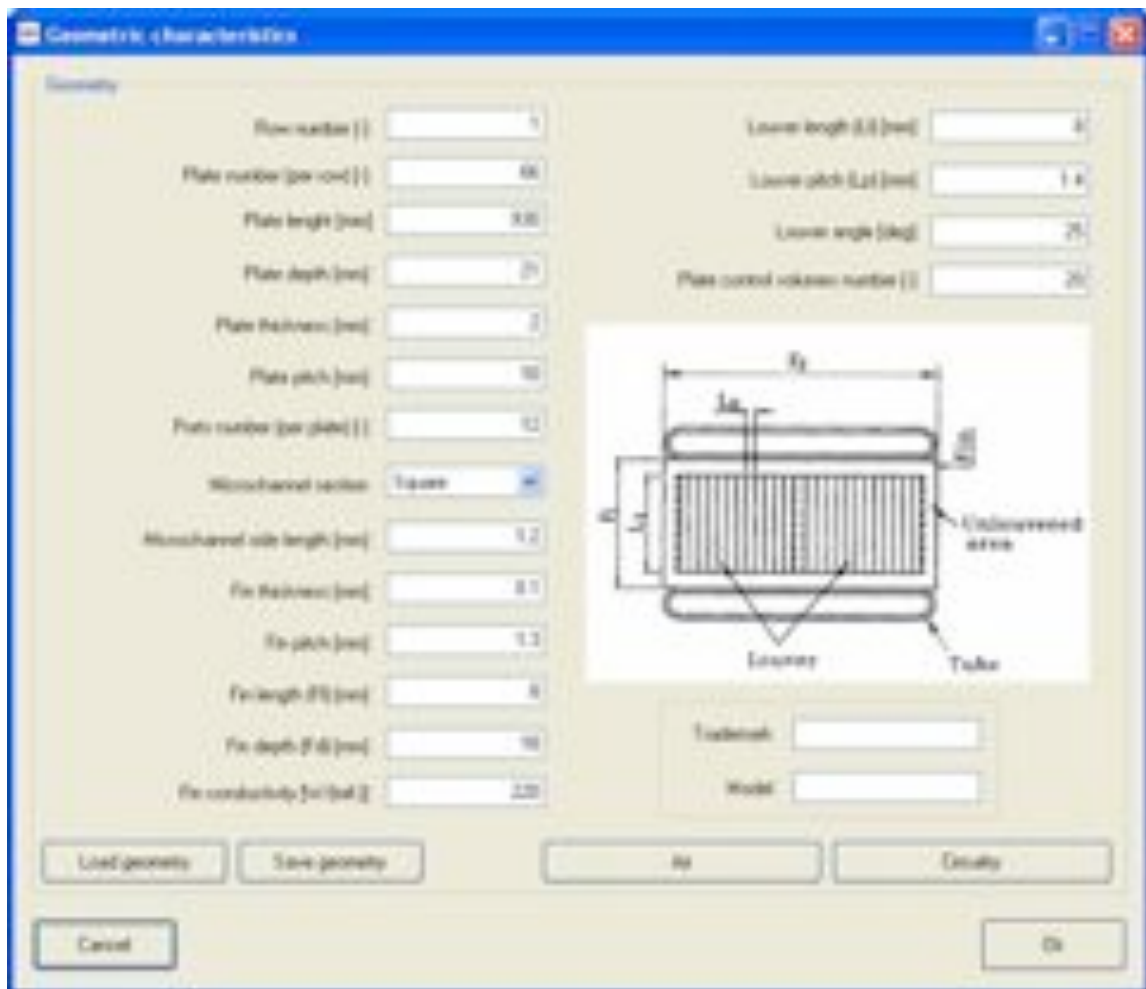


Figure 2.3.6. Window geometric characteristics

### Geometry

With reference to Figure 2.3.1 for the lengths quoted in it.

- Row number [-]: is the number of rows in the air direction.
- Plate number [-]: is the total plates number in each row (the plate number is the same in each row).
- Plate length [mm]: is the frontal length of the heat exchanger.
- Plate depth (Td) [mm]: is the depth of a single plate.
- Plate thickness (Dm) [mm]: is the thickness of the single plate.
- Plate pitch (Tp) [mm]: is the pitch between plates.
- Ports number (per plate) [-]: is the number of ports in each plate.
- Microchannel section allows the user to choose the port section between circular, square and rectangular.

If choice is the rectangular section, the window shown in Figure 2.3.7 will appear; in that window the user can insert the section side lengths.

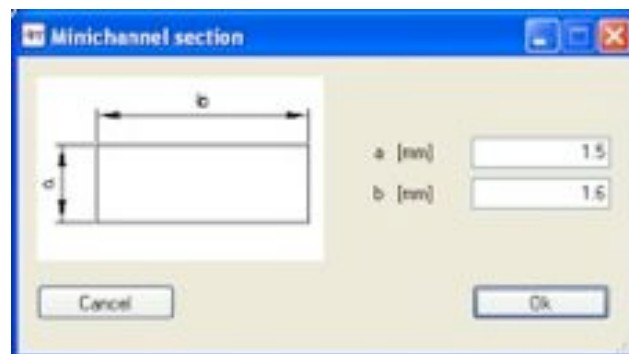


Figure 2.3.7. Port rectangular section window.

- Microchannel hydraulic diameter is the diameter in case of circular section and the side length in case of square section, it is calculated by the program in case of rectangular section.
- Fin thickness (Ft) [mm]: is the thickness of a single fin.
- Fin pitch (Fp) [mm]: is half the distance between two fin peaks (see Figure 2.3.1).
- Fin length (Fl) [mm]: is the length of the fin.

- Fin depth (Fd) [mm]: is the depth of the fin.
- Fin conductivity [W/(m•K)]: is the fin conductivity.
- Louver length (Ll) [mm]: is the length of the louvers.
- Louver pitch (Lp) [mm]: is the pitch between the louvers.
- Louver angle ( $\alpha$ ) [deg]: is the angle of louvers.

The function of the buttons is described in the following.

- Cancel button: allows coming back to the main window without saving the data.
- Ok button: allows the user to go forward to the main window with the inserted data saved.
- Trademark text box: allows the user to save the microchannel heat exchanger trademark.
- Model text box: allows the user to save the microchannel heat exchanger model.
- Load geometry button: allows loading a saved geometry, which includes the geometrical characteristics, the air inlet and the ventilation characteristics; that is all the geometric characteristics window data and those of its subwindows.
- Save geometry button: allows the user to save the heat exchanger geometry characteristics, the air inlet and the ventilation characteristics, thus all the geometric characteristics data and those of its subwindows in the \Documents\MPE 2010\Master File\Input\Components\“Simulation type” (Condenser or Evaporator) folder.

The file name proposed by the program is a string obtained by concatenating the trademark, the “\_” and the model; the user can change the filename in the File dialog windows.

This is the best way to save when the user wants save the minichannel geometry, the air thermohygrometric inlet condition and the ventilation without the refrigerant and its thermodynamic conditions.



- Air button: allows the user to define the inlet air condition and the ventilation to the heat exchanger.
- Circuitry: allows the user to insert the refrigerant circuitry of the minichannel heat exchanger.

### Inlet air condition window

In this window the user can define the air inlet conditions, the air side heat transfer coefficient, the pressure drops, and the ventilation.

In Figure 2.3.8 the “Inlet air condition” window is shown, then a description of how to insert data is reported.

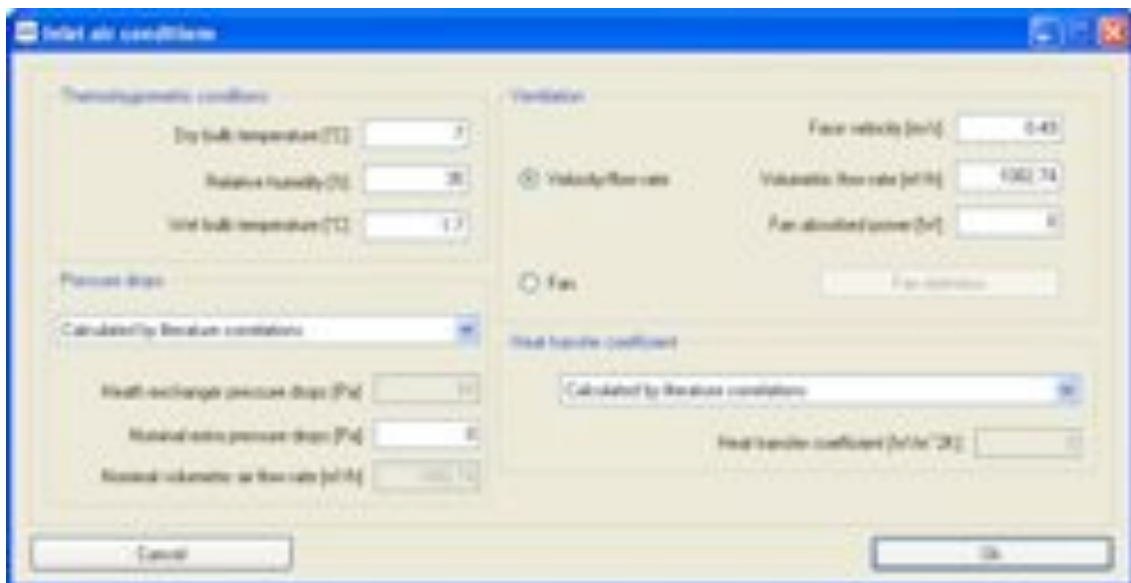


Figure 2.3.8. Air inlet condition window.

### Thermohygrometric conditions

- Dry-bulb temperature [°C]: is the air-dry bulb temperature value at the inlet of the minichannel heat exchanger.
- Relative humidity [%]: is the air relative humidity value at the inlet of the microchannel heat exchanger.
- Wet bulb temperature [°C]: is the air wet bulb temperature value at the inlet of the minichannel heat exchanger.

The model when the control of a text box is left will update the others.

### Pressure drops

- The user can choose if the pressure drops will be calculated by literature correlations or assign them.
- Heat exchanger pressure drops [Pa]: in case that the pressure drops are assigned by the user this text box becomes enabled, so this value can be inserted.
- Nominal extra pressure drops [Pa]: the user can insert extra pressure drops along the air path.
- Nominal volumetric air flow rate [m<sup>3</sup>/h]: it is the volumetric flow rate considered to calculate the extra pressure drops.

In case the “Velocity/flow rate” radio button is selected in the Ventilation group box, the nominal air volumetric flow rate is the same inserted in the Volumetric flow rate text box, else if the “Fan” radio button is selected the user can set the volumetric flow rate for which the nominal extra pressure drops are assigned.

### Heat transfer coefficient

The user can choose whether to calculate the air side heat transfer coefficient HTC by literature correlations or assign to it a constant value, or assign the product between the heat transfer coefficient and the fin surface efficiency.

- Heat transfer coefficient [W/m<sup>2</sup>K]: in case the user chooses to assign the HTC the text box becomes enabled for inserting this value.
- The same text box becomes enabled with a different label on the left, for inserting the product between HTC and the fin surface efficiency.

### Ventilation

The user can assign the frontal velocity, the air volumetric flow rate and the fan absorbed power, or assign a fan by selecting respectively the “Velocity/flow rate” or the “Fan” radio buttons. If the user selects the “Fan”

radio button the “Fan definition” button will be enabled and by a “click” on this button the “Fan” window will open.

- Face velocity [m/s]: is the air face velocity of microchannel heat exchanger.
- Volumetric flow rate [m<sup>3</sup>/h]: is the air volumetric flow rate corresponding to the face velocity.

The program when the control of one of these text boxes is left will update the others.

- Fan absorbed power is the power absorbed by the fan.

The *function of the other buttons* is described in the following.

- Cancel button: allows the user to come back to the “Geometric characteristics” window without saving the data.
- Ok button: allows the user to go forward to the “Geometric characteristics” window with the inserted data in the window and in its subwindow saved.

### **Fan window**

In this window the user can define the fan performances by inserting some working points: the fan air flow and the corresponding pressure drops and absorbed power.

A polynomial that correlates the pressure drops with the air flow rate will be calculated, this is the best interpolating the assigned fan working points.

In similar way a polynomial that correlates the fan absorbed power with the air flow rate will be calculated, if the fan absorbed power points are not assigned, the fan absorbed power will be set to zero.

The polynomial degree is set by the user.

The number of assigned points minus one cannot be lower than polynomial degree.

In Figure 2.3.9 the “Fan” window is shown.



Figure 2.3.9. Fan window.

The *function of the buttons* is described in the following.

- Cancel button: allows the user to come back to the “Inlet air conditions” window without saving the data.
- Ok button: allows the user to go forward to the “Inlet air conditions” window with the inserted data saved.
- Load fan button: allows the user to load a saved fan.
- Save fan button: allows the user to save the fan in the \Documents\MPE 2010\Master File\Input\Components\Fan” folder.

The file name proposed by the program is a string obtained by concatenating the trademark, the “\_” and the model; the user can change the filename in the File dialog windows.

## Circuitry window

The circuitry window allows the user to define the refrigerant circuitry in the minichannel heat exchanger.

In Figure 2.3.10 the “Circuitry” window without any circuitry inserted is shown.

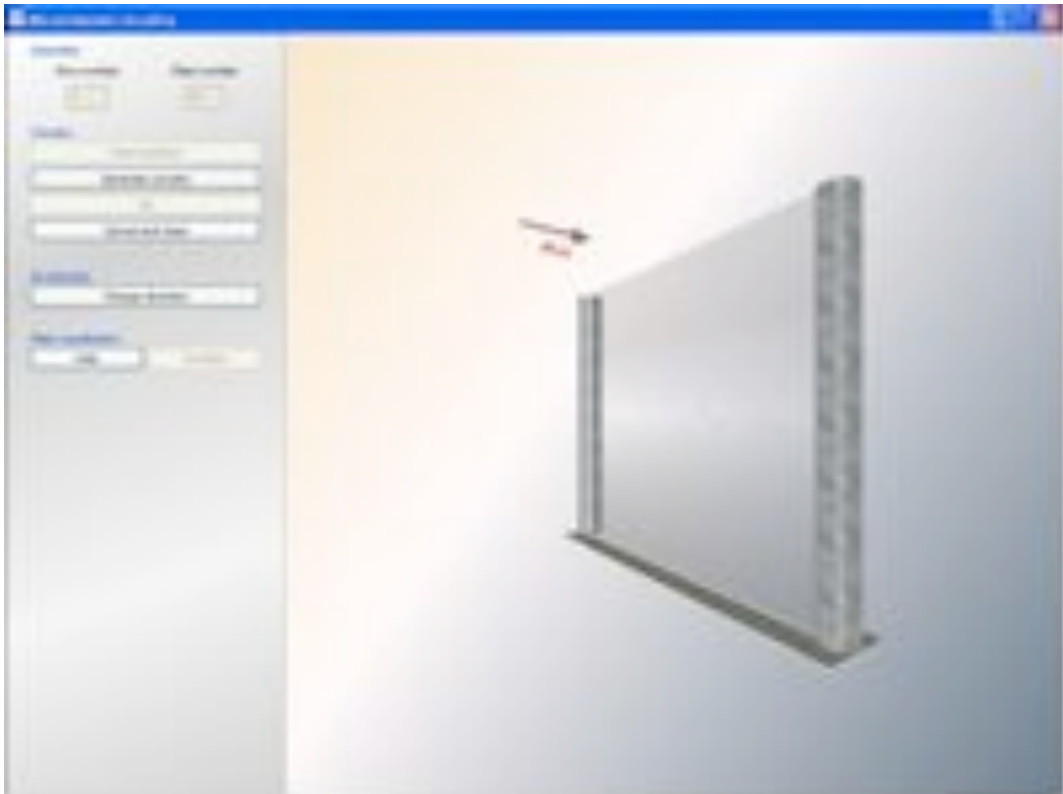


*Figure 2.3.10. Circuitry window without any inserted circuitry.*

### Geometry

- Rows number: this text box reports the number of rows as inserted in the “Geometric characteristics” window.
- Plate number: this text box reports the number of plates as inserted in the “Geometric characteristics” window.

### Circuitry

- Reset partition button: allows the user to clear all the header partitions.
- Generate circuitry button: allows the user to generate the circuitry by indicating the refrigerant inlet block for each row, after the last inlet block is inserted the program will automatically create the circuitry.
- Ok button: allows the user to go forward to the “Geometric characteristics” window with the inserted circuitry saved.
- Cancel and close button: allows the user to come back to the “Geometric characteristics” window without saving the circuitry modifies.

### Air direction

- Change direction button: an arrow corresponding to the actual air direction changes its direction by pushing this button, if there is only one row this direction is indifferent.

### Plate visualization

- Hide button: allows the user to hide the plates of the heat exchanger, only the headers remain.
- Visualize button: allows the user to show the plates of the heat exchanger when they are hidden.

By holding down the right mouse button and then moving it, the user can zoom in or zoom out the heat exchanger.

### Heat exchanger circuitry

The user has to click with the left mouse button above the chosen header, a dialog window will appear, in this window the block number of plates can be set.

The number of plates is counted from the top block in the same header (so first time it is counted from the top of the heat exchanger). After having confirmed the header plates of the inserted block, the corresponding header

partition will change color and then it will be possible to insert another header partition.

The “Circuitry” dialog window and an example of the header partition are shown in Figure 2.3.11.

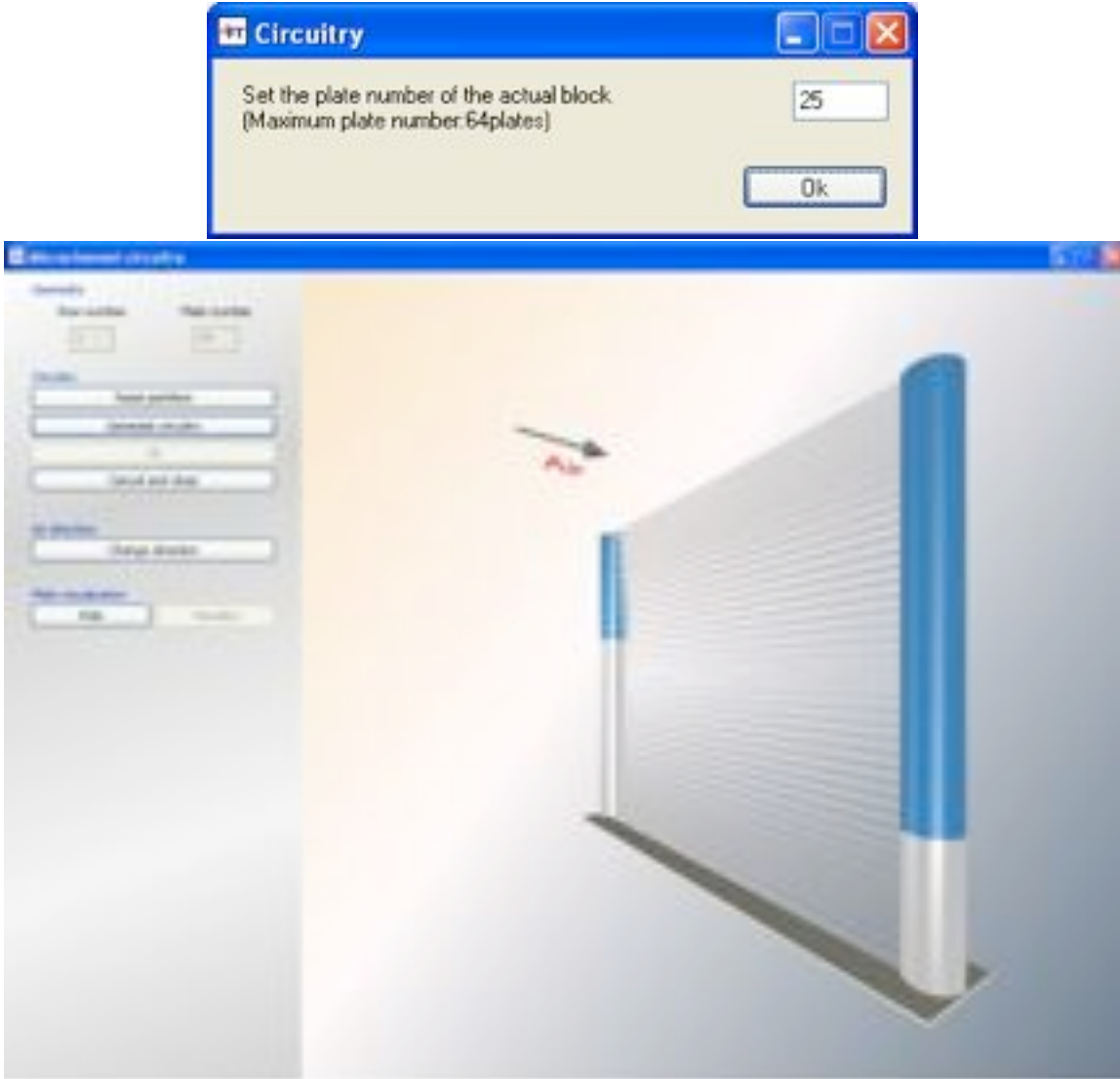
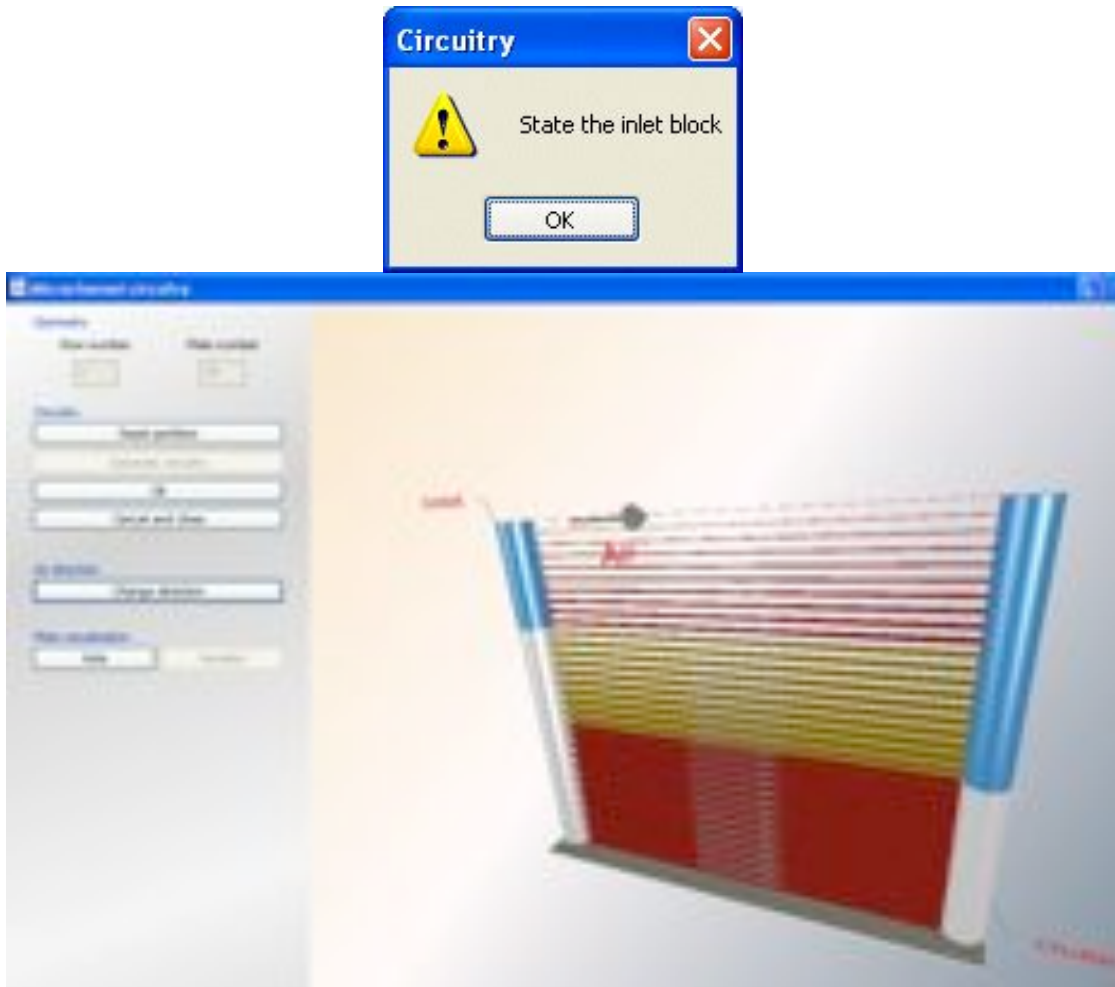


Figure 2.3.11. Circuitry dialog window for inserting the header partition, the maximum number of plates the user can set is indicated, the number of plates is counted from the upper partition. An example of header partition is reported too.

After that the header blocks have been created for creating the circuitry; the user has to click the “Generate circuitry” button, a dialog window will be shown, asking to state the inlet block of each row.

This dialog window and two examples of inserted circuitry respectively for one row and two rows heat exchangers are shown in Figure 2.3.12.





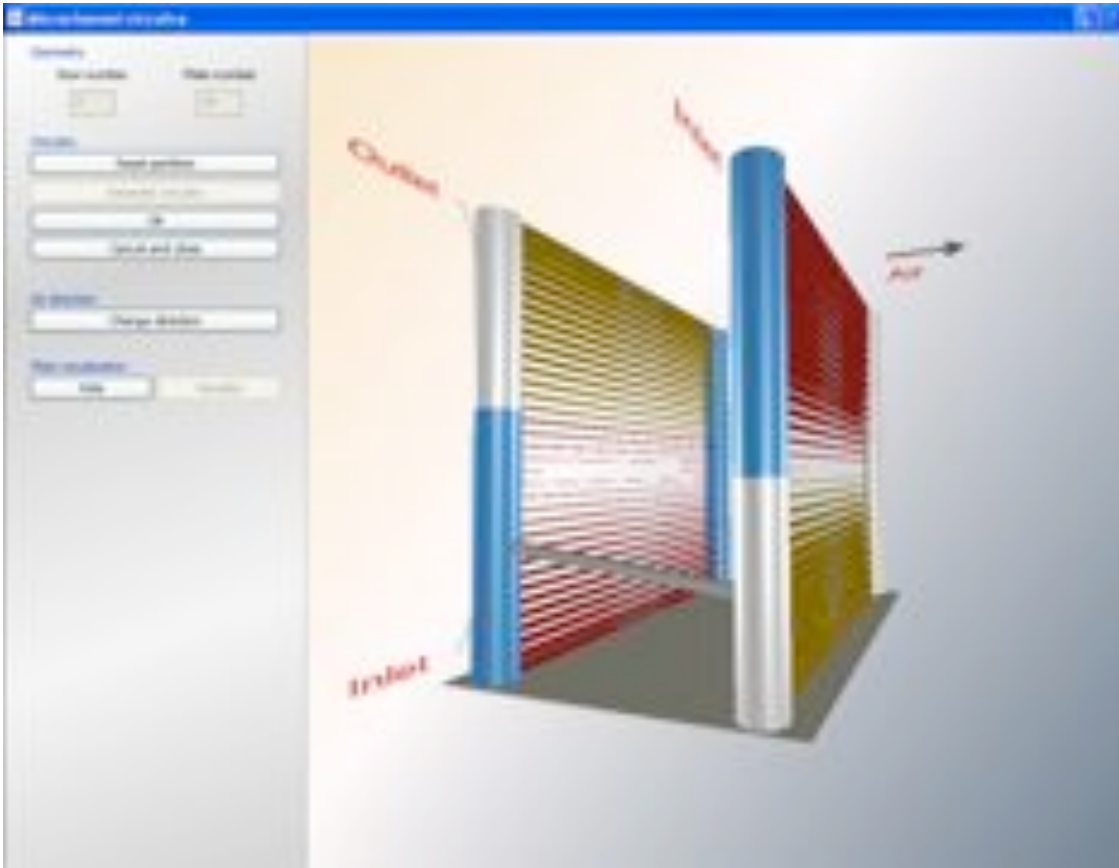


Figure 2.3.12. Dialog window for inserting the rows inlet block, and two examples of inserted circuitry respectively for one row and two rows, heat exchangers.

Finally, for deleting all the header partitions, the user has to click the “Reset partition” button, a dialog window for confirming the reset will appear. It is shown in the Figure 2.3.13.



Figure 2.3.13. Confirm reset partition dialog window.

## Results

When the simulation running is finished the “Results” button in the main windows is enabled.

The user has to click on it to see the Results window.

The result window is divided in two parts by a table control.

The first part shows a tree view with the performance of the heat exchanger, the overall refrigerant mass and volumetric flow rates.

On the refrigerant side the inlet and the outlet state, the overall pressure drops, the average heat transfer coefficient HTC, the mean void fraction and an estimation of the charge are given; the mean HTC and the pressure drops for all the refrigerant states are also reported.

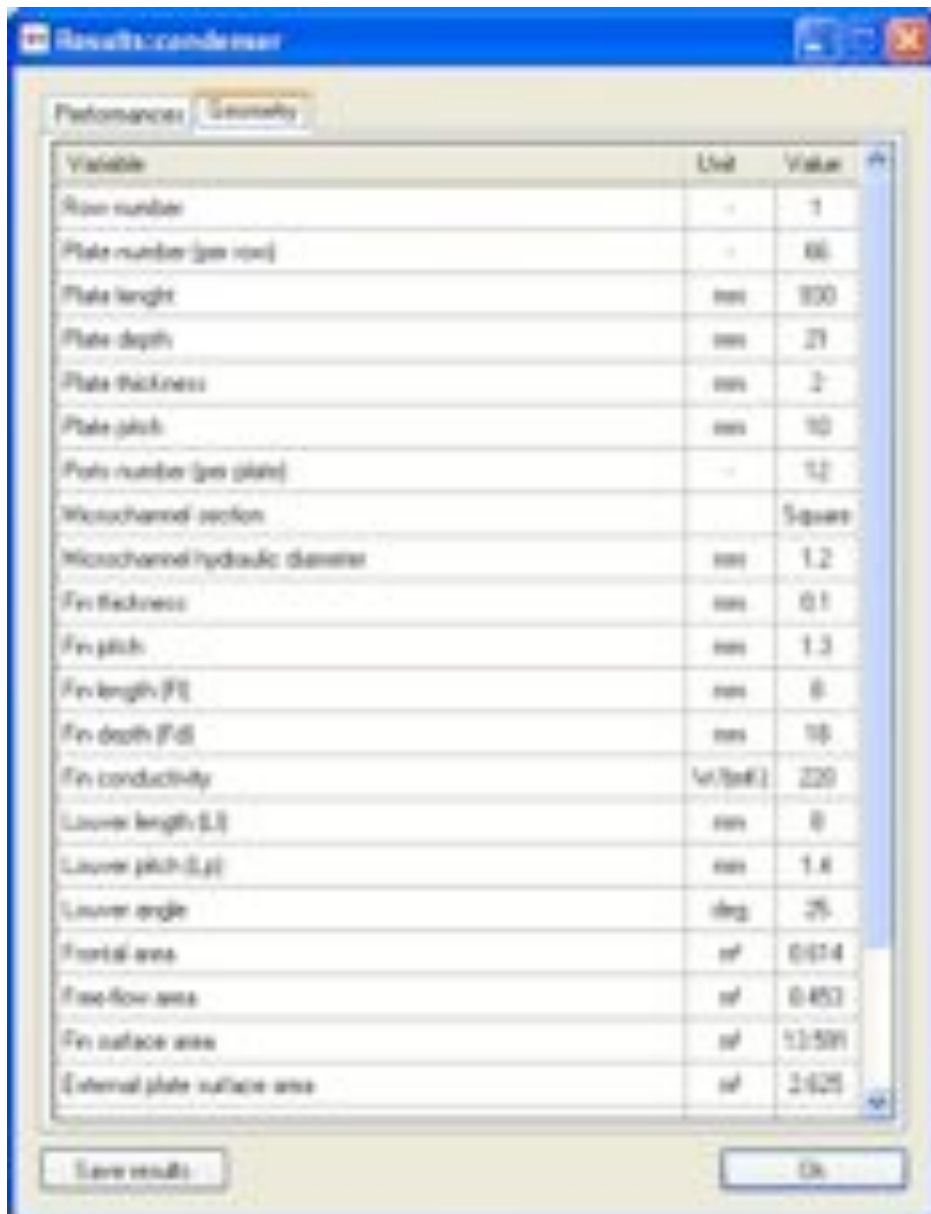
On the air side the mass and volumetric flow rates, the face velocity, the pressure drops, the average heat transfer coefficient, the inlet/outlet conditions and the fan features are reported.

In Figure 2.3.13 the “Results” window with the “Performance” part is shown.



Figure 2.3.14. Results window with the heat exchanger performance part.

The second part shows the geometrical parameters inserted by the user followed by the ones calculated by the program. It is shown in the Figure 2.3.15.



Results: condenser

Performance: Geometry

Variable	Unit	Value
Row number	-	1
Plate number (per row)	-	66
Plate length	mm	800
Plate depth	mm	29
Plate thickness	mm	2
Plate pitch	mm	10
Pore number (per plate)	-	12
Microchannel section		Square
Microchannel hydraulic diameter	mm	1.2
Fin thickness	mm	0.1
Fin pitch	mm	1.3
Fin length (FL)	mm	8
Fin depth (FD)	mm	10
Fin conductivity	W/mK	220
Louver length (LL)	mm	8
Louver pitch (LP)	mm	1.4
Louver angle	deg	25
Frontal area	m <sup>2</sup>	0.074
Free-flow area	m <sup>2</sup>	0.453
Fin surface area	m <sup>2</sup>	11.589
External plate surface area	m <sup>2</sup>	2.625

Save results      Ok

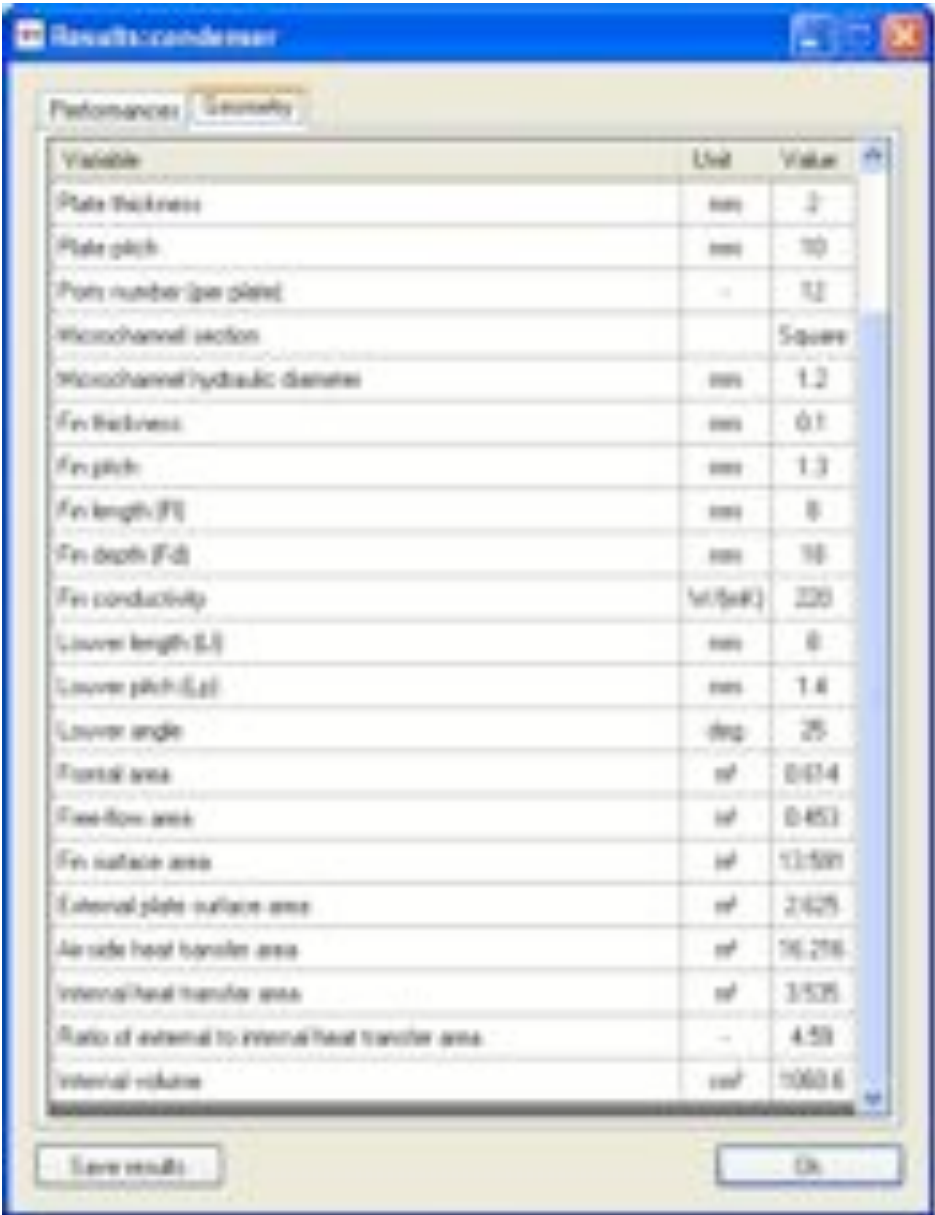


Figure 2.3.15. Results window with the heat exchanger geometry part.

The button “Save Results” allows the user to save in an excel file the results, the default folder is in \Documents\MPE 2010\Master File\Output\“Simulation type” (Condenser or Evaporator) folder; the user can change the path in the save dialog window.

The name of the file is a string obtained by concatenating the previous assigned trademark with the “\_” and with the assigned model, otherwise a

default file name is assigned; the user can change the name in the save dialog window.

The “Results” excel file has three sheets: Geometry, Global results and Nodal Results.

In the “Geometry” sheet the geometrical characteristics above described in the “Geometry” part of the “Result” window, are given. Then below the parameters of circuitry are reported.

In the “Global Results” sheet the same parameters described in the “Performance” part of the “Result” window, are reported.

In the “Nodal Results” sheet the nodal parameters are reported in the columns.

They are in reference to the mesh:

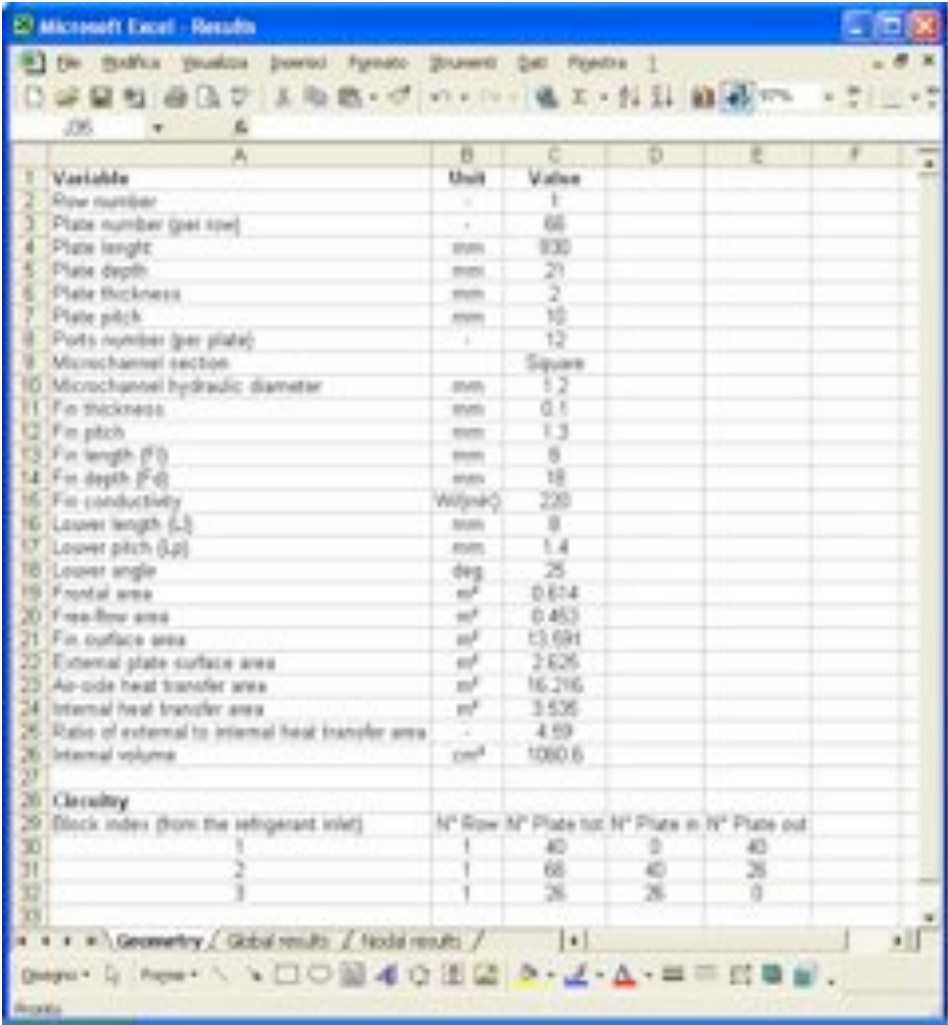
- Node: node number;
- T\_in\_ref: refrigerant inlet temperature;
- T\_out\_ref: refrigerant outlet temperature;
- T\_in\_air: air inlet temperature;
- T\_out\_air: air outlet temperature;
- Tdew\_out\_ref: refrigerant outlet dew temperature;
- Pres\_out\_ref: refrigerant outlet pressure;
- Quality: refrigerant average quality;
- Heat\_transfer\_coef\_ref: refrigerant heat transfer coefficient;
- Heat\_transfer\_coef\_air: air heat transfer coefficient;
- Fin\_efficiency: efficiency of the fin surface;
- Total\_heat\_capacity: heat transfer flux;
- Single-phase\_heat\_capacity: heat transfer flux exchanged while the refrigerant is in single phase state;
- Two-phase\_heat\_capacity: heat transfer flux exchanged while the refrigerant is in two phases state;
- Total\_pressure\_drops\_ref: refrigerant pressure drops;

- Void\_fraction: average void fraction;
- Ref\_charge: estimated refrigerant charge from the void fraction;
- Ref\_mass\_flow\_rate: refrigerant mass flow rate in the mesh.

The meshes of a representative plate of each block are reported one for each row, starting from the refrigerant inlet block to the refrigerant outlet block.

A further improvement of the program will enter the nodal analysis for all plates.

In Figure 2.3.16 the sheets of the “Results” excel file are shown.



	A	B	C
<b>Heating capacity</b>		W	4174
<b>Refrigerant R410A</b>			
1 Mass flow rate	kg/s	203.5	
2 Volumetric flow rate	m <sup>3</sup> /s	1.1	
3 Pressure drops	Pa (kPa)	3024.464 (0.3)	
4 Superheated zone	s	0.5	
5 Two-phase zone	s	0.7	
6 Subcooled zone	s	0.4	
7 Heat transfer coefficient	W/(m <sup>2</sup> ·K)	800.5	
8 Superheated zone	W/(m <sup>2</sup> ·K)	800.5	
9 Two-phase zone	W/(m <sup>2</sup> ·K)	800.5	
10 Subcooled zone	W/(m <sup>2</sup> ·K)	39	
11 Heat transfer regime			
12 Superheated area	m <sup>2</sup>	20.7	
13 Two-phase area	m <sup>2</sup>	37.3	
14 Subcooled area	m <sup>2</sup>	1	
15 Heat used fraction		74.5	
16 Refrigerant charge	kg	340	
<b>Indoor condition</b>			
17 Temperature	°C	19.5	
18 Pressure	hPa	1013	
19 Saturation temperature (dew point)	°C	12.7	
<b>Outdoor condition</b>			
20 Temperature	°C	41.4	
21 Pressure	hPa	1013	
22 Saturation temperature (dew point)	°C	17	
23 Subcooling	K	15	
<b>Secondary fluid Air</b>			
24 Mass flow rate	kg/s	1000	
25 Volumetric flow rate	m <sup>3</sup> /s	600.7	
26 Face velocity	m/s	3.43	
27 Total pressure drops	Pa	100	
28 Heat transfer coefficient	W/(m <sup>2</sup> ·K)	35	
29 Fan			
30 Fan absorbed power	W	1.8	
31 Fan efficiency	%	90	
<b>Indoor condition</b>			
32 Dry bulb temperature	°C	17	
33 Wet bulb temperature	°C	12	
34 Relative humidity	%	30	
35 Pressure	Pa	101325	
<b>Outdoor condition</b>			
36 Dry bulb temperature	°C	44.5	
37 Wet bulb temperature	°C	17	
38 Relative humidity	%	10	
39 Pressure	Pa	101314	



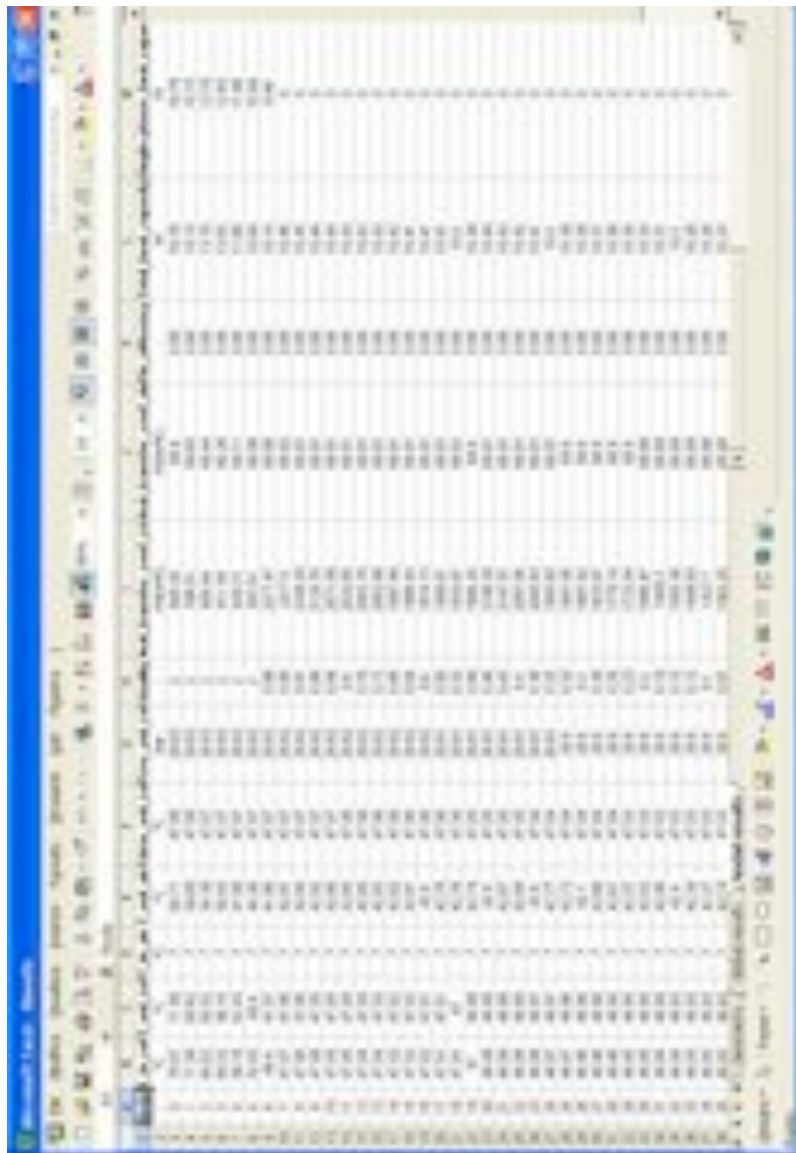
The image shows a screenshot of an Excel spreadsheet with multiple sheets. The sheets are organized into sections: 'Geometry', 'Global Results', and 'Nodal Results'. Each section contains a table of data. The 'Geometry' section includes parameters like 'Channel width', 'Channel height', and 'Pitch'. The 'Global Results' section includes 'Mass flow rate', 'Pressure drop', and 'Heat transfer rate'. The 'Nodal Results' section contains a large table of data for each node, including 'Node ID', 'Temperature', 'Pressure', and 'Heat flux'. The spreadsheet is displayed in a window with a blue title bar.

Figure 2.3.16. Sheets of the Results excell file, within the geometry, the global and the nodal results respectively.

### 2.3.3 Refrigerant property

The available refrigerant list has been presented in the introduction.

The program calculates the refrigerant property by interpolating the data in a table, the refrigerant data are read from a binary file and stored in jagged arrays, and they are changed only when the refrigerant is changed.

The use of jagged arrays is a very fast and precise way to access the refrigerant property.

For example, if we need to find a state between the two phases states stored in the matrix and the pressure is known, it is possible to find the saturation states before and after the pressure by an interpolation over the pressures. The two saturation states found are arrays of properties, so it is possible to obtain the new searched array of property in a very fast way with few rows of codes, and the same codes can be used if another saturation property is known by changing only an index.

The program while the simulation is running needs to access at the refrigerant property many times. Thus the access to refrigerant property directly affects the overall simulation time.

The precision depends on the step of the refrigerant property chosen for making the property tables.

To make the property table an excel macro was made it allows the user to choose the properties step and to write the tables.

The macro makes the refrigerant property tables as used by the program, from Refrop 7 [1]. IIR (International institute of refrigeration) reference state was considered for enthalpy,  $h=200$  KJ/kg and entropy  $s=1$  KJ/(kg·K) for the saturated liquid at 0°C.

In Figure 2.3.17 the main sheet of the excel workbook with the macro is shown, it can be pointed out that it is possible to choose the property step to obtain the desired precision in further interpolations of refrigerant property.

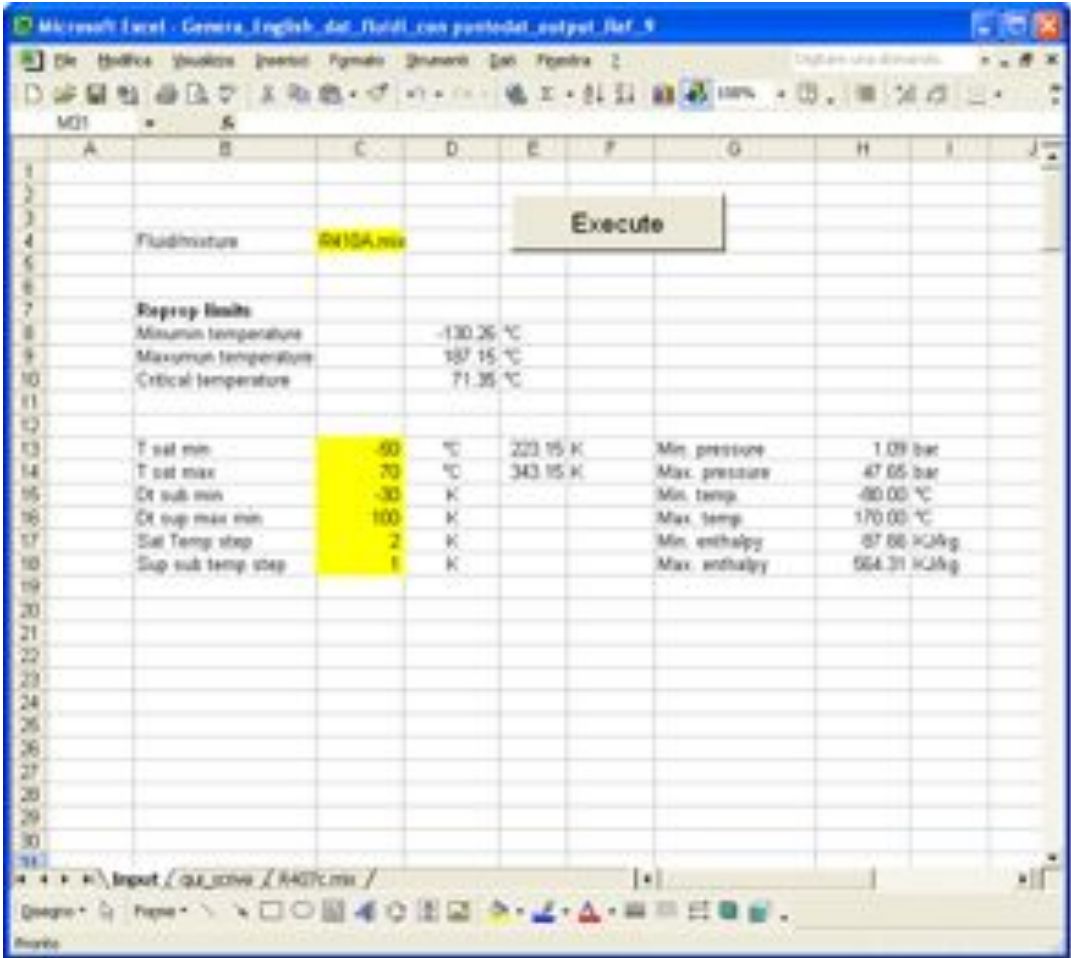


Figure 2.3.17. Main sheet of the excel workbook with the macro for create the refrigerant property tables utilized by the program.

In Table 2.3.1 the refrigerants database property are reported.

Fluids	Molar Mass kg/kmol	Critical temperature °C	Critical pressure bar	Composition %
<i>Halogenate pure fluid</i>				
R11	137.370	197.96	44.076	
R12	120.91	111.97	41.361	
R123	152.93	183.68	36.618	
R1234yf	114.042	94.97	33.822	
R1234ze(E)	114.042	109.37	36.363	
R125	120.020	66.02	36.177	
R134a	102.030	101.06	40.593	
R152a	66.051	113.26	45.168	
R22	86.468	96.15	49.900	
R32	52.024	78.11	57.820	
<i>Halogenate mixtures</i>				
R404A	97.604	72.046	37.289	R125 (44) R134a (4) R143 (52)
R407C	86.034	86.034	46.298	R125 (25) R134a (52) R32 (23)
R410A	72.585	71.358	49.026	R125 (25) R 32 (52)
R507A	98.859	70.617	37.050	R125 (50) R143 (50)
<i>Natural fluids</i>				
R290 (Propane)	44.096	96.675	42.471	
R600a (Isobutane)	58.122	134.670	36.400	
R717 (Ammonia)	17.030	132.250	113.330	
R744 (Carbon dioxide)	44.010	30.978	73.773	

Table 2.3.1. Refrigerant database property.

### 2.3.4 Numerical model

#### Domain discretization

The refrigerant undergoes a phase change process, it generally enters a condenser as superheated vapor state, and usually exits subcooling or saturated liquid state.

In an evaporator generally it enters into two-phases or saturated liquid state, then evaporates and exits in superheated state or two phases state, it depends on the type of evaporator; moreover if the evaporator external surface is below the air dew point temperature, the air water vapor will condensate on external surface.

These phase change processes determine strong variations of the heat transfer coefficients along the heat exchanger.

The heat transfer coefficient strongly depends on the refrigerant state during the two phases heat exchanger process, and the pressure drops too; the same occurs on the air side in presence of moisture condensation.

Thus in order to correctly evaluate the overall cooling/heating capacity the domain is divided into a finite number of volumes.

The domain is discretized by dividing each plate into a  $n$  integer number of volumes, the total number of meshes is the product between  $n$ , the number of plate for each row and the number of rows. Each volume is identified by a tern of indexes (i,j,k): i is the index along the plate, j is the plate index, k is the row index; each node has other four terns of indexes, two of these corresponding to the previous and the following nodes in the refrigerant path, the other two corresponding to air previous and following nodes in the air direction. The inlet from the header plate node has a special index as the plate outlet to the header node; the same is for the air side with the heat exchanger air inlet nodes and the outlet ones.

The user chooses the number  $n$  (see Figure 2.3.6, Plate control number) a control inside the program verifies that the number is not too high or too low.

In follows the terms node and mesh are used interchangeably to identify a volume.

Another index associated to number of plate block is set as nodes property, the number of block is counted from the inlet to the outlet of the refrigerant; this is not necessary but sometimes very helpfully.

In figure 2.3.18 a scheme of one volume with the indexes is reported.

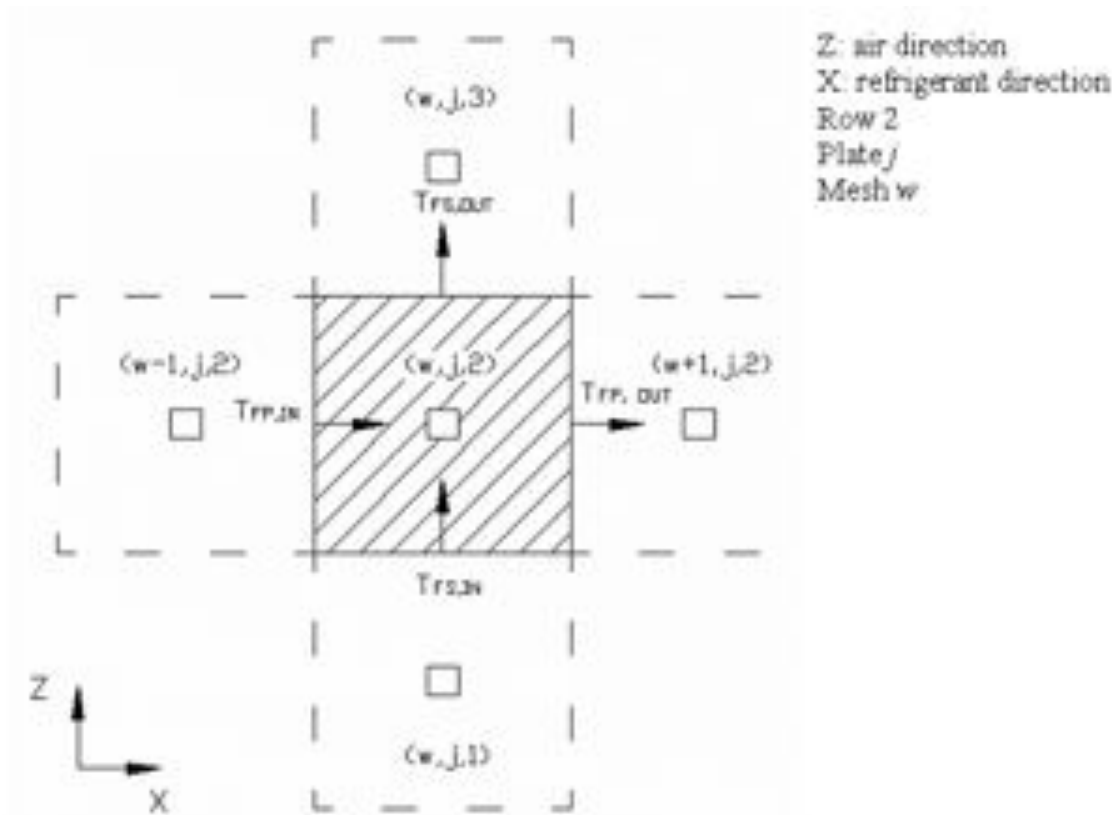


Figure 2.3.18. Scheme of one volume with the indexes in the plane defined from the air and the refrigerant directions; the inlet/outlet refrigerant and air (secondary fluid) temperatures are reported.

### Header refrigerant control volume

Each header block is associated to a refrigerant state inlet and outlet, the refrigerant inlet is obtained considering a perfect mixing hypothesis of the refrigerant inlet header from the inlet plates; the header outlet refrigerant state is calculated in perfect distribution hypothesis, so the outlet plates have all the same refrigerant state.

### Plate mesh heat exchanger

Each mesh is calculated by a P-NTU analytical solution of the continuity and the energy equations; the inlet refrigerant and air conditions are utilized as the

fluids state of the mesh. In this way it is possible to calculate the mesh heat transfer and the fluids outlet states.

The general P-NTU theory is briefly presented (for more detail, see [13]), the fluids are called generically fluid 1 and fluid 2, really as the program node class works, it can accept different kind of refrigerant and secondary fluids.

The parameter P and R and the relation between the number of transfer unit  $NTU_2$  and  $NTU_1$ , can be defined. The fluid 1 is supposed to enter at major temperature.

$$P = \frac{\Delta T_2}{\Delta T_{Max}} = \frac{T_{2,OUT} - T_{2,IN}}{T_{1,IN} - T_{2,IN}} \quad (2.3.1)$$

$$R = \frac{\dot{m}_2 \cdot c_{p,2}}{\dot{m}_1 \cdot c_{p,1}} = \frac{C_2}{C_1} \quad (2.3.2)$$

$$NTU_2 = \frac{K \cdot A}{C_2} = \frac{C_1}{C_2} \frac{K \cdot A}{C_1} = \frac{1}{R} \cdot NTU_1 \quad (2.3.3)$$

$$T_{2,OUT} = T_{2,IN} + P \cdot (T_{1,IN} - T_{2,IN}) \quad (2.3.4)$$

$$T_{1,OUT} = T_{1,IN} - R \cdot P \cdot (T_{1,IN} - T_{2,IN}) \quad (2.3.5)$$

For co-current.

$$P = \frac{1 - e^{-NTU_2(1-R)}}{1 + R} \quad (2.3.6)$$

For counter-current.

$$P = \frac{1 - e^{-NTU_2(1-R)}}{1 - R \cdot e^{-NTU_2(1-R)}} \quad (2.3.7)$$

For cross flow heat exchanger in unmixed hypothesis for the mesh.

$$K = 1 - e^{-NTU_2} \quad (2.3.8)$$

$$P = \frac{1}{R} \cdot (1 - e^{-K \cdot R}) \quad (2.3.9)$$

For each mesh the heat transfer coefficient HTC are calculated with the fluids inlet state, actually the program use the following equation:

- Cavallini et al. [2] correlation for condensation HTC.
- Sun-Mischima [3] correlation for evaporation HTC.
- Gnielinski [4] correlation for single phase HTC.

The user can choose if gives the dry HTC on the air side or utilizes a literature correlation.

In first case the dry air HTC is the value given by the user, in second case it is calculated by the Chang-Wang [5] correlation; the Jacobi [6] et alt. correlation has been implemented too, it is possible to switch between these correlations only by the code.

The traditional system utilized for calculating the fin efficiency is utilized. This fin efficiency correlation assumes adiabatic the fin at the middle section, and can be also applied at this kind of heat exchanger with acceptable accuracy, as demonstrated in Asinari et al [7].

Then the finned surface efficiency and the overall heat transfer coefficient  $K$  referred to the external surface are calculated.

Supposing that the air is the fluid 2 the  $NTU_2$  can be calculated and then with the equations (2.3.1-9) the mesh outlet fluids temperatures can be determined.



In presence of moisture on the air side, the temperature must be replaced with the enthalpy, the heat capacity rate and the air side HTC can be rewritten.

$$\begin{cases} C_1 = \dot{m}_1 \cdot c_{p,1} \cdot \frac{1}{\left(\frac{\partial h}{\partial T}\right)_s} \\ C_2 = \dot{m}_2 \end{cases} \quad (2.3.10)$$

$$\alpha_{WET} = \alpha_{DRY} \cdot \frac{\left(\frac{\partial h}{\partial T}\right)_s}{C_{p,2}} \quad (2.3.11)$$

Where  $\left(\frac{\partial h}{\partial T}\right)_s$  is the temperature enthalpy derivative of saturated air at the external surface temperature. Actually the program neglects the thermal conduction resistance of plates, thus the plate external surface temperature is equal to the refrigerant temperature.  $\alpha_{DRY}$  is the air dry and heat transfer coefficients.

Refrigerant pressure drops are calculated with Mischima-Hibiki [8] and Filonenko [9] correlations, respectively in two phases and in single-phase state.

On the air side the pressure drops are calculated by the Chang-Wang [10-11] correlation.

Pressure drops are applied to the calculated fluids state by applying an isenthalpic transformation.

The fin surface average temperature  $T_{fin}$  is calculated by:

$$T_{fin} \cong T_{air} \cdot \frac{K_e}{\alpha_e} (T_{air} - T_{ref}) \quad (2.3.12)$$

where refrigerant and air temperature are the average value in the mesh.

The program verifies if the fin surface temperature is below the air dew point temperature, if it is, the mass transfer phenomena must be accounted on the

exit air state. The air outlet humidity ratio is calculated based on the outlet air enthalpy along the line joining the inlet air state point to the saturated air at the average finned surface temperature point in the psychometric chart.

If the outlet temperature corresponding to the outlet humidity ratio and the enthalpy is below the air-saturated temperature calculated at the outlet enthalpy value, then the air exit in saturated conditions.

Thus it is possible to calculate the total heat transfer flux eventually subdivided in its sensible and latent components.

On refrigerant side if the refrigerant state cross a limit curve, to keep in count of the high heat transfer coefficient variation, that can give a considerable error in the mesh heat transfer, the mesh is recalculated by a further subdivision in a number of sub-mesh.

### Volumes initialization

The P-NTU method [13] is applied to the entire heat exchanger. For each mesh an axial coordinate  $x$  that starts from the refrigerant inlet and then follows the entire refrigerant path is introduced. This coordinate is normalized over the refrigerant path length, so it is 0 at refrigerant inlet and 1 at refrigerant outlet.

The heat transfer can be considered co-current or counter-current depending on air direction chosen in case the heat exchanger has more than one row.

The P-NTU method written as function of the  $x$  axial coordinate is:

– Counter-current

$$T_{1,x} = T_{1,in} - R \cdot (T_{2,OUT} - T_{2,x}) \quad (2.3.13)$$

$$T_{2,x} = \frac{1}{1-R} \cdot \left[ T_{1,IN} - R \cdot T_{2,OUT} - (T_{1,IN} - T_{2,OUT}) \cdot e^{x(NTU_2 - NTU_1)} \right] \quad (2.3.14)$$

– Co-current

$$T_{1,x} = T_{1,in} + R \cdot (T_{2,IN} - T_{2,x}) \quad (2.3.15)$$

$$T_{2,x} = \frac{1}{1+R} \cdot \left[ T_{1,IN} + R \cdot T_{2,IN} - (T_{1,IN} - T_{2,IN}) \cdot e^{-x(NTU_2 + NTU_1)} \right] \quad (2.3.16)$$

The initialization start with the calculation of first tentative overall refrigerant mass flow rate by an assigned constant HTC, then the overall mass flow rate that leading to convergence the refrigerant outlet state, set by the user, is calculated by a Levenberg-Marquardt algorithm. The meshes are reinitialized for each overall mass flow rate; the refrigerant heat transfer coefficient and pressure drops are kept constant and calculated by a weighted average fluid state and mass flow rate in all the mesh. The air HTC is kept constant and calculated at the inlet state condition

At the end of that procedure the mesh are initialized and an overall refrigerant mass flow rate, which will be used as tentative value for the following solution procedure, is determined.

That way allows finding a refrigerant mass flow rate approximately close to the real value, decreasing the number of iteration of the following slower procedure.

### **Solution procedure**

After determining the mesh initialization and found a refrigerant mass flow rate that allows the simulation to reach the refrigerant outlet border conditions, with the procedure detailed in the previous paragraph, the node by node calculation procedure starts.

The nodes are solved with the Gauss-Seide method, for each tentative of overall refrigerant mass flow rate.

The nodes are solved starting from the refrigerant inlet block by following the refrigerant path, each node is calculated with P-NTU method, by which the new refrigerant, the air outlet conditions and the finned surface average temperature are calculated.

Three errors are defined for each node:

- difference between the calculated and the actual node finned surface temperature;

- difference between the calculated and the actual node refrigerant outlet temperature;
- difference between the calculated and the actual node air outlet temperature.

When all the nodes have been calculated, the absolute maximum error is determined, if it is greater than the set minimum value, the program will recalculate each node by setting inlet conditions of refrigerant and air equal to the previous node calculated outlet conditions; for the refrigerant inlet block and frontal air inlet nodes, the inlet conditions are maintained equal to the heat exchanger border conditions. If the maximum error is lower the set minimum value, the control goes to the iterative procedure for determining the overall heat exchanger mass flow rate: the error between the refrigerant outlet calculated state and the outlet state set by the user is calculated, if it is lower than the set minimum value the simulation will stop, otherwise it tries with a new overall mass flow rate and go to recalculate all the nodes. This method utilizes Levenberg-Marquardt algorithm.

The node procedure is detailed with reference to node (w,j,2) of the Figure 2.3.18.

At each iteration the refrigerant, the air inlet temperatures and the finned surface temperature, respectively  $T_{ref,in}(w,j,2)$ ,  $T_{air,in}(w,j,2)$  and  $T_{fin}(w,j,2)$  are assigned or from initialization, or from the previous iteration.

The P-NTU method is applied to the node and the the  $T^*_{ref,out}(w,j,2)$ ,  $T^*_{air,out}(w,j,2)$  and a new  $T^*_{fin}(w,j,2)$  are calculated.

The three errors are calculated:

$$\begin{cases} \varepsilon_{ref} = abs(T^*_{ref,out} - T_{ref,out,old}) \\ \varepsilon_{air} = abs(T^*_{air,out} - T_{air,out,old}) \\ \varepsilon_{fin} = abs(T^*_{fin} - T_{fin,old}) \end{cases} \quad (2.3.17)$$

The maximum of all nodes errors is calculated.

$$\varepsilon = \max \left[ \max \left( \varepsilon_{ref}, \varepsilon_{air}, \varepsilon_{fin} \right)_{i,j,k} \right] \quad (2.3.18)$$

If the maximum error is greater than the minimum acceptable set value, the node inlet properties are reassigned and the procedure repeated.

A fast method in the refrigerant and air classes is implemented, considering Fluid 1 as the refrigerant and Fluid 2 as air, the reallocation of properties is shown below.

$$\begin{cases} Fluid,1,IN(w, j, K) = Fluid,1,OUT(w-1, j, K) \\ Fluid,2,IN(w, j, K) = Fluid,2,OUT(w, j, K-1) \\ T_{fin}(w, j, K) = T_{fin}^*(w, j, K) \end{cases} \quad (2.3.19)$$

### 2.3.5 Conclusion

A program for calculating a minichannel condenser or evaporator is developed.

The program is thought for calculating the performance and for optimizing these two types of heat exchangers. It is developed with the goal to be user-friendly and simple in the input data inserting and data saving, fast during the simulation, and easy to read and analyze the results.

The program needs to be validated, in the next chapter a first condenser validation is presented, further improvement and experimental data available, are needed for the evaporator, in particular considering the refrigerant maldistribution that strongly affects the evaporator performance as shown in Shao et al. [12]. Another improvement can be the possibility of inserting the air side maldistribution. After these improvements the evaporator can be better validated.

A further code improvement could be the inserting of the gas cooler heat exchanger; the transcritical carbon dioxide properties have been inserted in the refrigerant property tables for this purpose.

The classes of refrigerant, air, and the node can be easily reused, maybe in DLL form, in creating new codes for helping other research project, as well as the class node could be easily utilized to develop a calculation code for traditional finned tube round.

### 2.3.6 Reference

1. Lemmon E. W., Mc Linden M.O., Huber M.L. Refprop 7.0. NIST Standard Reference Database. (2002).
2. A. Cavallini, G. Censi, D. Del Col, L. Doretti, G.A.Longo, L. Rossetto. In tube condensation of halogenated refrigerants. Ashrae transaction (2002) pp. 146-161.
3. L. Sun, K. Mischima. An evaluation of prediction methods for saturated flow boiling heat transfer in minichannels. International journal of heat and mass transfer, Vol. 52 (2009) pp. 5323-5329.
4. V. Gnielinski. Heat transfer coefficients for turbulent flow in concentric annular ducts. Heat transfer engineering, Vol. 30 (2009) pp. 431-436.
5. Yu Juei Chang, Chi Chuan Wang. A generalized heat transfer correlation for louver fin geometry. International Journal heat mass transfer. Vol. 40. (1997). pp. 533-544.
6. Jacobi AM, Park Y, Zhong Y, Michna G, Xia Y. High performance heat exchangers for air-conditioning and refrigeration applications (non-circular tubes) – Final report. ARTI-21CR/605-20021-01, 2005.
7. P. Asinari, L.Cecchinato, E. Fornasieri. Effects of thermal conduction in microchannel gas cooler for carbon dioxide. International journal of refrigeration. Vol. 27. (2004). pp. 577-586.

8. K. Mischima, T: Hibiki. Some characteristics of air-water two-phase flow in small diameters vertical tubes. *International journal multiphase flow*, N44, Vol 22 (1996) pp.703-712.
9. G.K. Filonenko. *Teploenergetika* 1 (1954), p.40.
10. Yu Juei Chang, kuei Chang Hsu, Yur Tsai Lin, Chi Chuan Wang. A generalized friction correlation for lover fin geometry. *International Journal heat mass transfer*. Vol. 43. (2000). pp. 2237-2243.
11. Yu Juei Chang, Wen Jeng Chang, Ming Chia Li, Chi Chuan Wang. An emendament of the generalized friction correlation for louver fin geometry. *International Journal heat mass transfer*. Vol. 49 2006. pp. 4250-4253.
12. L. Shao, L. Yang, C. Zhang. Comparison of heat pump performance using fin-and-tube and microchannel heat exchanger under frost conditions. *Applied energy* (2009). Vol. 87. pp. 1187-1197.
13. G.F. Hewitt. *Heat Exchanger Design Handbook*. Hemisphere Publishing Corporation, 1983.

## **2.4 Automotive minichannel condenser: comparison of R1234yf and R134a refrigerants performance and simulation tool validation**

In this sub-chapter an experimental and a computational analysis of a minichannel air cooled condenser operating with R134a and R1234yf are described.

The experimental analysis was carried out in a test rig built at University of Padua for testing refrigerant equipment with air as the secondary fluid. This analysis was made in a minichannel condenser for an European car air conditioning system operating with R134a or R1234yf in the presence of circulating oil. The performance comparison between that refrigerants was done at the same air flow rate, with temperatures ranging between 15 °C and 35 °C.

The program, described in the previous sub-chapter 2.3 , was used for the computational analysis and a first program validation on the experimental data was obtained.

This first use of the simulation tool shows that it can usefully be used to make a parametric study to compare performance of two refrigerants.

### **2.4.1 Introduction**

The European Union's F-gas regulations (Regulation, 2006 and Directive 2006) [1], [2] specify that beginning on January 1, 2011 new models and on January 1, 2017 new vehicles fitted with air conditioning cannot be manufactured with fluorinated greenhouse gases having global warming potentials (GWP) greater than 150. R1234yf is being widely considered as a possible replacement for R134a in automotive applications, having normal



boiling temperature approximately 3.7 °C lower than R134a and GWP approximately of 4.

Several previous studies have concluded that R1234yf appears to be a promising candidate to replace R134a in automotive applications, with SAE (2010) [3] concluding R1234yf “can be used as the global replacement refrigerant in future mobile air conditioning systems and it can be safely accommodated through established industry standards and practices for vehicle design, engineering, manufacturing, and service.” Notwithstanding the preceding statement, several issues are still being investigated through ongoing research and development work.

Petitjean and Benouali (2010) [4] experimentally studied the effects of using an improved condenser, an improved evaporator, an adjusted (“tuned”) Thermal Expansion Valve (TXV), a modified compressor, and a liquid-line/suction-line heat exchanger (llsl-hx) in an automotive air conditioning system. If conventional heat exchangers are used, they concluded that the condenser plays a much more important role than the evaporator in the optimization of the R1234yf performance.

This also can be concluded from the study of Cavallini et al. (2010) [5] who showed analytically and the study of Del Col et al. (2010) [6] who showed experimentally that the condensation heat transfer coefficients (HTC) for R1234yf can be up to 30 % or so lower than R134a at high vapor qualities at the same mass flux and saturation temperature. On the other hand, Del Col et al. (2010) showed experimentally that the condensation HTCs for R1234yf are nearly the same as those of R134a for lower vapor qualities or for single phase liquid heat transfer. Therefore, one can conjecture that the R1234yf performance can be made to match the performance of R134a provided that the condenser design is optimized for R1234yf.

Another general issue to be considered is the relatively large amount of oil circulating inside automotive air conditioning systems (typically 1-5 %). This fact is well recognized in the literature (see for example Shen and Groll, 2005 [7]) to decrease the HTC and increase pressure drop in “macro” tube

condensers. On the other hand, the literature regarding HFCs condensing inside mini- and micro-channels in the presence of oil is rather limited; however, recently, Huang et al. (2010) [8] experimentally measured a 28.5 % degradation in the HTC of R410A condensing inside a horizontal, straight 1.6 mm diameter tube, with oil-in-circulation of 5 % by mass.

## 2.4.2 Test facility and test conditions

The condenser is a multiport minichannel tube-and-fin aluminum heat exchanger, with the main geometrical characteristics as listed in Table 2.4.1

Minichannel heat exchanger		
Face area	[m <sup>2</sup> ]	0.185
Minichannel tube section	[mm x mm]	16 x 1
Channel number per tube	[-]	21
Fin spacing (tube tip)	[mm]	3.2
Fin height	[mm]	8
Number of passages refrigerant-side	[-]	2
Number of tubes per passage	[-]	27-6
Total number of tubes	[-]	33
Tube length	[mm]	650
Elements per tube	[-]	20

*Table 2.4.1. Geometric characteristics of the minichannel condenser.*

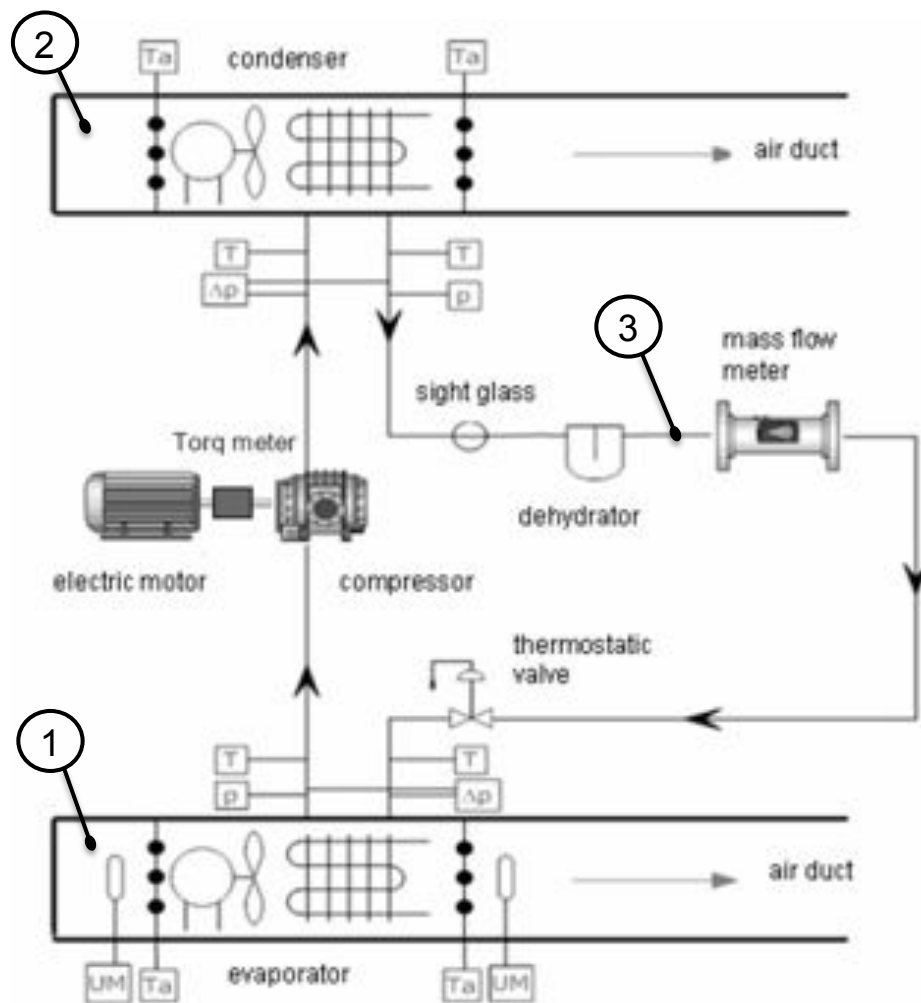


Figure 2.4.1. Schematic of the experimental apparatus

Figure 2.4.1 shows a schematic of the experimental apparatus, which consists of four basic systems: (1) a closed-loop air circuit for the evaporator, including centrifugal fan, electric resistance heater, humidification equipment, and associated controls, (2) a closed-loop air circuit for the condenser, including centrifugal fan, chiller, electric resistance heater and associated controls, (3) the refrigerant circuit, including a minichannel evaporator, a minichannel condenser, a variable volume swash-plate compressor, and a TXV, all components from the air conditioning system of a typical European compact automobile, and (4) the instrumentation system.

The inlet air temperatures for both the evaporator and the condenser are controlled using two closed-loop air circuits, whose ductwork configurations provide uniform temperature and velocity profiles at the inlet faces of the heat exchangers. The volumetric air flow rates are measured using ISA 1932 nozzles per ISO 5167- 4:2003 [18] to accuracies of  $\pm 0.8$  % of the measured values. A chiller supplies conditioned water to a cross-flow heat exchanger to maintain the condenser inlet air temperature to near the desired value. Then, a PID- controlled electric resistance heater located upstream from the condenser controls the inlet air temperature to the desired value. A separate, but similar, system controls the evaporator inlet dry-bulb air temperature to the desired value. A grid of nine evenly spaced type T thermocouples for the condenser are used to measure the mean inlet air temperature for the respective heat exchanger. The air downstream from each heat exchanger is well-mixed prior to its temperature being measured by separate grids of nine evenly spaced type T thermocouples. For both air circuits and for the refrigerant system, a Pt-100 platinum resistance thermometer with an accuracy of  $\pm 0.02$  °C was used to calibrate the temperature measuring system (consisting of thermocouple, electronic ice point and multimeter) to an accuracy of  $\pm 0.05$  °C.

Calibrated type T thermocouples measure the refrigerant temperature immediately before and after each major component. Strain gauge pressure transducers measure the absolute pressures in the evaporator to  $\pm 0.8$  kPa and in the condenser to  $\pm 1.6$  kPa.

A Coriolis flow meter located in the liquid line measures the refrigerant mass flow rate to an accuracy of  $\pm 0.1$  % of the measured value.

An asynchronous electric motor drives the compressor.

The total expanded uncertainties for the air-side heat transfer rate measurements are  $\pm 1$  %. The total expanded uncertainties for the refrigerant-side heat transfer rate measurements are  $\pm 4$  % for the evaporator and  $\pm 3$  % for the condenser.

The system tested is a typical R134a/PAG oil based one used in a compact European automobile. The system had a nominal cooling capacity of 5.8 kW at a compressor volumetric flow rate of  $7.8 \text{ m}^3 \text{ h}^{-1}$ . While the operating conditions were not meant to exactly duplicate actual in-vehicle conditions, they were chosen to cover typical European conditions. In particular, they covered three compressor speeds, three ambient temperatures (the inlet air temperature of both the evaporator and the condenser), and two relative humidity values for the evaporator inlet air stream. The evaporator fan speed (air volumetric flow rates) was held constant throughout the tests, while two different values were considered for the condenser. Table 2.4.2 provides the operating conditions.

Evaporator air inlet	°C	35			25			15		
Evaporator air humidity	%	40			80			80		
Evaporator air volumetric flow rate	$\text{m}^3 \text{ h}^{-1}$	$400 \pm 3 \%$			$400 \pm 3 \%$			$400 \pm 3 \%$		
Condenser air inlet	°C	35			25			15 °C		
Condenser air volumetric flow rate	$\text{m}^3 \text{ h}^{-1}$	$1580 \pm 3 \%$ and (*) $2600 \pm 2 \%$			$1580 \pm 3 \%$ and (*) $2600 \pm 2 \%$			$1580 \pm 3 \%$ and (*) $2600 \pm 2 \%$		
Compressor speed	rpm	900	2500	4000	900	2500	4000	900	2500	4000

Table 2.4.2. Operating conditions.

(\*): the later value ( $2600 \text{ m}^3 \text{ h}^{-1}$  refers to R134a only).

The energy balances on the airside and refrigerant-side for both the evaporator and the condenser differed by a maximum of 4 % for all tests.

The R134a/PAG oil circulation ratio (OCR) was measured per ASHRAE 41.4-1986 (R2006) [9]. Similar measurements were not performed for R1234yf since the experimental procedure consumes considerable fluid, which was not available at the time of the tests. Therefore, the R1234yf OCR values were assumed to be those of R134a at the same compressor displacement, which are reported in Table 2.4.3.

---

Compressor speed (rpm)	OCR (%)
900	3.0
2500	4.2
4000	4.5

---

*Table 2.4.3. Oil Circulation Ratio (OCR).*

### 2.4.3 Numerical analysis

The minichannel condenser model has been described in detail in the previous subchapter 2.3, here a brief summary of how the model works is reported; it is followed by a description of how the presence of oil been taken into account.

The minichannel condenser modelled subdivides the total heat transfer area into a three-dimensional array of cells that conform to the flow patterns of the two fluids (air and refrigerant), resulting from the composition of cross-flow elements. Each cell includes a small section of a refrigerant tube and the accompanying fins, with the boundary conditions determined by the adjacent cells. The model allows for the arrangement of tubes in a very general way, including divergences or convergences (manifolds). The total inlet refrigerant mass flow rate is distributed to each parallel refrigerant circuit. The air-side HTCs, including surface efficiency, are assumed to be uniform and are evaluated through experimental correlations developed using a modified Wilson plot procedure: to perform the mentioned semi-empirical approach the heat exchanger was fed with hot water with different mass flow rates. The refrigerant-side condensation HTC is determined from correlations chosen among a series of proposals available in the open literature in the present work the refrigerant-side HTC is evaluated using the Cavallini et al. (2006) [10] correlation; whereas, the refrigerant-side pressure drop is estimated using the Mishima and Hibiki correlation (2009) [11]. The refrigerant mass flow rate is determined through an iterative procedure given known values for the air flow rate, the inlet air temperature, and the inlet refrigerant pressure and

temperature. The iterative procedure is based on a Levenberg-Marquardt algorithm method with the error being the difference between the required and calculated values of the refrigerant subcooling.

The refrigerant property are calculated from tables generated using REFPROP 7 [12]

The oil concentration  $\omega$  is determined from:

$$\omega = \frac{m_{OIL}}{m_{OIL} + m_{REFRIGERANT,L}} = \frac{OCR}{100} \quad (2.4.1)$$

where:

$m_{OIL}$  is the local mass of liquid refrigerant;

$m_{REFRIGERANT,L}$  is the local mass of liquid refrigerant;

$OCR$ : oil concentration ratio [%].

The refrigerant/oil mixture enthalpy ( $i$ ) is determined from:

$$i_{MIXTURE} = i_{REFRIGERANT} \times (1 - \omega) + c_{p,OIL} \times T_{OIL} \times \omega \quad (2.4.2)$$

where:

$c_{p,OIL} = 2501 \text{ J kg}^{-1}\text{K}^{-1}$  per SAE J2765 [13];

$T_{OIL}$ : oil temperature.

The refrigerant/oil mixture viscosity  $\mu$  is determined as in Yokozeki [14]:

$$\ln(\mu_{MIXTURE}) = \xi_{REFRIGERANT} \times \ln(\mu_{REFRIGERANT}) + \xi_{OIL} \times \ln(\mu_{OIL}) \quad (2.4.3)$$

where:

$$\mu_{OIL} = \mu_{OIL,A} - \frac{\mu_{OIL,A} - \mu_{OIL,B}}{T_A - T_B} \times (T_A - T_{OIL});$$

$$\mu_{OIL,A} = 44.27 \text{ mPa} \times \text{s at } T_A = 40^\circ\text{C};$$

$$\mu_{OIL,B} = 9.73 \text{ mPa} \times \text{s at } T_B = 100^\circ\text{C};$$

$$\xi_{OIL} = \frac{M_{M,OIL} \times x_{OIL}}{M_{M,OIL} \times x_{OIL} + M_{M,REFRIGERANT} \times x_{REFRIGERANT}} ;$$

$M_M$  : molecular mass;

$x$  : molecular fraction.

The values obtained from equations (2.4.2)-(2.4.3) were then used for the calculation of the HTC and pressure drop using Cavallini et al. (2006) [10] and Mishima and Hibicki (1996) [11], together with a modified liquid thermal conductivity, respectfully, following Huang et al. (2010) [8].

In Figure 2.4.2 an image of the circuitry in the model, together with the HTC for R134a and R1234yf in the first condenser passage (refrigerant-side) are reported with reference to a typical working condition: saturation temperature =50°C, mass flow rate =196 kg m<sup>-2</sup> s<sup>-1</sup>, and OCR=4.2%.

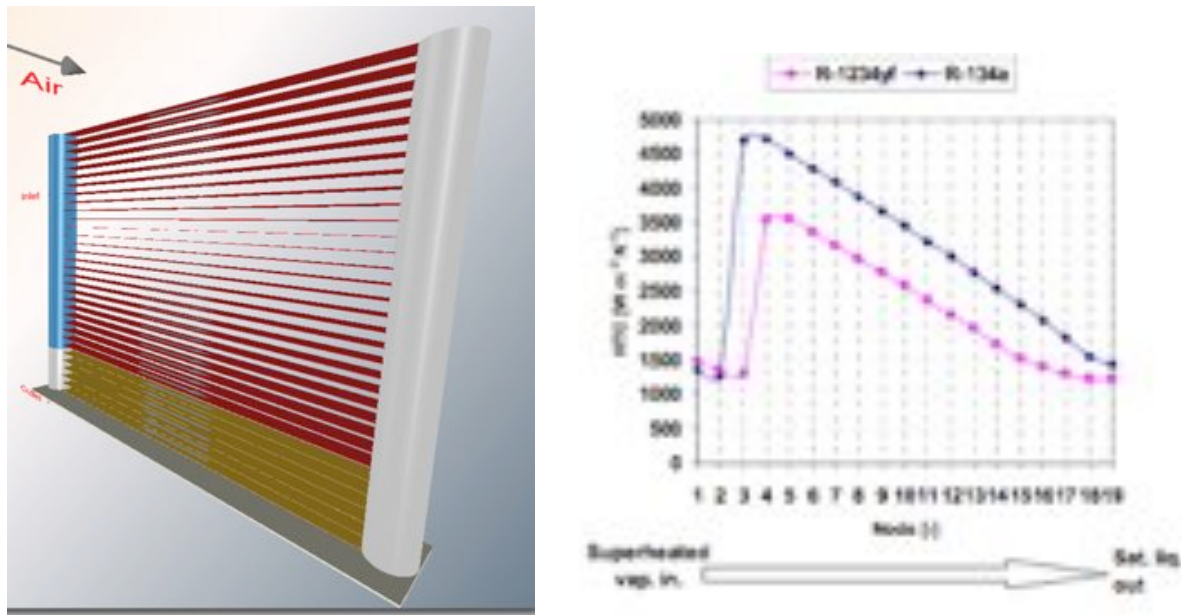


Figure 2.4.2. Image of the circuitry in the model together with the calculated HTC for R1234yf and R134a, in the first condenser passage; the operative conditions are  $T_{sat}=50^{\circ}\text{C}$ , mass flux=196 kg m<sup>-2</sup> s<sup>-1</sup>, and OCR=4.2%.



## 2.4.4 Results

The simulation results were compared to experimental measurements for pure R134a provided by the condenser manufacturer.

The absolute percentage error  $\varepsilon$  is defined by:

$$\varepsilon = 100 \times \left| \frac{\dot{q}_{EXPERIMENTAL} - \dot{q}_{CALCULATED}}{\dot{q}_{EXPERIMENTAL}} \right| \quad (2.4.4)$$

where  $\dot{q}$  is the heat transfer rate.

A mean percentage error  $e$  and an absolute mean percentage error  $e_{ABS}$  can then be defined:

$$e = \frac{100}{N} \sum_{i=0}^N \frac{\dot{q}_{EXPERIMENTAL} - \dot{q}_{CALCULATED}}{\dot{q}_{EXPERIMENTAL}} \quad (2.4.5)$$

$$e_{ABS} = \frac{100}{N} \sum_{i=0}^N \left| \frac{\dot{q}_{EXPERIMENTAL} - \dot{q}_{CALCULATED}}{\dot{q}_{EXPERIMENTAL}} \right| \quad (2.4.6)$$

where  $N$  is the total number of experimental points.

In Table 2.4.4 the percentage absolute error calculated by equation (2.4.4) are plotted for all the comparative tests between the heat fluxes from the manufacturer and calculated by model for pure R134a.

In all cases, the errors between the simulated and measured heat transfer rates differ by  $\varepsilon < 4.3\%$ , for pure R134a.

Simulation number	1	2	3	4	5	6	7	8
Percentage error [%]	1.98	3.39	5.40	5.41	6.37	6.15	5.61	4.76

Table 2.4.4. Percentage absolute error for all comparative tests between the heat fluxes from the manufacturer and calculated by model for pure R134a.

In Figure 2.4.3 the simulation and the experimental results are compared for R134a/oil mixture with the OCR as given in Table 2.4.2 and the operating conditions as given in Table 2.4.3.

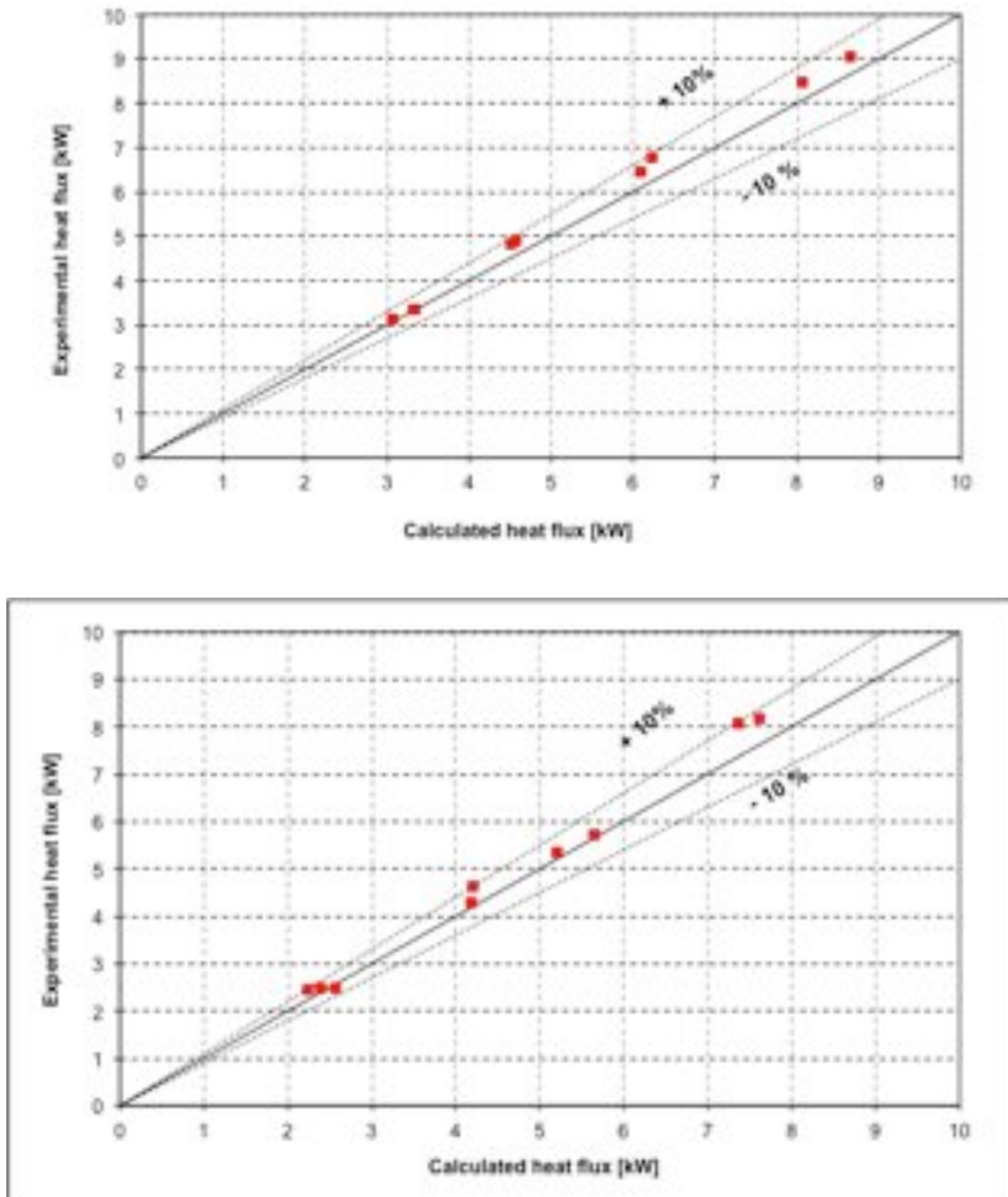


Figure 2.4.3. Simulates versus experimental heat transfer rates for R134a/oil mixture for an a) air volumetric flow rate of 2600 m<sup>3</sup>h<sup>-1</sup> and b) air volumetric flow rate of 1580 m<sup>3</sup> h<sup>-1</sup>.

The results demonstrate the ability of the simulation model to accurately capture the effects of the presence of the oil:  $e_{ABS} = 4.3\%$  for the air volumetric flow rate of  $2600 \text{ m}^3\text{h}^{-1}$ , while  $e_{ABS} = 5.2 \%$  for the air volumetric flow rate of  $1580 \text{ m}^3\text{h}^{-1}$ .

The mean percentage error is  $+ 4.2\%$  and  $+ 4.35\%$  respectively for the air volumetric flow rate of  $2600 \text{ m}^3\text{h}^{-1}$  and  $1580 \text{ m}^3\text{h}^{-1}$ , indicating a slight tendency of the model to underestimate the experimental values.

Thus, the simulation results for both pure R134a and for an R134a/oil mixture demonstrate the usefulness of the modeling approach, which will next be applied to an R1234yf/oil mixture.

In Figure 2.4.4 the simulation and experimental heat transfer rates for an R1234yf/oil mixture are compared for the OCR as given in Table 2.4.2, and the operating conditions given in Table 2.4.3. In these cases,  $e_{ABS} = 6.0 \%$ , which is somewhat higher than for R134a.

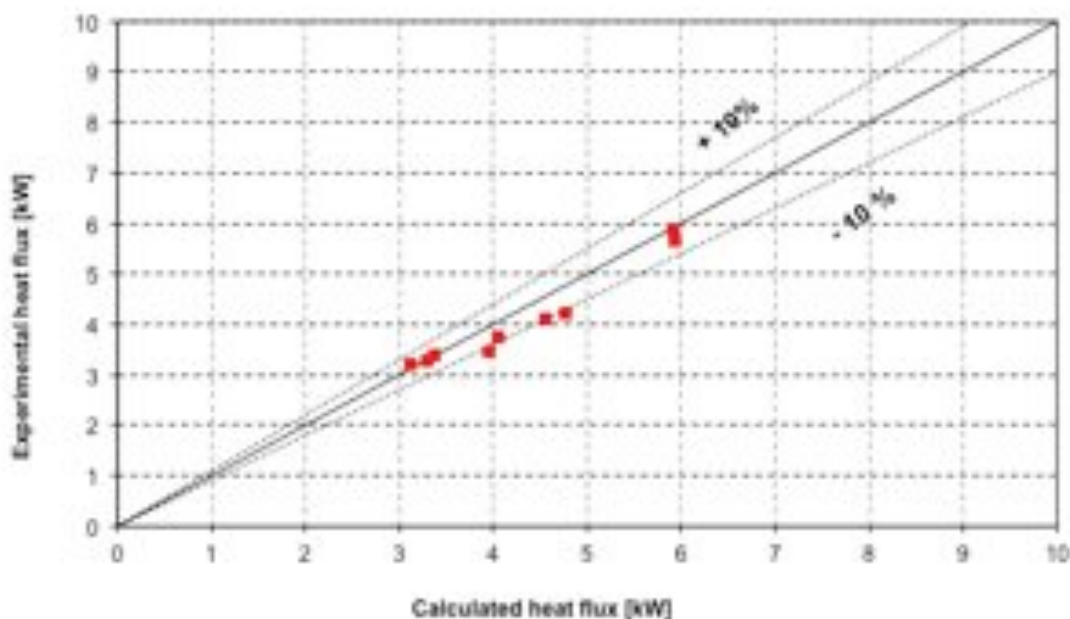


Figure 2.4.4. Simulated versus experimental heat transfers rates for R1234yf/oil mixture for an air volumetric flow rate of  $1580 \text{ m}^3\text{h}^{-1}$ .

It is interesting to note that the simulation results tend to over predict the measured heat transfer rates for the R1234yf/oil mixture ( $\varepsilon = -5.5\%$ ).

A few possibilities for this include that it has been assumed that the OCR for R1234yf is the same as for R134a. This assumption will need to be verified when sufficient quantities of R1234yf become available. It also is worth noting that per Bobbo et al. (2011) [15] the solubility of R1234yf in a commercial PAG was measured to be slightly different than for R134a, which may affect the amount of oil discharged from the compressor. Moreover, according to Spatz (2009) [16] and to Bobbo et al. (2011) [15], the miscibility of R1234yf is very different than for R134a for the same lubricant for typical condensation temperatures, with the possibility of separating into two liquid phases, one being rich in oil. This aspect was already reported by Spatz (2009) [16] with the possibility of having one or more minichannel multiport pipes being fed with a liquid phase very poor in refrigerant, particularly in the last part (second passage) of the condenser.

An attempt was made to confirm this hypothesis by using an infrared camera, with the result being shown in Figure 2.4.5.

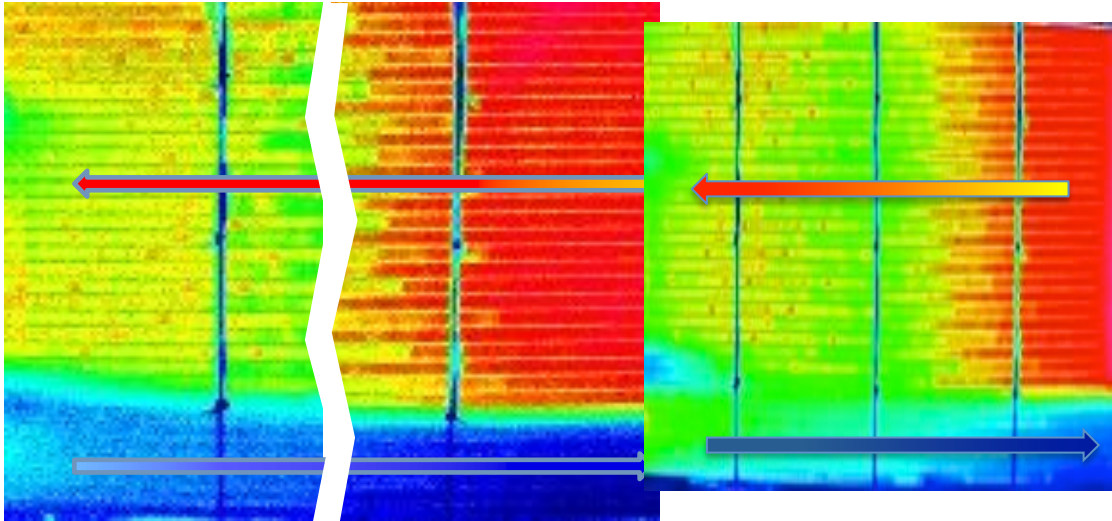


Figure 2.4.5. Thermographic photo of the condenser operating with R1234yf/oil mixture.

Note the two passage configuration of the condenser. At the bottom of the picture, it can be seen that the second passage (especially the bottom tube) is not fed uniformly. Evidently, one must keep into account the border effect reducing the air side coefficient and the internal heat conduction through fins between the hot and the cold parts of the condenser. However, similar analysis run for the same condenser with R134a did not display the same problem.

The issue is still worth of investigation especially if one considers that new lubricants expressly developed for R1234yf are appearing on the market (Dixon [17]).

### **2.4.5 Conclusion**

An off-the-shelf minichannel condenser for an European car air conditioning system was studied experimentally when operating with R134a or R1234yf in the presence of circulating oil. In addition, the simulation model described in the previous sub-chapter 2.3 was validated with experimental data, and then used to parametrically study the performance potential for the two refrigerants. The comparison of the simulation and experimental results for the R134a/oil mixture shows the ability of the model to accurately capture the actual performance of the condenser. However, the results for R1234yf/oil mixture indicate that there is a need for optimization of the condenser design, including the choice of a suitable oil.

Further experimental tests, where the R134yf OCR is measured, are probably necessary for a better analysis.

The issue is still worth of investigating especially if one considers that new lubricants expressly developed for R1234yf are appearing on the market, Dixon 2010 [17].

### **2.4.6 Reference**

1. Regulation (EC) No 842/2006 of The European Parliament and of the Council of 17 May 2006 on certain fluorinated greenhouse gases, 2006. Official Journal of the European Union. Retrieved online at: <http://eurlex.europa.eu/LexUriServ/LexUriServ.do?uri=OJ:L:2006:161:0001:0011:EN:PDF>, February 18, 2011.
2. Directive 2006/40/EC of the European Parliament and of the Council of 17 May 2006 relating to emissions from air-conditioning systems in motor

- vehicles and amending Council Directive 70/156/EC, 2006. Official Journal of the European Union. Retrieved online at: <http://eur-lex.europa.eu/LexUriServ/LexUriServ.do?uri=OJ:L:2006:161:0012:0018:ENPDF>, February 18, 2011.
3. SAE International, 2010. SAE International releases test results of the low GWP refrigerant for mobile air- conditioning. Retrieved online at: [http://www.sae.org/servlets/pressRoom?OBJECT\\_TYPE=PressReleases&PAGE=showRelease&RELEASE\\_ID=1109](http://www.sae.org/servlets/pressRoom?OBJECT_TYPE=PressReleases&PAGE=showRelease&RELEASE_ID=1109), July 7, 2010.
  4. Petijean S, Benouali J, 2010. R-1234yf validation & A/C system energy efficiency improvements, SAE Alternate Refrigerant Symposium AARS 2010, Scottsdale, (AZ) July 13-15.
  5. Cavallini A., Brown JS, Del Col D, Zilio C., 2010, In-tube condensation performance of refrigerants considering penalization terms (exergy losses) for heat transfer and pressure drop, *Int. J. Heat Mass Transfer* 53(13-14): 2886-2896.
  6. Del Col D., Torresin D., Cavallini A., 2010. Heat transfer and pressure drop during condensation of the low GWP refrigerant R1234yf, *International Journal of Refrigeration*, 33(7): 1307-1318.
  7. Shen B., Groll EA., 2005. A Critical Review of The Influence of Lubricants on the Heat Transfer and Pressure Drop of Refrigerants, Part II: Lubricant Influence on Condensation and Pressure Drop. *HVAC&R Res.*, 11(4): 511-525.

8. Huang X, Ding G, Hua H, Zhua Y, Peng H, Gao Y, Deng, B, 2010. Influence of oil on flow condensation heat transfer of R410A inside 4.18 mm and 1.6 mm inner diameter horizontal smooth tubes, *Int. J. Refrig.* 33(1): 158-169.
9. ASHRAE 41.4-1986 (R2006) - Standard Method for Measurement of Proportion of Lubricant in Liquid Refrigerant.
10. Cavallini A., Doretti L., Matkovic M., Rossetto L., 2006. Update on condensation heat transfer and pressure drop inside minichannels. *Heat Transfer Engineering* 27(4): 74-87.
11. Mishima K., Hibiki T., 1996. Some characteristics of air-water two-phase flow in small diameter vertical tubes. *International Journal of Multiphase Flow* 22, 703-712.
12. Lemmon E. W., Mc Linden M.O., Huber M.L. Refprop 7.0. NIST Standard Reference Database. (2002).
13. SAE J 2765-2008, Procedure for measuring system COP (Coefficient of Performance) of a mobile air conditioning system on a test bench.
14. Yokozeki A, 1994. Solubility and viscosity of refrigerant-oil mixtures, *Proc. Int. Compressors and Refrig. Conf. at Purdue*: 335-340.
15. Bobbo S, Groppo F, Scattolini M, Fedele L, 2011. R1234yf as substitute of R34a in automotive air conditioning. Solubility measurement in commercial PAG, *Proc. ICR 2011*, ID 528.
16. Spatz MW, 2009. HFO-1234yf Technology update – Part II, VDA Winter Meeting, Saafalden Austria, February 2009.



17. Dixon L, 2010, Results of Shrieve Evaluations of 1234yf Refrigerant on Mobile A/C Lubricant Performance and System Chemistry, SAE Alternate Refrigerant Symposium AARS 2010, Scottsdale, (AZ) July 13- 15.
18. International Standards Organization, 2004. ISO 5167-4:2003, Measurement of Fluid Flow by Means of Pressure Differential Devices Inserted in Circular Cross-Section Conduits Running Full—Part 4: Venturi Tubes.



# Chapter 3 **Design and experimental analysis of a water chiller using ammonia as refrigerant**

In this chapter the design, the simulation, and the experimental analysis of a water chiller using ammonia as refrigerant is described.

The aim of this work is to develop a water chiller with a cooling capacity of 120 kW using a natural refrigerant such as ammonia, and working with low refrigerant charge and high efficiency.

A simulation model was developed, at the same time the prototype was designed, developed and the experimental tests carried out.

The prototype and the experimental work was made in the SCM Frigo S.p.a.: the company purpose was to evaluate the possibility of manufacturing a chiller using a natural fluid such as ammonia as refrigerant.

The support of the engineer M. Bernabei at the experimental work is gratefully acknowledged.

The support and the works Mr A. Favaretto for design, Mr M. Viero and A. Cervato for experimental work, are gratefully acknowledged too.

## **3.1 Introduction**

Ammonia is widely used as a refrigerant in industrial system for food refrigeration, distribution, warehousing and process cooling. Today ammonia is gaining more and more favour thanks to its low environmental impact and its superior thermodynamic properties. In particular ammonia is seen as a viable

natural alternative of halocarbons for both refrigeration and water chilling for air conditioning system when handled correctly.

Ammonia has a zero ODP and negligible GWP, moreover it has superior thermodynamic properties in particular high latent heat, high critical temperature and high liquid thermal conductivity as shown in Chapter 1.1.

Larsen (2008) [1] carried out a TEWI comparison for air-conditioning chiller using different refrigerants: the ammonia chiller comes out best due to its superior thermodynamic properties and the importance of energy efficiency for the indirect contribution.

Toxicity and flammability are the main drawback of ammonia.

Ashrae 34/1992 [2] and also the European Standard 378 (2008), part 1 [3], provide a classification of refrigerants based on their toxicity and flammability.

Ammonia is classified, for both the standards, as a B2 refrigerant that means it has high toxicity and low flammability (lower flammable limit greater than  $0.10 \text{ kg/m}^3$  at air temperature of  $21 \text{ }^\circ\text{C}$  and air pressure of  $101 \text{ kPa}$ , for Ashrae).

In reference to the ammonia flammable limits, if it is possible for the concentration in air in the machinery room to reach a level of the 20% of the lower flammable limit then additional precautions must be taken. In some international safety code [3] automatic isolation of the electrical supply to machinery room is required, in other Ansi-Ashrae 15-2001 [4] a very high emergency ventilation, often exceeding one air change per minute, are mandated.

Despite this, ammonia burning velocity is relatively low, less than  $8 \text{ cm/s}$  as shown in Jabbour-Clodic [5], thus reducing the risk of structural damage in the event of ammonia fire. The compound produces nitrogen and water, so there is not risk for people injury through inhalation of toxic products of combustion.

In normal operating conditions, ammonia cannot burn in an open space without a catalyst or a support flame, the high concentration corresponding to the lower flammability limit does not allow the burning of ammonia in a ventilated machines room and a combustion in a enclosed space tends to be short-lived, as the available oxygen content is rapidly diminished. Moreover

ammonia has a minimum ignition energy of activation of 14mJ, greater than the hydrocarbons, methane, ethane and propene require 0.26 mJ, so the normal three-phase electrical sparks cannot ignite a flame, however ammonia is very difficult to ignite.

Another ammonia drawback is its aggressive behavior with the copper in the presence of very small traces of water. Palm [6] reports the lack of components suitable for small ammonia systems, in particular expansion valves and hermetic or semi-hermetic compressors instead of traditional open. The compressor windings, made by aluminum or copper, encased showed to date lower performance than the open ones.

Despite the hazards implicit in its use as a refrigerant, ammonia has been established as the pre-eminent industrial refrigerant for over 125 years and is used in a wide variety of applications throughout the world, including food production, storage and distribution, dairy processing, brewing and distilling, water chilling for air-conditioning, cooling of large computer halls and industrial heat pumps.

The experience and refinement in all fields has produced a clear understanding of what needs to be done to avoid accidents. In general, if the requirements of the existing safety codes are followed, ammonia systems are very efficient, reliable and safe.

The main growth area expected for ammonia in future is in the increased use of chillers for office, hotel, hospital, shopping center, university and conference center air conditioning, providing chilled water for central cooling plant. Such systems need to be designed to protect the general public from the adverse effects of ammonia releases, but numerous projects all round the world have demonstrated that this is feasible (IIR Guides, 2008) [7].

Several authors have described the benefits of using ammonia for water chilling applications in recent years. Apart from the efficiency improvement, said to be in the range 9–17%, Tychsen (2003) [8], there is also a significant improvement in heat transfer, both in the evaporator and the condenser,

Hrnjak and Park (2007) [9]. This offers the opportunity to make efficient chillers in smaller footprints, particularly when air-cooled condensers are used.

The goal of this work is the design, simulation, and construction of a prototype, of low charge ammonia chiller; the charge reduction has to be so significantly as to avoid the restriction of heavy regulations.

The reduction of ammonia charge offers also the opportunity to improve the efficiency in cycling due to the lower effect of refrigerant migration in an off period. Compared to other refrigerants, ammonia has excellent potential for charge reduction as described in Hrnjak, 2009 [10].

The charge reduction is obtained both with low internal volume heat exchangers and with a control of throttling process on the condenser outlet liquid subcooling.

## **3.2 Refrigerant charge normative constrains**

Some maintenance from the EN 378:2008, part 1 [3] are reported.

The normative divides the rooms where the machine is placed in 3 types: A type are generic locals the entered number of people is not controlled and they are not informed about the safety prescriptions (ex. hospital, reading room), B type are monitored locals, only a controlled number of people can enter and some of them are informed about the safety prescriptions (ex. laboratory, office); C type are locals where only authorized people can enter and they are informed about the safety prescriptions (ex. cooling central).

For an indirect system with all the components containing B2 (EN 378:2008 classification) refrigerant as ammonia in a machinery room, or outdoor, there are not charge restrictions if the machinery room does not directly communicate with the occupied spaces. If the occupied space is a B type and the machine is not in a machinery room, the maximum refrigerant charge is 10 kg for both direct and indirect systems. If the compressor and the receivers are placed in a not occupied machinery room, or outdoor, for a direct system the

maximum charge is 25 kg, there are not restrictions for an indirect system. Finally for the C local type and if the machine is not placed in a machinery room for a both direct and indirect systems the maximum refrigerant charge is 50 kg if the density of people is less than  $1/10 \text{ m}^2$  and there are sufficient number of safe exits, else it is 10 kg; only for a direct system if the compressor and the receiver are in a machinery room or outdoor the maximum charge is 25 kg if the people density in the occupied space is greater than  $1/10 \text{ m}^2$ .

If the charge exceeds 50 kg the receiver and the flooded evaporator must be able to be isolated, there are particular requirements for the safety valves, furthermore a leak detector must be installed. All the receivers must have a liquid level indicator, and all the plant parts at different pressures must be provided of a pressure transducer, if the refrigerant charge exceeds 25 kg.

For other requirements, refer to EN 378:2008.

In designing the aim is keeping the charge under 25 kg and reaching 10 kg, with the minichannel condenser to avoid the normative prescriptions.

### 3.3 System concept and design

In Figure 3.1 a schematic of the refrigerant circuit is shown.

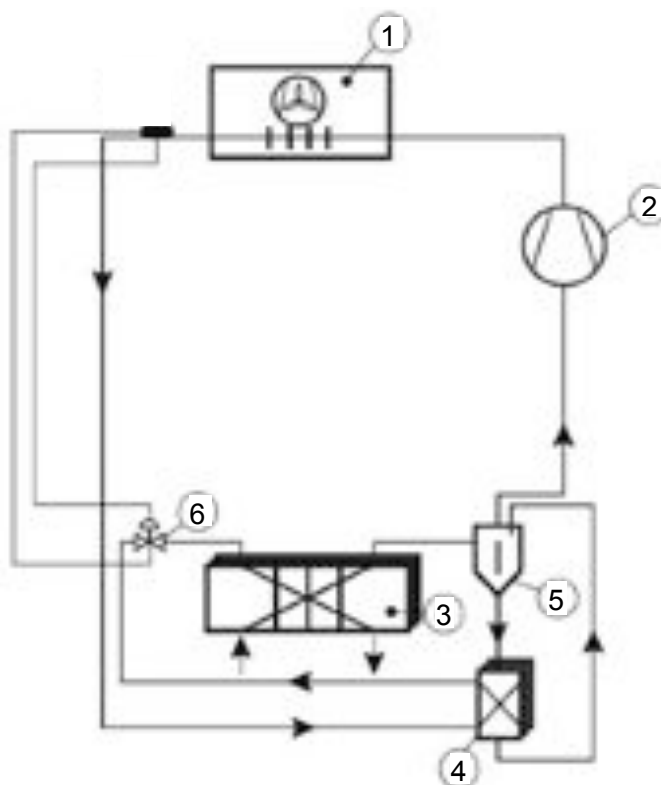


Figure 3.1. Schematic of the refrigerant circuit: 1)Condenser; 2)Compressor; 3)Evaporator; 4)Internal heat exchanger; 5)Low pressure receiver; 6)Throttling valve.

The main devices for the refrigerant charge reduction are the use of heat exchangers with low internal volume, and the throttling valve system control based on condenser outlet subcooling.

The evaporator (3) works as a direct expansion heat exchanger but its heat transfer area is completely wet by the liquid refrigerant in fact the evaporator outlet refrigerant quality is equal to 0.85 at design conditions, making it possible to avoid the dry-out phenomena, thus all the evaporator surface works with high heat transfer coefficient.

The presence of two-phase refrigerant at the evaporator outlet is related to the partial evaporation of ammonia in the internal heat exchanger IHX (4). This



heat exchanger is connected to a low pressure receiver (LPR) (5), by two pipes, a lower leg, which feeds the internal heat exchanger with saturated liquid, and an upper leg, which returns the partially evaporated liquid. The low pressure receiver was designed to maintain a suitable liquid holdup in all operating conditions, it has the function to even out changes in the void fractions inside the heat exchangers, allowing their optimal filling as the operating conditions vary. The internal heat exchanger is thus always filled with liquid and operates in a flooded thermosyphon mode as shown in Figure 3.2.

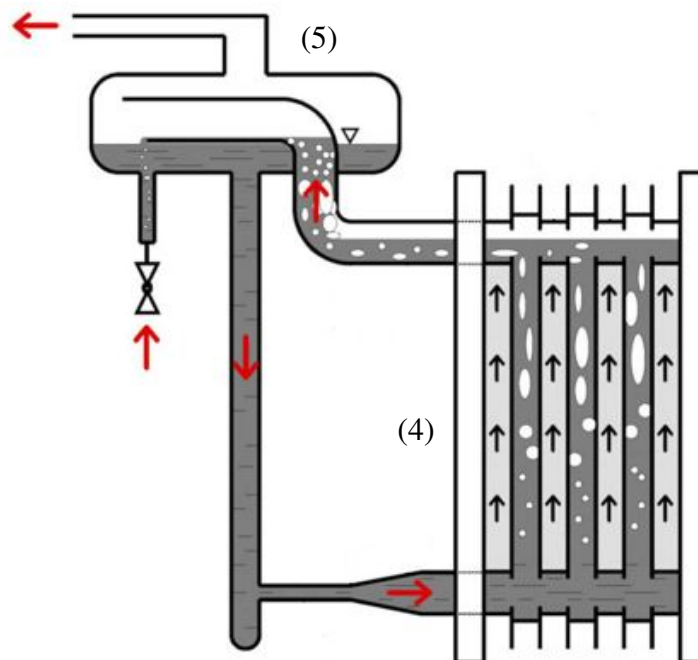


Figure 3.2. . Internal heat exchanger setup operating in thermosyphon mode.

The liquid subcooling obtained at high pressure side first enters the evaporator at very low refrigerant quality to avoid the liquid distributor, which is an added cost and implies high refrigerant pressure drops; second decreases the throttling process energy losses, but for ammonia it is not so high as shown in paragraph 1.1.

Because the liquid fraction exiting from the evaporator is evaporated into the IHX on low pressure side, the refrigerant at the compressor suction is

saturated vapor as in a flooded evaporator; so the compressor suction temperature is kept as low as possible to contain the discharge temperature, which is an ammonia drawback as described in Chapter 1.1, and to decrease the compressor input energy.

The higher is the liquid subcooling the higher is the condenser temperature and the lower is the throttling losses, so an optimum subcooling value exists, it depends from the refrigerant and from the ratio between the flooded and the dry condenser area, as detailed in Fornasieri and Cavallini [11] and in the Chapter 1.2.

Another reason because this evaporation design and this throttling valve control have been chosen is the ammonia behavior with the oil. A miscible oil should be used to ensure the dragging with a dry expansion evaporator; while with a flooded evaporator the utilized mineral oil is not miscible with ammonia, but the liquid drags the oil in the liquid receiver; this oil is more dense than ammonia and collects at the bottom of the receiver where it is recovered to the compressor carter.

With the chosen refrigerant circuit the oil collects at the bottom of the liquid line that connects the liquid receiver with the internal heat exchanger, an oil receiver (9, Figure 3.3) is placed in this line and the oil is periodically recovered.

In the Figure 3.3 the layout of the chiller prototype is shown, the oil recovery and the oil cooling circuits are reported together with the refrigerant ones.

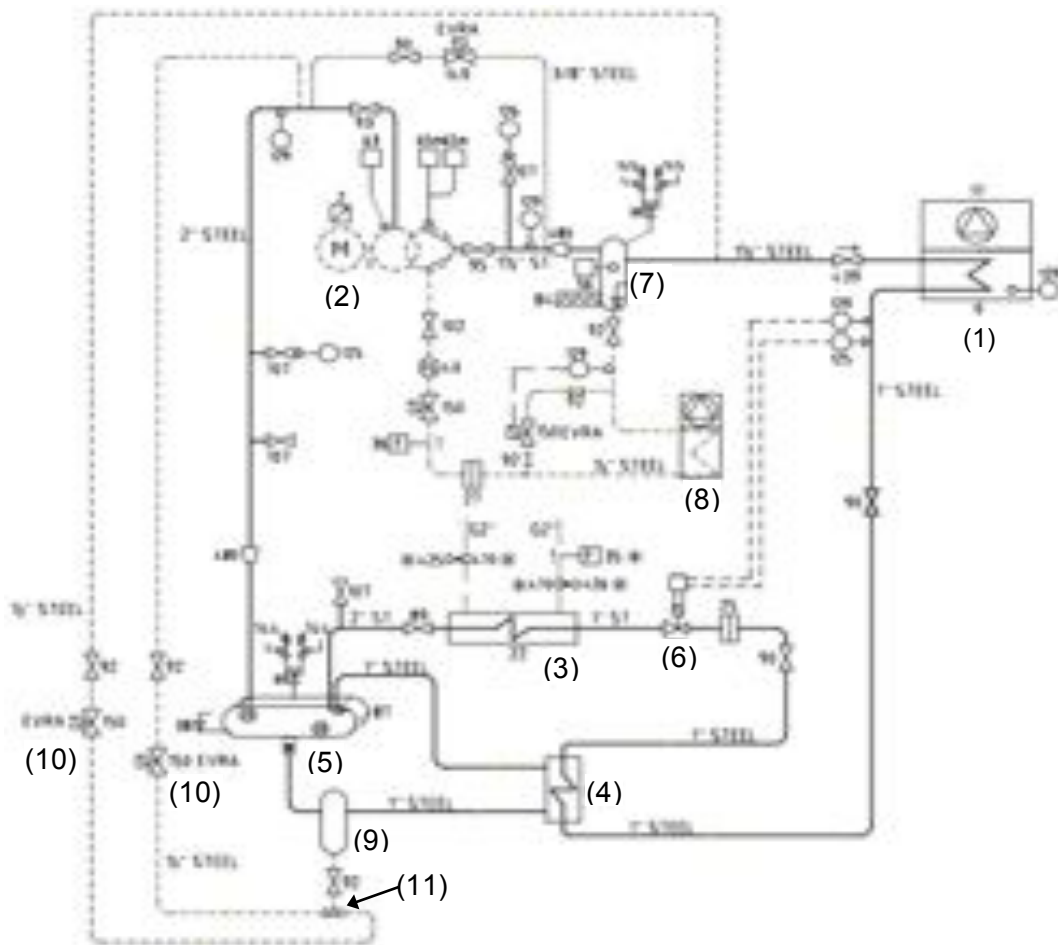


Figure 3.3. Schematic of the prototype refrigerant circuit: 1)Condenser; 2)Compressor; 3)Evaporator; 4)Internal heat exchanger IHX; 5)Low pressure receiver; 6)Throttling valve; 7)Oil separator; 8) Oil cooling; 9) Oil receiver.

A dashed line symbolizes the oil recovery and the oil cooling circuits, at the bottom of the oil receiver (9) an ejector (11) is placed, it is fed by the hot gas came from the compressor discharge and its low pressure inlet is connected to the oil receiver bottom; the valves (10) opens together at a set frequency and for a set period time.

The compressor discharge circuit is equipped with an oil separator (7) with sight glasses inserted for visual inspection of the oil returning to the compressor crankcase.

Oil is cooled by a finned coil heat exchanger (8) a finned coil bypass is provided for let the oil heating during the starting period time.

The condenser (1) is a low internal volume minichannel heat exchanger, it enables to contain the ammonia charge and to rejecting directly to the air the heat.

Both the evaporator and the IHX are plate heat exchangers.

The evaporator design working conditions are: cooling capacity of 110 kW, water temperature inlet/outlet 12/7 °C, inlet refrigerant quality lower than 0.15 (superior limit suggested by the supplier for avoiding the liquid distributor), outlet quality below 0.85 to avoid the dry out phenomena, and finally the water side pressure drops lower than 150 kPa (a practical limit given by SCM).

With this design condition the compressor was chosen, it is a screw open compressor OSKA 5361 model made by Bitzer, the compressor volumetric flow rate is 118 m<sup>3</sup>/h at 2900 rpm. The compressor selection software also gives the features for dimensioning the oil cooling: the volumetric oil flow rate, the capacity and the inlet oil temperature; the suggested oil is the Clavus G68/46/32. An inverter was provided to drive the compressor and the unit is controlled according to relay logic on secondary refrigerant outlet temperature. The evaporator is an Alfano HP 76-52H made by ALfalaval, it has 52 plates having high Chevron angle with overall dimension equal to 618x191 mm, the total heat transfer area is 5.2m<sup>2</sup>.

The internal heat exchanger is a plate flooded evaporator, it is chosen with low pressure drops on low pressure side, so low chevron angle, because it works in thermosyphon mode and the mass flow rate depends from the dynamic equilibrium between the pressure drops and the liquid column high (see Figure 3.2). The design outlet quality is 0.7 on low pressure side. The IHX has 20 plates with overall dimension of 526x111 mm, the total heat transfer area is almost 1 m<sup>2</sup>.

The condenser was in the project a minichannel heat exchanger, but supplier problems caused that initially a “traditional” finned coil was used, with a sensible charge increasing. The condenser finned coil main characteristics are reported in the Table 3.1 below.

Finned coil heat exchanger		
Tube arrangement (material)		Staggered (Inox)
Longitudinal tube spacing	[mm]	36
Traverse tube spacing	[mm]	31.2
Internal tube diameter	[mm]	9.12
Fins geometry (material)	[mm]	Wave (Al)
Fin spacing	[mm]	3
Fin thickness	[mm]	0.2
Number of row		4
Number of tube per row		32
Number of circuits		8
Tube length	[mm]	1950
Internal volume	[dm <sup>3</sup> ]	18.37

Table 3.1. Finned coil condenser geometric characteristics.

The minichannel heat exchanger chosen for the same design conditions has 5.7 dm<sup>3</sup> of internal volume at almost the same design conditions.

The prototype has two condenser coil placed in parallel, each one is coupled with two fans, their geometry allows a condenser temperature of 50°C with 35°C external air temperature and subcooling equal to 5°C; the nominal volumetric flow rate is 62000 m<sup>3</sup>/h and can be controlled by variation of the fan rotational speed.

The low pressure receiver has two functions: first separate the phases and provide an available volume to contain the components void fraction variation while changing the machine operative conditions. It is dimensioned for having sufficient liquid high to feed the IHX in every operative conditions, and to avoid liquid phase in the compressor suction line.

For space reason a horizontal liquid receiver is chosen, on one side it has a vertical part at the bottom of which the pipe for feeding the IHX is connected, the receiver is tilted on this side to be sure the liquid feeds the IHX avoiding to store a high liquid quantity (with a consequence charge increasing) and connects the oil into the IHX line, at the bottom of which the oil recovery system is placed.

The receiver is shown in Figure 3.4.

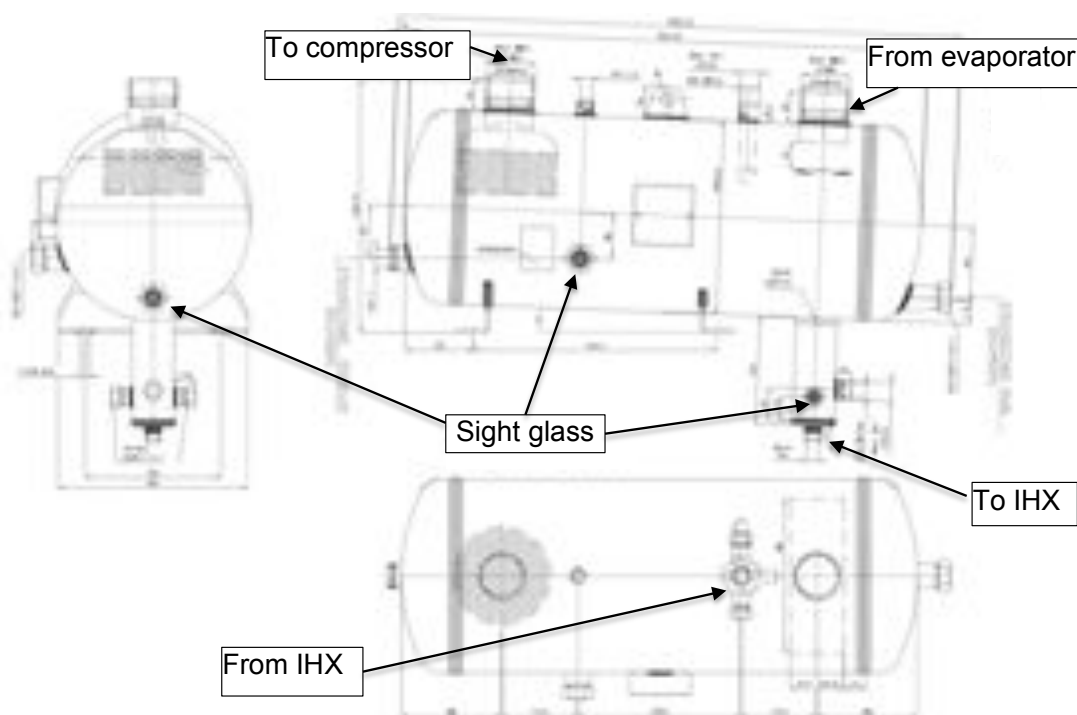
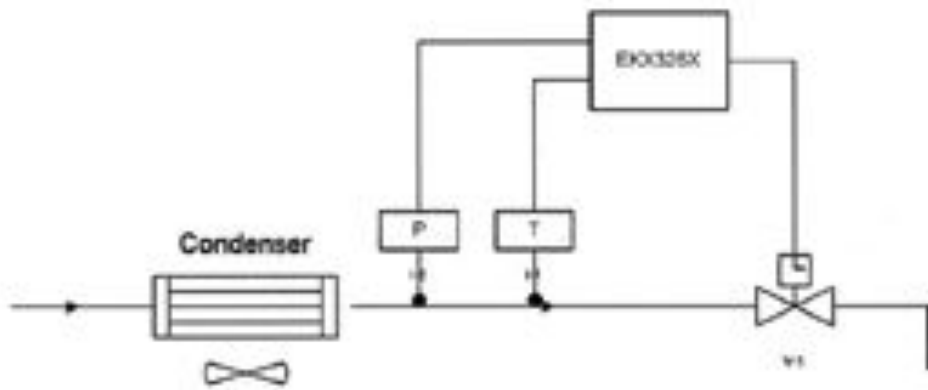


Figure 3.4. Low pressure receiver draw. The overall dimension are 0.95x0.35 . Three liquid sight glass are placed. It is tilted on the IHX feed line side.

The receiver is equipped with a demister in the compressor suction line, it is dimensioned following the procedure detailed in Jekel et al. [12].

It is provided of three sight glasses at different high so it is possible, during the experimental work, follow the liquid level; in particular it can be seen if the IHX is well fed in all the operative conditions. The pipes coming from the evaporator and from the IHX are bent in the direction of the receiver lateral surface, so that the high-speed liquid-phase could impact on the receiver surface and then slide along it.

The throttling valve (6, Figure 3.3) regulation system scheme, a photo in the prototype and the detailed valve scheme are shown in Figure 3.5, the valve has a set point subcooling and works with a PI controller.



a)



b)

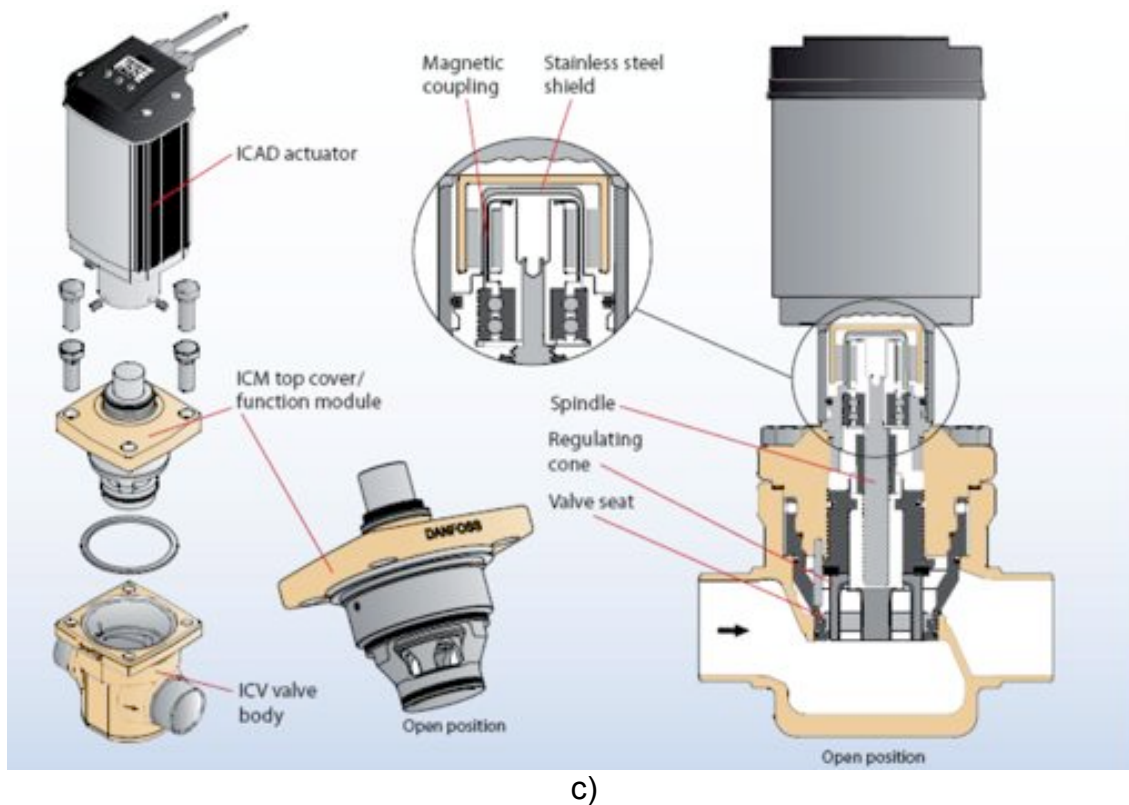
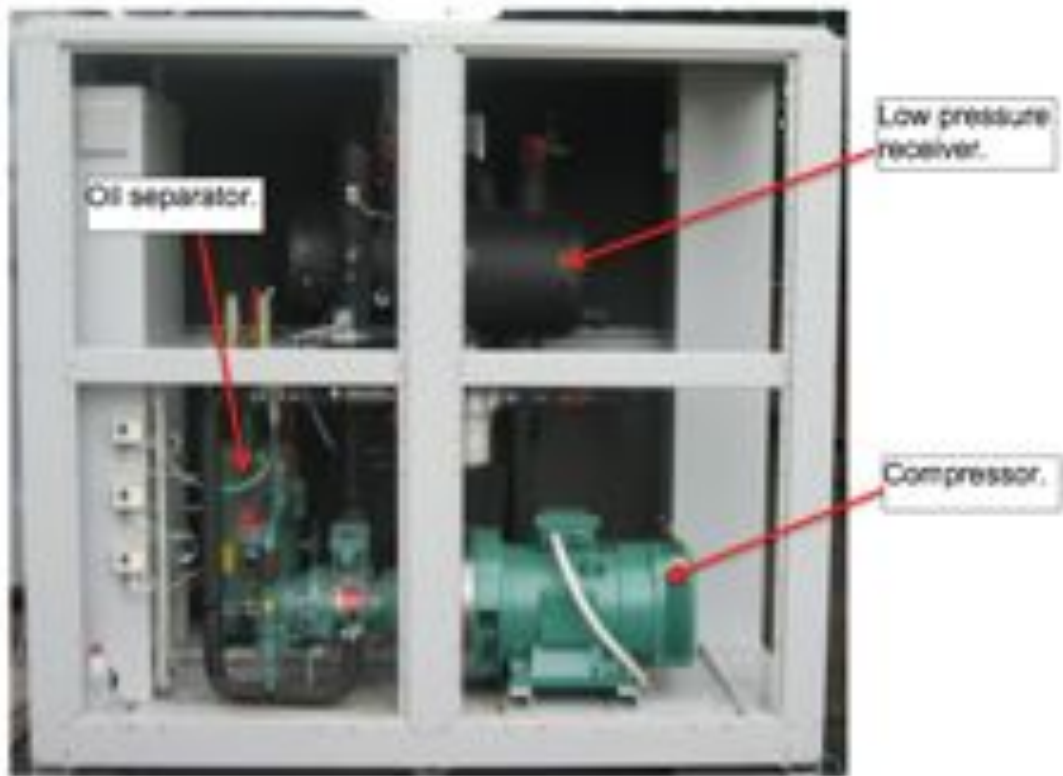


Figure 3.5. Throttling valve: a) regulation system scheme, b) photo in the prototype and c) valve detailed scheme

A Coriolis mass flow rate meter is placed in the liquid line between the condenser and the IHX, its working flow rate range is  $0 \div 2000$  kg/h, and its maximum measured error is  $\pm 0.5\% \pm [(zero\ point\ stability \div measured\ value) \cdot 100]$  of reading, the zero point stability is 0.2 kg/h. In Figure 3.6 some prototype photos are shown.





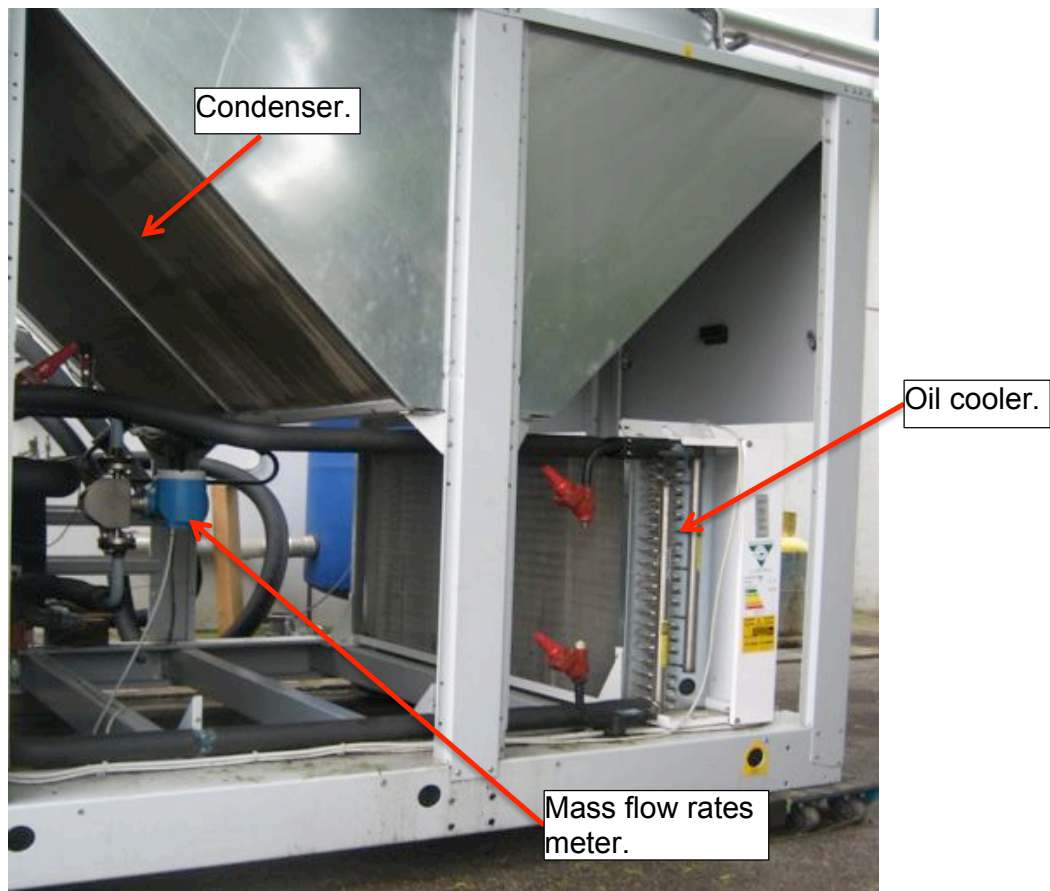




Figure 3.6. Prototype photos.

### 3.4 Test facility and testing procedure

The hydraulic circuit used for the tests is shown in Figure 3.7. The chilled water coming from the evaporator (line 1 in Figure 3.7) is warmed by a series of finned coil heat exchangers (dry-heater), placed outside the testing room and then collected inside a tank of 2 m<sup>3</sup> internal volume, having the function of heat storage. The hot secondary fluid coming from the heat recovery exchanger through the line 2 is introduced into the thermal storage tank where compensates for some amount of the refrigerant effect of the cycle. The temperatures of both the cool and the hot streams of secondary fluids entering respectively the evaporator and the recovery heat exchanger are controlled by mixing the fluid flows through two three-way valves that provide a way for bypassing, respectively, the external heat exchangers and the thermal storage. The volumetric flow rates of the hot and cool secondary fluid are

measured by two magnetic flow meters. The filling system of the whole test rig is represented by the line 5 in Figure 3.7.

The nominal performances of the pumps (at 2900 rpm) are 12-25 m<sup>3</sup>/h volumetric mass flow rate and 32.5÷36.5 m hydraulic head. The external dry-heaters are finned coils, with a face area of 3.9 m<sup>2</sup> (2610x1500 mm), 360 m<sup>2</sup> heat transfer area (referred to outside area), 2.1 mm fin spacing, 4 rows and 50 tubes per row. All temperature measurements are made with T-type thermocouples placed inside mixing chambers. A  $\pm 0.3^{\circ}\text{C}$  accuracy is estimated for all the temperature measurements. A T-type thermopile measures the water temperature difference between the evaporator inlet and outlet with an estimated accuracy of  $\pm 0.1^{\circ}\text{C}$ . Water volumetric flow rates are measured by electromagnetic meters (accuracy  $\pm 0.2\%$  of reading). The refrigerant pressures are recorded with strain-gauge transducers at compressor suction and discharge. The accuracy is  $\pm 9$  kPa according to the calibration report from the manufacturer. Electrical absorbed power is recorded with an electronic transducer (with an accuracy  $\pm 1.5\%$  of the reading value). All measurements signal are acquired with a 2 s sampling time.

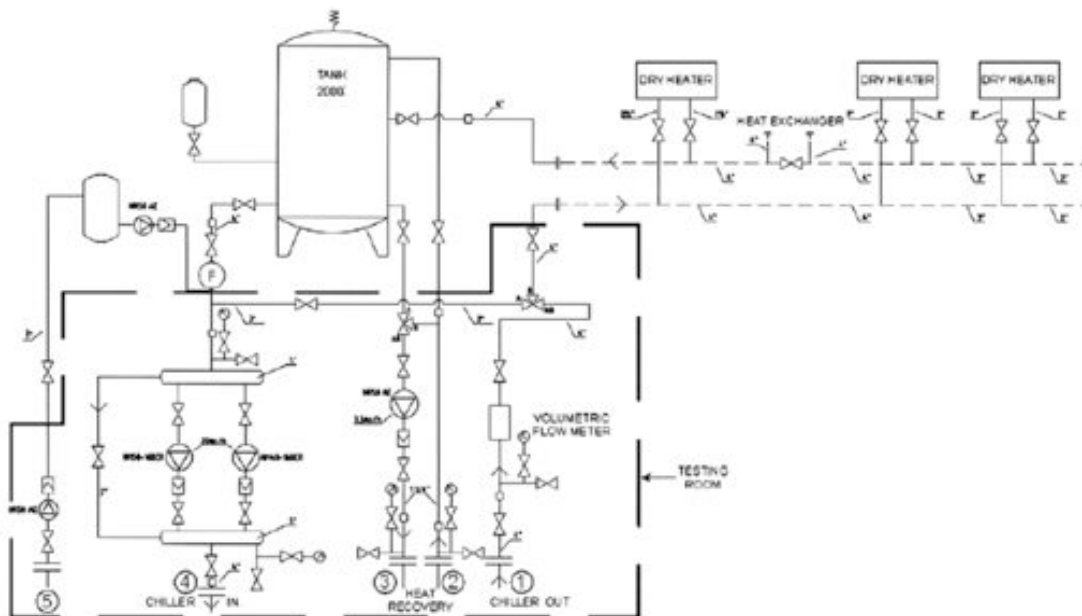


Figure 3.7. The hydraulic circuit used for the tests.

Tests have been carried out with the condenser placed at the exterior, thus the air inlet temperature is the uncontrolled external environment temperature. By controlling the heater thermal power, chillers have been tested in full load conditions with constant secondary fluid 7°C outlet temperature. The system efficiency in terms of COP was obtained by integrating the power absorption and the cooling capacity, computed from the instantaneous values of water mass flow rate and evaporator water temperature glide during stationary working conditions for at least 15 minutes. The equilibrium was reached when the water tank outlet temperature average value of a one minute working does not differ more than 0.2 K from the moving average value of the 4 previous minutes.

### 3.5 Simulation model

The system was designed with the aid of a simulation model of the overall refrigeration unit. For the numerical solution of heat exchangers, a Finite Volume (FVM) based model was adopted.

A schematic of finite volume discretization of the heat exchanger is shown in Figure 3.8.

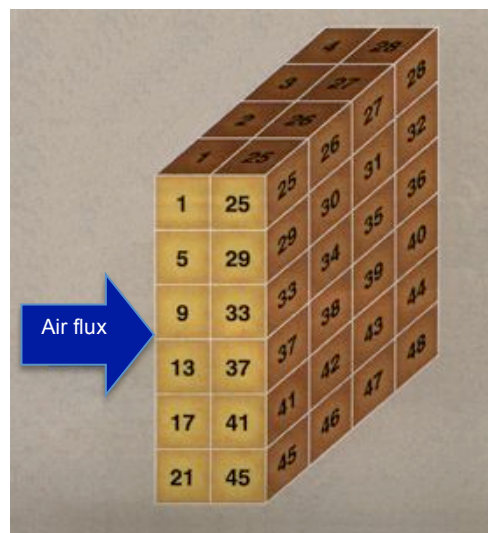


Figure 3.8. Schematic of the finite volume FVM heat exchanger subdivision.

In the code heat exchangers are defined by their geometrical parameters, and the phenomenological coefficients which characterize heat transfer and pressure drops are evaluated according to common correlations reported in open literature (see Table. 3.2).

The heat transfer coefficient in evaporation is calculated according to different correlations depending both on the chevron angle of plates and the boiling mechanisms. With high chevron angles and at nucleate boiling Danilova et al. (1981) [13] correlation, with Djordjevic and Kabelac (2008) [14] correction, was used. The dry-out prediction model of Mori et al. (2000) [15] was considered. The heat transfer coefficient in the dry-out zone was calculated according to a linear interpolation between the Martin (1996) [16] and the modified Danilova et al. (1981) [13] heat transfer coefficients. With low chevron angles the Danilova et al (1981) [13] and the Steiner and Taborek (1992) [17] correlations with Djordjevic and Kabelac (2008) [14] corrections were used, respectively at nucleate and convective boiling. The Thonon et al. (1997) [18] transition model from nucleate boiling to convective boiling was considered. Pressure drops are computed with Friedel (1979) [19] correlation. The void fraction model by Rouhani and Axelsson (1970) [20] is employed.

	Heat transfer $\alpha$ [W/m <sup>2</sup> K]	Pressure drops $f$ [-]
Air	Wang et al. 2000 [21]	Wang et al. 2000 [21]
Water	Gnielinski, 1976 [22]	Muley and Manglik, 1999 [24]
Ammonia two-phase condensation	Park and Hrnjak, 2008 [23]	Friedel, 1979 [19]
Ammonia single phase	Martin, 1996 [16]	Churchill, 1977 [25]

Table 3.2. Phenomenological coefficients used in numerical code.

The components charge is calculated by:

$$Charge = \sum_{i=0}^n (V \cdot \varepsilon \cdot \rho_v + V \cdot (1 - \varepsilon) \cdot \rho_l)_i \quad (3.1)$$

Where  $V$  is the  $i$ -volume value,  $\varepsilon$  is the  $i$ -volume average void fraction,  $n$  is the total number of volumes in which the heat exchange is subdivided,  $\rho_l, \rho_v$  are the  $i$ -volume average liquid and vapor density respectively.

For the compressor the EN 12900 polynomial coefficients, given by the supplier, are implemented.

The Mass flow rate, can be written as:

$$\begin{aligned} \dot{m} = & c_1 + c_2 \cdot T_{evap} + c_3 \cdot T_{cond} + c_4 \cdot T_{evap}^2 + c_5 \cdot T_{evap} \cdot T_{cond} + \\ & + c_6 \cdot T_{cond}^2 + c_7 \cdot T_{evap}^3 + c_8 \cdot T_{evap}^2 \cdot T_{cond} + c_9 \cdot T_{evap} \cdot T_{cond}^2 + c_{10} \cdot T_{cond}^3 \end{aligned} \quad (3.2)$$

Where  $T_{evap}$  and  $T_{cond}$  are the evaporator and the condenser temperatures.

Analogously polynomials coefficients for the absorbed power and the cooling power are given by the supplier.

For a complete vapor compression system, comprising an evaporator, a condenser, an internal heat exchanger, the governing equations of each component can be reduced to this general form:

$$f(p_i, p_o, h_i, h_o, \dot{m}) = 0. \quad (3.3)$$

Where  $p_i, p_o, h_i, h_o, \dot{m}$  are the component inlet and outlet pressure, inlet and outlet enthalpy and the refrigerant mass flow rate respectively. Therefore, the problem is reduced to calculate the solution to a non-linear system of equations written in the form of equation (3.3). The system of equations is solved using Powell's hybrid algorithm (Powell, 1977) [26].

In addition to the condenser geometry, the air inlet conditions and the face velocity or the volumetric flow rate, or the minimum compressor condensing temperature need to be insert in the program inputs, in the second case the face velocity and the fans speed are calculated by the program.

For the evaporator the water inlet flow rate and temperature has to be insert in the input data. The evaporation pressure and the condenser pressure (or

alternatively the condenser frontal velocity with the minimum compressor condenser temperature) are the independent variables; with these temperatures compressor, condenser and evaporator are solved and three mass flow rates are determined.

Two errors are calculated, first the difference between compressor and evaporator mass flow rates, second the difference between compressor and condenser mass flow rates, the total error is the sum of these two errors. The convergence method tries with different couple of evaporator and condenser pressures until this total error is below a set maximum error.

Further an external loop finds the evaporator water inlet that realize the water output of 7 °C. In Figure 3.9 the program flowchart is shown.

Finally an internal loop is implemented for the internal heat exchanger on low pressure side to find the mass flow rate knowing the liquid high (see Figure 3.2).

More details about the numerical models and their validation are reported in (Casson et al., 2002) [27], (Cecchinato et al., 2005) [28] and (Cavallini et al., 2008) [29].



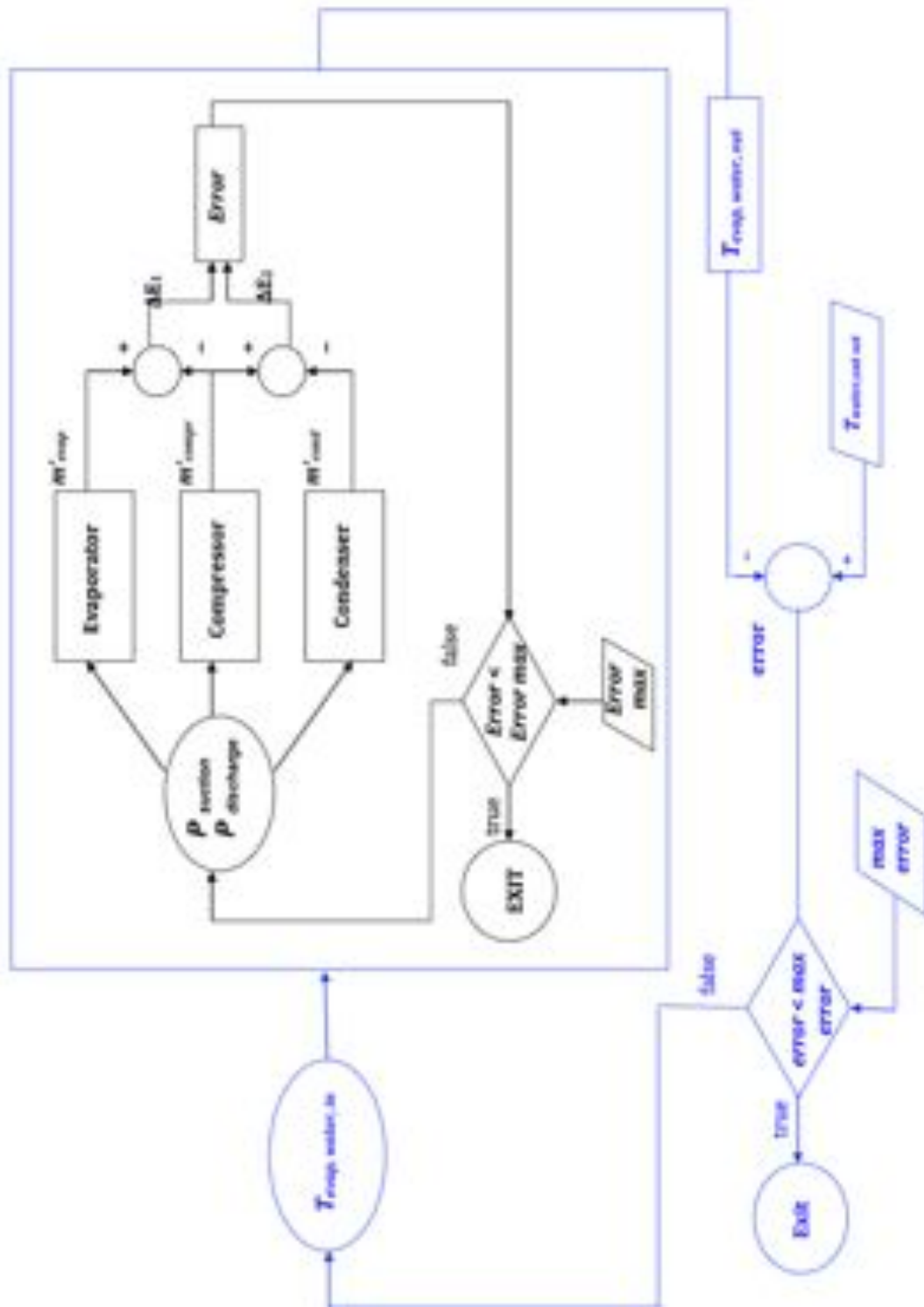


Figure 3.9. Simulation program flowchart. Circuit components with the total mass flow rate error (black) and external water temperature loop (blue).

The standard operation of the chiller is defined by constant mass flow rate (5.23 kg/s) and constant temperature inlet of the evaporator secondary fluid (12 °C).

In the diagram of Figure 3.10 the EER values (energy efficiency defined as the ratio of nominal cooling capacity and total power absorption, fans included) together with the EER and refrigerant charge variation resulting from the simulations at full load and design conditions (external air inlet at 35 °C) are plotting against the subcooling increases.

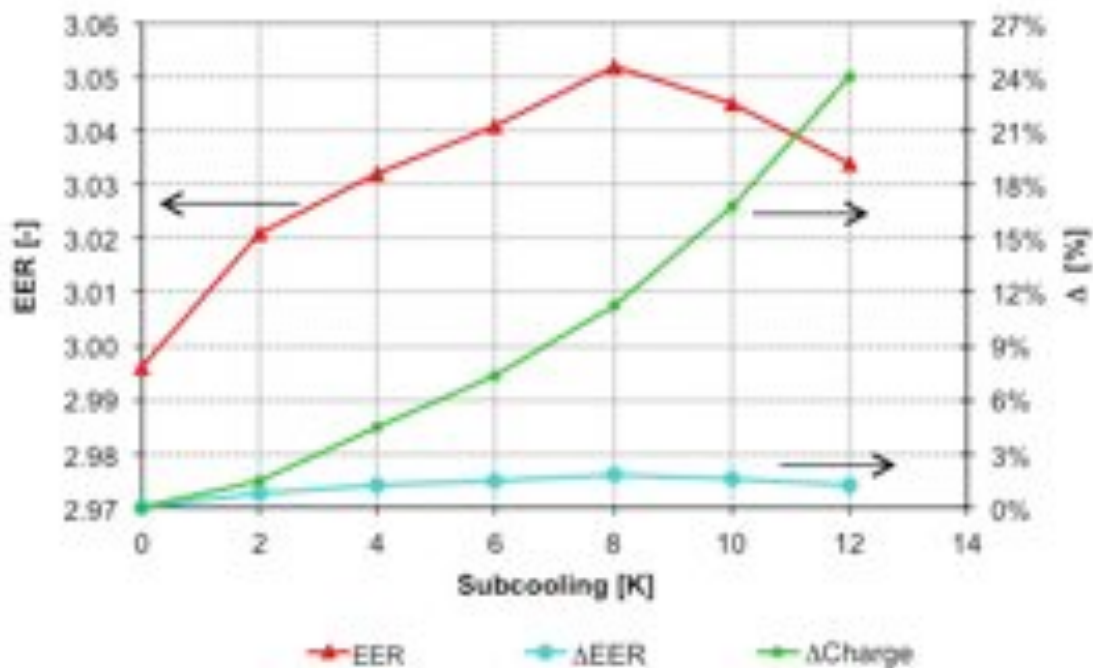


Figure 3.10. EER,  $\Delta$ EER,  $\Delta$ Charge vs. subcooling: simulation results at design conditions.

As can be easily predicted, the ammonia charge continuously rises as the subcooling increases. The EER rises till a subcooling value of 10 °C, ranging from about 2.995 to 3.050 at 0 °C and 8 °C of the subcooling respectively, and rapidly decreases for higher values, 3.035 at a subcooling of 12 °C. The presence of an optimal subcooling value in air cooled condensers is widely described by Cavaioni et al. [30] and it has been discussed in Chapter 1.2 too,

but in the case of ammonia the unit energy efficiency is not much sensitive to subcooling. Nevertheless a subcooling value of 4÷6°C seems to achieve the best compromise between charge containment and control stability requirements.

Figures 3.11 shows the charge amount in the unit components at design (a) and critical off-design (b) (25% compressor speed and 20 °C external air temperature) conditions respectively, these conditions are according the EN 14825 [31]. The ammonia charge contained the low pressure receiver ranges from 2.9 to 2.3 kg in condition (a) and (b) respectively.

The program considered total charge is almost 9.2 kg; it is obtained by imposing the minimum liquid high on the receiver to feed all the components in all considered operative conditions. Changes result from the variation of the void fractions inside the components, especially the heat exchangers.

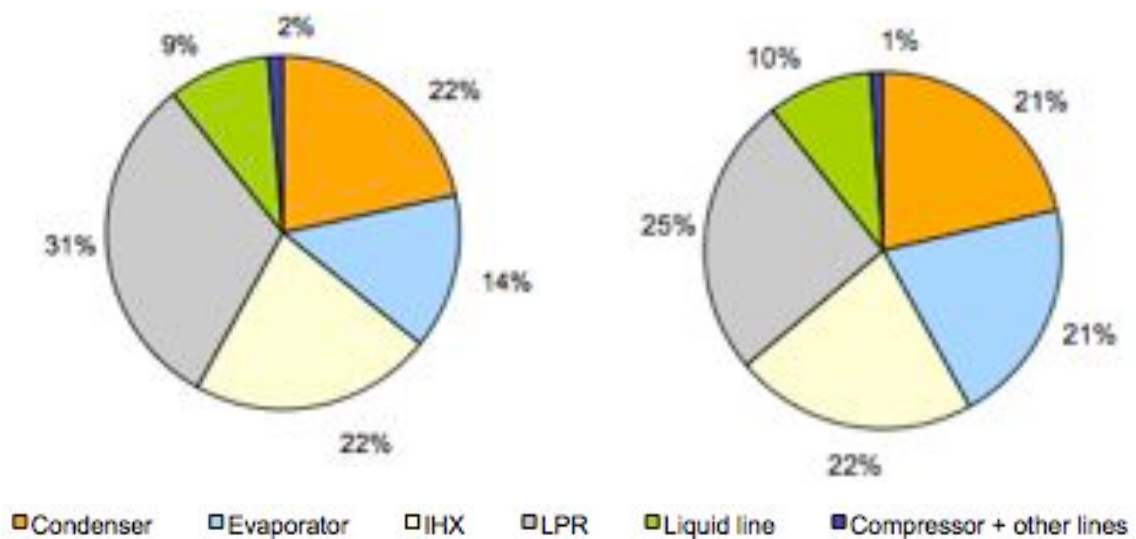


Figure 3.11. Components charge distribution at design (a) and off-design (b) conditions. The total charge is 9.2 kg.

In Figure 3.12 the condenser and the evaporator temperatures trends vs. the air temperature are shown at full load conditions, the evaporating temperature variation is contained between 0.07 and 1.23 at 10 °C and 40 °C respectively. As detailed in the previous paragraph the program can have a set point

condenser temperature, in case the face velocity is changed instead the condenser temperature while the operative conditions changes, this is imposed when the condenser temperature goes below the minimum value given by the supplier. The minimum condenser temperature value considered according to the supplier prescriptions is reported in the chart.

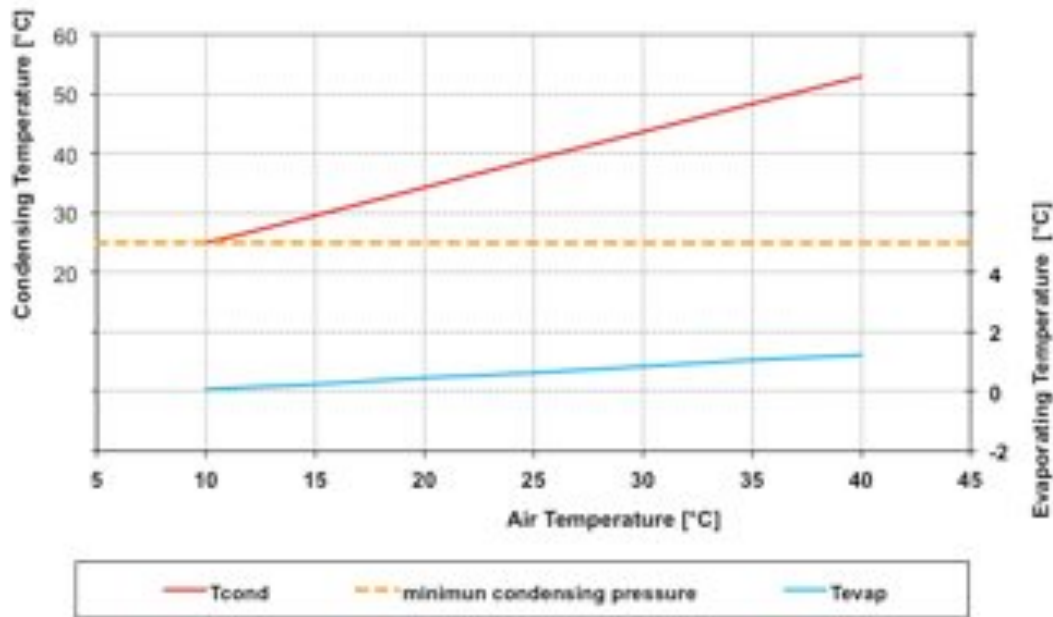


Figure 3.12. Condenser and evaporator temperatures trends vs. external air temperature at full load conditions.

In Figure 3.13 the EER simulation is plotted against the air temperature; as can be easily predicted, the chiller efficiency continuously reduces as the air temperature increases, ranging from about 2.72 to 5.05 at 40 °C and 10 °C external air temperature respectively.

The cooling capacity and the heat flux at the IHX are plotted in Figure 3.14. The cooling capacity decreases while the external temperature rises, ranging from about 116 to 137 kW at 40 °C and 10 °C external air temperature respectively. On the other side, the heat flow at the IHX monotonously increases with the air temperature, passing from 11 to 26 kW at 10 °C and 40 °C air temperature respectively.

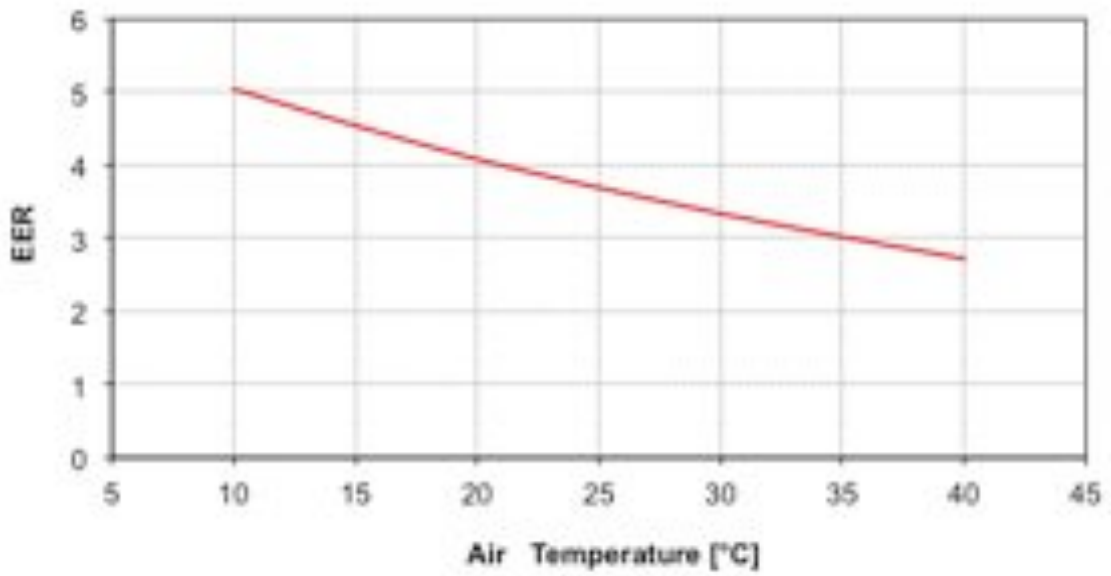


Figure 3.13. EER vs. external air temperature.

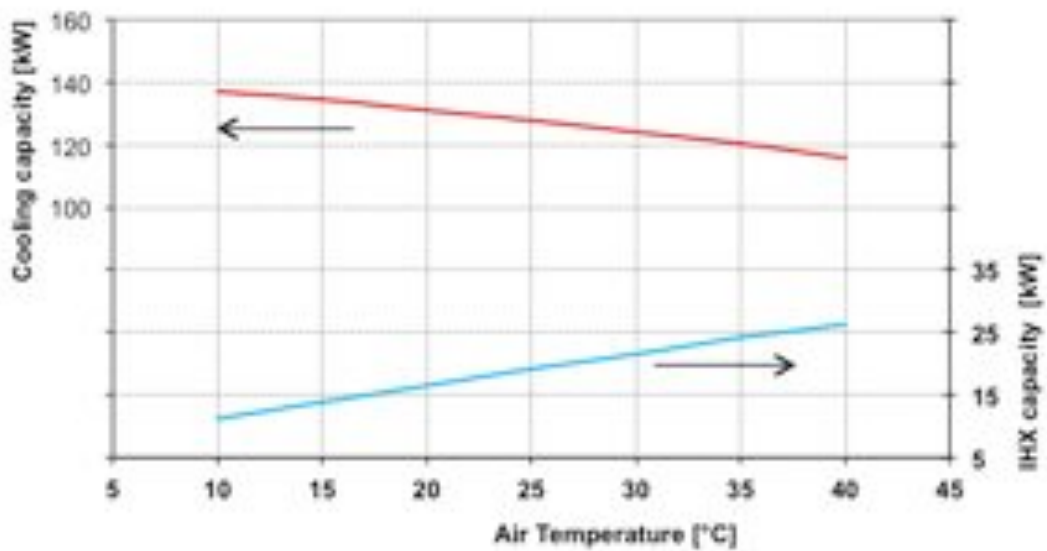


Figure 3.14. Cooling capacity and IHX heat flux vs. external air temperature.

## 3.6 Experimental results

The first experimental tests have shown oil recovery problems at the IHX they have been resolved with the system shown in Figure 3.3 and described in section 3.3.

It seemed also that with prolonged operation time some oil remains trapped in the evaporator, despite the direct expansion system this could be due to the height where the LPR is placed to feed the internal heat exchanger.

Pending is a redesign of the evaporator position in the layout, it has been asked to place in the actual prototype a small oil receiver below the evaporator inlet circuit, in that way when the machine is switch off the oil should go to this receiver and can be recovered at the following starting by a second ejector. In this way it was possible to understand if the low evaporator temperature shown by experimental tests were cause by oil presence, as it seems looking at the oil receiver level. Unfortunately the company placed just a tube from the bottom of the evaporator inlet to the IHX ejector low-pressure inlet to recover the oil with the same ejector used for IHX. But this solution does not work, it is a by-pass from the evaporator inlet and the bottom of low pressure receiver (where the pressure should be higher because the liquid high), from where the oil can go to the evaporator. So during the tests this circuit was closed and opened manually sometimes when the ejector was working, in this way it was roughly possible to see if the evaporator was trapping some oil.

In Figure 3.15 the new tube is shown with the shut-off manually valve.

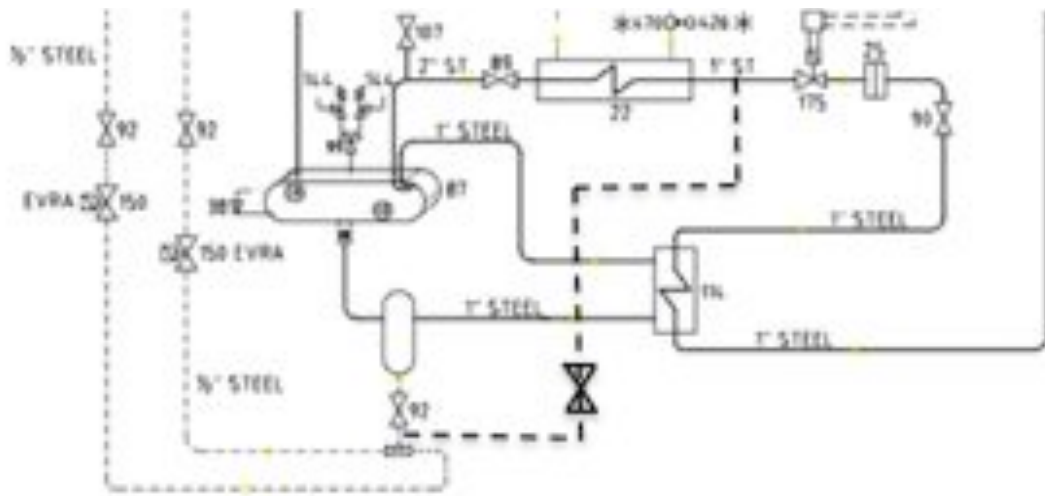
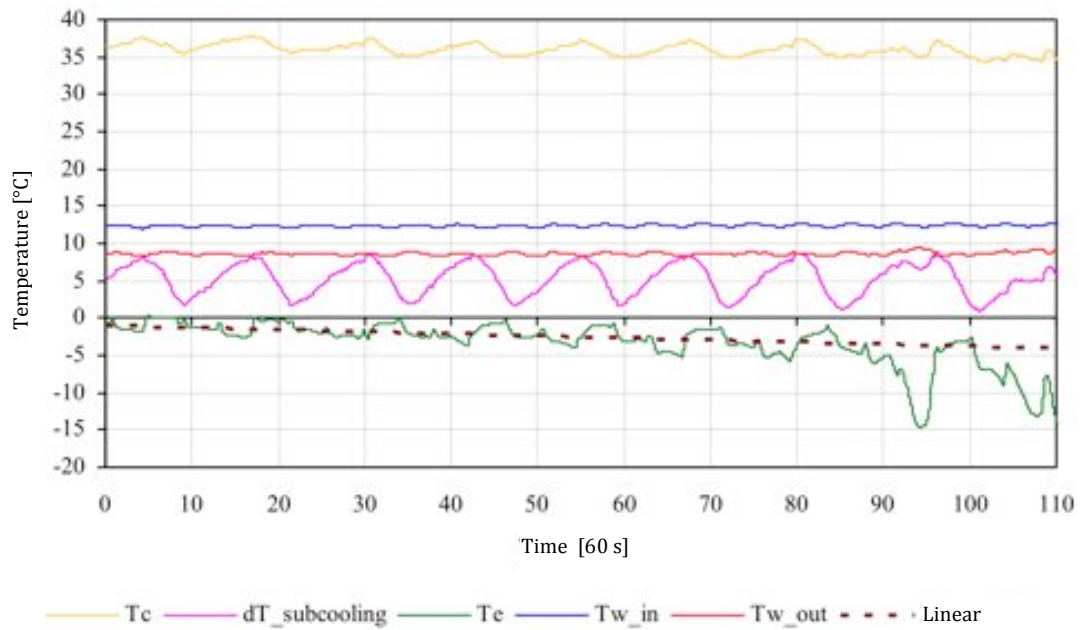
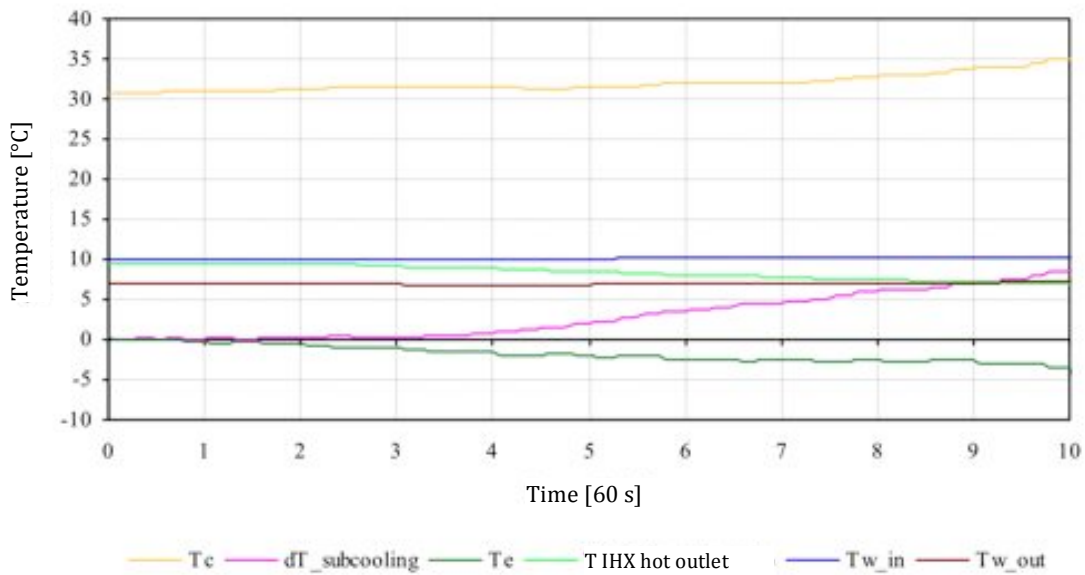


Figure 3.15. Evaporator oil recovery len, with the shut-off valve.

In Figure 3.16 the decreasing in evaporation temperatures over time can be seen.



a)



b)

Figure 3.16. Decreasing in the evaporation temperature over time.

Another issue occurred during the experimental work was the limited throttling valve “authority”, it was a prototype made for this machine; with the first tests it became clear the valve was sized too big for the plant. To demonstrate that a test was carried out: with the compressor working at full load, the valve was closing in steps, after each step some time was waiting to let the machine reaching the steady state condition, so it was possible to see when a condenser outlet subcooling occurred, it happened while the valve were at 4% of its maximum opening. It is clear that it was not able to adjust the refrigerant flow rate.

In Figure 3.17 the test is shown.



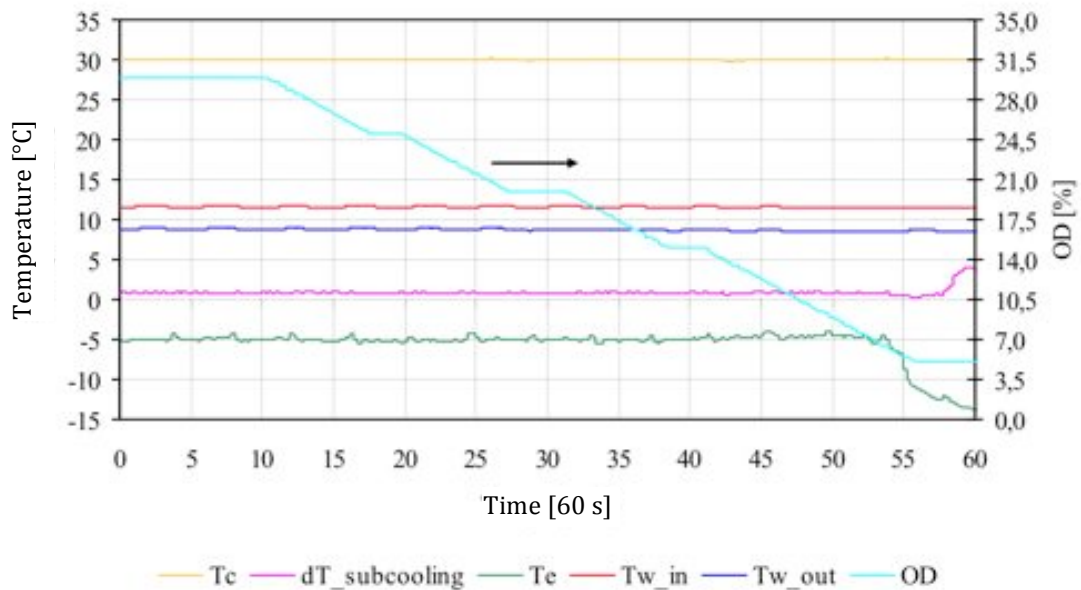


Figure 3.17. Test made by closing progressively the throttling valve, the subcooling is reached while the valve opening degree (OD) is almost the 4%.

A new valve was provided and equipped in the machine, its orifice has a diameter 1/3 of the previous one.

After changing the valve, new tests were carried out, unfortunately with the evaporator oil recovery system handicap as detailed above.

These tests seem to confirm the presence of the oil in the evaporator because the evaporator temperature is very small than the expected value, just at 50% of the compressor capacity the evaporator temperature is - 2 °C. Moreover looking at the oil separator the oil charge seems decreasing over the time. Another hypothesis is that the evaporator is too small, it sounds strange because it was dimensioned with the supplier selection software, confirmed and controlled by the supplier.

Other hypothesis could be possible, the right procedure should be to equip the prototype with an evaporator serious oil recovery system and then to carry out new tests and analyze them.

In Figure 3.18 the test at almost the 50% of the compressor capacity is shown.

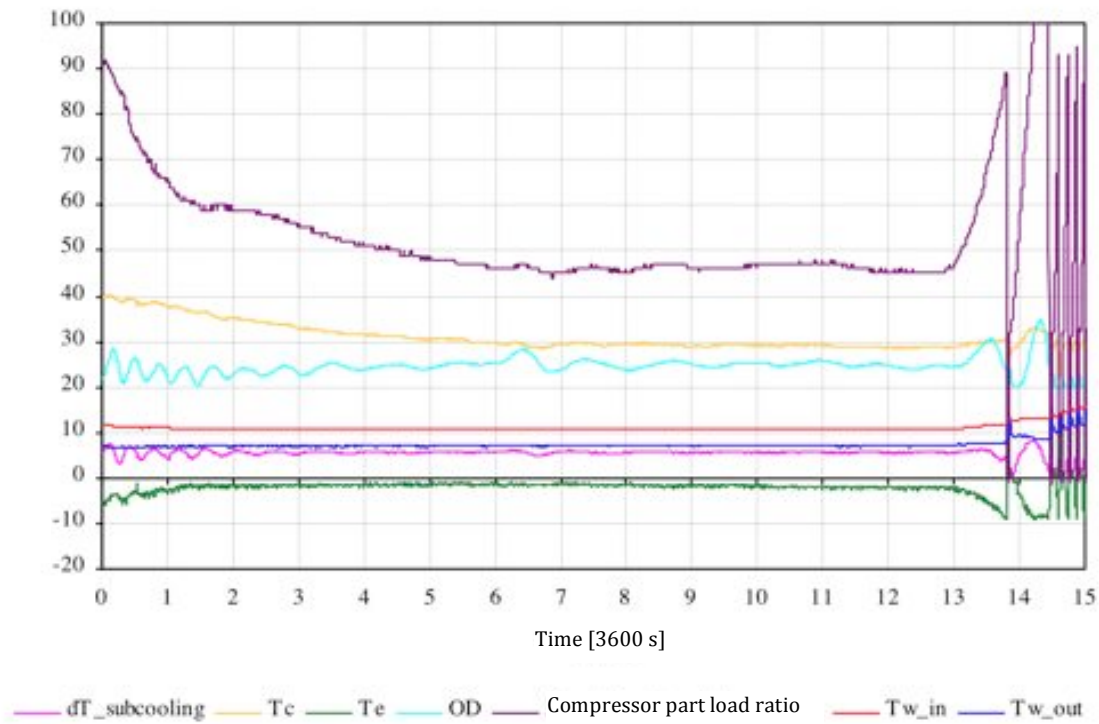


Figure 3.18. Test at almost the 50% compressor part load ratio.

Another test is reported in Figure 3.19 with the compressor capacity always below of the 70%.

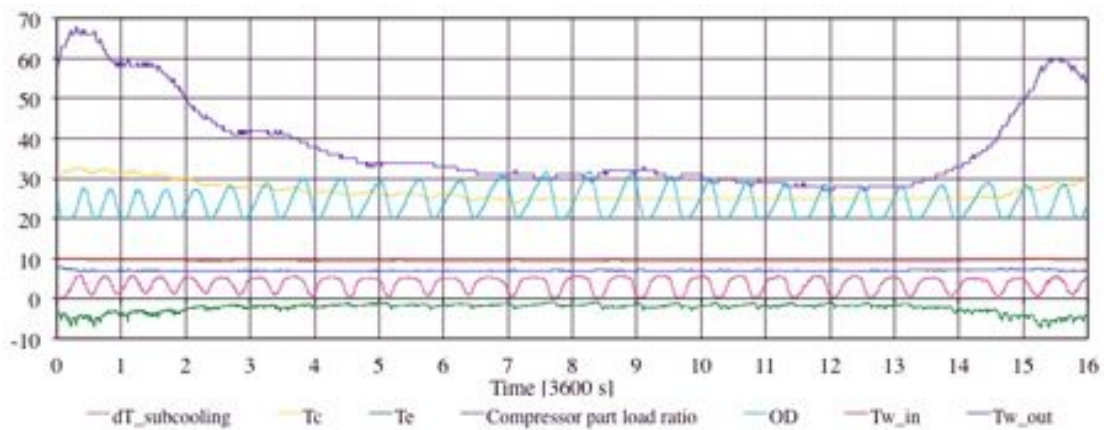


Figure 3.19. Test at almost the 50% compressor part load ratio.

It can be pointed out for both the Figures 3.18 and 3.19 that the new valve works between the 20-30% of its maximum opening; it still looks a little great sizing.

The machine works stably especially with high subcooling as in the test of Figure 3.18, with small set subcooling the machine works in a commuter around the set point and obviously the valve opening too, the PI controller looks as not the best for that system.

Finally in Table 3.3 different tests results are reported

Capacity [%]	G <sub>ammonia</sub>	P <sub>m.e.</sub>	T <sub>asp,if</sub>	T <sub>asp,if</sub>	η <sub>v</sub>	T <sub>air</sub>	T <sub>evap</sub>	P <sub>evap</sub>	H <sub>asp,if</sub>	S <sub>asp,if</sub>	H <sub>carco,if</sub>	P <sub>compres,is</sub>	η <sub>is</sub>	P <sub>cond</sub>	P <sub>cond</sub> /P <sub>evap</sub>	Fan: three-phase current	G <sub>(t20)</sub>	T <sub>out(t20)</sub>	T <sub>in(t20)</sub>	P <sub>0</sub>	Fan	n° <sub>fan</sub>	P <sub>fan</sub>	COP	
Unit	kg/h	kW	°C	kg/m <sup>3</sup>		°C	°C	bar	kJ/kg	kJ/(kg·K)	kJ/kg	kW	-	bar		A	A	°C	°C	kW	%	n°	kW		
100%	230,0	25,00	-4,70	2,66	0,73	26,00	-6,90	3,29	1603,25	6,21	1789,09	11,87	0,47	12,00	3,64	2,00	1,90	26,00	8,90	11,30	69,62	100	4	5,11	2,31
100%	238,0	25,20	-5,80	2,62	0,77	26,00	-7,40	3,23	1601,11	6,21	1789,51	12,45	0,49	12,00	3,72	2,00	1,90	26,00	7,90	10,20	66,72	100	4	5,11	2,20
100%	251,5	25,90	-6,00	2,61	0,82	23,00	-7,50	3,21	1600,74	6,21	1792,40	13,39	0,52	12,20	3,79	2,20	1,90	17,00	#	#	100	4	5,54	#	
100%	252,5	26,40	-3,40	2,78	0,77	27,00	-5,70	3,45	1604,95	6,19	1801,82	13,81	0,52	13,40	3,88	1,90	1,90	26,00	10,30	13,00	78,32	100	4	4,93	2,50
80%	198,7	20,00	-6,70	2,52	0,84	21,00	-8,40	3,10	1600,15	6,22	1761,89	8,93	0,45	9,80	3,16	2,20	1,50	17,00	8,80	12,50	70,18	100	4	5,54	2,75
80%	210,3	21,90	-5,70	2,65	0,84	21,00	-7,10	3,27	1600,96	6,20	1774,59	10,14	0,46	11,10	3,40	0,40	0,70	17,00	8,60	12,10	66,38	11,50	4	1,38	2,85
80%	212,5	24,00	-5,20	2,69	0,84	21,00	-6,70	3,32	1601,70	6,20	1798,96	11,64	0,49	13,00	3,92	0,80	0,70	17,00	8,30	11,80	66,38	12,80	2	0,95	2,66
60%	193,0	22,20	-1,50	3,16	0,86	29,00	-2,40	3,92	1605,14	6,13	1778,34	9,29	0,42	13,20	3,37	2,30	2,15	26,00	11,50	13,60	60,92	100	4	4,89	2,25
60%	189,0	21,90	-2,30	3,02	0,88	27,50	-3,60	3,75	1604,83	6,15	1781,73	9,29	0,42	12,90	3,44	2,00	1,30	26,00	10,60	12,70	60,92	100	4	3,89	2,36
60%	181,2	21,60	-4,40	2,78	0,92	22,00	-5,80	3,44	1602,52	6,18	1794,11	9,64	0,45	13,00	3,78	0,30	0,50	17,00	9,30	12,30	56,90	12	4	1,12	2,50
60%	211,0	24,60	-1,30	3,13	0,95	30,50	-2,60	3,89	1605,97	6,14	1801,81	11,48	0,47	15,00	3,85	0,19	0,25	26,00	10,30	12,50	63,82	10	4	0,55	2,54
40%	156,0	17,00	0,40	3,39	0,97	28,00	-0,40	4,23	1607,10	6,11	1757,34	5,13	0,30	12,30	2,91	2,00	2,00	26,00	11,20	12,90	49,31	80,00	4	5,19	2,22
40%	123,0	16,50	-4,70	2,79	0,94	25,00	-5,80	3,44	1601,74	6,18	1764,38	5,56	0,34	10,90	3,17	2,00	1,76	17,00	7,80	9,90	39,83	100,00	4	4,98	1,85
40%	127,0	17,40	-4,90	2,77	0,97	26,00	-6,00	3,41	1601,51	6,18	1795,33	6,84	0,39	13,10	3,84	1,10	1,10	17,00	8,00	10,20	41,73	12,00	4	2,73	2,07
40%	147,8	19,60	-6,50	2,59	1,21	24,00	-7,70	3,19	1599,73	6,21	1808,08	8,55	0,44	13,40	4,20	0,40	0,40	26,00	7,40	9,00	46,41	11,00	2	0,52	2,31

Table 3.3. Experimental results

### 3.7 Conclusion

The preliminary results of a research project aiming at developing a low refrigerant charge water chiller prototype operating with ammonia as the refrigerant are presented. The air-cooled chiller operates for refrigerating water down to 7 °C supply temperature adopting a direct expansion configuration for the evaporator. Its design and manufacturing process was described. A simulation model of the chiller was developed. To verify proper operation of the system under different operating conditions and to validate model results, some experimental tests were carried out.

The experimental tests highlighted some problems of oil recovery in the evaporator, a possible solution was suggested but the corresponding prototype modifications have not been made yet, after that new better tests could be made and the reason for the low evaporating temperature discovered, or at least well investigated.

Another open issue is the throttling valve regulation system, the subcooling is affected by the machine load, but also by the external temperature, when it changes the condenser temperature changes. The fans control system can vary their speed or for keeping the condenser temperature constant or for reaching a set difference with the external temperature; while the fans are reaching the condenser temperature, the valve is trying to set the subcooling and they can disturb each other. This can be easily seen when under a certain external air temperature the fans start to operate in ON-OFF mode causing high disturbance to the valve work. The regulation system needs to be further investigated.

During the tests the subcooling regulation system showed that the subcooling formation is slow, it can easily be completely lost when it needs to be decreased and the valve opens, if the valve opens a little more all the liquid can go to the receiver. If the valve opening speed is fast and a small subcooling is set, all the liquid goes easily to the receiver and then the

system tries to close the valve completely because the subcooling has become zero, so a minimum valve opening needs to be imposed. Moreover, closing the valve quickly implies that the evaporator pressure will decrease, in some cases it reaches such a low value that the machine is turned off by the safety control system. Only when the internal heat exchanger has evaporated a liquid quantity such that increasing the condenser subcooling, the valve starts to reopen and the evaporator pressure can increase.

Thus an appropriate design of the liquid circuit is required and the still big valve size enhances this phenomenon, so an appropriate valve sizing is needed and probably the subcooling value has to be increased.

On the contrary increasing the subcooling is very different, in this case the valve can close relatively fast without any problem.

So it is very difficult to choose appropriate parameters for the PI controller.

In the future when a minichannel heat exchanger condenser is available that problem should be solved or at least decreased because its low internal volume should allow a small diameter long liquid line to quickly reform the subcooling and contain the condenser liquid charge.

Furthermore, the control logic of the system probably needs to be improved to take into account the above-mentioned phenomena.

The charge target was reached, the prototype worked with a charge around 20 kg, but the charge in the receiver for the tests was kept deliberately high, with optimization it can reach 15 kg and probably with the minichannel condenser 10 kg.

In conclusion more experimental work with some important changes still need to be done: some components as the throttling valve and the condenser probably have to be improved, but first it is important to insert an oil recovery system on the evaporator.

The prototype was developed using components available on the market; this proves that the current technology can be almost ready for supplying the market with ammonia refrigerating plants though some components as the minichannel condenser are still missing.

### 3.8 Reference

1. J. Larsen, Future outlook for ammonia chillers in refrigeration and air-conditioning in Europe, 8th IIR Gustav Lorentzen Conference on Natural Working Fluids, Copenhagen, 2008.
2. ASHRAE Standard 34-1992.
3. EN 378:2008, Refrigerating Systems and Heat Pumps – Safety and Environmental Requirements, Comité Européen de Normalisation, Geneva.
4. ANSI-ASHRAE 15-2001, Safety Standard for Refrigeration System.
5. Jabbour T., Clodic D., ISO 817, TC86/SC8/WG5, Arlington, VA. Sept. 2003.
6. B. Palm, Ammonia in small capacity refrigeration and heat pump systems, Int. J. of Int. J. of Refrigeration 31 709-715, 2008.
7. IIR Guides, 2008, Ammonia as a refrigerant, Editor: Dr. A.B. Pearson, 3<sup>rd</sup> edition, 2008.
8. Tychsen H. Comparing R-134a Chillers v Packaged Ammonia Chillers for Air Conditioning Applications. International Institute of Ammonia Refrigeration, Albuquerque, 2003.
9. Hrnjak P., Park C.Y., 2007, In-tube heat transfer and pressure drop characteristics of pure NH<sub>3</sub> and CO<sub>2</sub> in refrigeration systems, in: IIR Conference: Ammonia Refrigeration Technology for Today and Tomorrow, Ohrid, 2007.
10. Hrnjak P. Low charge chillers based on microchannel HXs: opportunity for expanding use of ammonia. IIR Conference: Ammonia Refrigeration Technology, Ohrid, 2009.
11. E. Fornasieri, A. Cavallini. Recenti sviluppi delle conoscenze sull'uso dei fluidi operatori nei cicli frigoriferi, Padova, 2004. 44th Convegno internazionale AICARR. Milano. March 3rd-4th. Vol. 1, pp. 631-653.

12. T.B. Jekel, D.T. Reindl, J:m: Fisher. Gravity separator fundamentals and design, IAR 2001. Ammonia Refrigeration Convention and Exhibition.
13. Danilova D.N. et al., 1981, Heat transfer in different plate geometries, Kholod. Tek. 4 (1981), pp. 25-31.
14. Djordjevic E., Kabelac S., 2008, Flow boiling of R134a and ammonia in a plate heat exchanger, International Journal of Heat and Mass Transfer 51 (2008), pp. 6235-6242.
15. Mori H., Yoshida S., Ohishi K., Kakimoto T., 2000, Dryout quality and post-dryout heat transfer coefficient in horizontal evaporator tubes, 3rd European Thermal Sciences Conference (2000), Edizioni ETS, Pisa.
16. Martin H., 1996, A theoretical approach to predict the performance of chevron-type plate heat Exchangers, Chem. Eng. Process. 35 (1996), pp. 301-310.
17. Steiner D., Taborek J., 1992, Flow boiling heat transfer in vertical tubes correlated by an asymptotic model, Heat Transfer Eng. 13 (1992), pp. 43–69.
18. Thonon B., Feldman A., Margat L., Marvillet C., 1997, Transition from nucleate boiling to convective boiling in compact heat exchangers, Int. J. Refrigerat. 20 (8) (1997), pp. 592–597.
19. Friedel L., 1979, Improved friction pressure drop for horizontal and vertical two-phase pipe flow, in: Europ. Two-phase Flow Group Meet, Paper E2, Ispra, 1979.
20. Rouhani SZ, Axelsson E, 1970, Calculation of volume void fraction in the subcooled and quality region, Int. J. Heat and Mass Transfer 13 (1970), pp. 383-393.
21. Wang C., Chi K., Chang C., 2000, Heat transfer and friction characteristics of plain fin-and-tube heat exchangers, Int. J. Heat Mass Transfer 43 (2000), pp. 2693-2700.
22. Gnielinski V., 1976. New equations for heat and mass transfer in turbulent pipe and channel flow, Int. Chem. Eng. 16 (1976), pp.



359e368.

23. Hrnjak P., Park C.Y., 2007, In-tube heat transfer and pressure drop characteristics of pure NH<sub>3</sub> and CO<sub>2</sub> in refrigeration systems, in: IIR Conference: Ammonia Refrigeration Technology for Today and Tomorrow, Ohrid, 2007.
24. Muley A., Manglik R.M., 1999, Experimental study of turbulent flow heat transfer and pressure drop in a plate heat exchanger with chevron plates, *Journal of Heat Transfer*, ASME 121 (1999), pp. 110-117.
25. Churchill S.W., 1977, Friction-factor equation spans all fluid flow regimes, *Chem. Eng.* 7 (1977), pp. 91-92.
26. Powell M.J.D., 1977, Restart procedures for the conjugate gradient method, *Math. Program.* 12 (1977), pp. 241-254.
27. Casson V., Cecchinato L., Del Col D., Fornasieri E., Zilio C., 2002, An innovative model for the simulation of a finned coil evaporator, in: *Proc. 12th Heat Transfer Conference*, (2002), pp. 285-290.
28. Cecchinato L., Corradi M., Fornasieri E., Zamboni L., 2005, Carbon dioxide as refrigerant for tap water heat pumps: a comparison with the traditional solution, *Int. J. Refrig.* 28 (2005), pp. 1250-1258.
29. Cavallini A., Chiarello M., Fornasieri E., Zilio C., 2008, Experimental analysis of carbon dioxide coiled evaporators, in: *8th IIR Gustav Lorentzen Conf. on Natural Working Fluids*, Copenhagen, Denmark, 7-10 September, (2008), pp. 334-341.
30. Cavaioni P., Dal Belin Peruffo G., Fornasieri E., Foroni A., 2005, Design Optimization of Finned Coils as Condensers for R404A, *IIR Conference on Thermophysical Properties and Transfer Processes of Refrigerants*, Vicenza, Italy, 2005.
31. EN 14825:2008, Air conditioners, liquid chilling packages and heat pumps, with electrically driven compressors, for space heating and cooling - Testing and rating at part load conditions, *Comité Européen de Normalisation*, Geneva.



# Chapter 4 **Heat pumps with carbon dioxide working fluid**

This chapter includes two sub-chapters within:

- 4.1) an energy assessment of a heat pump used for winter heating, summer cooling and tap water production;
- 4.2) an experimental analysis of a heat pump working with an ejector as throttling device;

## **4.1 Energy assessment of a carbon dioxide heat pump for residential application**

In this sub-chapter the energy assessment of a water/water carbon dioxide R744 chiller/heat pump, working according to a transcritical cycle, used for winter heating, summer cooling and tap water production is described.

For simplicity reasons, the different functions (heating, cooling, hot water) are managed on the water side and therefore no inversion between the evaporator and gas cooler role is required. The components are easily available on the market.

The climate typical of North Italy is considered.

The analysis of the R744 chiller/heat pump is based on an original simplified method, which is able to predict the energy performance of the unit based only on its performance data at the nominal rating conditions. The method was validated against experimental data. A comparison with a state-of-the-art R410A unit is presented. The monthly analysis shows that the CO<sub>2</sub> unit is very efficient in hot water production, but penalized in heating and cooling

service, so that the total energy consumption in the year is 20% lower for the R410A.

### 4.1.1 Introduction

When Professor G. Lorentzen [1] first revived carbon dioxide as a refrigerant, he presented heat pumps as a privilege application for the CO<sub>2</sub> transcritical cycle.

As a matter of fact, carbon dioxide transcritical cycle is nowadays regarded as an energy efficient option for tap water heat pumps: the gas cooling process well fits the warming up of a finite stream of water, resulting in a quite large temperature lift in water without significant penalisation in COP, as it was clearly demonstrated in the technical literature Neksa et al., 1998 [2] and Neksa, 2002, [3].

The peculiarities of the transcritical cycle require the use of once-through heat exchangers (gas coolers) in association with storage tanks; in this way the best energy performance can be achieved, as it was demonstrated in Cecchinato et al. (2005) [4]. The reason lays on the fact that, whereas for a common cycle the condensation temperature is linked to the water maximum temperature (and so it is for COP), for transcritical cycles energy efficiency is instead strongly linked to the water inlet temperature, Neksa, 2002 [3], Cecchinato et al., 2005 [4].

For the above mentioned reason, as Professor Lorentzen himself [1] pointed out, if the CO<sub>2</sub> heat pump is intended for space heating, modifications to the simple vapour compression transcritical cycle should be put in place to limit the efficiency losses of the cycle. However, if low temperature heating is required, CO<sub>2</sub> might offer an efficient solution, especially if applied to low energy building, as it was recently demonstrated in Heinz et al., 2010 [5].

In order to take advantage from the temperature of the water from the main, solutions with two or three gas coolers in series have been proposed, Stene, 2005 [6]; Heinz et al., 2010 [5], providing simultaneously hot water for the tap

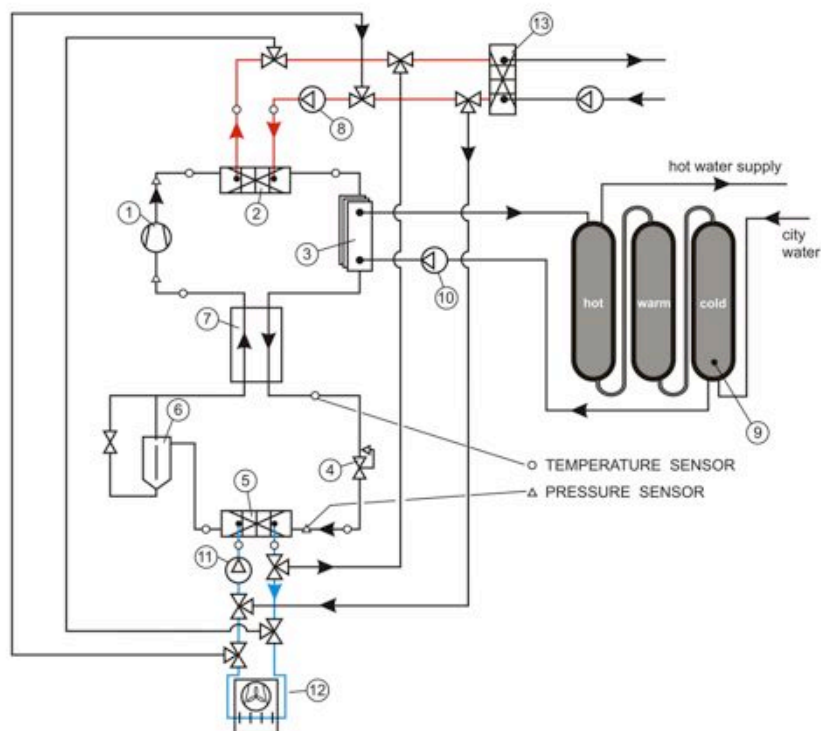
and the heating system. Efficiency of such systems depend very much on the ratio between the tap hot water and heating demand, and their management might result complicated.

In this sub-chapter a simple system where tap hot water and heating are provided alternately is proposed, in order to limit the plant complexity in design and management, as well as its cost. For the same reasons, when cooling is required, no flow inversion is provided in the CO<sub>2</sub> circuit, but every operation is managed on the water side.

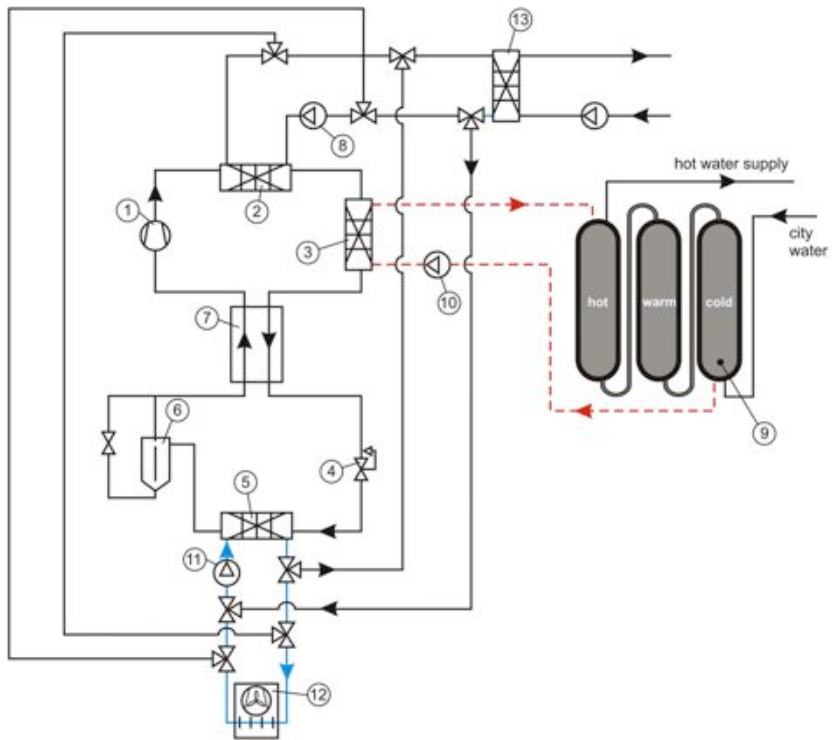
### 4.1.2 System layout

#### Chiller/heat pump

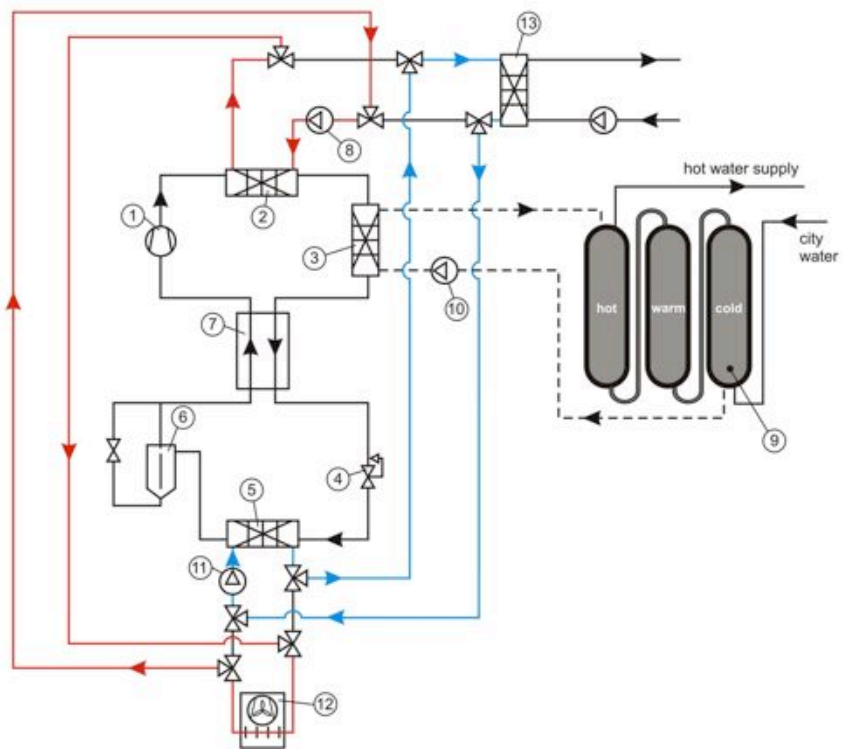
The layout of the chiller/heat pump is presented in Figure 4.1.1.



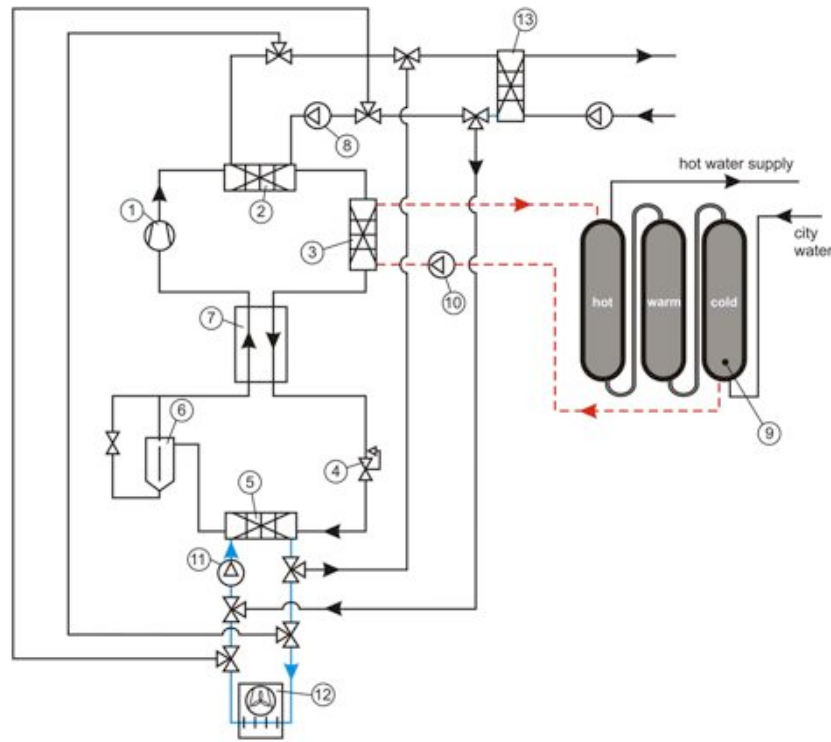
a)



b)



c)



d)

Figure 4.1.1 System layout. a) Winter operations: space heating. b) Winter operations: tap water heating. c) Summer operations: space cooling. d) Summer operations: space cooling and tap water heating.

The compressor (1) is a reciprocating semi-hermetic one, with swept volume per unit time of  $1.5 \text{ m}^3 \text{ h}^{-1}$ . An inverter allows capacity modulation. The overall compression efficiency  $\eta_{ic}$  and the volumetric efficiency  $\eta_v$  were provided by the manufacturer and they are expressed, as functions of the pressure ratio  $R_p$ , by the equations (4.1.1) and (4.1.2), which are valid for pressure ratios ranging from 1 to 5.5:

$$\eta_{ic} = -4 \cdot 10^{-15} \cdot R_p^4 + 6 \cdot 10^{-14} \cdot R_p^3 - 0.0137 \cdot R_p^2 + 0.0664 \cdot R_p + 0.5168 \quad (4.1.1)$$

$$\eta_v = -2 \cdot 10^{-14} \cdot R_p^4 + 2 \cdot 10^{-13} \cdot R_p^3 + 0.0037 \cdot R_p^2 - 0.1314 \cdot R_p + 1.1118 \quad (4.2.2)$$

Two brazed plate heat exchanger gas coolers are installed after the compressor. The first one (2) is intended for serving a low-temperature floor heating system, while the second one (3) provides hot water for the tap system; gas cooler is a double-wall plate heat exchanger, to avoid any water contamination in case of failure, Fornasieri et al., 2010 [7]. The gas coolers work alternatively, as it will be explained in next section. For this reason, during laboratory testing, only one double plate gas cooler was installed and tested both at heating and tap water production working conditions. The expansion device (4) is an electronically controlled step motor valve.

A brazed plate heat exchanger (5) is used as the evaporator. A low pressure receiver (6) is located at the evaporators exit. Evaporator overfeeding, as well as lubricant recovery to the compressor, are provided by continuous liquid and oil removal from the bottom of the low pressure receiver (6); the liquid exiting from the receiver (6) is completely evaporated in the suction gas heat exchanger (7), which is a coaxial type heat exchanger.

### ***Water system***

The water circuit, as it was designed for the utilization, is represented in Figure 4.1.1.

The heat pump produces hot water for the tap system, as well as hot or cold water for winter heating and summer cooling respectively. In order to avoid CO<sub>2</sub> flow inversion, which would result in system complexity, all operations are managed on the water side. Two and three-ways valves are installed in the water circuit to switch from one operation to another. Basically, during the wintertime, the heat pump uses the external air as the heat source and rejects heat to the heating system; both heat exchanges use a water loop as intermediate medium. External air is used as the heat source also for tap hot water production; tap water is heated in the gas cooler without any intermediate fluid, thanks to the double plate heat exchanger.



During the summertime, water from the cooling system represents the heat source, while heat is rejected to the external ambient.

### ***Winter operations***

During the wintertime when space heating is required, (Fig 1a), the pump (8) makes the water circulate into the gas cooler (2), thus warming up; heat is rejected to the heating system at the plate heat exchanger (9).

The water heating system is uncoupled from the gas cooler, since the secondary fluid at the compression circuit is an antifreeze mixture.

The gas cooler (2) water loop works with constant water flow.

The tap water heating system, (Fig 1b), includes three storage water tanks (9), connected in series (bottom to top, going from hottest to coldest) to avoid mixing between cold and hot water. The cold water drawn from the bottom of the colder tank feeds the gas cooler (3), while the hot water exiting from the gas cooler (3) is introduced at the top of the hottest tank, where it is drawn for consumption. This system is planned for operating with thermal storage; during the loading period, the surface separation between hot and cold water moves toward the bottom of the tank and then moves inside the next colder tank, whereas in the unloading period this surface moves in the opposite way. A variable speed pump (10) is used for tap water, so that a constant water delivery temperature can be maintained. As described by Minetto [8], there exist infinite couples of water mass flow and gas cooler pressure that satisfy the constrain of fixed water delivery temperature. An adaptive control adjusts the upper pressure value close to the one required for the maximum COP.

The external air is used as heat source, via a water loop, where a pump (11) makes the water to circulate from the external coil (12), where it absorbs heat, to the evaporator (5).

When space heating is required, no hot water production takes place. Tap hot water is loaded when no heating is required; temperature sensors are

located in each tank (9), so that, if the hot water level decreases too much, space heating is stopped and tap water is heated up.

### **Summer operations**

During the summertime, when space cooling is required, (Fig 1c), the pump (11) makes the water to circulate into the evaporator, thus cooling down the intermediate water, which flows to the plate heat exchanger (13), thus cooling down the water of the cooling system. If hot water is required (Fig 1d), heat is rejected via gas cooler (3); otherwise, it is rejected outside by means of gas cooler (2), water pump (8) and finned coil heat exchanger (13).

The design conditions for winter and summer operations are summarized in Table 4.1.1.

	External temperature [°C]	Water temperature to heating/cooling system [°C]	Heating/cooling capacity [kW]	Hot water at gas cooler inlet [°C]	Hot water heating power [kW]
Winter	-5	30	4.65	36.0	4.65
Summer	31	14	4.83	47.8	6.49

*Table 4.1. Design conditions for winter and summertime.*

### **4.1.3 Test facility**

The water circuit arranged for the tests simply consists of two water tanks, initially filled with water from the public system. Water, drawn from the bottom of each tank enters the gas cooler and the evaporator. The hot water from the gas cooler and the cold one from the evaporator can be either discharged into the drain or partly mixed inside the tanks if higher or lower water temperature is needed for testing purposes. A connection between the tanks allows further temperature regulation.

The heat pump and the water circuit were equipped with temperature and pressure sensors, as indicated in Figure 4.1.1-a. Temperature and pressure

measurements were acquired with an Agilent 34970A data logger equipped with two 34901A-20-channel modules.

Copper-constantan thermocouples (T-type) were used as temperature sensors. The estimated accuracy of the entire temperature measurement system is  $\pm 1.5$  °C.

Pressures were measured at the suction and discharge sides of the compressor. Two pressure sensors (Huba Control OEM relative pressure transmitters) were used, with the following measuring ranges: 0÷160 bar (discharge pressure) and 0÷60 bar (suction pressure). The accuracy of the pressure transducers is  $\pm 0.5\%$  FS.

The water flow rates were manually measured by means of a domestic water meter for ten minutes with an estimated average accuracy of  $\pm 0.02$  m<sup>3</sup> h<sup>-1</sup>.

#### **4.1.4 Experimental results**

The unit was tested under different values and mass flow rates of water entering both gas cooler and evaporator, corresponding to the operating conditions for tap water heating, space heating and cooling; high pressure was varied in order to identify the optimal working pressure. The experimental results were used to calibrate the simulation model of the system that provides the energy consumption along the year.

#### **4.1.5 Chiller/heat pump model**

In order to evaluate the energy consumption, an original in-house developed mathematical model providing an accurate estimation of cooling or heating capacity and power consumption out of nominal rating conditions was adopted, Cecchinato et al., 2011 [9].

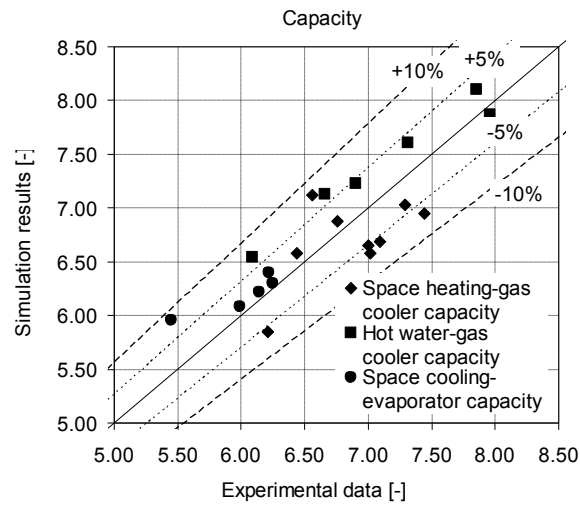
The chiller/heat pump unit was simulated with the code [9], based on a mathematical model able to predict the unit cooling or heating capacity and power consumption at different heat exchangers secondary fluids inlet temperatures only on the basis of the performance data at the nominal rating conditions. The efficiency of vapour compression chillers and heat pumps depends strongly on the temperature levels of the external sources and on the unit capacity control system. Moreover, considering vapour compression cycles adopting carbon dioxide as the refrigerant fluid, high pressure is an independently cycle controlled variable. Cecchinato et al., 2010 [10] and Cecchinato et al., 2011 [9] proposed a mathematical model providing an accurate estimation of chillers and heat pumps cooling or heating capacity and power input. This model does not require the knowledge of a large amount of geometric parameters and characteristics of the machine components since the performance evaluation is made out from nominal rating conditions. The proposed procedure essentially calculates heat exchangers design transmittance. For different secondary fluid temperature, the thermodynamic cycle operating conditions are calculated correcting the design transmittances to take into account the heat transfers coefficients variations associated to refrigerant and secondary fluid mass flow rates variations. The heat exchangers transmittance correction technique accounts also for the heat transfers coefficients dependence from carbon dioxide thermodynamic properties, which vary considerably during the overall gas cooling process. Further details can be found in Cecchinato et al. (2010) [10] and Cecchinato et al. (2011) [9].

The model was validated against experimental data, as presented in Table 4.1.2.

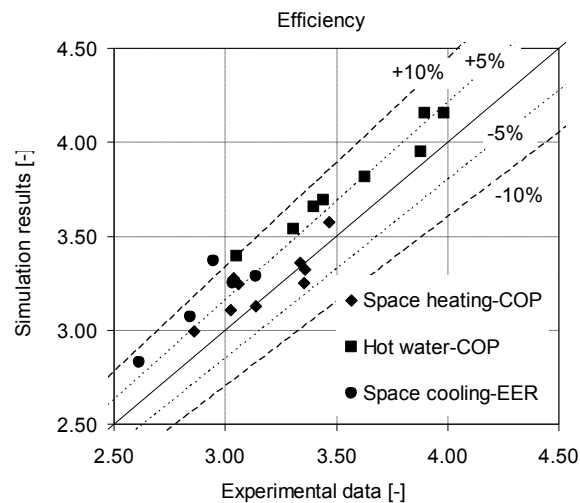
SPACE HEATING		H1	H2	H3	H4	H5	H6	H7	H8	H9
Water mass flow -gas cooler	kg s <sup>-1</sup>	0.200	0.200	0.200	0.200	0.200	0.090	0.090	0.090	0.114
Water mass flow -evaporator	kg s <sup>-1</sup>	0.476	0.476	0.476	0.476	0.476	0.476	0.476	0.476	0.476
Discharge pressure	10 <sup>5</sup> Pa	82.6	91.4	100.6	112.6	100	90.2	98.9	108.4	85.4
Evaporation temperature	°C	0.3	-0.4	-0.1	0.8	-0.6	0.4	1.0	1.2	-0.1
T water in gas cooler	°C	32.4	31	31.6	30.6	27.4	29.2	29.3	28.5	28.1
T water out gas cooler	°C	39.8	39.4	40	39.3	36.3	46.3	47.3	45.9	42.7
T water in evaporator	°C	4.2	4.1	4.2	5	3.7	4.4	5	5.4	4.4
Heating power	kW	6.21	7.02	7.09	7.29	7.44	6.44	6.76	6.56	7.00
Power input	kW	1.85	2.09	2.26	2.55	2.45	1.93	2.21	2.17	2.02
COP	-	3.36	3.36	3.14	2.86	3.04	3.34	3.06	3.02	3.47
SPACE COOLING		C1	C2	C3	C4	C5				
Water mass flow -gas cooler	kg s <sup>-1</sup>	0.105	0.105	0.105	0.105	0.105				
Water mass flow -evaporator	kg s <sup>-1</sup>	0.476	0.476	0.476	0.476	0.476				
Discharge pressure	10 <sup>5</sup> Pa	82.6	85.6	90.5	93.9	100.5				
Evaporation temperature	°C	6.1	5.8	8.5	7.9	6.0				
T water in gas cooler	°C	26.5	26.4	26.5	26.9	27.6				
T water in evaporator	°C	10.4	10.3	11.4	10.8	10.7				
T water out evaporator	°C	7.7	7.3	8.2	7.6	7.6				
Cooling power	kW	5.45	5.99	6.4	6.3	6.14				
Power input	kW	1.85	1.91	1.97	2.05	2.35				
EER	-	2.95	3.14	3.25	3.07	2.61				
HOT WATER		HW1	HW2	HW3	HW4	HW5	HW6	HW7	HW8	
Water mass flow -gas cooler	kg s <sup>-1</sup>	0.030	0.030	0.030	0.030	0.045	0.045	0.045	0.045	
Water mass flow -evaporator	kg s <sup>-1</sup>	0.48	0.48	0.48	0.48	0.48	0.48	0.48	0.48	
Discharge pressure	10 <sup>5</sup> Pa	81.4	89.4	98.8	108.0	80.7	89.5	99.8	107.3	
Evaporation temperature	°C	3.1	3.6	4.0	4.2	5.2	5.6	5.5	5.3	
T water in gas cooler	°C	14.6	14.6	14.8	15.3	16.8	16.2	16.1	16.0	
T water out gas cooler	°C	63.1	67.6	73.0	78.7	53.4	57.9	60.8	62.3	
T water in evaporator	°C	6.7	7.5	8.1	8.3	9.1	9.9	10.3	10.7	
Heating power	kW	6.09	6.66	7.31	7.96	6.90	7.85	8.42	8.71	
Power input	kW	1.77	1.96	2.21	2.61	1.77	1.97	2.17	2.40	
COP	-	3.44	3.40	3.31	3.05	3.90	3.98	3.88	3.63	

Table 4.2. Experimental results.

Figures 4.1.2-a and 4.1.2-b show the simulated gas cooler capacity and COP, for space heating and hot water heating, and evaporator cooling power and EER in the case of space cooling, as functions of the measured values. 100% of the predicted cooling and heating capacity and 90% of COP and EER values are consistent with the measured data within a relative deviation of  $\pm 10\%$ .



a)



b)

Figure 4.1.2 Model validation. a) Simulated gas cooler capacity (space cooling and hot water production) and evaporator capacity (space cooling) as functions of experimental values, as reported in Table 4.1.2. b) Simulated COP (space cooling and hot water production) and EER (space cooling) as functions of experimental values, as reported in Table 4.1.2.

The chiller/heat pump, whose cooling and heating capacity at nominal conditions are summarised in Table 4.1.1, was simulated under different temperature values of water entering the gas cooler and the evaporator; the

influence of gas cooler pressure was considered, in order to find out the optimal high pressure at each working condition.

The P-NTU approach Shah and Sekulić, 2003 [11] was applied to heat exchangers (12, Figure 4.1.1) and (13, Figure 4.1.1) to correlate the external temperature and heating/cooling system temperature to the gas cooler and evaporator water temperature.

The heat pump/chiller simulation produced polynomial expressions for calculating cooling and heating capacity and power input at different working conditions.

#### **4.1.6 Building model**

A seasonal dynamic building energy simulation was carried out in the climate of Treviso (Northern Italy). The building was simulated with a commercial code, US Department of Energy, 2009 [12].

A two floor residential building was simulated; the total area is 115.84 m<sup>2</sup>; the longest dimension is east oriented. Total windows surface is 20.18 m<sup>2</sup>; the overall heat transfer coefficient of external wall, floor, roof and windows was respectively 0.29, 0.335, 0.215 and 3.094 W m<sup>-2</sup>K<sup>-1</sup>.

Simulations were based on Treviso test reference year; Treviso is a town located in the North-Est of Italy (North 45° 40', Est 12° 15').

In summertime, the air conditioning set point is 26°C, while in the wintertime the set point for ambient heating is 18°C. Air change rate is assumed to be 40 l/s, which corresponds to the need of 4 persons.

The building was simulated with EnergyPlus (US Department of Energy, 2009) [12] to calculate at hourly intervals the thermo-hygrometric variables and the thermal energy exchanged.

The peak heating load was 4.65 kW on January, 15<sup>th</sup>, while the maximum cooling demand, 3.97 kW, was registered on July 15<sup>th</sup>.

The hourly hot water demand profile was modelled according to Jordan and Vajen, 2001 [14]. An average daily water consumption of  $143 \cdot 10^{-3} \text{ m}^3$  at  $45^\circ\text{C}$  was assumed, which corresponds to the need of 4 persons, according to UNI TS 11300 [15]. In the wintertime, hot water production at  $70^\circ\text{C}$  occurred during the night, unless the daily consumption was higher than the water storage capacity; in this case the hot water was produced also during the day. In the summertime, hot water was produced when space cooling was required, thus completely recovering the gas cooler heat. When no major cooling or heating was needed, hot water was produced during the day, thus taking benefit from warm external air.

Figure 4.1.3 represents the month energy requirement for heating, cooling and hot water production.

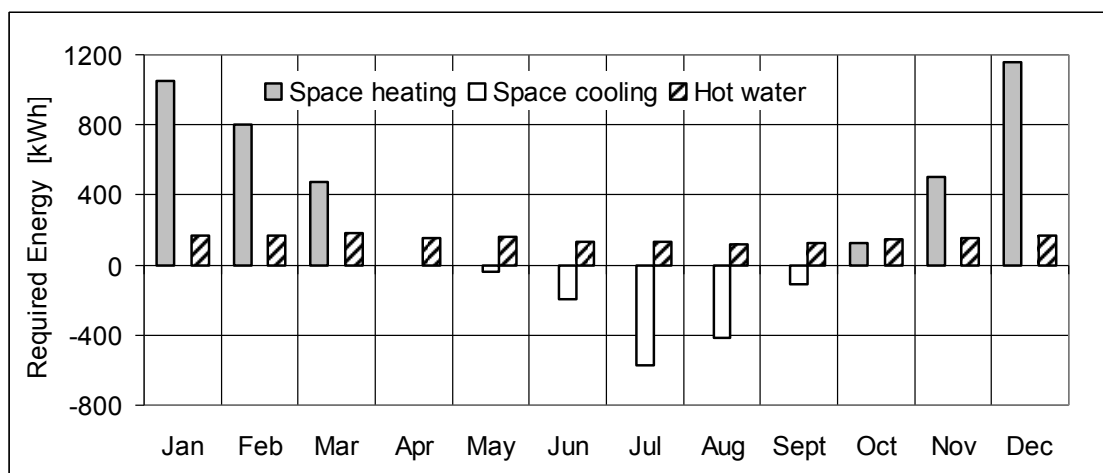


Figure 4.1.3 Month energy requirement for heating, cooling and hot water production.

The hourly building load was matched to the heat pump/chiller performance curves, to find out, hour by hour, the energy consumption required to satisfy the load.

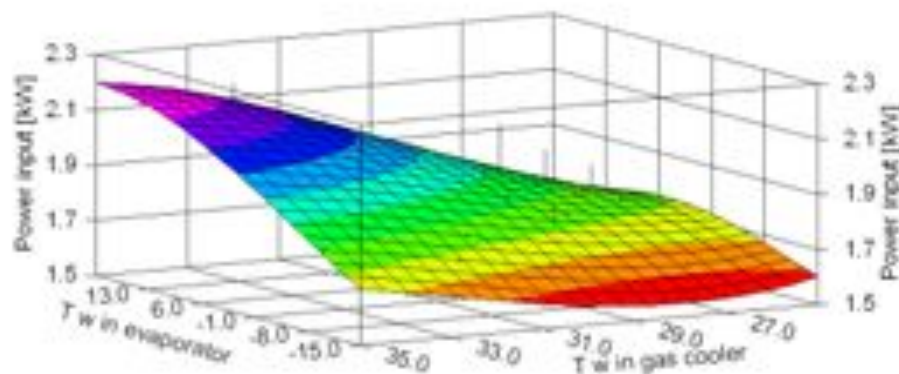


### 4.1.7 Simulation results

#### *Heat pump/chiller*

The heat pump/chiller simulation produced polynomial expressions for calculating cooling and heating capacity and power input at different working conditions at the optimal high pressure values.

Figures 4.1.4-a and 4.1.4-b represent the correlation between the water inlet temperature to the evaporator and the gas cooler and the unit power input and heating capacity when space heating is activated. Water mass flow rates were  $0.45$  and  $0.12 \text{ kg s}^{-1}$  respectively at the evaporator and gas cooler.



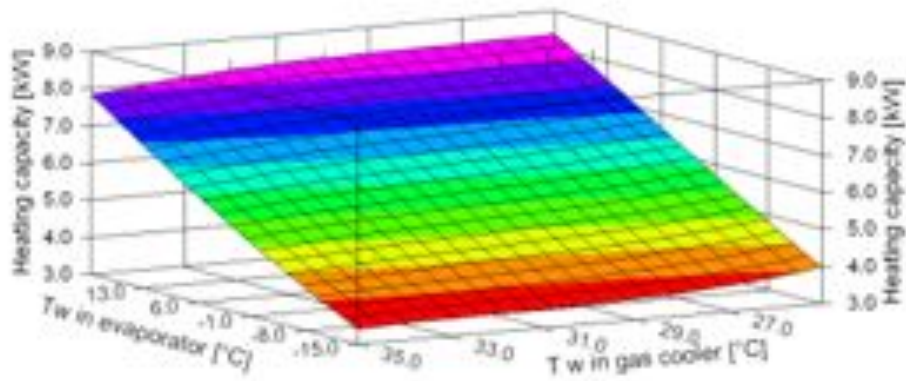


Figure 4.1.4 a) Power input as a function of gas cooler and evaporator water temperature (space heating). b) Heating capacity as a function of gas cooler and evaporator water temperature (space heating).

Similar expressions were derived also for space cooling, at for 0.45 and 0.12  $\text{kg s}^{-1}$  water mass flow rates at the evaporator and gas cooler and tap water heating, with delivery temperature at 70°C and evaporator water mass flow rate 0.45  $\text{kg s}^{-1}$ .

The polynomial expressions maximum standard deviation of residual is 1.504.

### *Energy consumption*

Figure 4.1.5 shows the month energy consumption and overall efficiency for space heating, cooling and hot water production.

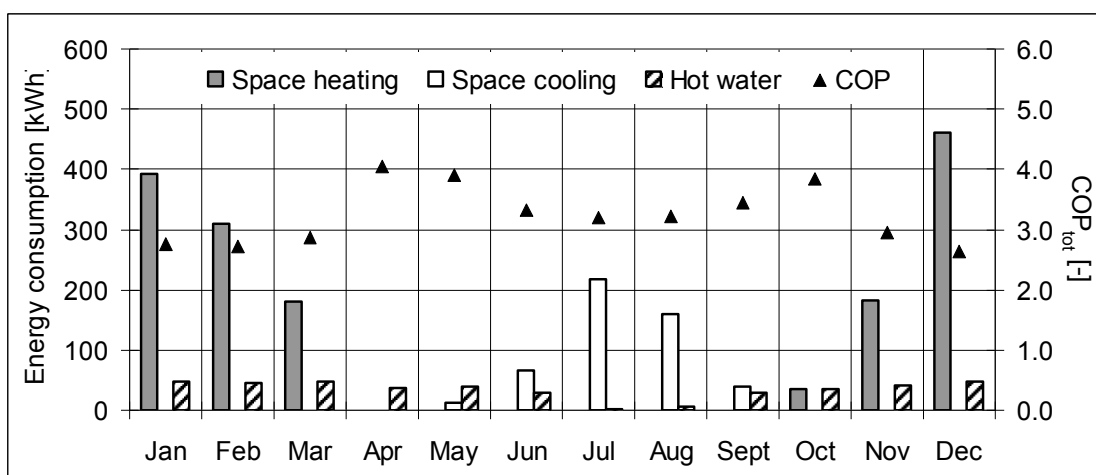


Figure 4.1.5 COP<sub>tot</sub> and energy consumption for space heating, cooling and hot water production.

In order to benchmark the CO<sub>2</sub> chiller/heat pump with current technology, a typical R410A unit on the market was simulated at the same conditions. The unit is a traditional air/water heat pump, where cycle is reversed in the summertime for the cooling service

The R410A heat pump/chiller was simulated according to Cecchinato et al. [10], coherently with the CO<sub>2</sub> unit.

Table 4.1.3 summarises CO<sub>2</sub> and R410A results, showing energy consumption and overall efficiency month by month.

Month	Energy Consumption [kWh]						COP <sub>tot</sub> [-]	
	CO <sub>2</sub>			R410A			CO <sub>2</sub>	R410A
	Space heating	Space cooling	Hot water	Space heating	Space cooling	Hot water	COP <sub>tot</sub>	COP <sub>tot</sub>
Jan	392.2		51.5	284.1		69.1	2.77	3.45
Feb	308.9		50.9	217.8		66.8	2.72	3.39
Mar	180.1		48.1	131.0		71.9	2.87	3.23
Apr			37.5			54.8	4.05	2.77
May		13.4	38.5		5.8	55.1	3.90	3.34
Jun		67.1	30.0		28.2	42.0	3.32	4.59
Jul		218.0	3.0		86.0	40.7	3.19	5.56
Aug		160.0	5.3		61.6	36.6	3.22	5.43
Sept		39.6	29.0		16.3	41.7	3.46	4.08
Oct	34.8		35.3	35.1		52.2	3.83	3.08
Nov	181.8		42.0	137.2		60.3	2.94	3.33
Dec	460.2		52.7	313.7		69.3	2.63	3.49
Seasonal	1557.9	498.1	423.9	1118.8	197.9	660.5	2.93	3.67

Table 4.3. CO<sub>2</sub> vs. R410A energy consumption and overall efficiency.

During the springtime and in the Autumn when the hot water production mainly influences the  $COP_{tot}$ ,  $CO_2$  strongly overcame R401A, achieving a peak  $COP_{tot}$  of 4.05 vs 2.77 in April; during summertime when hot water is required, the  $CO_2$  chiller/heat pump took the double benefit of operating with cold water from the main at the gas cooler inlet, thanks to the stratification tank concept, thus producing hot water almost for free, thanks to total heat recovery. However,  $CO_2$  is penalised both during the wintertime and the summertime, when space heating or cooling is required; as a consequence, the total energy consumption in the year was 20% lower for the R410A unit in comparison with the  $CO_2$ .

The penalisation mainly concerns gas cooler operation close to the critical temperature, when the efficiency of the transcritical cycle rapidly deteriorates; moreover, in the chosen design, in the summertime the  $CO_2$  unit rejects heat via the water loop, thus further increasing the gas cooler outlet temperature.

The double compression and expansion cycles Cecchinato et. al, 2009 [15] or the use of the ejector might mitigate the problem Boulawz Ksayer E.et al., 2007 [16].

Although the R410A chiller efficiency, which operates accordingly to a subcritical cycle, can hardly be approached by a simple transcritical cycle, the intrinsic inefficiency of the transcritical cycle at high ambient temperature was quite limited.

### **4.1.8 Conclusions**

A simple concept of transcritical refrigerant circuit for multi-purpose application (low/high temperature heating and cooling) is presented. Its strong point is no need for cycle inversion, since the inversion of heating/cooling service is accomplished water side; this means reliable operations, simple design and easily available components.

However the dark side is the impossibility of direct heat exchange between the refrigerant and the process fluid, because an antifreeze mixture always is

used as intermediate fluid and this involves a loss in energy efficiency. In spite of this penalisation the COP is still acceptable, even if it is lower than that expected with a traditional system. Hot water heating is always more energy efficient in CO<sub>2</sub> system, but not enough to compensate for the loss during heating and cooling service.

It is interesting to change the climate by choosing a north Europe place and a hot and humid climate and then make the same building analysis and comparison with traditional unit. Another option is changing the building type, a hotel should be interest because it has a greater ratio between the tap water and the space heating/cooling thermal powers.

In reference to the use of an ejector as throttling device instead the valve, some experimental tests were made, they are detailed in the next sub-chapter.

#### **4.1.9 Reference**

1. G. Lorentzen. Revival of carbon dioxide as a refrigerant. 1994 Int. J. Heat Mass Transfer Vol.17 (5), 1994, pp. 292-301.
2. Neksa, P., Rekstad, H., Zakeri, G. R. and Schiefloe, P. A. CO<sub>2</sub>-Heat Pump Water Heater: Characteristics, System Design and Experimental Results. Int. Journal of Refrigeration. Vol. 21, 1998, pp. 172-179.
3. Neksa P. CO<sub>2</sub> heat pumps systems. Int. J. Refrigeration. Vol. 25, 2002, pp. 421-427.
4. L. Cecchinato, M. Corradi, E. Fornasieri, L. Zamboni. Carbon dioxide as refrigerant for tap water heat pumps: a comparison with the traditional solution. International J. of Refrigeration. Vol. 28, 2005, pp. 1250–1258.
5. Heinz A., Martin K., Rieberer R., Kotenko O. Experimental analysis and simulation of an integrated CO<sub>2</sub> heat pump for low-heating-energy buildings, *9th IIR Gustav Lorentzen Conference*, 2010. Sydney, Australia.

6. Stene J., 2005 Residential CO<sub>2</sub> heat pump system for combined space heating and hot water heating. *International J. Refrigeration*. Vol. 28, 2005, pp. 1259-1265.
7. Fornasieri E., Girotto S., Mancini F., Minetto S. A carbon dioxide domestic hot water heat pump with double wall plate heat exchanger gas cooler, *9th IIR Gustav Lorentzen Conference*, 2010. Sydney, Australia.
8. Minetto S. Theoretical and experimental analysis of a CO<sub>2</sub> heat pump for domestic hot water. *International J. of Refrigeration*. Vol. 34, 2011, pp. 742-751.
9. Cecchinato L., Corradi M., Minetto S. A simplified method to evaluate the energy performance of CO<sub>2</sub> heat pump units, submitted to *Int. J. of Thermal Sciences*, 2011.
10. Cecchinato L., Chiarello M., Corradi M. A simplified method to evaluate the seasonal energy performance of water chillers, *Int. J. of Thermal Sciences*. Vol. 49, 2010, pp. 1776-1786.
11. Shah R.K., Sekulić D.P., *Fundamentals of heat exchanger design*, 1st edition, New York; Wiley, 2003.
12. US Department of Energy, Energy Plus-version 4.0.0, <http://apps1.eere.energy.gov/buildings/energyplus/>, 2009.
13. Jordan U., Vajen K. Realistic Domestic Hot-Water Profiles in Different Time Scales, *IEA SHC Task 26: Solar Combisystems*. [solar@physik.uni-marburg.de](mailto:solar@physik.uni-marburg.de). 2001.
14. UNI TS 11300. Italian application of UNI EN ISO 13790, 2008.
15. Cecchinato L., Chiarello M., Corradi M., Fornasieri E., Minetto S., Stringari P., Zilio C.. Thermodynamic analysis of different two-stage transcritical carbon dioxide cycles, *International Journal of Refrigeration*. Vol. 32, 2009, pp. 1058-1067.
16. Boulawz Ksayer E., Clodic D., 2007 CO<sub>2</sub> ejector refrigeration cycle. Design, Tests and results. *22° IIR Int. Cong. of Refrigeration, Beijing, China*, August 21-26.

## **4.2 Experimental analysis of a R744 heat pump with an ejector**

In this sub-chapter the experimental analysis of a prototype R744 water/water heat pump which was equipped with a two-phase ejector is described.

According to the traditional lay-out, the energy that was recovered from the expansion process inside the ejector improved the circulation of refrigerant through the evaporator. The same heat pump was also provided with a back-pressure valve as the expansion device, i.e. a direct comparison of the performance was possible between the heat pump systems, either equipped with the ejector or the expansion valve.

The Enex S.r.l. company has made the heat pump available and hosted the experimental activities, it is gratefully acknowledged.

### **4.2.1 Introduction**

Applying a transcritical R744 ejector in the refrigeration system is one of the most promising methods to increase the system efficiency and reduce the throttling losses. In addition, the ejector simplicity of construction (no moving parts), its low cost and reasonable efficiency make it close to practice. Therefore, a great effort has been devoted to theoretical and experimental evaluation of two-phase ejector performance, with respect to geometrical parameters and to its impact on the COP of transcritical CO<sub>2</sub> cycles, as already illustrated by Li and Groll [1], Deng et al. [2], Elbel and Hrnjak [3] and Elbel [4].

The work presented is based on former investigations illustrated by Zha et al. [5], Drescher et al. [6], Drescher et al. [7], Banasiak et al. [8], where the development of the ejector is illustrated and a very good COP improvement

potential for the R-744 transcritical process employing the two-phase ejector was determined.

Tests were performed to evaluate the performance when the heat pump produced hot tap water, i.e. heating water from the main waterworks temperature to storage temperature ( $\sim 60^{\circ}\text{C}$ ). Additionally, an investigation took place to understand how the system performed when space heating was required, i.e. providing hot water with a limited temperature lift, however at relatively high inlet temperatures.

Experiments demonstrated that the ejector is helpful to improve the heat pump performance, thus promoting the diffusion of R744 units also for domestic space heating and air conditioning

However, further work still has to be done to investigate the effect of the ejector in final installations, where technological issues, such as lubricant circulation and recovery, and specific design of the circuit need to be faced.

### **4.2.2 Heat pump and ejector design**

A prototype  $\text{CO}_2$  heat pump using a back pressure valve as the expansion device was modified and equipped with a two-phase ejector.

The heat pump nominal heating power is 5.5 kW at  $0^{\circ}\text{C}$  evaporation temperature, 100 bar gas cooler pressure,  $35^{\circ}\text{C}$  gas cooler outlet temperature.

The basic requirement of minimizing the impact on the original system was met with pipe deviations and ball valves. The low pressure receiver, which was part of the original system, was not modified. This choice brought about some problems about oil recovery that will be described later in the manuscript.

The lay-out of the system is represented in Figures 4.2.1-a and 4.2.1-b.



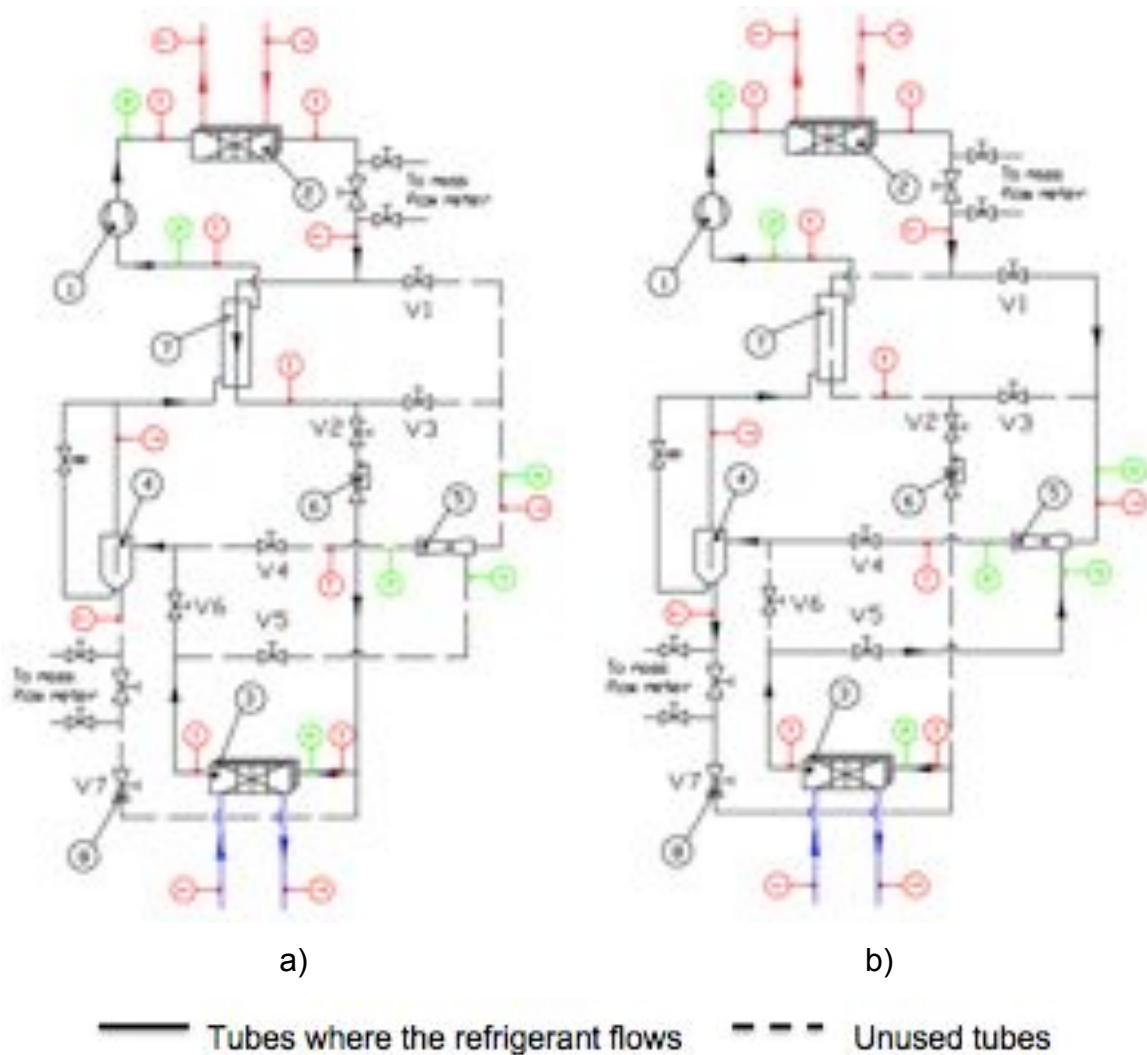
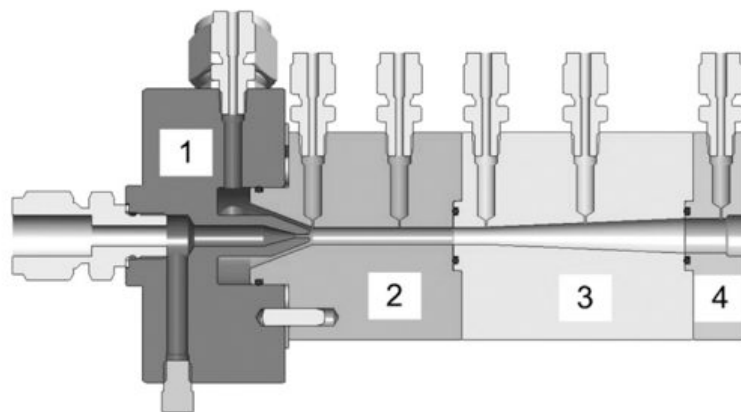


Figure 4.2.1 Heat pump layout a) back pressure valve working. b) ejector working.

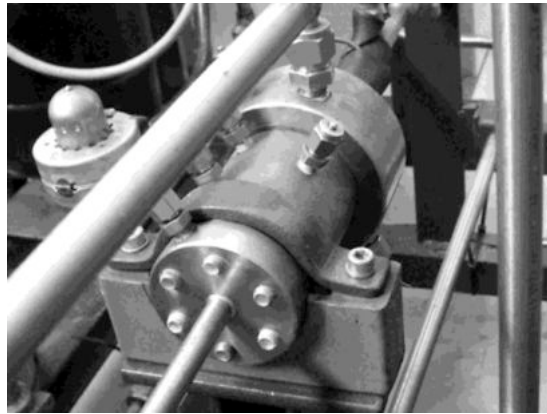
A reciprocating semi-hermetic compressor (1) with swept volume of  $1.46 \text{ m}^3\text{h}^{-1}$  was installed. The gas cooler (2) is a double-wall plate heat exchanger, with heat transfer area equal to  $0.74 \text{ m}^2$ . The evaporator (3) is a plate heat exchanger with heat transfer area equal to  $0.98 \text{ m}^2$ . A liquid receiver (4) is located after the evaporator. The ejector (5) was installed between the gas cooler (2) and the low pressure receiver LPR (4), sucking refrigerant from the evaporator (3). An electronic expansion valve (6), which can be controlled according to a back pressure logic, was positioned in parallel to the ejector, so that the system can be run as a traditional back pressure valve, low

pressure receiver circuit; in this case, liquid, together with oil, is removed from the low pressure receiver and evaporated in the internal heat exchanger IHX (7), thus assuring evaporator overfeeding, while preventing liquid flow-back to the compressor. When the ejector is used, the back pressure valve and the internal heat exchanger are by-passed. CO<sub>2</sub> from the gas cooler (2) flows to the ejector motive port (5); two phase refrigerant out of the ejector is collected into the LPR (4), where liquid, together with oil, is removed from the bottom, through the evaporator, to the ejector suction port. A regulation valve (8) can be manually adjusted to modify the flow resistance of the ejector suction line circuit.

The CO<sub>2</sub> 2-phase ejector section is represented in Figure 4.2.2-a, while Figure 4.2.2-b is a picture of the ejector in the final installation.



a)



b)

Figure 4.2.2 a) Ejector section, b) Ejector in the heat pump installation.

The installed ejector is a prototype made up of four parts (A, B, C, D) joint together; the modular concept allows different assembly configurations and was developed at Sintef Energy Research for laboratory purposes. However, in the heat pump installation dimensions are fixed and parts are not replaced. In the ejector there are no moving parts.

The examined motive nozzle geometry consists of two conical ducts bored in a steel cylinder arranged in a converging-diverging channel; the throttle cross-section is 0.7 mm.

The mixing section was designed as a straight tube with a conical inlet, which in combination with the motive nozzle head created a suction nozzle. The internal diameter of the channel is equal to 2 mm, and the length of the passage is equal to 10 mm.

The diffuser was shaped as a conically diverging channel with an outlet diameter equal to 6 mm.

The simplified circuit, when the ejector is active, is shown in Figure 4.2.3-a, while the corresponding thermodynamic cycle is represented in the  $p-h$  diagram of Figure 4.2.3-b.

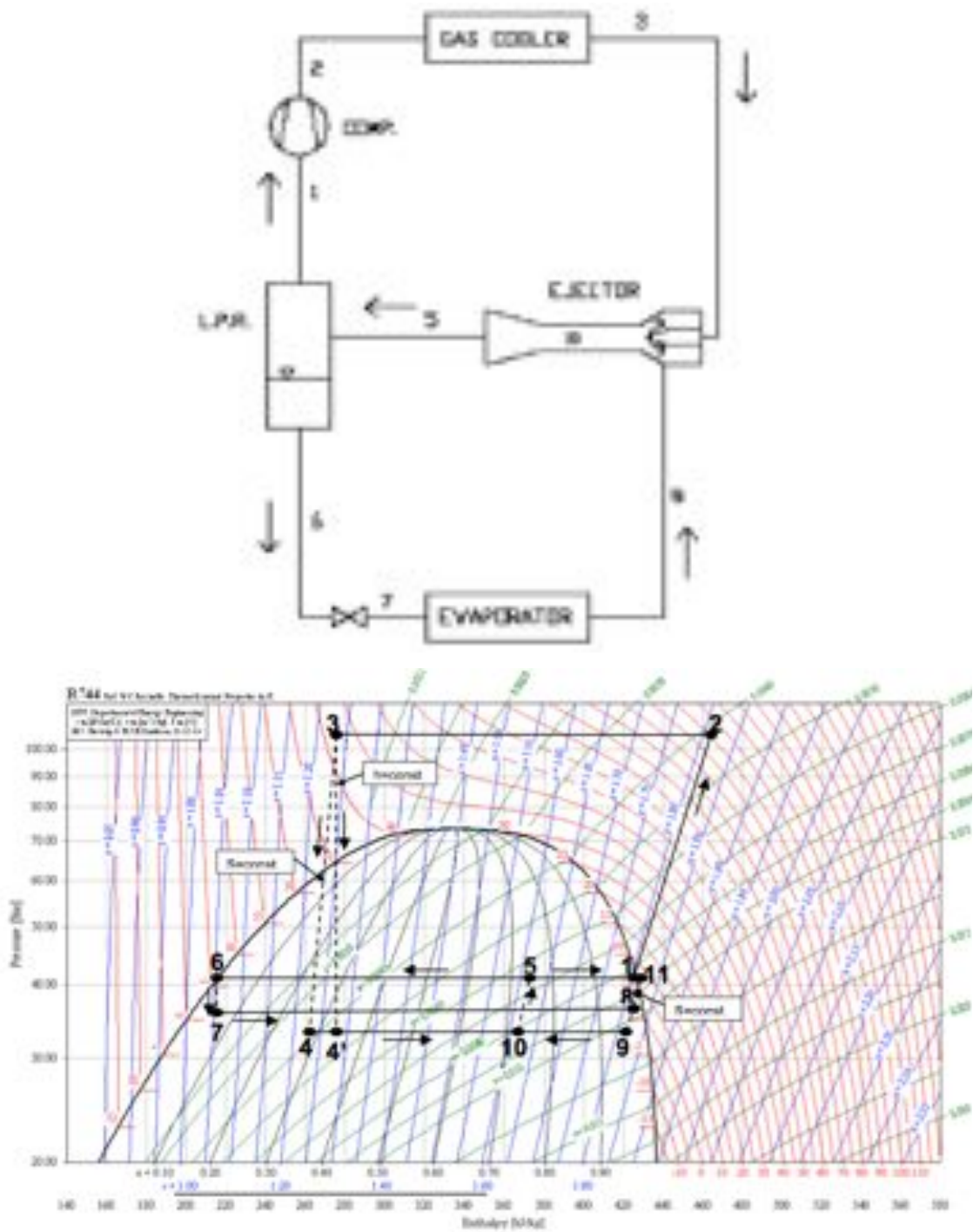


Figure 4.2.3. a) Simplified ejector lay-out. b) Ejector cycle in the p-h diagram.

### 4.2.3 Test rig

For testing purpose, a water circuit was assembled. A water tank was dedicated to the gas cooler: a variable speed pump forced the water through the gas cooler; water coming from the gas cooler can be either poured back into the tank or drained off.

A second tank was installed to provide water to the evaporator; the centrifugal pump is equipped with continuous speed control. Cold water coming from the evaporator can come back to the tank or be drained off; hot water from the gas cooler tank can be transferred to the evaporator tank when necessary.

The heat pump and the water circuit were equipped with temperature and pressure sensors located as shown in Figure 4.2.1.

Copper-constantan thermocouples (T type) were used as temperature sensors. The estimated accuracy of the entire temperature measurement system is  $\pm 0.5$  °C

Pressures were measured at the suction and discharge sides of the compressor and in six sections of the ejector. The maximum deviation of pressure transmitters is  $0.06 \cdot 10^5$  Pa.

Two refrigerant mass flow meters with a nominal flow of  $0.167 \text{ kg s}^{-1}$  were installed out of the gas cooler and out of the LPR to the evaporator (when the ejector was active); their maximum deviation was  $\pm 0.14\%$  of their readings.

Water flow rate to the gas cooler and to the evaporator was measured with an accuracy of  $\pm 0.14\%$  of the reading.

Electric power to the compressor was acquired with 1% accuracy of the reading of full scale.

#### 4.2.4 Experimental results and discussion

Tests in the ejector configuration (Figure 4.2.1-b and Figure 4.2.3.a) aimed at describing both the ejector and the heat pump performance.

The parameters that were used to characterise the ejector were the mass entrainment ratio  $F$  and the suction pressure lift  $\Delta p$ , where  $F$  is the ratio between the suction mass flow rate, that circulates at the evaporator, and the motive mass flow rate, i.e. the mass flow rate out of the gas cooler and  $\Delta p$  indicates the relative pressure increase by the ejector.

$$\Phi = \frac{\dot{m}_8}{\dot{m}_3}; \quad (4.2.1)$$

$$\Delta p = p_5 - p_8. \quad (4.2.2)$$

The heat pump performance was described by the heating power  $Q_h$  and the coefficient of performance in the heating mode:

$$COP_h = \frac{Q_h}{W}. \quad (4.2.3)$$

The heating power  $Q_h$  was evaluated on the water loop and the power input to the compressor  $W$  was measured.

Test sets were grouped according to the water delivery temperature (40°C, 50°C and 60°C); for each family, different water flow rates and water temperature inlet to the evaporator and gas cooler were tested. For the same water loops mass flow rates and temperatures, multiple tests were performed, corresponding to different opening degrees of the regulation valve (8, Figure 4.2.1).

Average water mass flow rates and temperatures for each test set are listed in Table 4.2.1

Test nr.		26	30	38	17	24	25	36	35	42
$T_{w \text{ in gas cooler}}$	[°C]	19.8	18.4	22.0	35.5	42.6	35.6	31.1	17.6	21.7
gas cooler water mass flow rate	[kg/(60s)]	1.7	1.8	2.0	3.0	4.4	5.0	4.4	3.6	4.6
$T_{w \text{ in evaporator}}$	[°C]	15.0	16.4	13.1	16.5	24.2	23.5	12.1	12.4	13.9
evaporator water mass flow rate	[kg/(60s)]	3.0	4.0	4.0	3.0	4.0	3.0	6.2	4.0	4.5

Table 4.4. Average water side operating conditions for some ejector tests with water delivery temperature at about 60°C.

Results for water delivery temperature around 60°C are presented in Figures 4.2.4-a ÷ 4.2.4-d.

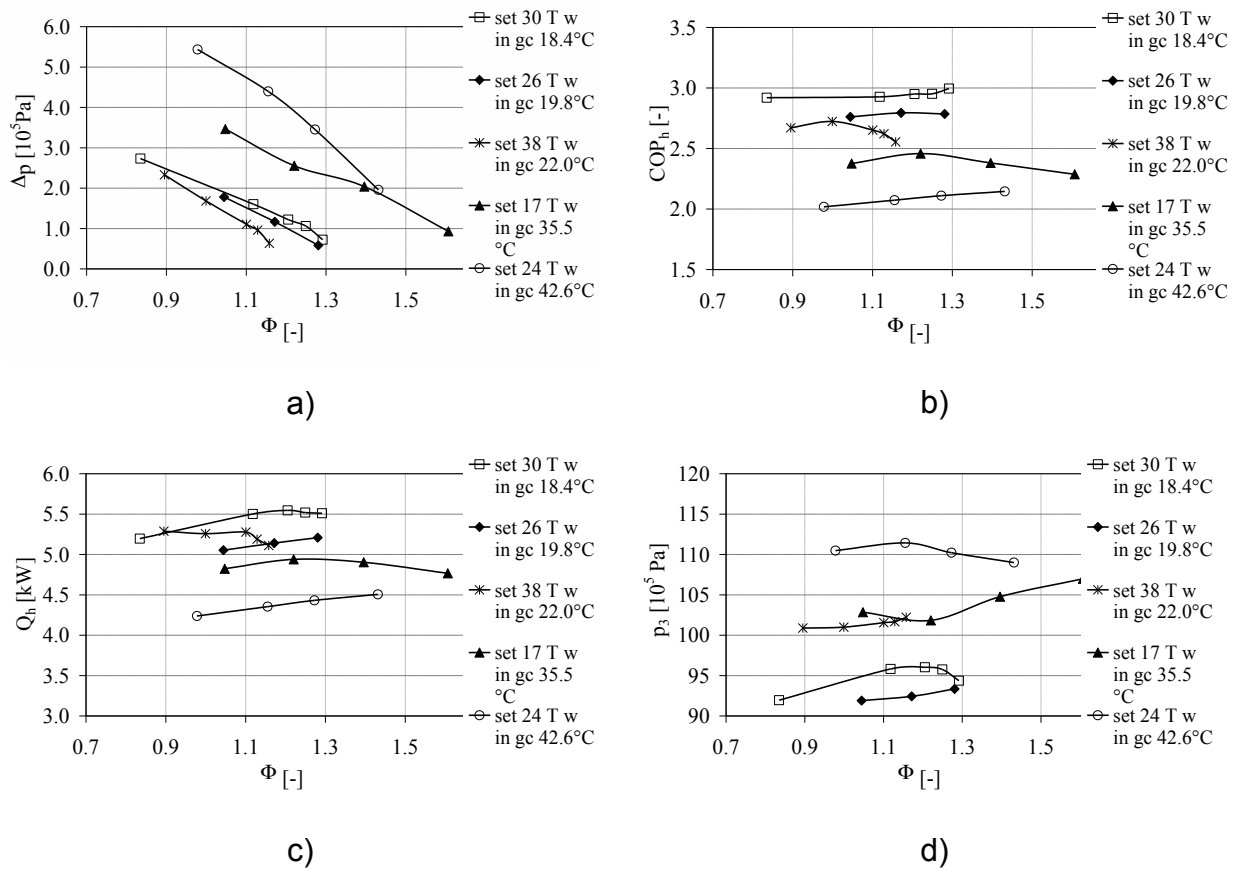


Figure 4.2.4. a) Suction pressure lift (water 60°C); b) Heat pump  $COP_h$  (water 60°C); c) Heat pump heating power  $Q_h$  (water 60°C); d) Inlet pressure  $p_3$  to motive nozzle (water 60°C).

The suction pressure lift  $\Delta p$  provided by the ejector is shown in Figure 4.2.4-a as a function of the mass entrainment ratio  $F$  as the regulating valve (8,

Figure 4.2.1) is progressively opened, the pressure lift  $\Delta p$  decreases, while the CO<sub>2</sub> mass flow rate to the evaporator increases.

The performance of the heat pump is presented in Figures 4.2.4-b and 4.2.4-c. The  $COP_h$  exhibits a maximum value; the high pressure value ( $p_3$  in Figure 4.2.4-d), which is not actively controlled, plays the traditional role in the transcritical cycle optimisation. For the same reason, also the  $Q_h$ , presented in Figure 4.2.4-c, depends on the mass entrainment ratio. In Figure 4.2.4-d, the pressure inlet to motive nozzle  $p_3$  for test set 26 is lower than the corresponding value in test set 30 because, for similar secondary loop condition at gas cooler, the evaporator water mass flow at the evaporator is lower for test 26, thus resulting in lower evaporator and suction pressures, which determines lower high pressure values.

Experiments were also conducted for gas cooler water delivery temperature at 50°C and 40°C (working conditions in Table 4.2.1). Results about ejector performance are presented in Figures 4.2.5-a and 4.2.5-b, respectively. Tests 35 and 42 are characterised by much lower enthalpy of CO<sub>2</sub> at motive nozzle inlet; this condition justifies the lower  $\Delta p$ , shown in figure 4.2.5-a, in comparison to previously presented test sets.

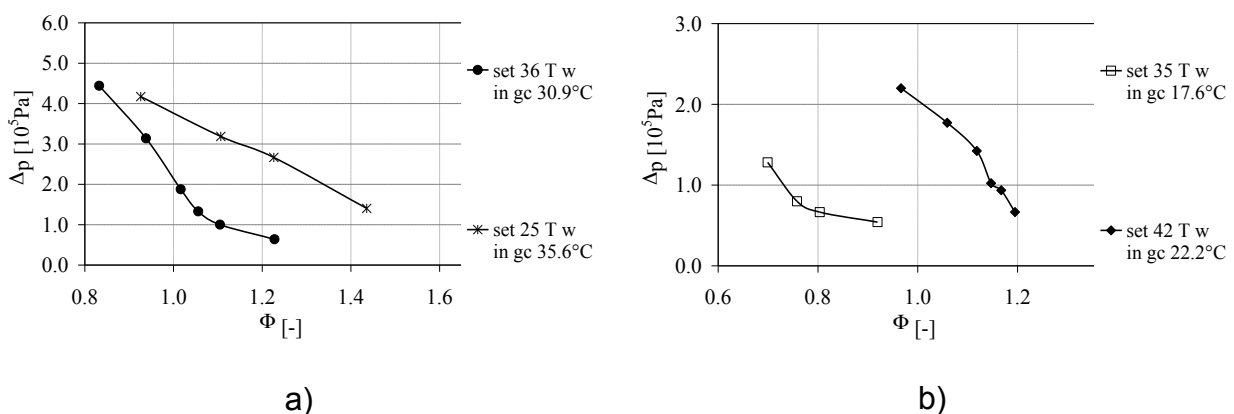


Figure 4.2.5. a) Suction pressure lift (water 50°C). b) Suction pressure lift (water 40°C).



Finally, some comparative tests were performed, switching from the ejector-based lay-out (Figure 4.2.1-b) to the back pressure one (Figure 4.2.1-a).

The same water flow rate and inlet temperature to the gas cooler and the evaporator were maintained for each couple of tests. In the case of back pressure valve, different gas cooler pressures were investigated, around the expected optimal one, while in the case of ejector, the regulation valve (8) was manually adjusted to change the operating conditions for the ejector itself.

During the tests, the evaporation temperature resulted always significantly lower when the ejector was active than it was in the case of back pressure. Being aware that no oil recovery was admitted during ejector tests and that oil was driven through the evaporator to the suction port of the ejector, some calculations were performed in order to evaluate the evaporator performance. Being the evaporator operated in flooded conditions, the overall thermal transmittance  $UA$  could be easily calculated, starting from the evaporator cooling power, evaluated on water side, and the mean logarithmic temperature difference. The calculation showed that the overall thermal transmittance  $UA$  was significantly lower during ejector operations, thus confirming the negative effect of lubricant flowing to the evaporator.

Figure 4.2.6 shows the  $UA$  values calculated for comparable ejector and back pressure valve tests (tests 36 and 37 in Table 4.2.2) as functions of refrigerant mass flow rate in the evaporator.

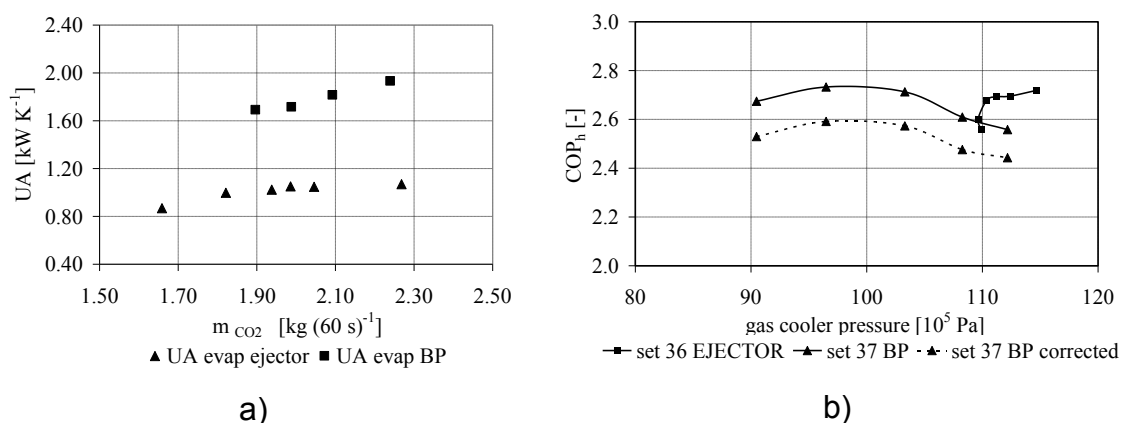


Figure 4.2.6. Tests 36 and 37. a) Overall heat transfer coefficient for comparable back pressure and ejector tests as functions of evaporator  $\text{CO}_2$  mass flow rate; b) Heat pump  $\text{COP}_h$  for ejector, back pressure and corrected back pressure tests as functions of gas cooler pressure.

To make tests comparable, the UA values that were extrapolated from the ejector tests were used to correct the evaporation temperature in the back pressure tests, according to the P-NTU method (Shah, 2003) [9]. Once that new evaporation temperature values were obtained for the back pressure tests, their  $\text{COP}_h$  were corrected taking into account the new value for the compression power. Overall compression efficiency was evaluated as a function of compression ratio from experimental data and contributed to the correction of the compression power. Figure 4.2.6-b shows the obtained heat pump  $\text{COP}_h$  as a function of the motive nozzle, or back pressure valve, inlet pressure  $p_3$ , for the tests with ejector, back pressure valve and for the corrected back pressure data. The ejector tests data correspond to different regulating valve (8, Figure 4.2.1) opening degree. Both the back pressure and the ejector tests display an optimal gas cooler pressure, which leads to the maximum  $\text{COP}_h$ . The performance of the ejector for test 36 was previously presented in Figure 4.2.5-a.

Table 4.2.2 shows the best  $\text{COP}_h$  that was obtained from each ejector test set, with optimal regulation of valve (8, Figure 4.2.1), and the corresponding value for the back pressure test at optimal gas cooler pressure; the back pressure  $\text{COP}_h$  was amended as described above.

Test nr.		37	36	26	27	42	43	16	19
Type		Ej	BP	Ej	BP	Ej	BP	Ej	BP
$T_{w \text{ in gas cooler}}$	[°C]	30.6	31.1	19.8	21.8	21.7	22.5	33.2	34.8
gas cooler water									
mass flow rate	[kg (60 s) <sup>-1</sup> ]	4.4	4.4	1.7	1.7	4.6	4.6	3.3	3.0
$T_{w \text{ in evaporator}}$	[°C]	11.9	12.1	15.1	16.7	13.9	13.9	16.7	15.4
evaporator water									
mass flow rate	[kg (60 s) <sup>-1</sup> ]	6.2	6.2	3.0	3.0	4.5	4.5	3.0	3.0
Gas cooler pressure	[10 <sup>5</sup> Pa]	111.2	96.5	92.4	99.9	96.3	85.6	99.3	99.9
Evaporator pressure	[10 <sup>5</sup> Pa]	37.7	38.6	34.2	33.6	34.8	34.8	35.9	36.2
$D_p$	[10 <sup>5</sup> Pa]	1.88		1.17		0.94		1.81	
F	[-]	1.02		1.17		1.17		1.22	
$COP_h$	[-]	2.70	2.59	2.79	2.46	3.10	2.79	2.52	2.01
$Q_h$	[kW]	5.84	5.12	5.14	4.78	5.94	5.07	5.02	4.07
$DCOP_h = COP_{h,Ej}/CO$									
$P_{h,BP-1}$	[%]	+14.1		+7.5		+17.1		+23.3	

Table 4.5. Experimental results of the ejector tests (Ej) and back pressure valve (BP) tests, both of them at optimized working conditions. Back pressure valve tests are amended to meet evaporator UA values of corresponding ejector tests.

Results (+23.3% maximum improvement) are particularly promising for the ejector, when compared to Banasiak et al. (2011) [8] and similar to those predicted by Deng et al. (2007) [2]. However a further step in experimentation, including an oil separator, might help in eliminating the uncertainties related to the UA extrapolations and  $COP_h$  correction.

The  $COP_h$  values are plotted in Figure 4.2.7 as a function of the throttling exergy losses, referred to the isenthalpic expansion process, starting from the gas cooler outlet condition to the evaporation pressure; the water inlet temperature to the evaporator was assumed as the reference temperature.

The benefit of the ejector on the heat pump  $COP_h$  increases as the throttling exergy losses of the isenthalpic process increase, thus demonstrating the potentialities of the ejector for applications such as medium and high temperature space heating or air conditioning, with high return temperatures of the gas cooler secondary fluid, water or air.

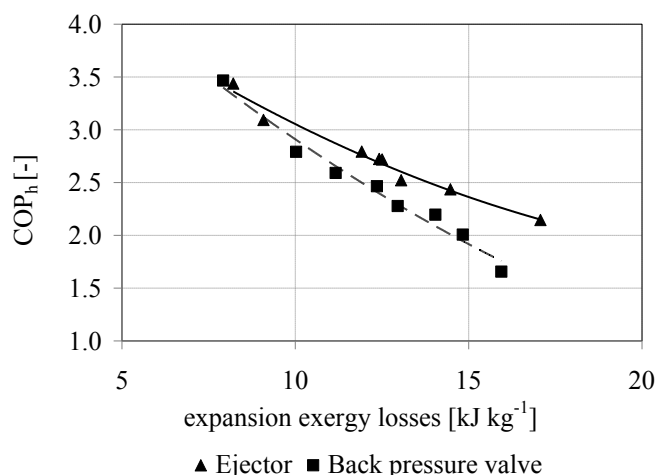


Figure 4.2.7.  $COP_h$  as a function of the throttling exergy losses, referred to the isenthalpic expansion process, starting from the gas cooler outlet condition to the evaporator pressure.

### 4.2.5 Conclusions

The performance of a two-phase ejector replacing the expansion valve in a R744 heat pump was experimentally mapped at different conditions of secondary loops temperature and mass flow rate. The mass entrainment ratio was varied between 0.8 and 1.6. The suction pressure lift was over  $5 \cdot 10^5$  Pa, depending on working conditions.

When comparing the performance of the heat pump equipped with ejector and with back pressure valve, up to +23% improvement in  $COP_h$  could be found.

However, technological problems related to lubricant recovery from the low pressure side of the circuit were found, thus emphasizing that a proper system for oil recovery must be put in place. Experimental results needed to be amended accordingly to oil circulation, in order to evaluate the heat pump performance.

New tests are planned with a high efficiency oil separator to evaluate the ejector performance vs. the back pressure; moreover an oil recovery system has to be designed and tested for a machine working in a final installation.

#### 4.2.6 Reference

1. Li D., Groll E.A. Transcritical CO<sub>2</sub> refrigeration cycle with ejector-expansion device, *International Journal of Refrigeration* 28(2005) 766-773.
2. Deng L., Jiang P., Lu T., Lu W. Particular characteristics of transcritical CO<sub>2</sub> refrigeration cycle with an ejector. *Applied Thermal Engineering* 27 (2007) 381–388.
3. Elbel, S., Hrniak P. Experimental validation of a prototype ejector designed to reduce throttling losses encountered in transcritical R744 system operation *International Journal of Refrigeration* 31(2008) 411-422.
4. Elbel, S. 2011, Historical and present developments of ejector refrigeration systems with emphasis on transcritical carbon dioxide air-conditioning applications. *International Journal of Refrigeration* 34(2011) 1545-1561.
5. Zha S., Jakobsen A., Hafner A., Neksa P. Design and Parametric Investigation on Ejector for R-744 Transcritical System, Proc. The 22nd International Congress of Refrigeration, Beijing, 2007.
6. Drescher M., Hafner A., Jakobsen A., Neksa P., Zha S. Experimental Investigation of Ejector for R-744 Transcritical Systems, Proc. The 22nd International Congress of Refrigeration, Beijing, 2007.
7. Drescher M., Hafner A., Banasiak K. Experimental Parameter Investigation of R744 Ejector, Proceedings of 8th IIR Gustav Lorentzen Conference on Natural Working Fluids, Copenhagen, 2008.
8. Banasiak K., Hafner A., Andresen T. Experimental and numerical investigation on R744 ejector geometry. International Congress of Refrigeration 2011, August 21-26 - Prague, Czech Republic.
9. Shah R.K., Sekulić DP., *Fundamentals of heat exchanger design*, 1st edition, New York; Wiley, 2003.



# Chapter 5 **Flow boiling performance of refrigerants considering exergy losses for heat transfer and pressure drops**

In this chapter the boiling heat transfer potential in plain evaporator tubes of several conventional refrigerants and two newer fluorinated propene isomers possessing low GWP are analyzed.

The two penalization quantities expressed in terms of refrigerant saturation temperature drop due to the pressure drop, and driving temperature difference, (detailed in chapter 1.3), are calculated and combined in a single performance evaluation criteria: the Total Temperature Penalization (TTP, equation 1.7).

Using the two penalization terms and the TTP, several refrigerants including the newer fluorinated alternatives R1234yf ( $\text{CF}_3\text{CF}=\text{CH}_2$ ) and R1234ze(E) ( $\text{CF}_3\text{CH}=\text{CHF}$ ), are evaluated for their boiling heat transfer performance potentials in plain evaporator tubes, and the usefulness of the technique is illustrated through several examples of the optimization of evaporator tube length.

## **5.1 Introduction**

With the ongoing and impending phase-out of Hydrochlorofluorocarbon (HCFC) refrigerants, increasing pressures to regulate and replace hydrofluorocarbon (HFC) refrigerants with ones possessing low global warming potentials (GWP), increasing awareness of energy efficiency, and

an increasing drive toward sustainable refrigeration solutions, it is becoming increasingly more important to optimize individual components and subsystems, as well as overall refrigeration systems.

This chapter is focused on flow boiling heat transfer potential of several refrigerants, including more traditional ones and two newer fluorinated propene isomers possessing low GWP. Several previous studies have investigated the optimization of the evaporator, although most did not specifically focus on the effects of refrigerants. Some representative previous works will be highlighted so as to put the present one in the context.

Granryd [3] determined the optimum pressure drop for evaporators operating with R22 and showed his technique to be equivalent to ones based on minimization of entropy generation.

Cavallini et al. [2] applied the heat transfer correlation of Gungor and Winterton [3] and the pressure drop correlation of Friedel [4] to investigate the flow boiling heat transfer performance potential of R22 and its leading replacement refrigerants. They used a form of the “penalty factor” in their analysis. The “penalty factor” is a performance evaluation criterion that can be shown to represent the exergy loss due to pressure drop. Cavallini et al. [5] applied the penalty factor approach for in-tube condensation for several refrigerants, including R1234yf, and Brown [6] provided the penalty factor for condensation for seven additional fluorinated propene isomers.

Ezeora [7] used an entropy generation minimization technique to determine the optimum combination of tube length, tube diameter, and tube volume for the two-phase flow of CO<sub>2</sub> in an evaporator tube.

Singh et al. [8] used an entropy generation minimization technique coupled with a heat exchanger modeling tool to optimize an air-cooled finned-tube evaporator operating with R134a.

Domanski et al. [9] investigated optimized finned-tube evaporators for six different refrigerants using a detailed evaporator model, where the refrigerant circuitry was optimized using a non-Darwinian learnable evolutionary model. They then incorporated the optimized evaporators into a complete vapor



compression refrigeration system simulation model to compare the effects of the various refrigerants on COP.

The state-of-the-art heat transfer and pressure drop correlations are applied to the flow boiling of several refrigerants, including newer ones possessing low GWP, in a plain tube evaporator to determine their heat transfer performance potentials. Moreover, to illustrate the usefulness of the technique for optimization studies, it is applied to the simple cases of the optimization of (1) tube length and (2) heat duty for an evaporator. While the technique can be shown to be equivalent to exergy or entropy generation analyses, it is instead presented in terms of penalization quantities which are further expressed as temperature drops (similar to what is done by Cavallini et al. [5]). One of the primary reasons, but by no means the only one, for this approach is that temperature drop is a more familiar term than exergy or entropy generation for many heat transfer engineers and heat exchanger designers.

## 5.2 Nomenclature

*B<sub>ext</sub>* specific effective external resistance per unit reference internal heat transfer surface area ( $\text{m}^2 \text{K W}^{-1}$ );

*D* tube inner diameter (m);

*G* refrigerant mass flux ( $\text{kg m}^{-2} \text{s}^{-1}$ );

*h* refrigerant heat transfer coefficient (based on the reference internal heat transfer surface area) ( $\text{W m}^{-2} \text{K}^{-1}$ )

*i* specific enthalpy ( $\text{J kg}^{-1}$ )

*L* tube length (m)

*$\dot{m}$*  mass flow rate ( $\text{kg s}^{-1}$ )

*P* pressure (kPa)

*PEC* Performance Evaluation Criterion

*q* heat flux per unit reference internal heat transfer surface area ( $\text{W m}^{-2}$ )

$DT$	temperature differences (see Figure 5.1 for subscripts) ( $^{\circ}\text{C}$ or K)
$T$	temperature (see Figure 5.1 for subscripts) ( $^{\circ}\text{C}$ or K)
$T_s$	refrigerant saturation (evaporation) temperature ( $^{\circ}\text{C}$ or K)
$TTP$	Total Temperature Penalization ( $^{\circ}\text{C}$ or K)
$x$	thermodynamic quality

#### Subscripts

$cm$	cooling medium
$dcm$	driving difference – cooling medium
$dr$	driving difference – refrigerant
$ext$	external
$i$	inlet
$o$	outlet
$r$	refrigerant
$tot$	total
$c$	condenser

### 5.3 Evaporator model

Similar to the condenser model of Cavallini et al. [5] (see Figure 1.3), Figure 5.1 illustrates a simple counter-flow evaporator model described by temperature profiles for the refrigerant, the external cooling medium, and the tube surface. It is assumed that the heat transfer processes occur at steady-state and that the operating conditions for the refrigerant and the cooling medium can be represented with bulk average properties.

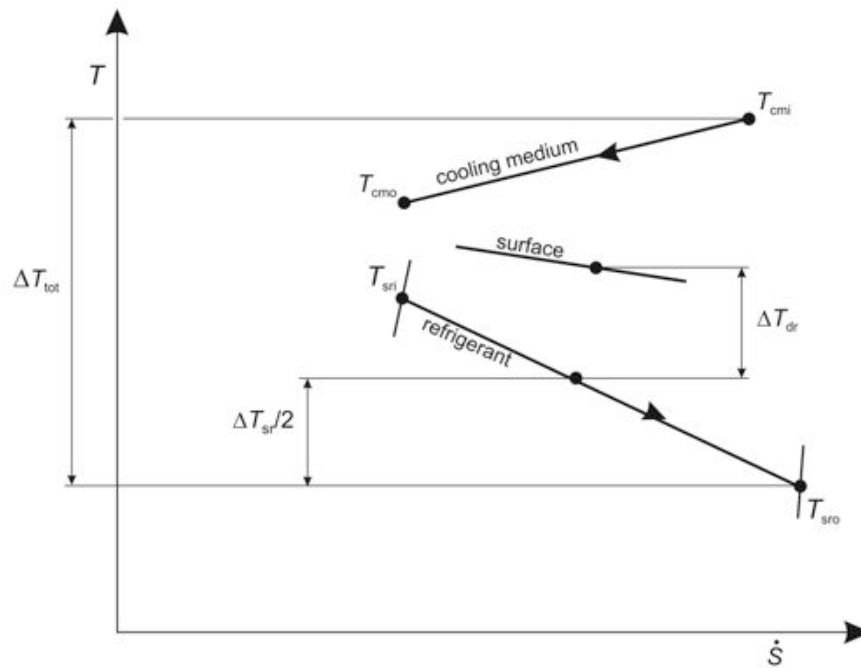


Figure 5.1. Idealized temperature profiles in a counter-current evaporator.

The focus is on the effects that various refrigerants have on the refrigerant-side heat transfer process in an evaporator, and the application of these simple methodologies to the optimization of evaporator tubes. Furthermore, only plain tubes will be considered, though the methodology could easily be extended to include enhanced tubes.

In paragraph 1.3 the two exergy losses components in a two-phases heat exchange have been described, that concepts are detailed in the flow boiling heat exchange.

The flow boiling heat transfer performance potentials of refrigerants are expressed in terms of two temperature differences:  $DT_{sr}$ , the saturation temperature drop which occurs due to the refrigerant pressure drop, and  $DT_{dr}$ , the driving temperature difference given by:

$$DT_{dr} = q/h = G\Delta i/h \quad (5.1)$$

where  $q$  is the specific refrigeration capacity,  $h$  is the refrigerant-side heat transfer coefficient,  $G$  is the refrigerant mass flux, and  $Di$  is the refrigerant enthalpy change during the heat transfer process.

It should be noted that  $DT_{sr}$  and  $DT_{dr}$  both reduce the overall refrigeration system energetic and exergetic efficiencies by increasing the required compressor power to achieve the same refrigeration effect.

In addition to considering the two temperature drops independently from one another, similar to Cavallini et al. [5], they can be combined into one PEC termed Total Temperature Penalization (TTP) given by:

$$TTP = \left( DT_{dr} + \frac{1}{2} DT_{sr} \right) \quad (5.2)$$

where the first term on the right-hand side represents the penalization term related to heat transfer and the second term on the right-hand side represents the penalization term related to pressure drop. Note: the 1/2 is included to recognize that roughly only 1/2 of the saturation temperature drop is lost as heat transfer driving potential. Although not included herein, as noted in Cavallini et al. [5], TTP and the other penalization terms can be related to the more conventional concepts of exergy losses or entropy generation.

Now returning our focus to the effects that particular refrigerants have on TTP, equation (5.1) shows that  $DT_{dr}$  is a function of both  $G$  and  $h$ , and as noted previously  $DT_{sr}$  is a function of  $DP$ , which furthermore is a function of  $G$ , among other parameters. Therefore, to better understand the functional dependence of the various parameters on TTP, we note that  $h$  is given by:

$$h = \text{fnc} \left( G, \Delta T_{dr}, T_s, x, D, \text{refrig} \right) \quad (5.3)$$

and that  $DP$  is given by:

$$\Delta P = \text{fnc}(G, x, D, L, \text{refrig}) \quad (5.4)$$

where  $T_s$  is the refrigerant saturation temperature,  $x$  is the refrigerant quality,  $D$  is the tube diameter,  $L$  is the tube length, and “refrig” indicates the particular refrigerant, and includes the effects of transport properties. equation (5.3) and (5.4) show for a given refrigerant and heat exchanger geometry ( $D$  and  $L$ ), and for fixed  $DT_{dr}$ ,  $T_s$ , and  $x$  that  $h$  and  $DP$  are both simply functions of  $G$ . Although the equations do not provide the functional relationships,  $h$  varies more or less proportionally with  $G$ , whereas,  $DP$  varies more or less proportionally with  $G^2$ . Therefore, if the goal is to optimize the overall heat exchanger performance, one important parameter to consider is  $G$ . However, simply comparing the performance potentials of different refrigerants at constant  $G$  can be misleading since its functional dependences on  $h$  and  $DP$  (and hence exergy losses due to heat transfer and pressure drop) are different. Thus, a better approach would be to isolate and compare the pressure drop penalization terms for different refrigerants at constant  $h$  (in this way the exergy losses due to heat transfer will be the same refrigerant-to-refrigerant) for fixed  $D$ ,  $L$ , and  $x$ .

## 5.4 Evaporator optimization

### *Case 1 – optimization of evaporator circuit length*

Consider an evaporator of defined overall geometry, fixed refrigeration capacity, and fixed operating conditions for the cooling medium. Furthermore, if the total mass flux and the total tube length are fixed and if each refrigerant circuit is of equal length and operating at the same conditions, then the only variable left to a design engineer for optimizing the evaporator performance is to select the number of parallel refrigerant circuits. Under the stated constraints,  $G$  is inversely proportional to the number of parallel refrigerant

circuits. That is, the fewer the number of parallel circuits, the higher will be  $G$ ,  $h$ , and  $DP$ , and thus the lower will be  $DTdr$  and the higher will be  $DTsr$ . Therefore, as can be understood from equation (5.2), an optimum circuit length must exist.

A simple calculation with a single tube with constant diameter and variable length has been made, the considered operative conditions are:

- tube diameter = 8 mm;
- evaporation outlet temperature = 5 °C;
- evaporation outlet quality = 1;
- condenser outlet temperature = 40 °C;
- condenser outlet subcooling = 0 °C;
- heat flux per unit reference internal heat transfer surface area = 10 kW·m<sup>-2</sup>.

The heat transfer coefficient and the pressure losses are calculated under constant average quality  $(x_i+x_o)/2$ . The literature correlations utilized for calculating the heat transfer coefficient and the pressure drop are reported in Table 5.1; on the air side, the face velocity found is the value that allows the set specific heat flux to be obtained.

The Refrigerants properties are calculated using Refrop 9 [14].

Refrigerant-side two-phase heat transfer coefficient and pressure drop correlations	Wojtan <i>et al.</i> [10] Moreno [11]
Refrigerant-side single-phase heat transfer coefficient and pressure drop correlations	Dittus Boelter (heat transfer) Blausius (pressure drop)
Refrigerant void fraction	Rouhani and Axelsson [12]
Air-side heat transfer coefficient and pressure drop correlations	Wang <i>et al.</i> [13] Wang <i>et al.</i> [13]

Table 5.1. Correlations used in Simple Design Model.

Clearly, an optimal circuit length occurs at the minimum point of the curve. To the left of the minimum point, the heat transfer penalization term dominates; whereas, to the right of the minimum point, the pressure drop penalization term dominates.

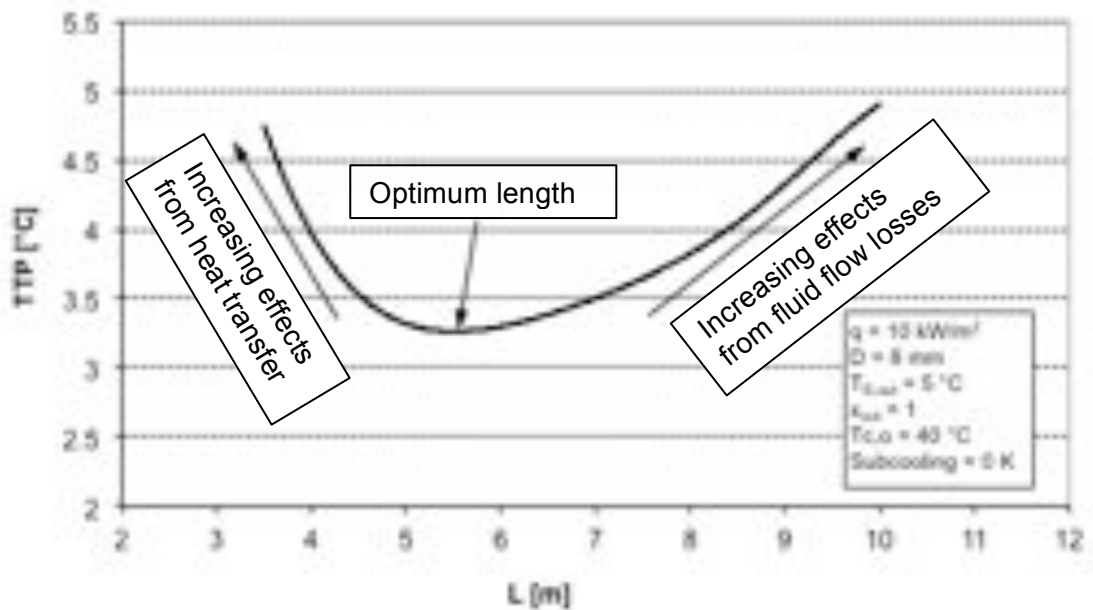


Figure 5.2. Total Temperature Penalization versus heat exchanger length for R134a for convective boiling heat transfer in a plain tube calculated using the heat transfer coefficient correlation of Wojtan et al. [10] and the pressure drop correlation of Moreno Quiben and Thome [11].

Figure 5.3 shows the data of Figure 5.2 together with results for two other tube diameters. It can be seen that the optimal length increases with increasing diameter as expected.

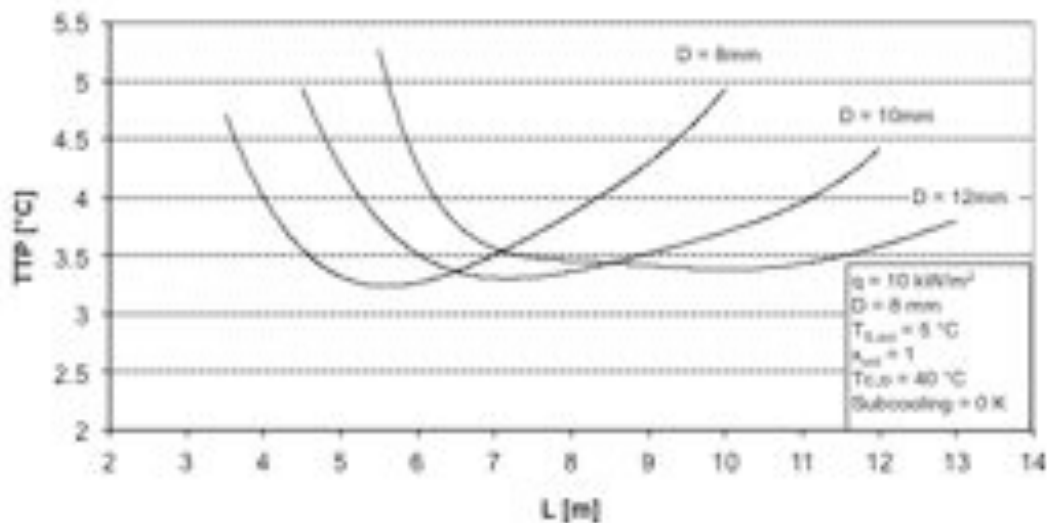


Figure 5.3. Total Temperature Penalization versus heat exchanger length for R134a for convective boiling heat transfer in three plain tubes calculated using the heat transfer coefficient correlation of Wojtan et al. [10] and the pressure drop correlation of Moreno Quiben and Thome [11].

Figure 5.4 shows optimization results for three additional refrigerants: R22, R1234yf, and R1234ze(E). It can be seen that the two fluorinated propene isomers have larger values of TTP at their optimum tube lengths than do either R22 or R134a. Furthermore, the optimum tube lengths are different for each of the four refrigerants.



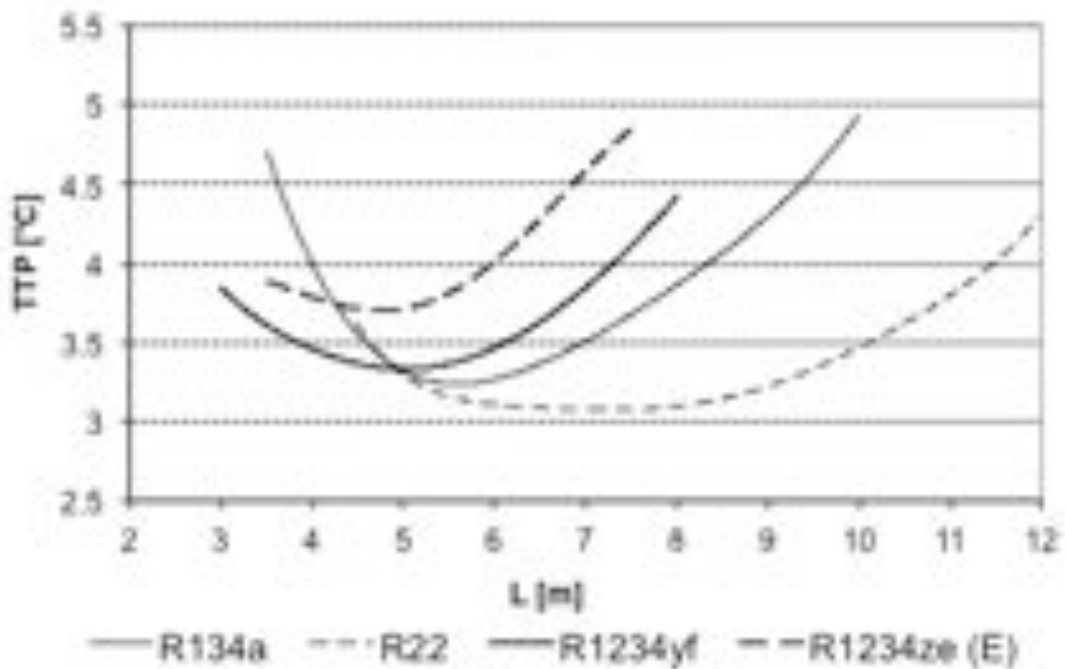


Figure 5.4. Evaporator refrigeration capacity versus heat exchanger length for four refrigerants for convective boiling heat transfer calculated using the heat transfer coefficient correlation of Wojtan et al. [10] and the pressure drop correlation of Moreno Quiben and Thome [11].

The results of Figures 2-4 suggest for the newer alternative refrigerants R1234yf and R1234ze(E) that without optimization of the heat exchangers the energetic and exergetic efficiencies will be lower in many applications than those of traditional refrigerants such as R22 and R134a.

#### Case 2 – optimization of evaporator refrigeration capacity

Consider an evaporator of defined overall geometry, fixed  $T_{sr,o}$ , and for the external cooling medium fixed  $\dot{m}_{cm}$  and  $T_{cm,i}$ . For this case, the refrigerant circuitry can be optimized to obtain the maximum refrigeration capacity. As before, the individual refrigerant circuits are considered to be of equal length and operating at the same conditions, so that the only variable left to a design engineer for optimizing the evaporator performance is to select the

number of parallel refrigerant circuits. With the stated assumptions, the total temperature difference  $DT_{\text{tot}} = (T_{\text{cmi}} - T_{\text{sro}})$  remains constant:

$$DT_{\text{tot}} = (T_{\text{cmi}} - T_{\text{sro}}) = DT_{\text{dem}} + \frac{1}{2}DT_{\text{cm}} + DT_{\text{dr}} + \frac{1}{2}DT_{\text{sr}} = DT_{\text{ext}} + \text{TTP} \quad (5.5)$$

where  $DT_{\text{ext}}$  is the temperature drop on the cooling medium side, which can be rewritten in terms of the refrigeration capacity  $q$ , namely  $DT_{\text{ext}} = q \cdot B_{\text{ext}}$ , where  $B_{\text{ext}}$  is the total specific external resistance to heat transfer.  $B_{\text{ext}}$  remains nearly constant since the external cooling medium conditions remain nearly constant. equation. (5.5) can now be rewritten as:

$$q = \frac{\Delta T_{\text{tot}} - \text{TTP}}{B_{\text{ext}}} \quad (5.6)$$

Under the stated assumptions for equation (5.6),  $DT_{\text{tot}}$  and  $B_{\text{ext}}$  are constant; therefore, maximization of  $q$  implies minimization of TTP. In what follows, values for  $DT_{\text{tot}}$  and  $B_{\text{ext}}$  are assumed to be 21.27 K and  $1.78 \times 10^{-3} \text{ m}^2 \text{ K W}^{-1}$ , respectively. As for Case 1, minimization of TTP implies optimizing  $G$  through optimization of the circuit length. The minimum TTP point implies a balance between heat transfer and pressure drop exergy losses.

Figure 5.5 shows optimization results for equation (5.6) for R134a, R22, R1234yf, and R1234ze(E).

The different markers indicate the simulation results (the circuit length varies in steps), while the smooth curves connecting the markers are simply interpolations to aid the readers understanding.

R22 has the highest optimum value for  $q$  followed by R134a and R1234yf, which have very similar values approximately 1.1 % lower than the R22 value. R1234ze(E) has the lowest optimum  $q$  value, which is approximately 3.3 % lower than the R22 value. The optimum circuit length decreases in the order of R22, R134a, and R1234yf/R1234ze(E). It should be noted that the

slope of R1234yf curve away from the optimum circuit length is much steeper than the R134a curve, which implies that optimization of the evaporator circuitry for R1234yf is much more critical than it is for R134a (the fluid which R1234yf is meant to replace in several applications).

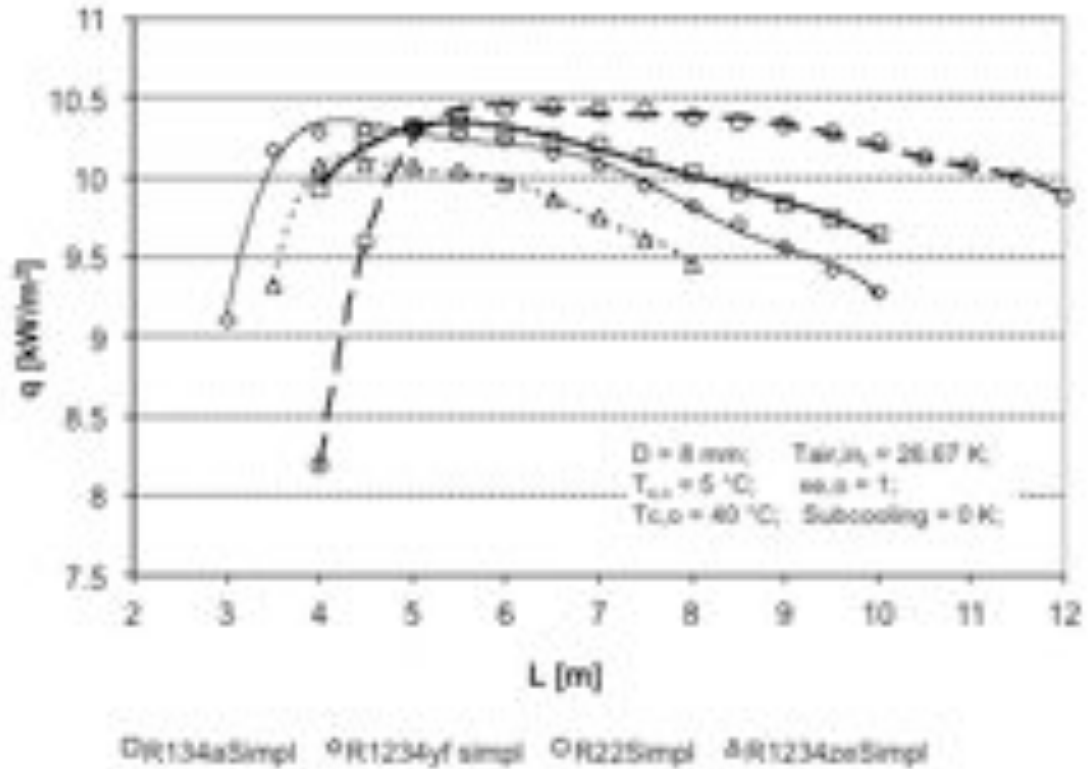


Figure 5.5. Evaporator refrigeration capacity versus heat exchanger length for four refrigerants for convective boiling heat transfer calculated using the heat transfer coefficient correlation of Wojtan et al. [10] and the pressure drop correlation of Moreno Quiben and Thome [11]

## 5.5 Validation of model

The vapor compression refrigeration cycle model (referred to as 3D Design Model) used to validate the simple model described in Paragraph 5.4 is described in detail in Casson [15]. Herein, only the tube-fin evaporator sub-model of 3D Design Model is applied, within some small changes to better fit.

The refrigerant-side heat transfer, pressure drop, and void fraction correlations are listed in Table 5.1. The air-side heat transfer coefficient is assumed to be uniform and given by a constant value.

*Case 1 – optimization of evaporator circuit length*

The evaporator simulation sub-model was applied first to a single tube placed in one row and second to a finned coil evaporator whose geometry is described in Table 5.2.

Tube arrangement		Staggered
Tube material		Cu
Longitudinal tube spacing (parallel to the air flow)	(mm)	21.7
Transverse tube spacing (normal to the air flow)	(mm)	25
Inside tube diameter	(mm)	8/10/12
Outside tube diameter	(mm)	10/12/14
Inside tube surface		Smooth
Fin geometry (material)		louvered (Al)
Fin spacing	(mm)	2.1
Fin thickness	(mm)	0.11
Number of rows		4
Face area	(m <sup>2</sup> )	0.25
Face air velocity	(m s <sup>-1</sup> )	2.0
Outlet refrigerant saturation temperature	(°C)	5.0
Inlet refrigerant quality		0.25

*Table 5.2. Geometrical characteristics of the simulated tube-fin evaporator for varying diameters for Optimization, Case 1.*

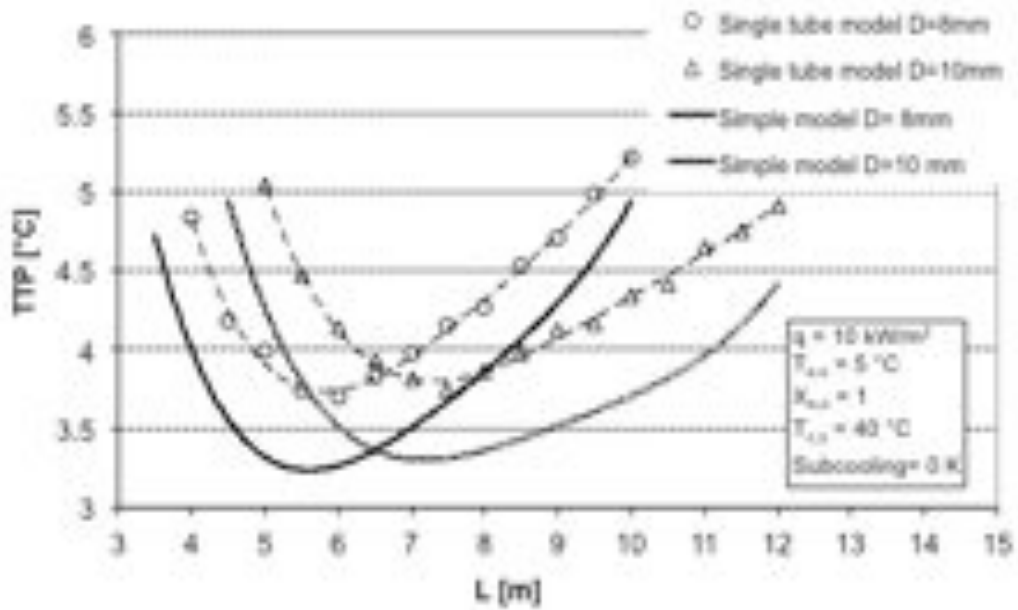
For all the next figures, the different markers indicate the simulation results (the circuit length varies in steps), while the smooth curves connecting the markers are simply interpolations.

A comparison between:

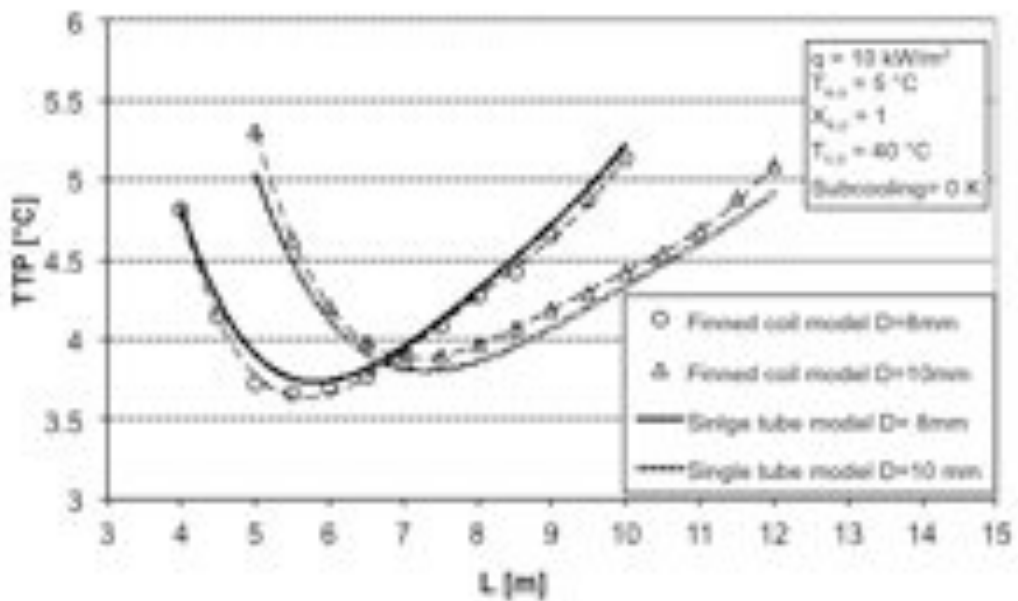
- the single tube detailed simulation results and the simple model described in Paragraph 5.4;
- the single tube detailed simulation results and the finned coil detailed simulation results (only the trendline is reported for the single tube);

Flow boiling performance of refrigerants considering exergy losses for heat transfer and pressure drops

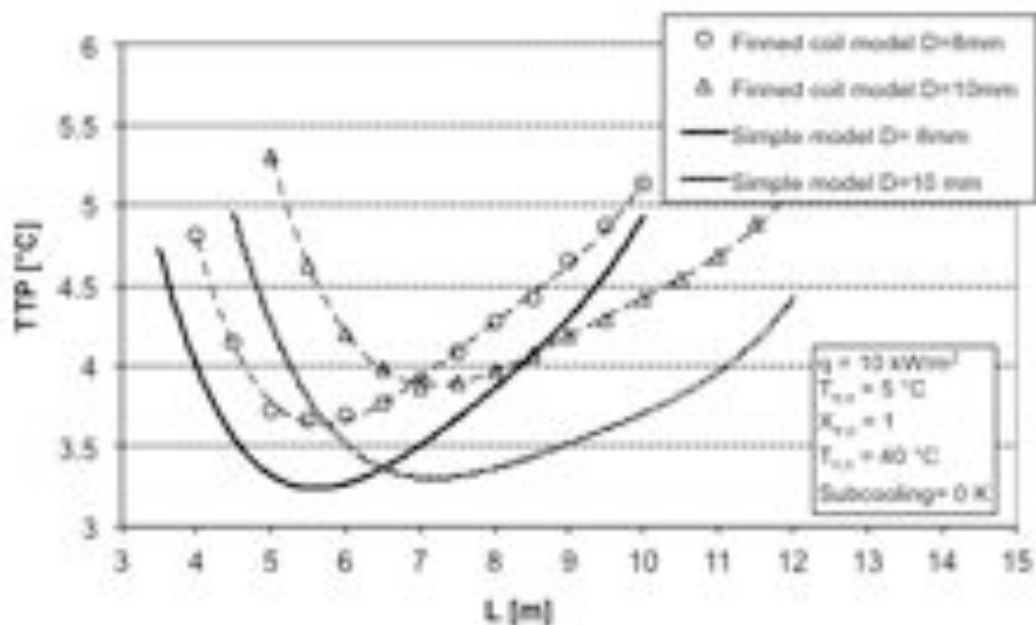
- the simple model described in Paragraph 5.4 and the finned coil detailed simulation results;
- are shown in Figure 5.6 a-b-c respectively for R134a for  $D = 8 \text{ mm}$  and  $D = 10 \text{ mm}$ .



a)



b)



c)

Figure 5.6. Comparison of results from detailed simulation model applied to a single tube and a finned coil, and the simple model: a) Single tube detailed simulation and simple model; b) single tube and finned coil; detailed simulation models c) simple model and finned coil detailed simulation model. Total Temperature Penalization versus heat exchanger length for R134a for convective boiling heat transfer in two plain tubes calculated using the heat transfer coefficient correlation of Wojtan et al. [10] and the pressure drop correlation of Moreno Quiben and Thome [11].

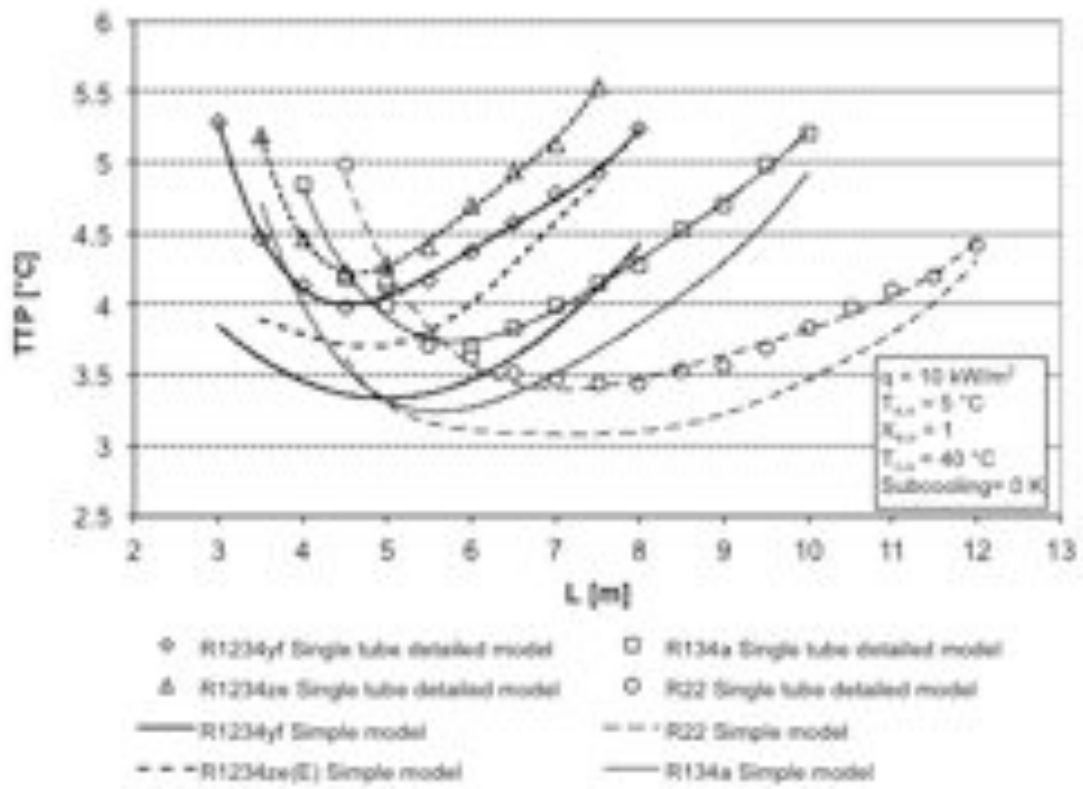
The same analysis was applied to an evaporator with slightly different geometry as described in Table 5.3 to investigate the performance potentials of R22, R134a, R1234yf and R1234ze(E).

Flow boiling performance of refrigerants considering exergy losses for heat  
transfer and pressure drops

Tube arrangement		staggered
Tube material		Cu
Longitudinal tube spacing (parallel to the air flow)	(mm)	12.7
Transverse tube spacing (normal to the air flow)	(mm)	21
Inside tube diameter	(mm)	8
Outside tube diameter	(mm)	10
Inside tube surface		Smooth
Fin geometry (material)		louvered (Al)
Fin spacing	(mm)	2.1
Fin thickness	(mm)	0.11
Number of rows		4
Face area	(m <sup>2</sup> )	0.21
Face air velocity	(m s <sup>-1</sup> )	3.2
Outlet refrigerant saturation temperature	(°C)	5.0
Inlet refrigerant quality		0.25

*Table 5.3. Geometrical characteristics of the simulated tube-fin evaporator for various refrigerants for Optimization Case 1.*

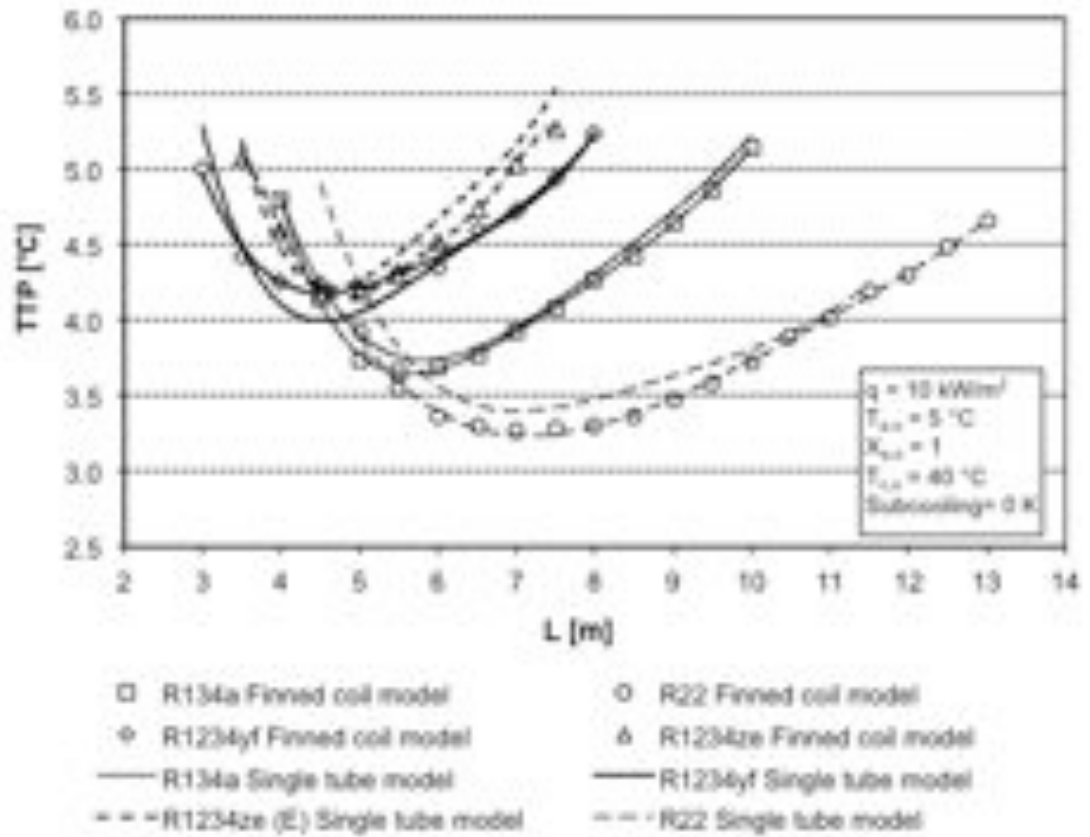
The results are shown in Figure 5.7 a-b-c for: a) the single tube detailed model and the simple model, b) the single tube and the finned coil detailed models, c) the simple model and the finned coil detailed model. In the second case only the trendline is reported for the single tube detailed model compared with the finned coil one for aiding the reading.



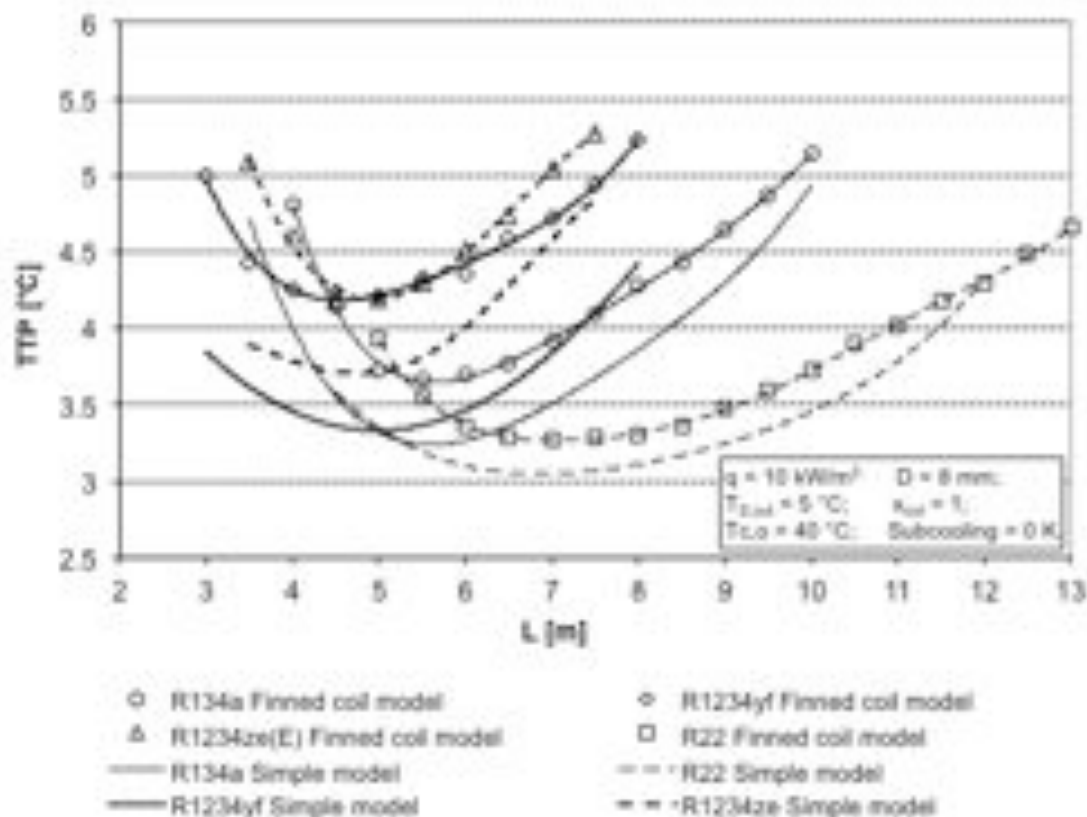
a)



Flow boiling performance of refrigerants considering exergy losses for heat transfer and pressure drops



b)



c)

Figure 5.7. Comparison of results from detailed simulation model applied to a single tube and a finned coil, and the simple model: a) Single tube detailed simulation and simple model; b) single tube and finned coil detailed simulation models; c) simple model and finned coil detailed simulation model. Total Temperature Penalization versus heat exchanger length for four refrigerants for convective boiling heat transfer calculated using the heat transfer coefficient correlation of Wojtan et al. [10] and the pressure drop correlation of Moreno Quiben and Thome [11].

It can be pointed out the simple model is able to calculate the optimal circuit length with an acceptable approximation, while it underestimates the TTP value, because the heat transfer coefficient  $h$  is kept constant and calculated for the inlet/outlet average quality, so it is higher than the finite volumes weight average  $h$  calculated by the detailed simulation model.

In Figure 5.8 the  $h$  and the temperature drops trends are reported, from the tube inlet to the outlet refrigerant quality, for a single tube detailed simulation,

the average weighted  $h$  is  $3604.7 \text{ W}\cdot\text{m}^{-2}\cdot\text{K}^{-1}$ , while the constant value is almost  $4964.7 \text{ W}\cdot\text{m}^{-2}\cdot\text{K}^{-1}$ . Each marker corresponds to a finite volume element in which the tube length is divided by the model. The temperature drops are slightly overestimated with the simple model, but not so much to compensate the driven temperature term in the TTP calculation.

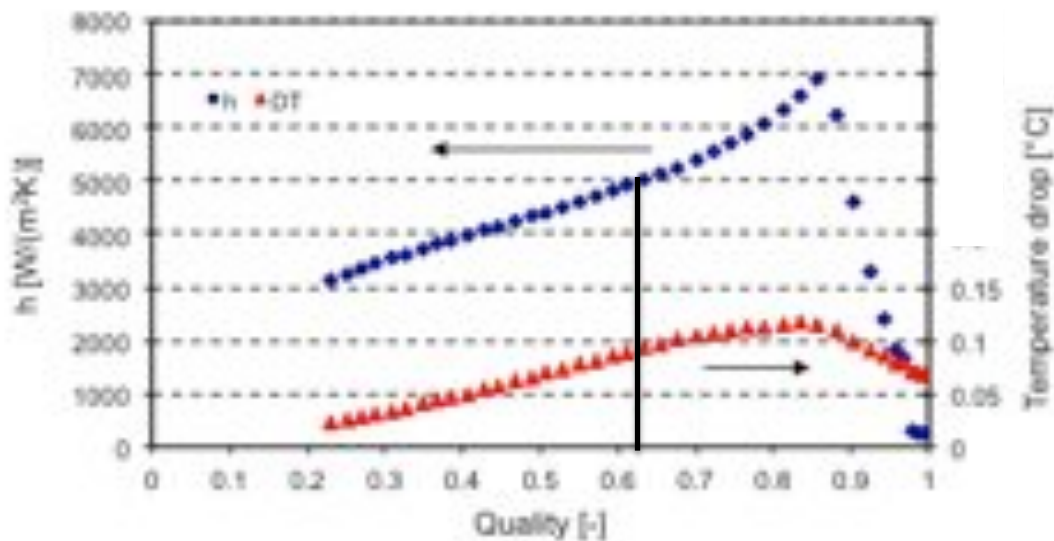


Figure 5.8. Heat transfer coefficient  $h$  and temperature drops trends reported, from the tube inlet to the outlet refrigerant quality, for a single tube detailed simulation, the refrigerant is R134a and the tube length is 8m. The vertical black line indicates the average quality considered

The single tube detailed model can well predict the optimal circuit length and well approximate the TTP value.

#### Case 2 – optimization of evaporator refrigeration capacity

The evaporator simulation sub-model was applied to a single tube and to the finned coil evaporator whose geometry is described in Table 5.4.

Tube arrangement		staggered
Tube material		Cu
Longitudinal tube spacing (parallel to the air flow)	(mm)	12.7
Transverse tube spacing (normal to the air flow)	(mm)	21
Inside tube diameter	(mm)	8
Outside tube diameter	(mm)	10
Inside tube surface		smooth
Fin geometry (material)		louvered (Al)
Fin spacing	(mm)	2.1
Fin thickness	(mm)	0.11
Number of rows		4
Face area	(m <sup>2</sup> )	0.21
Face air velocity	(m s <sup>-1</sup> )	2.0
Inlet air temperature	(°C)	26.67
Inlet air relative humidity	(%)	50
Outlet refrigerant saturation temperature	(°C)	5.0
Inlet refrigerant quality		0.25

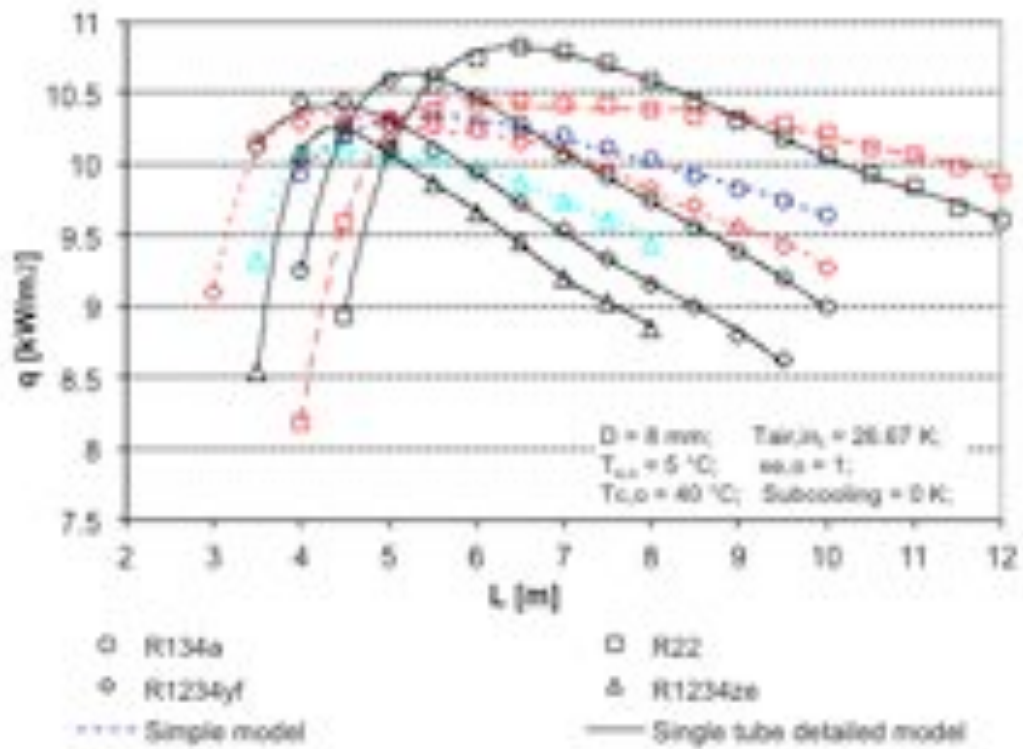
*Table 5.4. Geometrical characteristics of the simulated tube-fin evaporator for various refrigerants for Optimization Case 2.*

The finned coil has four rows. To get a middle way model between the entire finned coil simulation and the simple model, with a single tube detail model, as in case 1, the single tube length is divided in four rows.

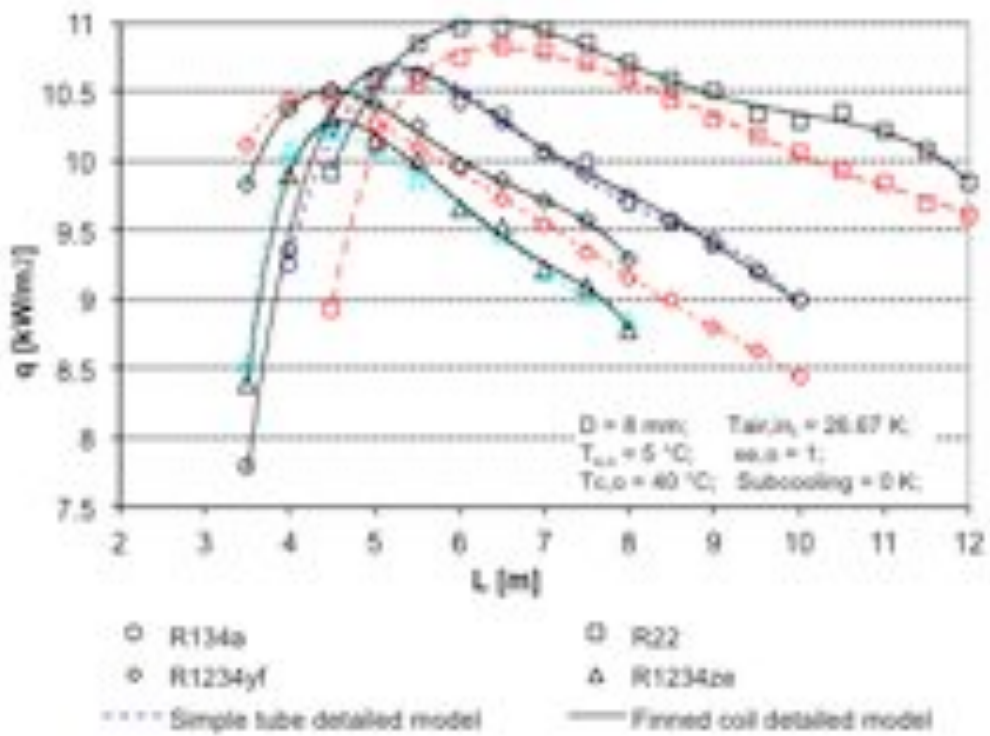
A comparison between the detailed simulation results and the simple model are shown in Figure 5.11 for R22, R134a, R1234yf, and R1234ze(E). As before, the different markers indicate the simulation results (the circuit length varies in steps), while the smooth curves connecting the markers are simply interpolations to aid the readers understanding.

The results are shown in Figure 5.9 a-b-c as in the previous case for: a) the single tube detailed model and the simple model, b) the single tube and the finned coil detailed models, c) the simple model and the finned coil detailed model

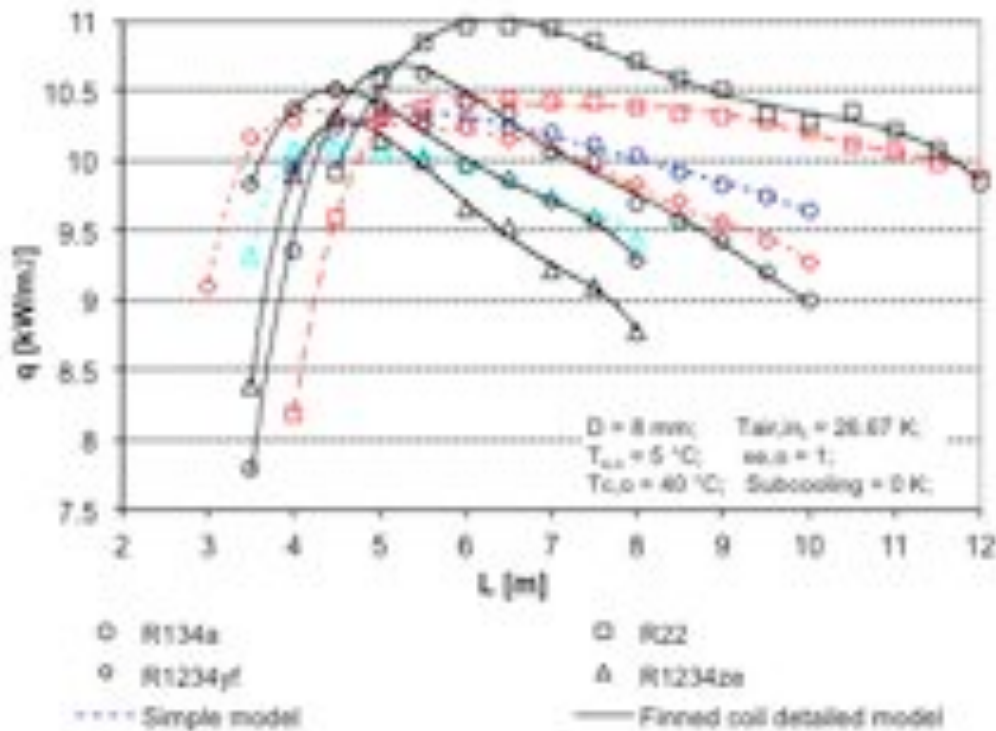
Flow boiling performance of refrigerants considering exergy losses for heat transfer and pressure drops



a)



b)



c)

Figure 5.9. Comparison of results from detailed simulation model applied to a single tube and a finned coil, and the simple model: a) Single tube detailed simulation and simple model; b) single tube and finned coil detailed simulation model; c) simple model and finned coil detailed simulation model. Evaporator refrigeration capacity versus heat exchanger length for four refrigerants for convective boiling heat transfer calculated using the heat transfer coefficient correlation of Wojtan et al. [10] and the pressure drop correlation of Moreno Quiben and Thome [11].

The results demonstrates the simple model can well predict the optimal tube length corresponding to the maximum specific heat flux, while the value and curve slope are not well predicted, due to the heat transfer internal coefficient and the pressure drops both calculated at the average quality, and to the external thermal resistance have been kept constant. The single tube detailed model well calculates the optimal tube length, and well approximates the specific heat flux and the curve slope.

The validation confirms the newer R1234yf and R1234ze(E) refrigerants has lower heat exchange potential than R134a and R22 ones; and their curves (Figure 5.8) away from the optimum value are much steeper so the

optimization of the evaporator circuitry is much more critical for them than for the R134a and R22.

## 5.6 Conclusion

The heat transfer coefficient correlation of Wojtan et al. [10] and the pressure drop correlation of Moreno Quiben and Thome [11] were used to analyze the boiling heat transfer performance potentials in plain evaporator tubes of several conventional refrigerants and two newer fluorinated propene isomers possessing low GWP. These correlations were used to calculate two penalization quantities expressed in terms of the refrigerant saturation temperature drop due to pressure drop and the driving temperature difference. Several refrigerants were assessed using the pressure drop penalization term at a constant heat transfer coefficient (constant heat transfer penalization term). Higher pressure refrigerants have smaller pressure drop penalization values than medium and lower pressure refrigerants, indicating that newer refrigerants such as R1234yf and R1234ze(E) have lower heat transfer potential than more traditional refrigerants such as R22 and R134a.

The Total Temperature Penalization (TTP) performance criterion was used to optimize evaporator tube length for an idealized heat exchanger operating under two optimization cases. Again, the results show that R1234yf and R1234ze(E) will have lower energetic and exergetic efficiencies than more traditional refrigerants such as R22 and R134a indicating the need to optimize the refrigerant circuitry for these newer refrigerants. The results of the simple model described herein were confirmed with simulation results from a detailed evaporator model.

## 5.7 Reference

1. E. Granryd, Optimum circuit tube length and pressure drop on the refrigerant side of evaporators, in: Proceedings of the International Refrigeration and Air Conditioning Conference, West Lafayette, Indiana, 1992.
2. A. Cavallini, G. Censi, D. Del Col, L. Doretti, L. Rossetto, G.A. Longo, Reduction of global warming impact in the HP/AC industry by employing new HFC refrigerants, in: Proceedings of Clima 2000/Napoli 2001 World Congress, Naples, Italy, 2001.
3. K.E. Gungor, R.H.S. Winterton, A general correlation for flow boiling in tubes and annuli, *Int. J. Heat Mass Transfer* 29 (3) (1986) 351-358.
4. L. Friedel, Pressure drop during gas/vapor-liquid flow in pipes, *Int. Chem. Eng.* 20 (3) (1980) 352-367.
5. A. Cavallini, J.S. Brown, D. Del Col, C. Zilio, In-tube condensation performance of refrigerants considering penalization terms (exergy losses) for heat transfer and pressure drop, *Int. J. Heat Mass Transfer* 53 (13-14) (2010) 2886-2896.
6. J.S. Brown, HFOs: New, low global warming potential refrigerants, *ASHRAE J.* 51 (8) (2009) 22-29.
7. O. Ezeora, Entropy generation analysis and optimum tube length of two-phase flow evaporator tube, in: Proceedings of the International Refrigeration and Air Conditioning Conference, West Lafayette, Indiana, 2008.
8. V. Singh, V. Aute, R. Radermacher, Usefulness of entropy generation minimization through a heat exchanger modeling tool, in: Proceedings of the International Refrigeration and Air Conditioning Conference, West Lafayette, Indiana, 2008.
9. P.A. Domanski, D. Yashar, M. Kim, Performance of a finned-tube evaporator optimized for different refrigerants and its effect on system efficiency, *Int. J. Refrig.* 28 (6) (2005) 820-827.



10. L. Wojtan, T. Ursenbacher, J.R. Thome, Investigation of flow boiling in horizontal tubes: Part II– Development of a new heat transfer model for stratified-wavy, dryout and mist flow regimes, *Int. J. Heat Mass Transfer* 48 (14) (2005) 2970-2985.
11. J. Moreno Quiben, J.R. Thome, Flow pattern based two-phase frictional pressure drop model for horizontal tubes, Part II: New phenomenological model, *Int. J. Heat Fluid Flow* 28 (5) (2007) 1060-1072.
12. S.Z. Rouhani, E. Axelsson, Calculation of volume void fraction in the subcooled and quality region, *Int. J. Heat Mass Transfer* 13 (10) (1970) 383-393.
13. C. Wang, C. Lee, C. Chang, S. Lin, Heat transfer and friction correlation for compact louvered fin-and-tube heat exchangers, *Int. J. Heat Mass Transfer* 42 (11) (1998), 1945-19
14. E.W. Lemmon, M.L. Huber, M.O. McLinden, NIST Standard Reference Database 23, Reference Fluid Thermodynamic and Transport Properties (REFPROP), Version 9.0, National Institute of Standards and Technology, 2010.
15. V. Casson, A. Cavallini, L. Cecchinato, D. Del Col, L. Doretti, E. Fornasieri, L. Rossetto, C. Zilio, Performance of finned coil condensers optimized for new HFC refrigerants, *ASHRAE Transactions* 108 (2) (2002) 517-528.



## Chapter 6 **Conclusions**

In this work some aspects related to heat pump and refrigeration systems energy efficiency improvement, to refrigerant charge reduction and to natural refrigerants use are faced.

In this thesis a brief general introduction to a refrigerant system energy efficiency, with respect to the working refrigerant properties (an appropriate choice of operative fluid is one of the basic steps in system design), to the condenser subcooling and to the exergy losses during a two-phase heat exchanger, was presented.

The use of louvered finned flat tube with internal minichannel in the refrigeration industry is investigated as a way to reduce the system charge and costs; a state of the art review within the actual main constraints in the use of this type of heat exchangers is detailed.

The development and the experimental analysis of an air-water reversible heat pump working with R410A refrigerant is reported. The air-side minichannel heat exchanger was properly designed, installed in a commercial heat pump and tested in a climate room. During tests the heat exchanger was modified to achieve a good liquid distribution on the parallel tubes in evaporating conditions. Two identical heat pumps with either the minichannel or the finned coil heat exchanger were placed outdoor and tested during the wintertime in the same operative conditions, while frosting/defrosting cycles occur, the data analysis is presented.

An user-friendly simulation model for calculating the minichannel heat exchangers working as condenser/evaporator was developed and a first validation of the condenser was made using the experimental data carried out on an automotive minichannel condenser working with R134a and R1234yf. The code was modified to take into account the dragged oil

presence in the condenser; the validation showed a good agreement with experimental data.

A prototype water chiller using ammonia as refrigerant with low charge was designed, simulated and tested; the goal was to achieve a low ammonia charge (ammonia is toxic and flammable so the standards are strict about the system charge in relation to the place). Simulation results confirm the low charge and the high efficiency of the system while the experimental work highlighted some technological problems due to the absence on the market of appropriate components.

The use of carbon dioxide in a simple system for heating, cooling and tap water production was analyzed. An appropriate tool was developed and validated over experimental data to simulate the refrigeration system in a widely range of operative conditions. A typical north Italian building was also simulated to analyze its energy demand. Finally, the refrigeration system and the building simulation results were coupled to assess the building yearly energy consumption. The same work was conducted for a commercial heat pump using R410A as refrigerant and the two refrigeration systems performance were compared.

The use of an ejector instead the back pressure valve as throttling device in a heat pump working with carbon dioxide was experimentally investigated; a prototype was made with both the ejector and the back pressure valve with the possibility to switch each other to compare the performance in the same operative conditions. The experimental activity highlighted oil recovery problems, thus the prototype was modified and now a new experimental work is in course.

Finally a method for evaluating the exergy losses during a two-phase heat exchange is detailed and applied in plain evaporator tubes (though it can be utilized for other kind of tube/heat exchanger). Using this method the newer fluorinated R1234yf and R1234ze(E) refrigerants show a lower heat exchange potential compared to R134a and R22. This method was used to calculate the optimal heat exchanger tube length. The analysis showed that

for the newer fluorinated refrigerants the optimization of the circuitry length it is more important compared to the traditional refrigerants.



## *Ringraziamenti*

Desidero ricordare e ringraziare con gratitudine tutti coloro che durante questi 3 anni di dottorato mi hanno supportato ..... e anche sopportato.

Innanzitutto mia madre per il suo costante appoggio.

I professori Ezio Fornasieri e Claudio Zilio per la disponibilità con cui mi hanno seguito e per tutto quello che mi hanno insegnato.

Il professor Zilio assieme al professor James Steve Brown per avermi dato la possibilità di svolgere un periodo di ricerca presso la Catholic University of America ed il Nist: una meravigliosa esperienza molto formativa sia dal punto di vista professionale che personale.

Luca Cecchinato e il mio compagno d'ufficio Marco Corradi che con la loro esperienza e capacità mi hanno seguito assieme ai professori in molti lavori. Silvia Minetto che assieme al prof. Zilio mi ha coinvolto e seguito nelle attività sperimentali sulla CO<sub>2</sub>. L'ing. Sergio Giroto presso la cui azienda si è svolta in parte tale l'attività sperimentale, per avermi ospitato a fare le ore F.S.E.

Il mio compagno d'ufficio Simone Mancin per le nostre lunghe chiacchierate.

I miei compagni d'ufficio durante i primi mesi: Manuel Chiarello che prima di finire il suo dottorato mi ha voluto a fianco per passarmi il lavoro sui minicanali che aveva iniziato, Giovanni Schiochet e Valeria de Giuli.